A STUDY OF COSMIC-RAY POSITRON AND ELECTRON SPECTRA IN INTERPLANETARY AND INTERSTELLAR SPACE AND THE SOLAR MODULATION OF COSMIC RAYS

Thesis by

Alan Coffman Cummings

In Partial Fulfillment of the Requirements

for the Degree of

Doctor of Philosophy

California Institute of Technology

Pasadena, California

1973

(Submitted March 26, 1973)

ACKNOWLEDGEMENTS

This thesis would not have been possible without the guidance and support of my faculty advisor, Professor Rochus Vogt. His invaluable help throughout all phases of this research project is greatly appreciated.

I also wish to express my gratitude to Professor Edward C. Stone for his many suggestions and ideas. He has made substantial contributions to this thesis.

I would like to particularly thank Dr. Carl J. Rice, whose thesis was the predecessor of the work presented here. His aid during the initial phase of my research effort was indispensable. I am also grateful to Dr. Klaus Beuermann. He worked jointly in the 1969 balloon flight program and also supplied the computer programs for calculating atmospheric secondary electrons. In addition, Dr. Rice and Dr. Beuermann, together with Dr. Vogt, developed and flew the original version of the $e^{\pm}$ instrument in 1968, prior to my involvement in the project.

It is a pleasure to acknowledge my friends Dr. Tom Garrard and Dr. John Lupton. Their counseling on many matters, both technical and non-technical, is greatly appreciated. I also thank fellow graduate student and former office-mate Solomon Vidor for commenting upon my day-to-day problems over the past few years.

My theoretical efforts have benefited greatly from discussions with Professor J. R. Jokipii. I also appreciate talks with Professor Alan T. Moffet and Drs. Catherine and Diego Cesarsky.

I am grateful for frequent consultations with Mr. William Blodgett who designed the electronic system of the instrument. Thanks are also due Mr. Ronald Willner, the project's electronic technician, for his assistance during the balloon flight programs of 1970 and 1971.

My thanks go to Messers. John Ullmann, Craig Todd and Greg Whitten, all of whom assisted at various times in this research project.

I wish to thank Professor Robert L. Walker for permission to calibrate the $e^{\pm}$ detector at the Caltech Synchrotron and also Mr. Al Neubeiser for operating the Synchrotron during the calibrations.

I am indebted to the flight crew of Raven Ind. and the members of the Office of Naval Research for the success of the flight operations at Fort Churchill.

I would like to acknowledge the staff of Graphic Arts for their excellent and efficient service. My thanks are extended to Marty Neale and Elinor Murphy for typing some of the rough drafts of this thesis, to Virginia Franklin and Sharon Higley for typing portions of the final draft, and special thanks to Eileen Gribben for her neat and fast typing of the major portion of the final draft.

During part of my graduate study I received financial support from a NASA Traineeship. The research effort described in this thesis was supported by the National Aeronautics and Space Administration under Grants NGL 05-002-007 and NGR 05-002-160.

ABSTRACT

We have measured the differential energy spectra of cosmic-ray positrons and negatrons with energies between ~11 and 1500 MeV during the period 1968-1971 using a balloon-borne magnetic spectrometer. These measurements fill a gap in the previously existing data and permit us to determine, within quantitative limits, the interstellar spectra of cosmic-ray positrons and electrons ($e^+ + e^-$). Knowledge of these spectra provides a crucial tool for studies of the distribution and density of matter and magnetic fields in the interstellar medium and the origin and dynamics of energetic particles contained in the fields.

From a study of the near-Earth electron spectra and their relationship to the interstellar spectrum derived from the galactic non-thermal-radio-background emission, and from a study of the near-Earth positron spectra and their relationship to the interstellar positron spectrum calculated from collisions of cosmic-ray nuclei with the interstellar matter, we have found that the differential energy spectrum of interstellar electrons may be represented as a power-law, $j \propto T^{-1.8}$ for 100 MeV $\lesssim T \lesssim$ 2 GeV, but must flatten considerably at lower energies. From the measured electron charge composition, which we find to be little affected by solar modulation, we have concluded that the majority of cosmic-ray electrons with energies above ~10 MeV are not the result of nuclear collisions in the galaxy but presumably originate in "primary" sources.

In the energy range of our measurements the near-Earth

intensities of cosmic-ray positrons and electrons, as well as the intensity of cosmic-ray nuclei, are significantly lower than their interstellar intensities because the particles are scattered by magnetic irregularities imbedded in the outward-flowing plasma of the solar wind. Long-term changes in the scattering properties of the interplanetary medium, i.e. in the cosmic-ray diffusion coefficient, κ, are responsible for the observed long-term variations in the near-Earth cosmic-ray intensities which are as large as a factor of 10 from "solar minimum" to "solar maximum". We have used the cosmic-ray positron and electron spectra as tools to study the solar modulation mechanism. By using numerical solutions of the cosmic-ray transport equation to relate the near-Earth electron spectra to the interstellar electron spectrum, we have found that the magnetic rigidity dependence of the interplanetary cosmic-ray diffusion coefficient at rigidities from ~100 MV to ~10 GV may be represented as $\kappa \propto R^b$ with b increasing from 0 to ~1-2 with increasing rigidity. However, from a comparison of the near-Earth and interstellar positron spectra we find that below ~60 MV the diffusion coefficient must increase with decreasing rigidity.

The magnitude of the diffusion coefficient at 1 AU derived from the electron and positron modulation studies depends on the assumed radial dependence of κ. In order to place limits on this radial dependence and to make estimates of the size of the solar modulation region, we have also evaluated diffusion coefficients from measurements of the power spectrum of the interplanetary magnetic field near 1 AU. Assuming $\kappa(r) \propto r^n$, we have found that $n \lesssim 1.1$ in order that the calculated modulation beyond 1 AU agrees with the observed

modulation. For κ independent of radius, we obtained consistency between the diffusion coefficients derived by the two methods for boundary distances of the solar modulation region in the range of 6-25 AU.

These diffusion coefficients derived from the electron modulation study must also apply to the cosmic-ray nuclei. As a consistency check, we have used the electron diffusion coefficients to calculate solutions of the transport equation for cosmic-ray protons and He nuclei for four different time periods from 1965 to 1970. Assuming a particular, time-independent form for the interstellar spectra of these particles, we have derived spectra at 1 AU which are consistent with the observations over the full range of intensity variations observed during this solar half cycle.

TABLE OF CONTENTS

Part	Title	Page
I.	INTRODUCTION	1
II.	DETECTOR SYSTEM	7
	A. Overall Description	7
	B. The Gas Čerenkov Counter	11
	C. The Magnet	14
III.	BALLOON FLIGHTS	17
IV.	DATA ANALYSIS	22
V.	RESULTS	31
VI.	DISCUSSION OF SOLAR MODULATION	46
	A. Introduction and Statement of the Problems	46
	B. Background Physics	52
	C. Review of Analytic Approximations to the Transport Equation	55
	1. The Diffusion-Convection (DC) Approximation	56
	2. The Force-Field (FF) Approximation	57
	3. The Convection-Adiabatic Deceleration (CAD) Approximation	59
	D. General Results from Numerical Solutions to the Transport Equation	61
	1. Analysis of Analytic Approximations	62
	a. The CAD Approximation	62
	b. The FF and DC Approximations	65

Part	Title	Page
	2. General Remarks Concerning the Solution of the Transport Equation	68
	a. Effects of the Radial Dependence of the Diffusion Coefficient	69
	b. Effects of Adiabatic Deceleration	71
	c. Discussion of the "Flat" Portion of the Electron Spectra and Rough Estimates of the Modulation (ψ)	73
E.	Quantitative Study of Solar Modulation	82
	1. Determination of the Interstellar Electron Spectrum from the Galactic Non-Thermal-Radio-Background Emission	82
	2. Interstellar Positron Spectra from Galactic Nuclear Collisions	87
	3. Derivation of Modulation Parameters and Implications for the Low-Energy Interstellar Electron Spectrum	90
	a. Comparisons of Measured and Calculated Electron Spectra	91
	b. Comparisons of Measured and Calculated Positron Spectra	95
	4. Relation of Cosmic-Ray Diffusion Coefficient to Power Spectra of the Interplanetary Magnetic Field and Implications for the Radial Dependence of the Diffusion Coefficient	101

Part	Title	Page
	5. Comparisons of Measured and Calculated Spectra of Cosmic-Ray Protons and He Nuclei	109
VII.	SUMMARY	114
Appendix A -	Details of Data Analysis	119
	1. Selection Criteria for Data Analysis	119
	a. Spark-Chamber Performance	119
	b. Trajectory-Consistency Check	120
	2. Rigidity Resolution	124
	3. Raw Flux Parameters	129
	a. Live Time (t_L)	129
	b. Spark-Chamber Efficiency ($D_{GC\check{C}}$)	129
	c. Gas Čerenkov Efficiency Factor ($\check{C}_{eff}$)	131
	4. Background Corrections	135
	a. Upward-Moving Particles	135
	b. Atmospheric Muons and Pions	136
	c. Secondaries Produced in the Gas Čerenkov Counter	136
	d. High-Energy Cosmic-Ray Nuclei	141
	e. Accidental Gas Čerenkov Coincidences	142
	f. Spark-Chamber Alignment	142
Appendix B -	Interstellar Electron Spectrum from Non-Thermal-Radio-Background Data	153
References		170
Figures		179

LIST OF FIGURES

Figure Number	Title	Page
II-1	Cross-Section of the $e^{\pm}$ Detector System	179
II-2	Exploded View of a Spark-Chamber Module	180
II-3	Exploded View of the MOD-2 Magnet and Magnet Guard Counter	181
II-4	Electronic Block Diagram	182
II-5	Gas Čerenkov Counter Light Output as a Function of Particle Energy	183
II-6	Magnetic Flux Density in the Gap of the Analyzing Magnet Versus Position	185
II-7	Geometrical Factor of the MOD-2 Detector Versus Particle Rigidity	186
II-8	Range of the Trajectory Deflection Angles in the MOD-2 Detector as a Function of Particle Rigidity	188
III-1	Trajectories of Three Typical Balloon Flights	189
III-2	Two Representative Time-Altitude Profiles	190
III-3	Deep River Neutron Monitor Counting Rate Versus Time for the Years 1962-1971	192
IV-1	Typical Event Rate Versus Local Time	194
IV-2	Representative Examples of the Measured Event Rate Versus Atmospheric Depth	196
V-1	Primary Positron and Electron Spectra for 1968	197
V-2	Primary Positron and Electron Spectra for 1969	198
V-3	Primary Positron and Electron Spectra for 1970	199
V-4	Primary Positron and Electron Spectra for 1971	200

Figure Number	Title	Page
VI-1	Selected Near-Earth Electron Spectra for the Period 1965-1971.	202
VI-2	Illustration of the Dependence of the Modulated Spectrum on the Magnitude of the Diffusion Coefficient	204
VI-3	Comparisons of the 1 AU Spectra Derived from Analytic Approximations and Numerical Solutions of the Transport Equation	208
VI-4	Radial and Rigidity Dependences of the Diffusion Coefficient Used in Studying the Behavior of Solutions to the Transport Equation	210
VI-5	Calculated Electron Spectra at 1 AU for Different Radial Dependences of κ and for Different Values of the Boundary Distance	212
VI-6	Illustrative Calculation of the Energy-Loss of Cosmic-Ray Positrons Due to Adiabatic Deceleration	215
VI-7	Calculated Electron Spectra at 1 AU for a Diffusion Coefficient Whose Rigidity Dependence Changes at 750 MV	217
VI-8	Frequency Spectrum of the Non-Thermal-Radio Background in the Galactic Anticenter Direction	218
VI-9	Interstellar Electron Spectra Derived from the Non-Thermal-Radio-Background Data	219
VI-10	Calculated Radio Spectra for Three Different Models of the Interstellar Electron Spectra and the Galactic Parameters	220
VI-11	Interstellar Positron Spectra Calculated from Galactic Nuclear Collisions by Different Investigators	221
VI-12	Electron Modulation Parameters for the Period 1965-1971	223
VI-13	Calculated and Measured Electron Spectra at 1 AU for the Period 1965-1971	228

Figure Number	Title	Page
VI-14	Positron Modulation Parameters for the Period 1965-1971	230
VI-15	Calculated and Measured Positron Fractions as a Function of Energy	236
VI-16	Positron and Electron Spectra at 1 AU Derived From a Modulation Parameter Appropriate for 1968	238
VI-17	Approximate Range of the Interstellar Electron Spectrum above 10 MeV	239
VI-18	Observed Power Spectra of the Interplanetary Magnetic Field	240
VI-19	Parallel Diffusion Coefficients Calculated from the Power-Spectra Data	241
VI-20	Radial Diffusion Coefficients Derived from the Electron Modulation Study and from the Power-Spectra Data	242
VI-21	Comparison of Radial Diffusion Coefficients as a Function of Boundary Distance	243
VI-22	Limits on Boundary Distance for Various Radial Dependences of the Diffusion Coefficient	244
VI-23	Comparisons of Measured and Calculated Proton Spectra	246
VI-24	Comparisons of Measured and Calculated Spectra of Helium Nuclei	248
A-1	Definition of Parameters Used for Self-Consistency Checking of Particle Trajectory	249
A-2	Measured Distributions of the Trajectory Parameter Δ	251
A-3	Calculated Electron Scattering-Angle Distribution	252
A-4	Distribution of Measured Deflection Angles in a 790 MeV Positron Beam	253

Figure Number	Title	Page
A-5	Distribution of Small Deflections Measured During the Nighttime Period of Flight 71C2	254
A-6	χ^2 Versus σ_A for Fitting Calculated to Measured Angular Distributions of Cosmic-Ray Protons	255
A-7	Deflection Resolution of the Detector	256
A-8	Measured Count Rates of GC and NON-GC Events for Flight 71C2	257
A-9	Gamma-Ray Spectrum Used in Calculating Secondaries Produced in the Gas Cerenkov Counter	258
A-10	Secondary Positrons and Negatrons Produced by Interactions of γ-Rays in the Gas Cerenkov Counter	259
A-11	Deflection-Angle Distribution of GC Events for 1971	260
A-12	Response Functions of MOD-2 Detector	261
B-1	Model of the Galactic Structure Used in the Calculations of the Synchrotron Intensity	262
B-2	Relative Contribution to Synchrotron Intensity at 10 MHz from Cosmic-Ray Electrons of Different Energies	263
B-3	Correspondence Between Radio Frequency and Electron Energy	265
B-4	Relative Variation of Interstellar Electron Spectrum for Different Galactic Parameters	267

LIST OF TABLES

Table Number	Title	Page
III-1	Balloon Flights	18
IV-1	MOD-1 and MOD-2 Parameters	26
V-1	1968 Positron and Negatron Fluxes	32
V-2	1969 Positron and Negatron Fluxes	34
V-3	1970 Positron Fluxes	36
V-4	1970 Negatron Fluxes	38
V-5	1971 Positron Fluxes	40
V-6	1971 Negatron Fluxes	42
VI-1	Fractional Energy Loss for Representative Values of the Modulation Parameter, $\psi(1,T)$, and the Boundary Distance, D.	74
VI-2	Diffusion Coefficient Parameters - Electron Modulation Study	94
VI-3	Diffusion Coefficient Parameters - Nuclei Modulation Study	111
A-1	Gas Čerenkov Efficiency Factors ($\check{C}_{eff}$)	134
A-2	Summary of Corrections Discussed in Section A.4	144
B-1	Galactic Parameters Used in the Analysis	163
B-2	Power-Law Approximations of the Calculated Galactic Electron Spectra: $j = AT^{\gamma}$	168
B-3	Galactic Parameters Corresponding to the Galactic Electron Spectra of Figure VI-9	169

I. INTRODUCTION

Cosmic-ray electrons were known to exist long before their discovery near Earth in 1960 by Earl (1961) and Meyer and Vogt (1961). Radio astronomers have observed the synchrotron radiation from relativistic electrons in such places as the Sun, Jupiter, the interstellar medium, supernovae envelopes, and other galaxies. Thus they are almost universal in nature.

Because of their universality and their energy losses due to synchrotron radiation and inverse Compton collisions with photons, cosmic-ray electrons represent unique probes for determining physical conditions in the universe. For example, from an analysis of the observed galactic synchrotron background radiation, information on the galactic magnetic field, the structure of the interstellar medium, and the average interstellar electron spectrum can be obtained. On a larger scale, an argument for galactic confinement of the bulk of cosmic rays is that if cosmic-ray electrons were present in the same numbers throughout the universe as they are in our galaxy, then inverse Compton collisions with the universal black-body photons would give rise to an isotropic flux of x-rays far in excess of what is observed. Hence the observation and interpretation of the cosmic-ray electron flux has important implications on the distribution of matter and fields in both interstellar and intergalactic space.

The origin of the electron component of cosmic rays has long been debated. Their existence in expanding supernovae shells suggests that they are directly accelerated in such sources. On the

other hand, collisions of the cosmic-ray nuclei with the interstellar matter give rise to "secondary" electrons through pion decays. Above ~10 MeV the calculated fraction of positrons* in the collision-source model is much higher than that observed near Earth, giving strong evidence for the existence of sources of directly accelerated negatrons (Beuermann et al., 1970, Fanselow et al., 1969). Below ~10 MeV secondary knock-on negatrons outnumber those produced in nuclear interactions (Abraham et al., 1966), and the calculated intensity is consistent with the observed average flux (Cline and Porreca, 1970). However, the flux of low-energy electrons is highly variable, even during solar quiet times (McDonald et al., 1972). The origin of these variations is uncertain, and hence the origin of the low-energy particles themselves remains in doubt.

Many solutions to problems in cosmic-ray astrophysics depend on a knowledge of the energy spectra of the particles at their source. However, near Earth we observe the spectra which are modulated by the outward-flowing solar plasma. The study of this long-term modulation, which is anti-correlated with the 11 year sunspot cycle, has two immediate aims: 1) the determination of the local interstellar spectra of cosmic rays, and 2) information on the state of the interplanetary medium through which the particles diffuse and lose energy. Although electrons comprise only a small fraction of the total cosmic-ray flux, the study of their modulation provides us with important

---

*In this thesis the designations "positron" and "negatron" will be used whenever the charge sign is relevant to the discussion. The term "electron" will refer either to the sum $e^+ + e^-$ or to the electron component of cosmic rays without regard to sign.

advantages over nuclei studies in realizing these aims. Among these advantages are:

1) The possibility of independent knowledge of the interstellar spectra of electrons and positrons from the non-thermal-radio-background data and calculations of galactic nuclear collisions, respectively. For the nuclei studies we can only estimate the interstellar spectrum by extrapolating the high-energy, near-Earth data to low energies using an arbitrary power law.

2) The relatively high sensitivity of the near-Earth electron spectrum to the interplanetary cosmic-ray diffusion coefficient and the interstellar spectrum. It has now been realized that the low-energy ($<$1GeV/nucleon) spectra of nuclei, where most of the available data fall, are shaped primarily by convection and adiabatic deceleration and are relatively insensitive to the low-energy values of both the interstellar spectrum and diffusion coefficient (Goldstein et al., 1970a; Rygg and Earl, 1971; Urch and Gleeson, 1972; Garrard, 1973). Because electrons are relativistic in the energy region of 10 - 1000 MeV, they lose energy through adiabatic deceleration at a slower rate than the nuclei. The total effect of adiabatic deceleration is diminished further for electrons because the diffusion coefficient is proportional to velocity. Hence, electrons diffuse much faster than nuclei of the same energy and, therefore, lose less energy in penetrating to the Earth from the boundary.

We emphasize that the study of cosmic-ray electron spectra involves a great number of interrelated topics in astrophysics. For example, the study of the modulation of electrons and positrons has

direct bearing on the state of the interplanetary medium and the interstellar intensity of both electrons and nuclei. Many galactic parameters, e.g. the magnetic field strength and the temperature of the interstellar medium, are involved in relating the interstellar electron intensity to synchrotron radiation in the galaxy. Similarly, the calculation of the negatron and positron spectra from galactic nuclear collisions depends on physical conditions in the interstellar medium. The propagation and confinement of cosmic rays also depend on these galactic parameters. Hence, the interpretation of the cosmic-ray electron flux observed near Earth has bearing on the condition of both local and interstellar space.

Information on the galactic parameters used in these studies involves a wide variety of experimental and theoretical physics. The magnitude of the average magnetic field in the galaxy has been estimated to be in the range 3 - 5 μ-gauss on the basis of the dynamical balance of the cosmic-ray pressure with the pressure of the galactic magnetic field (Parker, 1969a). This range is in rough agreement with the observations of Faraday rotation and dispersion of pulsar signals. The dispersion measurements also yield information on the number density of thermal electrons in interstellar space. The temperature and number density of the thermal electrons in interstellar clouds are obtained from observations of 21 - cm absorption. These parameters of the interstellar medium are important in determining the absorption of synchrotron radiation.

Similarly, physical conditions in interplanetary space are inferred from a variety of sources. For example, observations of the

power spectrum of the interplanetary magnetic field yield important information on the cosmic-ray diffusion coefficient. Further information on this diffusion coefficient comes from studies of the modulation of cosmic-ray nuclei and from studies of solar-flare particle propagation (Lupton, 1972).

In this thesis we shall discuss these interrelated phenomena and attempt to form a consistent picture of our knowledge of cosmic-ray electrons. We shall make use of cosmic-ray positron and negatron data derived from observations with Caltech instruments in the range from ~11-1500 MeV over the period 1968-1971. We shall supplement our data with those of other experimenters to cover the solar half-cycle beginning in 1965. We shall discuss the use of numerical solutions to the equation describing particle propagation in the interplanetary medium in determining the parameters governing the modulation of electrons. To calculate the diffusion coefficient in the interplanetary medium necessary to explain the observations, we shall need a knowledge of the local interstellar spectrum of electrons. For this purpose we reanalyze the non-thermal-radio-background data and derive a band of possible electron spectra above ~100 MeV. With these spectra we arrive at the rigidity dependence of the diffusion coefficient. An independent method of calculating this dependence is to use the power spectrum of the interplanetary magnetic field. We shall compare the diffusion coefficients calculated in the two ways to gain information on both the rigidity and radial dependences of the diffusion coefficient. Below ~100 MeV the radio data yield little information on the interstellar electron spectrum. At these energies

we use the near-Earth positron data and the calculated interstellar positron spectrum to obtain information on solar modulation and the interstellar spectrum. We shall also check the electron-derived solar modulation parameters for their applicability to cosmic-ray nuclei.

Investigations similar to portions of the study presented here have been carried out by Beuermann et al. (1969, 1970) and Urch and Gleeson (1972). Beuermann et al. used their 1968 cosmic-ray positron data to discuss the absolute modulation of positrons below ~200 MeV. The present study significantly extends their work by including more recent positron data and by including a detailed discussion of solar modulation of both positrons and electrons from ~10 MeV to 10 GeV over the solar half-cycle beginning in 1965. Urch and Gleeson (1972) derived the rigidity dependence of the diffusion coefficient above a few hundred MeV from the near-Earth electron data and an interstellar electron spectrum calculated from the non-thermal-radio-background data. These diffusion coefficients were then used in fitting the cosmic-ray proton and He-nuclei data. The present study extends their work in several ways, e.g. by 1) including a detailed study of the transport equation for electrons using numerical solutions, 2) including the positron data in the study to provide information on the interstellar spectrum and diffusion coefficient at low energies 3) quantitatively correlating positron and electron modulation results to determine consistent interstellar spectra of these particles, and 4) quantitatively correlating power-spectra data and electron modulation results to derive information on both the radial and rigidity dependence of the diffusion coefficient.

II. DETECTOR SYSTEM

A. Overall Description

The positron and negatron data presented in this thesis were derived from observations with a balloon-borne magnetic spectrometer near the top of the atmosphere. The instrument determined the charge sign and magnetic rigidity (momentum divided by charge) of particles by measuring their deflection in a magnetic field. Observations have been performed with the detector in two forms, hereafter referred to as MOD-1 and MOD-2. MOD-1 was used in 1968 and 1969 and has been described in detail by Rice (1970). It has a 1000-gauss permanent magnet and an effective rigidity range of 6-200 MV. MOD-2 was flown in 1970 and 1971 and is identical to MOD-1 except that it employs a 2300-gauss magnet and an additional gas Čerenkov counter. Its rigidity range is 15-1500 MV. A brief overall description of MOD-2 will be given for completeness, but emphasis will be placed only on the modifications to the original instrument. A schematic cross-section of MOD-2 is shown in Figure II-1.

An "event" (observation of a charged particle) is defined by a triple coincidence between Telescope Counter #1 (T1), Telescope Counter #2 (T2), and the Lucite Čerenkov Counter (LČ), and the absence of a pulse from any of the guard counters. This coincidence produces the fast-gate pulse (FG) which triggers the high voltage to the spark chambers and initiates the data read-out cycle. The two 4-gap spark chambers are used to define the particle's trajectory before and after passing through the gap of the permanent magnet. An exploded view of a spark-gap module is shown in Figure II-2. The

wires are .0022" diameter silver-coated beryllium copper and are evenly spaced at 48 per inch. The active area of each module is 5" x 9". The magnetostrictive technique is used in determining the spark locations. We measure the time delay between a fiducial pulse (fiducial wires are located outside the active chamber area at each end of the module) and a subsequent spark pulse. The spatial resolution is approximately gaussian with a standard deviation of ≈.008". If more than one spark is present in a chamber, the location of the spark nearest the pickup coil is recorded and a multiple-spark-indicator (MSI) bit is set. The modules are continuously flushed during flight by standard "spark-chamber neon" (90% neon and 10% helium). An ethanol admixture acts as a quenching agent.

The lucite Čerenkov counter was retained from the MOD-1 version and serves two functions:

1) It eliminates a large portion of the cosmic-ray nuclei flux, thereby increasing the effective live time for electron events.
2) It eliminates approximately 96% of the upward-moving splash albedo particles.

The velocity threshold for Čerenkov radiation in lucite is 0.67 c which corresponds to rigidity thresholds of 0.46, 845, and 1690 MV for electrons, protons, and alpha particles, respectively. Electronic data handling effectively increases these thresholds by ~15%.

The gas Čerenkov counter (GČ) was added to the MOD-1 detector system in order:

1) to eliminate contamination due to cosmic-ray nuclei above LČ threshold; because of the larger MOD-2 magnet, these particles would be indistinguishable from high-energy electrons, and

2) to further discriminate against upward-moving particles. Its velocity threshold is 0.9984 c which corresponds to rigidity thresholds of 0.0091, 16.8, and 33.6 GV for electrons, protons, and alpha particles, respectively. Each of the two phototubes of the counter (see Figure II-1) acts independently; a coincidence between the fast-gate pulse and the output of one phototube generates a data bit which is recorded as part of the event's data word.

The specially designed magnet guard counter (MA) is shown with the magnet in an exploded isometric projection in Figure II-3. The pole faces and the upper surface of the magnet are covered with a plastic scintillator which prevents the analysis of particles that might interact or scatter in the magnet. The 3-cm x 12-cm open passage, together with T1 and T2, determines the acceptance cone of the detector.

The sides and top of the instrument, except for the telescope aperture, are surrounded by guard counters. These counters are in active anti-coincidence and eliminate particles which enter the detector from outside the acceptance cone and which might interact, providing particles which trigger the telescope counters.

A general block diagram of the electronics system is shown in Figure II-4. An Accutron clock is used as a timing device. It drives a 4-bit time scaler (16 minute cycle) whose output is used to control the data-collection cycle. During the first 15 minutes (referred to as Phase A) of each cycle, particles which satisfy the coincidence requirements initiate a readout of the data, which requires 350 msec for completion. Each data word, consisting of 8

spark locations, the MSI bits, the two $\check{C}$ bits, the time, and temperature, is recorded on 16-channel magnetic tape. The remaining minute of the 16-minute cycle is referred to as Phase B; during this time the normal coincidence trigger input is blocked and the following rates are scaled: $\check{C}$, T1 ^ T2, T1 ^ T2 ^ $\check{C}$, MA, and TA (sum of all guard counters except MA). These rates are monitored to check counter performance, to detect variations in background radiation, and to determine detector dead time due to the guard counters. At the beginning of Phase B an internal trigger is generated which results in the application of high voltage to the chambers and the initiation of the readout cycle. Since no particle is normally present in the chambers, the spacing between the fiducials is thus recorded to provide a check of the digitizing circuitry.

The atmospheric pressure during flight is recorded by a photobarograph, a device which photographs a Wallace-Tiernan aneroid barometer (FA 160), a clock, and a thermometer at 5-minute intervals. The barometer is calibrated before and after each flight and is accurate to $\pm$ 0.1 mb at 2.4 mb, our typical float altitude. Usually, two redundant photobarographs were flown on each flight.

In the following we discuss in more detail the gas Čerenkov counter and the 2300-gauss magnet, the two major additions to the MOD-1 detector.

B. The Gas Čerenkov Counter

The gas Čerenkov counter (see Figure II-1) contains sulfur hexafluoride at 2.2 atmospheres absolute pressure. This configuration has a velocity threshold of v = 0.9984c. The absolute kinetic energy threshold for various particles are:

electrons	8.62 MeV
muons	1.78 GeV
pions	2.50 GeV
protons	15.7 GeV
alpha particles	62.9 GeV

The two flat mirrors serve to reflect the Čerenkov light into the phototube faces. The mirrors are constructed of 1/8-inch lucite and are aluminized on their upper surfaces. The conical mirrors are made of spun aluminum with their interior surfaces aluminized. A coating of magnesium fluoride covers all mirror surfaces to retard oxidation which would otherwise cause poor reflectivity at ultraviolet wavelengths. The conical and flat mirrors are mounted on a thin aluminum basket which is not shown in the figure. Of these pieces, only the flat mirrors are within the acceptance cone of the detector.

The phototubes are EMI 9531 QB (Whittaker Corp., Plainview, N. Y.) which have quartz faces 3 1/2 inches in diameter. A 1/2-inch-thick fused-silica window (Corning Glass Works, Orange, California) is mounted in front of each phototube to protect them from the gas pressure. High voltage for the tubes is supplied by DC-DC converters (Crestronics, Crestline, California) which are mounted inside the phototube housings. In addition, electronic pulse-discrimination and

coincidence circuitry is mounted inside the housings which also serve as a shield from the spark noise. A coincidence between the fast-gate pulse and the discriminator output of either phototube generates a data bit for the phototube involved.

The counter was calibrated at the Caltech Synchrotron using 300-MeV positrons. Forty-five incident beam directions were chosen to cover the acceptance cone of the detector. For each incident direction a pulse-height analysis was made, and from the resulting distribution the mean number of photoelectrons emitted from the cathode was determined. For each phototube this number varied from approximately 4-10 over the range of incident directions. The average over direction was about 6 photoelectrons. The electronic discrimination level was set just above the one photoelectron level, which results in an average efficiency of approximately 98%. However, the efficiency of the counter slowly decreases with time due to oxidation of the mirror surfaces. Therefore, we determined the efficiency of the gas Čerenkov counter directly from the flight data by a procedure described in Appendix A.3.c. We found that the efficiency was approximately 93% and 84% for 1970 and 1971, respectively.

The effective energy "threshold" is not precisely determined since the actual number of photoelectrons emitted from the photocathode is Poisson distributed about the mean; hence, any particle above the absolute velocity threshold has a finite probability of producing enough photoelectrons to trigger the discriminator. In Figure II-5 we show a plot of the Čerenkov light output for singly-

charged particles versus $\gamma = \frac{W}{mc^2}$ where W is the total energy of the particle and m is the rest mass. Particles with γ greater than about 3 times the absolute threshold value produce more than 90% of the output level of completely relativistic particles. We roughly estimate the "effective" threshold as 50% of the full output. The corresponding effective kinetic-energy thresholds for the various particles are:

electrons	12 MeV
muons	2.5 GeV
pions	3.4 GeV
protons	22 GeV
alpha particles	67.5 GeV

The noise rate of the phototubes was monitored during the Phase B period. At float altitude typical values of the combined noise rate were 600/sec and 1200/sec in 1970 and 1971, respectively. The probability of an accidental coincidence is given approximately by the product of the noise rate and the sum of the widths of the fast-gate and the discriminator output pulses, which was about 10^{-6} seconds. Thus these probabilities were roughly .0006 and .001 in 1970 and 1971, respectively.

C. The Magnet

The 2300-gauss magnet (Indiana General Corp., Valparaiso, Ind.) used in the MOD-2 configuration is shown in Figure II-3. The construction is similar to the 1000-gauss magnet employed in the MOD-1 configuration as described by Rice (1970). Alnico-8 permanent magnets are used, and a magnetic circuit of steel reduces external fields as much as possible. The three orthogonal components of the field were measured at 1-cm intervals throughout the volume accessible to the particles out to a distance of 8 cm above and below the magnet. In Figure II-6 we show a plot of these three components along three representative paths through the magnet gap. The locations refer to a right-handed coordinate system with the origin at the center of the gap. The z-axis is vertical and positive upward; the x-axis is perpendicular to the pole faces and positive toward the south pole (see Figure II-3). The magnetic field was monitored before and after each flight by a permanently mounted Hall effect device (F. W. Bell, Inc., Columbus, Ohio); no change in the field strength greater than ~10 gauss was noted on any of the flights.

The geometrical factor of the MOD-2 detector was determined at 7 different rigidities between 12 and 400 MV by the Monte-Carlo method described by Rice (1970). In Figure II-7 we show the geometrical factor as a function of rigidity. The error bars represent the fluctuation due to the finite number (1000) of valid trajectories used in the calculation.

The deflection of a particle of rigidity R (MV) in a magnetic field B is given by

$$\theta(\text{rad}) = \frac{3 \times 10^{-4}}{R} \int B_{\perp} \, d\ell \qquad \text{(II-1)}$$

where $B_{\perp}$ (gauss) is the component of the field normal to the trajectory and $d\ell$(cm) is an increment of distance along the path. The line integral in equation II-1 is referred to as the magnetic path, M. The Monte-Carlo program that calculates the geometrical factor also computes the value of M along each particle trajectory. In Figure II-8 we show the mean values of R times θ in MV-radians at 7 rigidities between 12 and 400 MV. The solid error bars refer to the rms deviation and the dashed error bars represent the extreme values. At each rigidity the value of $R\theta$ is within 2% of 8.85 MV-radians. The rms deviation is typically less than 2% of the mean and the extreme values are within about 7% of the mean. Since the resolution of the detector, FWHM (see Appendix A.2) is $\gtrsim$ 16% we can use the mean value with negligible error. Thus we use the following approximate relationship between deflection angle and rigidity for all particles:

$$R = \frac{8.85}{\theta} \text{ MV} \quad \text{(MOD-2)} \qquad \text{(II-2a)}$$

The corresponding relationship for the MOD-1 detector, using a 1000-gauss magnet, is

$$R = \frac{3.55}{\theta} \text{ MV} \quad \text{(MOD-1)} \qquad \text{(II-2b)}$$

(Rice, 1970).

The complete sheathing of the magnet by the magnet guard counter eliminates particles which interact in the magnet pole faces

and thus eliminates the necessity of detailed trajectory reconstruction. It is thus sufficient to read out spark locations in the y-z projection only, which saves considerable data storage and detector live time.

III. BALLOON FLIGHTS

The Caltech data presented in this thesis were derived from 10 high-altitude balloon flights launched from Ft. Churchill, Manitoba during the summers of 1968, 1969, 1970, and 1971. (The data from 1968 were previously published. (Beuermann et al., 1969, 1970)) We summarize in Table III-1 the relevant information on these flights.

In Figure III-1 we show trajectories of three typical flights. We also show in the figure the invariant latitude contours, calculated from the internal field only (Cain et al., 1967), in order to indicate the trajectories in the geomagnetic field.

Figure III-2 shows two typical altitude profiles. The solid curve is from flight 71C2 and is representative of the altitude profiles of eight of the flights. In each of these eight flights the launch was timed so that the instrument passed through 70 g/cm^2 altitude after the evening transition to low geomagnetic cutoff. This timing ensured that the ascent data used in the separation of atmospheric secondaries were not contaminated by return albedo electrons. (See Chapter IV.) The dashed curve in Figure III-2 is from flight 69C1. This step profile and a similar one from flight 69C2 were used to more accurately define the atmospheric depth dependence of the electron flux in 1969.

The relationship of our flights to the 11-year solar modulation cycle is shown in Figure III-3. We have plotted the daily average of the hourly count rate of the Deep River neutron monitor (Steljes, 1965-1971) for the period 1962-1971. Ground-based neutron monitors record the near-Earth flux of high-energy cosmic-ray nuclei ($\gtrsim$ 1 GeV/nucleon) and serve as a convenient continuing reference of the

TABLE III-1

Balloon Flights

Flight No.	68C1	68C2	68C3	69C1	69C2	69C3	70C1	70C2	71C1	71C2
Launch Date	7/16	7/21	7/29	6/14	6/29	7/5	7/5	7/18	7/11	7/17
Launch Time (UT)	00:27	01:04	01:31	21:37	22:51	23:08	02:51	23:44	01:19	02:11
Begin Float (UT)	03:49	04:09	04:53	01:18 6/15	01:29 6/30	02:06 7/6	05:40	02:54 7/19	04:24	05:34
End Night Float[a] (UT)	09:09	09:45	10:45	12:30	10:02	09:18	12:36	09:50	11:04	10:06
Total Live Time at Float Altitude-Night (Min)	251	254	265	266	239	340	334	330	297	201
Average Float Altitude Night (g/cm^2)	2.4	2.4	2.4	3.4	3.3	2.9	2.5	3.5	2.4	2.4
Terminate (UT)	17:15	19:18	01:11 7/30	14:34	19:54	15:47	18:20	21:28	16:11	17:56
Total Live Time at Float Altitude (Min)	625	695	932	(b)	(c)	591	462	874	520	543
Average Float Altitude (g/cm^2)	2.3	2.3	2.5	(b)	(c)	2.7	2.4	3.3	2.4	2.4

high-energy cosmic-ray intensity. The neutron monitor intensities reach a maximum during the period of minimum solar activity (1965-1966) and a minimum during solar maximum (1969-1970). The dates of our flights are marked with vertical lines in Figure III-3. The flights cover the period near solar maximum. We shall supplement our data with those of others to cover the solar half-cycle beginning in 1965.

Since we are interested in the long-term modulation of galactic cosmic-ray electron spectra, it is important to identify short-term variations that might affect our measurements. Short-term fluctuations are generally associated with solar activity. The energy spectra of particles emitted from the sun are usually quite steep and, hence, the effect of solar emission is most significant at low energies. In addition, Forbush decreases usually follow large solar flares and produce a general depression of the galactic cosmic-ray flux below several GeV.

We have examined the following sources of data relating to solar activity during the period of our balloon flights:

1) ESSA bulletins (ESSA Solar Geophysical Data, 1968-1971), which contain, for example, data from solar proton monitors on Explorer 34 and 41 satellites ($E_p \geq 10$ MeV) and on the ATS-1 satellite ($E_p \geq 5$ MeV), geomagnetic indices, and daily average of neutron monitor rates.
2) Caltech cosmic-ray experiment on the OGO-6 satellite, which provided information on low-energy protons and electrons from June 1969 - July 1970.
3) Goddard Space Flight Center cosmic-ray experiment on the IMP series of satellites, which provided almost continuous data on 3 - 12 MeV

electrons from November 1963 - September 1969. (A summary of the electron counting rates from these experiments is given by McDonald et al., 1972.)

The observations of 1968, 1969, and 1970 were made during or just after the recovery phases of Forbush decreases, as indicated by the neutron monitor counting rate (see Figure III-3). However, from examination of the data from the other sources, we have concluded that short-term solar activity, e.g. solar flares, did not contaminate our electron fluxes.

We have also examined the Goddard Space Flight Center 3 - 12 MeV electron data for evidence of the large quiet-time increases observed below ~25 MeV (L'Heureux et al., 1971; McDonald et al., 1972). We have concluded that our 1968 balloon flights corresponded to quiescent flux levels. No comparisons could be made for the summer of 1969 since the published 3 - 12 MeV data extend only to mid-March 1969. However, the raw fluxes from different flights during the 1969 summer are not significantly different. Hence, we may assume that our data are typical of undisturbed times.

We have made similar comparisons of the raw fluxes from different flights for the summers of 1968, 1970, and 1971. In the absence of significant differences we have combined the data from the flights of the same summer for greater statistical accuracy.

IV. DATA ANALYSIS

The data analysis procedure for the observations made with the detector in the MOD-1 configuration has been previously described (Rice, 1970). The procedure for the MOD-2 data is similar; however, the addition of the gas Čerenkov counter and the larger magnet does require some new considerations. We shall give a general outline of the procedure; details of the analysis technique are described in Appendix A.

The basic information provided in the data word for an event consists of: the spark location in each of the eight spark-gap modules (4 above and 4 below the magnet), the multiple-spark-indicator bits, the gas Čerenkov bits, and the time and temperature (see Chapter II). In the initial phase of the analysis we sort the events according to spark chamber performance. The selection criteria for this sorting are reviewed in Appendix A.1.a. Roughly 15% of the data are rejected from analysis in applying these criteria.

In the process of determining chamber performance, the particle trajectory through each spark chamber (4 spark modules) is determined for the analyzable events by making a least-squares fit to the measured spark locations to a straight line. The bending angle through the magnet is then computed. A trajectory-consistency check is made to determine whether the calculated trajectories in the two spark chambers are consistent with the bending expected in the magnetic field for the computed deflection angle. The selection criterion established for this test is described in Appendix A.1.b. The criterion depends on the resolution of the instrument (see Appendix A.2) and is such that

there is very little probability that an event with a misfit trajectory, etc., is accepted. Because of resolution effects approximately 11% of valid MOD-1 events and about 7% of valid MOD-2 events are also rejected.

The deflection angle computed from the trajectories is inversely proportional to particle rigidity (equations II-2a and b). The relationship between this computed rigidity and the true particle rigidity involves a study of the resolution of the detector. The ability of the detector to measure the rigidity of a particle is affected primarily by 1) multiple scattering within the chambers or magnet gap, and 2) intrinsic angular resolution resulting from the spatial resolution (≈.008") of each spark location measurement. Both effects, as well as the results of calibrations at the Caltech Synchrotron, are discussed in Appendix A.2. The result is that the angular probability distribution, $P(\theta, \theta')d\theta'$ = probability that a particle with rigidity R corresponding to deflection angle θ will actually be observed to have deflection angle between θ' and $\theta' + d\theta'$, is approximately Gaussian, i.e.,

$$P(\theta,\theta') = \frac{1}{\sigma_\theta\sqrt{2\pi}} \exp\left[\frac{-(\theta-\theta')^2}{2\sigma_\theta^2}\right] \qquad \text{(IV-1)}$$

where σ_θ is the standard deviation. From Appendix A.2 we have:

$$\sigma_\theta = \sqrt{(.17\theta)^2 + (.0025)^2} \qquad \text{MOD-1} \qquad \text{(IV-2a)}$$

$$\sigma_\theta = \sqrt{(.068\theta)^2 + (.0025)^2} \qquad \text{MOD-2} \qquad \text{(IV-2b)}$$

The deflection resolution P, FWHM, is given by:

$$P \equiv \frac{2.36\sigma_\theta}{\theta} = \sqrt{(.40)^2 + \left(\frac{.0059}{\theta}\right)^2} \qquad \text{MOD-1} \qquad \text{(IV-3a)}$$

$$P = \sqrt{(.16)^2 + \left(\frac{.0059}{\theta}\right)^2} \qquad \text{MOD-2} \qquad \text{(IV-3b)}$$

A plot of the resolution is shown in Figure A-7. Note that the effect of multiple scattering (constant term in equations IV-3a and b) is dominant below ~100 MV and is insignificant above ~500 MV. For MOD-2 the angular resolution has a minimum value of ~16% and increases to 100% at ~1500 MV ($\theta \approx .006$ radians).

Once the bending angles are determined for the analyzable events, the data are sorted into deflection-angle (energy) bins over appropriate time intervals. In determining the flux of electrons, only data tagged with a gas $\check{C}$erenkov bit are used. The raw flux in units of particles/(m^2 sec sr MeV) for a given time interval is defined by:

$$F_i = \frac{N_i}{t_L \, \bar{G}_i \, D_{GC\check{C}} \, C_{eff} \, \Delta T_i} \qquad \text{(IV-4)}$$

where:

i = energy interval index

N_i = number of GC$\check{C}$ events in ith energy interval during specified time interval

t_L = total live time during the time interval

$\bar{G}_i$ = average geometrical factor for the ith energy interval

$D_{GC\check{C}}$ = spark chamber efficiency factor

ΔT_i = width of ith energy interval

C_{eff} = gas $\check{C}$erenkov efficiency factor.

For convenience, we list in Table IV-1 the deflection-angle intervals, the corresponding energy intervals, and the average geometrical factors for both MOD-1 and MOD-2 data. The parameters t_L, D_{GC} (typically 0.75 - 0.85), and C_{eff} (0.93 in 1970 and 0.84 in 1971) are discussed in Appendix A.3.

In this thesis we are interested in discussing the implications of the flux of primary electrons, i.e. galactic particles which have penetrated through the interplanetary medium to 1 AU. Therefore, in analyzing electron fluxes observed near Ft. Churchill, Manitoba it is important to distinguish between fluxes at rigidities above the geomagnetic cutoff rigidity, which consist of primary electrons and atmospheric secondaries, and those fluxes below cutoff, which consist of re-entrant albedo electrons and atmospheric secondaries. Recent calculations (Smart, 1971; Smart and Shea, 1972), based on a magnetospheric model with magnetic fields of both internal and external origin, have shown that the geomagnetic cutoff rigidity for Ft. Churchill ($\Lambda \approx 70^{\circ}$) is approximately 150 MV during local daytime (~0600 to ~1800 local magnetic time) and has an abrupt transition (due to the asymmetry of the magnetosphere) to a value below 20 MV for local nighttime. Since the intensity of re-entrant albedo electrons is found to be larger than that of primary electrons, this cutoff rigidity transition is observed in balloon-borne electron detectors as a change in the counting rate of low-energy electrons ($\lesssim$ 150 MeV). Such transitions have been observed near Ft. Churchill in the data from the Caltech instrument (Rice, 1970), as well as in the data from other experiments (Jokipii et al., 1967; Hovestadt and Meyer, 1970; Israel and Vogt, 1969).

TABLE VI-1

A. MOD-1 Parameters

Index (i)	Deflection Angle Interval (Radians)	Energy Interval at Detector (MeV)	Average Geometrical Factor (cm^2 sr)
1	.6 - .3	5.4 - 11.3	2.52(e^+) 2.17(e^-)*
2	.3 - .144	11.3 - 24.1	3.50
3	.144 - .072	24.1 - 48.8	3.70
4	.072 - .036	48.8 - 98.1	3.70
5	.036 - .018	98.1 - 197	3.70

*The asymmetry in the geometrical factor in the lowest energy range is due to a slight asymmetry in the geometry of the detector.

B. MOD-2 Parameters

Index (i)	Deflection Angle Interval (Radians)	Energy Interval at Detector (MeV)	Average Geometrical Factor (cm^2 sr)
1	.6 - .3	14.3 - 29.0	2.14
2	.3 - .15	29.0 - 58.5	3.14
3	.15 - .072	58.5 - 122	3.62
4	.072 - .036	122 - 245	3.80
5	.036 - .018	245 - 491	3.80
6	.018 - .009	491 - 983	3.80
7	.009 - .006	983 - 1475	3.80

An example of a typical transition is shown in Figure IV-1. We show the hourly count rate plotted versus local time for the five lowest energy intervals of flight 71C2. Positrons (dotted histogram) and negatrons (solid histogram) are shown separately. In the low-energy intervals ($\lesssim$ 245 MeV) we use only the indicated nighttime (low-cutoff) period in deriving electron intensities. Since no night-day transition was observed above 245 MeV on any of the flights of 1970 or 1971, the total float period is used in computing the fluxes for the three highest energy intervals for these years. The raw flux measurements at float altitude for 1968, 1969, 1970, and 1971 will be presented in Chapter V.

These properly selected raw fluxes at float altitude consist of primary cosmic-ray electrons and secondary electrons generated in the atmosphere above the detector. We have also considered the following possible sources of contamination: upward-moving particles (splash albedo and those due to γ-ray interactions in the lucite Čerenkov counter), atmospheric muons and pions, secondaries produced in the gas Čerenkov counter, high-energy cosmic-ray nuclei above gas Čerenkov threshold (which could be incorrectly identified as electrons), accidental gas Čerenkov coincidences, and spark chamber misalignment. For the highest energy interval of the MOD-2 data it was necessary to make small corrections for contamination from high-energy nuclei, accidental gas Čerenkov coincidences, and spark chamber misalignment. In all other MOD-2 energy intervals the corrections were negligible. In the case of MOD-1 data, small corrections in the lower energy intervals for upward-moving particles were necessary. The investigation of all the sources of contamination mentioned above is described in Appendix A.4. The

values of the significant corrections are listed in the data tables of Chapter V.

At our typical float altitude (2.4 g/cm^2) atmospheric secondary electrons represent a large contribution to the flux below a few hundred MeV. The procedure for separating these particles from the primary electrons has been described in detail (Rice, 1970). We shall only briefly describe the method.

The atmospheric depth dependences of the positron and negatron rates* in a given energy interval are determined from the data collected during ascent and descent. We represent these observed rates, $r_i^{\pm}$, by:

$$r_i^{\pm}(d) = a_i^{\pm}\, s_i^{\pm}(d) + b_i^{\pm}\, p_i^{\pm}(d) \qquad \text{(IV-5)}$$

where d is the atmospheric depth, $s_i^{\pm}(d)$ and $p_i^{\pm}(d)$ represent the calculated depth dependence of the rates of secondary and primary positrons or negatrons, respectively, and $a_i^{\pm}$ and $b_i^{\pm}$ are parameters giving the relative contribution of each component. We use the calculations of Beuermann (1971) to evaluate the functions $s_i^{\pm}(d)$ and $p_i^{\pm}(d)$. The $s_i^{\pm}(d)$, the secondaries generated by the nuclei component of the cosmic rays, are calculated using an incident nuclei spectrum adjusted from year to year according to changes in the Mt. Washington

*Local rates (number observed in a given energy interval per second) rather than fluxes (N/m^2.sec.sr.MeV) are used for convenience because the average geometrical factor depends on the energy dependence of the spectrum which changes with depth.

neutron monitor rate (Lockwood, private communication) and in the integral flux of nuclei above 400 MeV/nucleon which is measured directly by our detector. To calculate the $p_i^{\pm}(d)$ it is necessary to assume specific forms for the primary positron and negatron spectra incident at the top of the atmosphere.

A least-squares fit is made to determine the values of $a_i^{\pm}$ and $b_i^{\pm}$, as well as their standard deviations $\sigma_{a_i^{\pm}}$ and $\sigma_{b_i^{\pm}}$. The local rate at float altitude of primary positrons and negatrons is then given by

$$e_i^{\pm} = b_i \; p_i^{\pm}(d = \text{float altitude}). \qquad \text{(IV-6)}$$

The rates are converted to fluxes and corrected to the top of the atmosphere by a procedure described in Appendix A.5. The corrected fluxes are then used to estimate a new primary input spectrum in an iterative calculation. In practice the derived spectrum at the top of the atmopshere is not very sensitive to the assumed input spectrum, and the process converges quickly.

The procedure described above for the separation of the primary and secondary components by a fitting technique is used for the lowest energy intervals ($\lesssim$ 245 MeV) where the growth curves can be measured with reasonable statistical accuracy. For the highest-energy intervals (MOD-2) these growth curves are statistically not as well defined. At these energies, however, the atmospheric secondaries correction is sufficiently small so that the secondary component can be calculated and simply subtracted from the observed flux to give the

primary contribution.

Two examples of the fitting technique for determining the primary and secondary components of the measured flux are shown in Figure IV-2. Figure IV-2a illustrates a case in which a relatively large contribution of residual primaries is obtained; Figure IV-2b shows a case in which zero primary flux is determined. The upturn at large atmospheric depths in the residual primary curve of Figure IV-2a is due to the energy dependence of the incident primary spectrum and its changes due to energy loss in the atmosphere.

V. RESULTS

In this capter we present the results of the analysis described in Chapter IV and Appendix A. Since the energy range and the data analysis procedure were somewhat different for the two detector configurations of our instrument, we discuss the results from MOD-1 and MOD-2 observations separately.

The 1968 and 1969 observations were made with the MOD-1 detector configuration. The absence of the gas Čerenkov counter and the smaller 1000-gauss bending magnet restricted the rigidity range to 6-200 MV and required corrections at the low energies for gamma-ray-induced background and splash albedo. The method of correcting for gamma-ray interactions in the lucite Čerenkov counter has been described by Rice (1969). His results have been changed slightly and the estimated errors reduced as a result of further calibrations at the Caltech Synchrotron. In addition, the splash-albedo corrections of Rice (1970) have been reduced by one-third. This change in the correction was made after calibrations showed that electrons entering the detector from the backward direction had a higher probability of being rejected from analysis than forward-moving particles (see Appendix A.4.a). The results for 1968 are shown in Table V-1 and Figure V-1, and the 1969 results are given in Table V-2 and Figure V-2. In some cases a small negative primary flux was obtained from the fitting procedure, indicating that the data were dominated by atmospheric secondaries. In these cases a 1-σ upper limit above zero flux has been listed. In 1969 the atmospheric contamination was more severe than in 1968 because

TABLE V-1

A. 1968 Positron Fluxes $(m^2 \cdot sec \cdot sr \cdot MeV)^{-1}$

Rigidity interval at the detector (MV)	6-12	12-25	25-50	50-100	100-200
Flux from combined flights	.71±.13	.44±.06	.24±.03	.130±.015	.075±.008
Least-squares fit separation					
1) "Primaries"	.44±.13	.15±.07	.030±.041	-.021±.026	.010±.012
2) "Secondaries"	.26±.05	.28±.04	.21±.03	.15±.02	.065±.009
Background corrections					
1) Splash albedo (1)	.02±.01	.02±.01	.011±.003	.003±.003	.0007±.0002
2) γ-ray (1)	.11±.08	.043±.020	.010±.003	.0014±.0005	.00028±.00012
Corrected primary positrons at 2.4 g/cm^2 residual atmosphere	.31±.15	.087±.073	.009±.041	0±.026	.009±.012
Energy interval at top of atmosphere (MeV)	11.1-17.1	17.1-30.2	30.2-55.2	55.2-104.9	104.9-203.9
Flux at top of atmosphere	.30±.15	.084±.071	.0088±.0400	0±.026	.009±.012

(1) Error limits are estimated errors.

TABLE V-1 (Cont.)

B. 1968 Negatron Fluxes $(m^2 \cdot sec \cdot sr \cdot MeV)^{-1}$

Rigidity interval at the detector (MV)	6-12	12-25	25-50	50-100	100-200
Flux from combined flights	2.80±0.30	.81±.08	.30±.03	.11±.02	.084±.008
Least-squares fit separation					
1) "Primaries"	.72±.40	.26±.10	.072±.047	-.038±.030	.030±.014
2) "Secondaries"	2.05±.29	.55±.07	.22±.03	.15±.02	.051±.009
Background corrections					
1) Splash albedo (1)	.02±.01	.02±.01	.011±.003	.003±.003	.0007±.0002
2) γ-ray (1)	.20±.10	.05±.02	.0078±.0023	.002±.001	.0002±.00009
Corrected primary negatrons at 2.4 g/cm^2 residual atmosphere	.50±.41	.19±.10	.053±.047	0±.030	.029±.014
Energy interval at top of atmosphere (MeV)	11.1-17.1	17.1-30.2	30.2-55.2	55.2-104.9	104.9-203.9
Flux at top of atmosphere	.49±.40	.18±.10	.052±.046	0±.030	.029±.014
Flux of $(e^+ + e^-)$ at top of atmosphere	.79±.43	.26±.12	.061±.061	0±.040	.038±.018

(1) Error limits are estimated errors.

TABLE V-2

A. 1969 Positron Fluxes $(m^2 \cdot sec \cdot sr \cdot MeV)^{-1}$

Rigidity interval at the detector (MV)	6-12	12-25	25-50	50-100	100-200
Flux from combined flights	.59±.10	.33±.05	.21±.03	.14±.02	.007±.008
Least-squares fit separation					
1) "Primaries"	.38±.10	.07±.06	-.044±.038	-.008±.024	.009±.013
2) "Secondaries"	.20±.04	.26±.03	.24±.02	.14±.02	.068±.008
Background corrections					
1) Splash albedo (1)	.02±.01	.02±.01	.011±.003	.003±.003	.0007±.0002
2) γ-ray (1)	.11±.08	.043±.020	.010±.003	.0014±.0005	.00028±.00012
Corrected primary positrons at 2.9 g/cm^2 residual atmosphere	.25±.13	.007±.064	0±.038	0±.024	.0083±.0133
Energy interval at top of atmosphere (MeV)	11.7-18.1	18.1-31.2	31.2-56.3	56.3-106.0	106.0-204.9
Flux at top of atmosphere	.24±.12	.007±.061	0±.037	0±.024	.0083±.0133

(1) Error limits are estimated errors.

TABLE V-2 (Cont.)

B. 1969 Negatron Fluxes $(m^2 \cdot sec \cdot sr \cdot MeV)^{-1}$

Rigidity interval at the detector (MV)	6-12	12-25	25-50	50-100	100-200
Flux from combined flights	2.23±.24	.61±.07	.22±.03	.126±.015	.057±.006
Least-squares fit separation					
1) "Primaries"	-.039±.34	-.086±.085	-.071±.037	-.030±.023	-.016±.012
2) "Secondaries"	2.11±.25	.66±.06	.28±.02	.15±.02	.071±.008
Background corrections					
1) Splash albedo (1)	.02±.01	.02±.01	.011±.003	.003±.003	.0007±.0002
2) γ-ray (1)	.20±.10	.05±.02	.0078±.0023	.0016±.0006	.00021±.00009
Corrected primary negatrons at 2.9 g/cm^2 residual atmosphere	0±.35	0±.088	0±.037	0±.023	0±.012
Energy interval at top of atmosphere (MeV)	11.7-18.1	18.1-31.2	31.2-56.3	56.3-106.0	106.0-204.9
Flux at top of atmosphere	0±.33	0±.084	0±.036	0±.023	0±.012
Flux of $(e^+ + e^-)$ at top of atmosphere	.24±.35	.007±.104	0±.052	0±.033	.0083±.0179

(1) Error limits are estimated errors.

TABLE V-3

A. 1970 Low-Energy Positron Fluxes $(m^2 \cdot sec \cdot sr \cdot MeV)^{-1}$

Rigidity interval at the detector (MV)	14.8-29.5	29.5-59.0	59.0-122.9	122.9-245.8
Flux from 70Cl ($2.5\ g/cm^2$)	.169±.084	.087±.025	.052±.016	.023±.007
Least-squares fit separation				
1) "Primaries"	-.076±.082	-.052±.047	.003±.022	-.020±.011
2) "Secondaries"	.236±.056	.165±.032	.077±.014	.042±.008
Energy interval at top of atmosphere (MeV)	23.5-38.7	38.7-68.7	68.7-133.0	133.0-256.3
Flux at top of atmosphere	0±.079	0±.050	.003±.025	0±.013

TABLE V-3 (Cont.)

B. 1970 High-Energy Positron Fluxes $(m^2 \cdot sec \cdot sr \cdot MeV)^{-1}$

Rigidity interval at the detector (MV)	246-492	492-983	983-1475
Number from combined flights	58	37	14
Background corrections			
1) Protons (1)	0	0	4±2
2) Accidental gas Čerenkov coincidences (1)	0	0	1.3±.7
3) Calculated atmospheric secondaries	49.8±12.5	23.3±5.8	5.9±1.5
Net number of positrons corrected to 2.5 g/cm^2	8.2±14.6	13.7±8.4	2.8±4.6
Flux at 2.5 g/cm^2	$(1.84\pm3.28)\times10^{-3}$	$(1.54\pm.94)\times10^{-3}$	$(.32\pm.52)\times10^{-3}$
Energy interval at top of atmosphere (MeV)	256-503	503-994	994-1486
Flux at top of atmosphere	$(1.69\pm3.70)\times10^{-3}$	$(1.52\pm1.59)\times10^{-3}$	$(.43\pm2.14)\times10^{-3}$

(1) Error limits are estimated errors.

TABLE V-4

A. 1970 Low-Energy Negatron Fluxes $(m^2 \cdot sec \cdot sr \cdot MeV)^{-1}$

Rigidity interval at the detector (MV)	14.8-29.5	29.5-59.0	59.0-122.9	122.9-245.8
Flux from 70Cl (2.5 g/cm^2)	.191±.087	.166±.042	.087±.019	.024±.007
Least-squares fit separation				
1) "Primaries"	-.082±.121	.007±.050	.012±.024	-.002±.011
2) "Secondaries"	.309±.084	.167±.031	.078±.015	.029±.007
Energy interval at top of atmosphere (MeV)	23.5-38.7	38.7-68.7	68.7-133.0	133.0-256.3
Flux at top of atmosphere	0±.120	.007±.054	.012±.028	0±.011
Flux of $(e^+ + e^-)$ at top of atmosphere	0±.218	.007±.073	.016±.037	0±.016

TABLE V-4 (Cont.)

B. 1970 High-Energy Negatron Fluxes $(m^2 \cdot sec \cdot sr \cdot MeV)^{-1}$

Rigidity interval at the detector (MV)	246-492	492-983	983-1475
Number from combined flights	56	81	72
Background corrections			
1) Protons (1)	0	0	5.6±2.8
2) Accidental gas Čerenkov coincidences (1)	0	0	0
3) Calculated atmospheric secondaries	41.3±10.3	19.2±4.8	5.0±1.2
Net number of negatrons corrected to 2.5 g/cm^2	14.7±12.7	61.8±10.2	61.4±9.0
Flux at 2.5 g/cm^2	$(3.31\pm2.86)\times10^{-3}$	$(6.95\pm1.15)\times10^{-3}$	$(6.90\pm1.01)\times10^{-3}$
Energy interval at top of atmosphere (MeV)	256-503	503-994	994-1486
Flux at top of atmosphere	$(2.56\pm2.78)\times10^{-3}$	$(5.23\pm1.95)\times10^{-3}$	$(4.91\pm3.85)\times10^{-3}$
Flux of $(e^+ + e^-)$ at top of atmosphere	$(4.25\pm4.63)\times10^{-3}$	$(6.75\pm2.49)\times10^{-3}$	$(5.34\pm4.40)\times10^{-3}$

(1) Error limits are estimated errors.

TABLE V-5

A. 1971 Low-Energy Positron Fluxes $(m^2 \cdot sec \cdot sr \cdot MeV)^{-1}$

Rigidity interval at the detector (MV)	14.8-29.5	29.5-59.0	59.0-122.9	122.9-245.8
Flux from combined flights	.256±.082	.269±.039	.087±.017	.047±.008
Least-squares fit separation				
1) "Primaries"	-.046±.094	.069±.057	-.037±.024	.001±.012
2) "Secondaries"	.298±.077	.193±.039	.122±.018	.044±.009
Energy interval at top of atmosphere (MeV)	23.3-38.5	38.5-68.5	68.5-132.8	132.8-256.0
Flux at top of atmosphere	0±.094	.072±.064	0±.031	.001±.015

TABLE V-5 (Cont.)

B. 1971 High-Energy Positron Fluxes $(m^2 \cdot sec \cdot sr \cdot MeV)^{-1}$

Rigidity interval at the detector (MV)	246-492	492-983	983-1475
Number from combined flights	52	37	25
Background corrections			
1) Protons (1)	0	0	6±3
2) Accidental gas Čerenkov coincidences (1)	0	0	4±2
3) Calculated atmospheric secondaries	50.2±12.5	24.2±6.0	6.3±1.6
Net number of positrons at 2.4 g/cm^2	1.8±14.4	12.8±8.5	8.7±6.4
Flux at 2.4 g/cm^2	$(.48 \pm 3.60) \times 10^{-3}$	$(1.59 \pm 1.06) \times 10^{-3}$	$(1.08 \pm .79) \times 10^{-3}$
Energy interval at top of atmosphere (MeV)	256-502	502-994	994-1486
Flux at top of atmosphere	$(.33 \pm 3.19) \times 10^{-3}$	$(1.11 \pm 1.60) \times 10^{-3}$	$(.89 \pm 2.59) \times 10^{-3}$

(1) Error limits are estimated errors.

TABLE V-6

A. 1971 Low-Energy Negatron Fluxes $(m^2 \cdot sec \cdot sr \cdot MeV)^{-1}$

Rigidity interval at the detector (MV)	14.8-29.5	29.5-59.0	59.0-122.9	122.9-245.8
Flux from combined flights	.432±.100	.192±.038	.112±.018	.030±.007
Least-squares fit separation				
1) "Primaries"	.055±.123	-.067±.057	.034±.024	-.018±.011
2) "Secondaries"	.362±.083	.252±.044	.075±.016	.047±.009
Energy interval at top of atmosphere (MeV)	23.3-38.5	38.5-68.5	68.5-132.8	132.8-256.0
Flux at top of atmosphere	.048±.116	0±.058	.035±.025	0±.013
Flux of $(e^+ + e^-)$ at top of atmosphere	.048±.149	.072±.086	.036±.040	.001±.018

TABLE V-6 (Cont.)

B. 1971 High-Energy Negatron Fluxes $(m^2 \cdot sec \cdot sr \cdot MeV)^{-1}$

Rigidity interval at the detector (MV)	246-492	492-983	983-1475
Number from combined flights	57	100	80
Background corrections			
1) Protons (1)	0	0	4±2
2) Accidental gas Čerenkov coincidences (1)	0	0	0
3) Calculated atmospheric secondaries	41.2±10.3	19.8±5.0	5.2±1.3
Net number of negatrons at 2.4 g/cm^2	15.8±12.8	80.2±11.1	70.8±9.3
Flux at 2.4 g/cm^2	$(3.92\pm3.18)\times10^{-3}$	$(9.96\pm1.38)\times10^{-3}$	$(8.80\pm1.16)\times10^{-3}$
Energy interval at top of atmosphere (MeV)	256-502	502-994	994-1486
Flux at top of atmosphere	$(2.58\pm2.77)\times10^{-3}$	$(7.56\pm2.32)\times10^{-3}$	$(7.42\pm4.91)\times10^{-3}$
Flux of $(e^+ + e^-)$ at top of atmosphere	$(2.91\pm4.22)\times10^{-3}$	$(8.67\pm2.82)\times10^{-3}$	$(8.31\pm5.55)\times10^{-3}$

(1) Error limits are estimated errors.

1) only lower float altitudes could be reached during the 1969 observations and 2) the primary fluxes were lower due to increased solar modulation. For low-energy positrons the atmospheric secondaries contamination is smaller than for low-energy negatrons since the knock-on component is not present. As a result, measurable low-energy positron fluxes were obtained for both years.

The 1970 and 1971 data were collected with the MOD-2 detector. The addition of the gas Čerenkov counter and the larger 2300-gauss magnet eliminated the necessity to correct for upward-moving particles and also allowed an extension of the rigidity range to 15-1500 MV. The observed fluxes were corrected to the top of the atmosphere using the matrix-inversion procedure described in Appendix A.5. The 1970 results are shown in Tables V-3 and V-4 and Figure V-3, and the 1971 data are given in Tables V-5 and V-6 and Figure V-4. (The subdivision of the tables, corresponding to the low-energy ($\lesssim$ 245 MeV) and high-energy data, is due to the different analysis procedures used at low and high energies (see Chapter IV).)

The relatively large error limits of the data reflect the difficulty in measuring the charge composition of the electron spectrum within the atmosphere. In our energy range of 6-1500 MeV, which is of major interest to solar modulation studies, a magnet spectrometer, such as the Caltech detector, is the only instrument which can effectively determine this composition. Such instruments unambiguously determine the charge sign and offer excellent energy resolution since the electrons pass through little mass in traversing the magnet spectrometer. The upper limits and error bars of the data primarily reflect the contamina-

tion from atmospheric secondaries at balloon altitudes. The size and weight of the instrument necessary to record the relatively low flux of cosmic-ray electrons have made it unsuitable as a payload for satellites so far. Thus balloon-borne spectrometers are presently our only source of information on positron data in this important energy range. Indeed, during the period 1968-1971 the Caltech positron observations represent the only published data in this energy range.

Despite the uncertainties, these positron data allow important definitive conclusions regarding the low-energy interstellar electron spectrum and the low-energy cosmic-ray diffusion coefficient. Indeed, below ~100 MeV the positrons represent the only direct tool for studying solar modulation.

VI. DISCUSSION OF SOLAR MODULATION

A. Introduction and Statement of the Problems

The study of the solar modulation of electrons provides information on physical conditions of the interplanetary medium, e.g. the cosmic-ray diffusion coefficient, as well as information on the local interstellar spectra of electrons and positrons. These spectra carry the signature of their origin, i.e. of their sources and of the interstellar medium in which they were stored. The electron modulation study also contributes to the understanding of the modulation of cosmic-ray nuclei, providing important parameters for the deduction of their interstellar spectra.

The Caltech electron data shown in Chapter V were acquired over the period 1968-1971 and extend over the energy range from ~11 - 1500 MeV. We show in Figure VI-1 our 1968 and 1971 electron fluxes together with selected data from other authors which extend over the energy range 10 MeV to 10 GeV and cover the period since the last solar minimum in 1965-66. The effects of the long-term solar-cycle variation are readily apparent in the hundred MeV range in Figure VI-1a. For example, at ~300 MeV there is about a factor of 10 difference in the 1965-66 and 1970 fluxes. Above ~10 GeV no distinct long-term variations have been observed and hence we shall ignore this region of the spectrum in our solar modulation study. Below ~25 MeV observations from detectors on the IMP and OGO-5 satellites have shown short-term variations by factors of ~3-5 over time intervals of a few days (L'Heureux et al., 1972; McDonald et al., 1972). These increases occur

during solar quiet times, are essentially energy independent from 3-25 MeV, and are often anti-correlated with low-energy solar-proton events. It has been suggested that the low-energy electrons observed during quiet-time increases, as well as during quiescent times, are of galactic origin. Because of these short-term variations, the long-term modulation at these energies is not well-determined. McDonald et al. have put an upper limit of a factor of 2.3 on the intensity variation from solar minimum to solar maximum. It is important to note that the short-term variations are not observed above 25 MeV (L'Heureux et al., 1972).

Our observations using balloon flights, each of which lasts ~20 hours, and which are separated by a few days, are not well suited to the study of the short-term variations. The period of our 1968 data corresponds to quiet-time conditions as observed in the 3-12 MeV electron fluxes from the IMP-4 satellite (McDonald et al., 1972). The data from Simnett and McDonald (1969) for 1967 and L'Heureux et al. (1972) for 1968 in Figure VI-1a represent the average flux level during solar quiet times. This thesis, therefore, addresses itself to the long-term effects of solar modulation only.

We shall present a quantitative analysis of the solar-modulation process which uses the electron and positron data for its basis but which provides a consistent picture of the modulation for all cosmic-ray particles. Some of the outstanding problems of solar modulation studies are:

1) <u>Interstellar Electron and Positron Spectra</u>

In order to make deductions on the absolute solar modulation of

electrons it is necessary to have an estimate of their interstellar spectrum. Previous investigations have used either a) a power-law extrapolation to low energies of the observed high-energy spectrum (>10 GeV), which is expected to be little affected by solar modulation (Meyer et al., 1971; Schmidt, 1972) or b) a spectrum above a few hundred MeV calculated from the non-thermal-radio-background data with a power-law extrapolation to lower energies (Burger and Swanenburg, 1971; Lezniak and Webber, 1971; Urch and Gleeson, 1972). These extrapolated interstellar spectra differ considerably, e.g. about a factor of 10 at 100 MeV. Nonetheless, by using different approximations to the transport equation and different diffusion coefficients, the authors have made the different interstellar spectra consistent with the data observed near Earth. In addition, the interstellar positron spectrum has been calculated by several authors, e.g. Ginzburg and Syrovatskii (1964), Hayakawa et al. (1964), and more recently by Ramaty and Lingenfelter (1966, 1968), Perola et al. (1968), Beedle (1970), and Arai (1971). These calculated intensities also differ by factors of ~10.

2) Diffusion Tensor

Another problem in solar modulation studies is the evaluation of the interplanetary cosmic-ray diffusion coefficient, κ. The diffusion of cosmic-ray particles results in part from pitch-angle scattering due to the irregular fluctuations of the interplanetary magnetic field. Several authors have derived equations relating the diffusion coefficient to the power spectrum of the interplanetary

magnetic field (Jokipii, 1966, 1967, 1971; Hasselmann and Wibberentz, 1968; Roelof, 1968; Earl, 1972b). However, observations of the power spectrum are available for only a few limited time periods and generally do not cover a large enough frequency range to establish the rigidity dependence of the diffusion coefficient below a few hundred MV. Moreover, these measurements have all been made relatively near Earth and thus there are few observational data on the radial dependence of the diffusion coefficient. A further point of controversy is the question of the separability of κ. Some authors (Burger and Tanaka, 1970; Burger, 1971; Burger and Swanenburg, 1971; L'Heureux et al., 1972) argue that the diffusion coefficient must be a non-separable function of radius and rigidity in order to fit the cosmic-ray nuclei and electron data, whereas others have assumed a separable function in interpreting the data (Gleeson and Axford, 1968; Goldstein, Fisk and Ramaty, 1970; Fisk, 1971; Gleeson and Urch, 1971; Lezniak and Webber, 1971; Meyer et al., 1971; Urch and Gleeson, 1972; Garrard, 1973).

3) Modulation Region

Considerable speculation exists concerning the heliocentric radial distance to the "boundary" of the modulation region. Solar-flare studies have generally indicated a rather nearby boundary in the vicinity of 3-6 AU, whereas some studies of solar modulation have used much larger boundary distances, e.g. ~25 AU (Burger and Swanenburg, 1971; Fisk, 1971).

4) Analytic Approximations to the Transport Equation

Several investigators have used sufficiently simple approxi-

mations to the cosmic-ray transport equation such that analytical solutions are obtained (e.g. Gleeson and Axford, 1967, 1968; Meyer et al., 1971; Earl, 1972a;Schmidt, 1972). These analytic solutions diverge at low energies and hence the interstellar spectra and diffusion coefficients derived from these approximations necessarily differ.

In this chapter we shall attempt to resolve some of these discrepancies. We shall first briefly review the basic physics of solar modulation and discuss our results of a numerical analysis of the cosmic-ray transport equation for electrons. We shall then discuss the results of a self-consistent study of solar modulation. The major elements of this study are:

1) A new calculation of the possible range of interstellar electron spectra from the galactic non-thermal-radio-background data. From this range we shall discuss the absolute modulation of electrons above ~100 MeV.
2) An interstellar positron spectrum from nuclear collisions in the interstellar medium. This spectrum is chosen by requiring agreement between electron and positron modulation above ~100 MeV.
3) The rigidity dependence of the diffusion coefficient from ~10 MeV to ~10 GeV derived from comparisons of numerical solutions of the transport equation, using the interstellar spectra derived in 1) and 2), with the best available near-Earth data. At low energies ($\lesssim$ 100 MeV) the results allow us to comment on the so-far unknown interstellar electron spectrum.

4) A comparison of these diffusion coefficients with those derived from the available power spectra of the interplanetary magnetic field. From this comparison we comment on the possible radial variation of κ and make estimates of the size of the modulation region.

5) Numerical solutions of the transport equation for the cosmic-ray nuclei using the electron-and positron-derived diffusion coefficients.

B. Background Physics

The physics of the interplanetary medium responsible for solar modulation is well-established. The solar corona is dynamically unstable and expands outward from the Sun at supersonic velocity (Parker, 1963). The magnetic field of the Sun is frozen into the hot, fully ionized, highly conducting plasma and is swept outward into interplanetary space. The rotation of the Sun (with angular velocity Ω) causes the magnetic lines of force to have, on the average, the shape of an Archimedes' spiral. Superimposed on this average shape are irregular fluctuations. Charged particles penetrating into the interplanetary medium are spiraling about this solar magnetic field and those with gyroradii comparable to the wavelength of the fluctuation undergo resonant pitch-angle scattering. This effect gives rise to a random walk of particles along the average field-line direction. In addition, particles are transported perpendicular to the field lines because the lines of force also execute a random walk. In general, this diffusive process is described by a diffusion tensor (Jokipii, 1971) which includes other effects such as curvature drift and the gradient of the average magnetic field. These curvature and gradient drifts are not expected to be significant for galactic energetic particles (Jokipii, 1970). In this thesis we shall ignore these terms of the diffusion tensor and treat only $\kappa_{\parallel}$ and $\kappa_{\perp}$, the diffusion coefficients parallel and perpendicular to the interplanetary magnetic field, respectively.

The fluctuations which scatter the charged particles are being convected outward with the solar wind; hence, cosmic-ray particles are

convected away from the Sun producing a radial gradient which leads to diffusion in the opposite direction. In addition, the particles are scattering from field-line fluctuations which are, on the average, moving away from each other; hence, in these collisions the particles lose energy (adiabatic deceleration).

In a recent review, Jokipii (1971) describes how the inclusion of these effects leads to the following equation describing the propagation of galactic cosmic-rays in the interplanetary medium:

$$\nabla\cdot(\vec{V}U) - \frac{\vec{\nabla}\cdot\vec{V}}{3}\frac{\partial}{\partial T}(\alpha TU) - \vec{\nabla}\cdot(\overline{\overline{\kappa}}\cdot\vec{\nabla}U) = 0 \qquad \text{(VI-1)}$$

where $U(r,T)$ is the number of particles per unit volume per unit energy at radial distance r with kinetic energy T ($U = 4\pi j/\beta c$ where j is the intensity and βc is the particle velocity), $\vec{V}$ is the solar-wind velocity, $\alpha(T)$ is a parameter given by

$$\alpha(T) = \frac{\partial\ \ell n\ T}{\partial\ \ell n\ p} = \frac{T + 2m}{T+m},$$

where p is the particle momentum, m is the particle rest energy, and $\overline{\overline{\kappa}}$ is the particle diffusion tensor. For electrons with energy above a few MeV, α is essentially unity. The three terms in equation VI-1 represent, respectively, convection, adiabatic deceleration, and diffusion of charged particles in the interplanetary medium.

Some direct information is available on the principal parameters, $\vec{V}$ and $\overline{\overline{\kappa}}$, which enter into the solution of equation VI-1. The solar-wind velocity is relatively constant from year to year and

s an average value near 400 km/sec (Gosling et al., 1971). Existing measurements of the power spectrum of the interplanetary magnetic field near 1 AU yield information on the rigidity dependence of the diffusion coefficient. In addition, further information is provided by solar-flare studies, since propagation of energetic flare particles is governed by a time-dependent equation of the same general form as equation VI-1. It is the long-term variation of these parameters, particularly $\overline{\overline{K}}$, which produces the time variation of the cosmic-ray intensities.

C. Review of Analytic Approximations to the Transport Equation

In order to treat equation VI-1 analytically or numerically it is necessary to construct a simplified model of physical conditions in the interplanetary medium. Several reviews have been published on the physics of the solar wind (Parker, 1965a; Dessler, 1967; Parker, 1969a). In general, the presence of the solar wind is attributed to the radial expansion of the solar corona. The wind velocity becomes supersonic beyond a few tens of solar radii and roughly maintains a constant magnitude until the shock-termination boundary is reached. At this point the stream-flow pressure, which falls as $1/r^2$, is no longer able to sweep back the interstellar medium. This termination boundary is not necessarily the same as the cosmic-ray modulation boundary since the fluctuations of the interplanetary magnetic field, which scatter the particles, may be damped out in a shorter distance. On this basis we assume the solar-wind velocity, $\vec{V}$, to be independent of heliocentric radius, r, and furthermore, for simplicity, we assume both $\vec{V}$ and the cosmic-ray density, U, are independent of angle about the Sun.

Under these assumptions, the transport equation VI-1 becomes

$$\frac{V}{r^2}\frac{\partial}{\partial r}(r^2U) - \frac{2V}{3r}\frac{\partial}{\partial T}(\alpha TU) - \frac{1}{r^2}\frac{\partial}{\partial r}\left(r^2\kappa\frac{\partial U}{\partial r}\right) = 0 \qquad \text{(VI-2)}$$

where κ is a scalar quantity, the radial diffusion coefficient, defined by (Jokipii, 1971)

$$\kappa = \kappa_{rr} = \kappa_{\parallel}\cos^2\theta + \kappa_{\perp}\sin^2\theta \qquad \text{(VI-3)}$$

where θ is the angle between the radius vector from the Sun and the outward direction along the interplanetary magnetic field ($\sim 48^{\circ}$ at 1 AU), and $\kappa_{\parallel}$ and $\kappa_{\perp}$ are the parallel and perpendicular components of the diffusion tensor, respectively.

Even with the assumptions made so far, no general, analytic solutions to equation VI-2 have been found. Several further approximations to the equation have been made which lead to analytic solutions. We shall discuss the most important of these approximations as they apply to electrons. (Garrard (1973) has given a detailed discussion relevant to the cosmic-ray nuclei).

1. The Diffusion-Convection (DC) Approximation

If we neglect the adiabatic deceleration term in equation VI-2 we obtain:

$$\frac{\partial}{\partial r}\left(r^2 VU - r^2 \kappa \frac{\partial U}{\partial r}\right) = 0$$

In the absence of sources or sinks at the origin this equation may be written:

$$VU = \kappa \frac{\partial U}{\partial r}, \qquad \text{(VI-4)}$$

which is a statement of the balance between the outward current of particles due to convection and an inward current due to diffusion. The solution to the DC equation is:

$$U(r,T) = U(\infty,T) \exp\left[-\int_r^{\infty} \frac{V}{\kappa(r',T)}\, dr'\right] \qquad \text{(VI-5a)}$$

If we assume there is a boundary at distance D beyond which V/κ is zero,

then

$$U(r,T) = U(D,T) \exp\left[-\int_r^D \frac{V}{\kappa(r';T)}\, dr'\right] \qquad \text{(VI-5b)}$$

$$= U(D,T)\ e^{-\psi(r,T)} \qquad \text{(VI-5c)}$$

where the quantity ψ, defined by:

$$\psi(r,T) = \int_r^D \frac{V}{\kappa(r';T)}\, dr' \qquad \text{(VI-6)}$$

is called the "modulation parameter" or simply the "modulation". It will be shown to be the determining parameter in the study of the solar modulation of electrons. It has also been found to be the important parameter in the discussion of the high-energy ($\gtrsim$ few GeV) solution of the transport equation for nuclei (Garrard, 1973).

It is interesting to note that if the near-Earth and interstellar electron spectra are known, then the modulation parameter at 1 AU, $\psi(1,T)$, is determined in the DC approximation from equation VI-5c, i.e.,

$$\psi(1,T) = \ell n \left[\frac{U(D,T)}{U(1,T)}\right] \qquad \text{(VI-7)}$$

If the radial and energy dependences of the diffusion coefficient are separable, i.e. $\kappa(r,T) = \kappa_1(r)\ \kappa_2(T)$, then the energy dependence of κ is determined from $\psi(1,T)$ (see equation VI-6).

2. The Force-Field (FF) Approximation

Gleeson and Axford (1967, 1968) have derived an approximate

solution in the case of small modulation by making use of the radial differential current density (or streaming), S, defined as:

$$S = VU - \kappa \frac{\partial U}{\partial r} - \frac{V}{3} \frac{\partial}{\partial T} (\alpha T U) \qquad \text{(VI-8)}$$

The second term on the right represents the contribution from diffusion. The remaining two terms represent the effective radial current due to the transformation between a frame of reference at rest with respect to the solar wind and the observer's reference frame (the Compton-Getting effect). The first term represents the contribution due to convection. The origin of the third term can be visualized by imagining that we observe particles at a single energy T with a "directional" detector. Then if we point the detector toward the Sun, the velocity of the solar-wind frame effectively adds energy, $+\Delta T$, to the particles we are observing. Thus in our frame we observe the rate of particles corresponding to the intensity at energy $T-\Delta T$ in the solar-wind frame. If we point the detector radially away from the Sun we observe the rate of particles corresponding to a different part of the solar-wind-frame spectrum, i.e. corresponding to the intensity at $T+\Delta T$. Since these intensities are usually different, there is an effective radial current.

Gleeson and Axford present arguments to show that S is negligible whenever $VL/\kappa \ll 1$, where L is a length characteristic of the radial variation of the diffusion coefficient. If one assumes $S = 0$ and that κ is a separable function of radius and energy, then one obtains the so-called force-field solution (Gleeson and Axford, 1968)

$$\frac{j(r,W)}{W^2 - m^2} = \frac{j(D, W + \Phi)}{(W+\Phi)^2 - m^2} \qquad \text{(VI-9)}$$

where j is the particle intensity, W is the total energy of the particle, m is its rest energy, and Φ is a spectral shift parameter which is determined from the diffusion coefficient.

This simple equation (VI-9) has been used by several investigators in interpreting electron data. We shall show that the zero-streaming assumption breaks down at low energies ($\lesssim$ 200 MeV) for certain forms of the diffusion coefficient and the unmodulated spectrum. In general, it is difficult to predict the range of applicability of the FF solution. In the following section we shall investigate some cases of interest in the light of results of a numerical solution of the full cosmic-ray transport equation.

3. The Convection-Adiabatic Deceleration (CAD) Approximation

If one assumes that the diffusion term (containing $\kappa \frac{\partial U}{\partial r}$) in equation VI-2 is small compared to the other terms, we have

$$\frac{V}{r^2} \frac{\partial}{\partial r} (r^2 U) - \frac{2V}{3r} \frac{\partial}{\partial T} (\alpha T U) = 0 \qquad \text{(VI-10)}$$

Rygg and Earl (1971) solved this equation, assuming α to be constant, by

$$U(r,T) = T^{3/\alpha - 1} \mathcal{J} (r\, T^{3/2\alpha})$$

For $\alpha = 1$ (relativistic electrons),

$$U(r,T) = T^2 \mathcal{J} (r\, T^{3/2}) \qquad \text{(VI-11)}$$

The function $\mathcal{J}$ is an arbitrary function to be determined by the boundary condition. If the boundary condition is $U(r,T_0)$ = constant = $U(D,T_0)$ at some boundary energy T_0 (i.e. no modulation for $T \geq T_0$), the

solution reduces to:

$$U(r,T) = (T/T_0)^2 \, U(D,T_0) \qquad \text{(VI-12)}$$

or

$$j(r,T) = AT^2$$

where A is a constant. The corresponding solution for non-relativistic cosmic-ray nuclei is $j = AT$.

It is interesting to note that in this model particles at the boundary with energy $T < T_0$ do not propagate into 1 AU since $\kappa\ (T < T_0)$ is assumed zero. However, the intensity of particles with energy $T \geq T_0$ is the same at all radial distances since $\kappa\ (T \geq T_0)$ is assumed infinite. Therefore, in this model particles arrive near Earth with energy $T < T_0$ only by being decelerated from higher energies.

D. General Results from Numerical Solutions to the Transport Equation

A numerical solution to the transport equation VI-2 has advantages over the analytic approximations. For example, numerical solutions can be readily obtained for any specified radial and energy dependence of κ, whereas the analytic approximations are often restricted to certain functional forms of the diffusion coefficient. In addition, the numerical solution can be obtained for all values of radius and energy of interest; these solutions can then be used to test the validity of the analytic approximations.

We have constructed a numerical solution to equation VI-2 based on the Crank-Nicholson technique outlined by Fisk (1971). In this technique the continuous radius-energy plane is replaced by a grid with maximum radial distance D and an energy range from T_{min} to T_{max}. The transport equation is expressed as a finite difference equation in terms of grid location. By specifying three boundary conditions, the resulting set of simultaneous equations can be solved for all the radius-energy grid points.

The boundary conditions which we must specify are:

1) r = D: We assume that beyond the boundary the modulation is negligible at all energies. Thus U(D,T) ≡ galactic spectrum. For electrons and positrons we have information on these spectra from the non-thermal-radio-background data and galactic nuclear collisions, respectively. For nuclei one generally has to rely on power-law extrapolations of the high-energy data.

2) r = 0: In order to eliminate source-like solutions at r = 0, we transform the equations so that the dependent variable is $X = \sqrt{r}U$

and require $X \rightarrow 0$ as $r \rightarrow 0$. This transformation implies that the solutions are not valid for small r ($\lesssim$0.2 AU typically).

3) $T = T_{max}$: We assume that at sufficiently high energy, T_{max}, the modulation is negligible. Thus $U(r,T_{max}) = U(D,T_{max})$ for all r. In our work we assume T_{max} = 10 GeV for electrons.

1. Analysis of Analytic Approximations

a. The CAD Approximation

The solution of the CAD (convection-adiabatic deceleration) approximation is $j = AT^2$. If we examine the spectra of Figure VI-1 we find that, in view of the error limits, the data for 1969-1971 might be consistent with $j \propto T^2$ over a limited energy range (~100 - 500 MeV). It has been suggested (Luhmann, 1971; Earl,1972a) that such a segment is due to the validity of the CAD approximation (the low-energy turn-up is attributed to the dominance of diffusion below ~100 MeV). However, we shall now show that such a turn-over to $j \propto T^2$ would not be due to the dominance of adiabatic deceleration and convection over diffusion. In fact, it will be noted later in the discussion of the DC solution (Section VI.D.1.b) that such a turn-over can also exist in that solution which totally ignores adiabatic deceleration.

In discussing the CAD solution it is useful to define the phase-space density, F (the number of particles per unit volume ($d^3r\, d^3p$) in the six-dimensional r, p phase space), by:

$$F = j/p^2$$

Therefore, $j \propto T^2$ is equivalent to F = constant for relativistic electrons. From the numerical solution of the transport equation over

the entire radius-energy plane it is easy to determine if F is constant over some portion of the plane and therefore to determine over what region the CAD approximation is valid. As an illustration, we show in Figures VI-2a and b the numerical solution of equation VI-3 using the interstellar spectrum and diffusion coefficient assumed by Meyer et al. (1971) in interpreting the 1970 data. This diffusion coefficient in cm^2/sec is represented by:

$$\kappa(R) = \begin{cases} 4.94 \times 10^{17}\ \beta R & R \geq R_c = 440\ MV \\ 4.94 \times 10^{17}\ \beta R_c & R \leq R_c \end{cases} \qquad \text{(VI-13)}$$

where βc is the particle velocity, R is the particle rigidity, and a constant radial dependence for κ is assumed. Figure VI-2a shows electron intensity versus kinetic energy at 1 AU. As we shall point out shortly the numerical solution and the force-field approximation, used by Meyer et al., disagree at low energies and hence the assumed parameters do not lead to a good fit to the low-energy data. However, we use the solution at this point for purposes of illustration. In Figure VI-2b we show a plot of the contours of equal phase-space density in r,T space for the numerical solution. A region containing few contour lines would imply F $\approx$ constant and would possibly indicate that the CAD approximation is valid. In the figure adjacent contours are separated by a factor of 2 in F. (Note that the contour lines are horizontal in the large r region only because of the assumed boundary distance of 3 AU.) We observe only a slight spreading in the lines near 500 MeV for r $\lesssim$ 1.5 AU. This spreading reflects the turn-over in the

spectrum and is not necessarily an indication that diffusive effects are small (it is an indication that $j \propto T^2$ over a limited energy range, however). Since no large area with F = constant is indicated, we conclude that the CAD approximation is inappropriate for the case considered.

We expect the CAD approximation to be valid when diffusion can be neglected, i.e. when the diffusion coefficient is small or equivalently when the modulation parameter, ψ (see equation VI-6), is large. We shall show below (Section VI.D.2.a) that the numerical solutions of the transport equation at radius r using a given interstellar electron spectrum are primarily determined by $\psi(r,T)$ (defined by equation VI-6). Therefore, to determine the region of r,T space in which the CAD approximation is valid, we determine the minimum ψ which yields F ≈ constant. As an illustration, we show in Figures VI-2c and d (solid lines) the numerical solution for the same parameters as in Figures VI-2a and b, except that R_c, the rigidity at which the diffusion coefficient changes form, is lowered from 440 to 100 MV. The effect of lowering R_c is to lower the diffusion coefficient by roughly a factor of 4 at rigidities below 100 MV. It is evident from Figure VI-2c that the intensity at 1 AU is roughly proportional to T^2 at low energies (compare with dashed $j \propto T^2$ line), and in Figure VI-2d a large region where F is nearly constant does exist. Thus by sufficiently lowering the diffusion coefficient, we find, as expected, that the CAD approximation (which ignores diffusion), is approximately valid, although the spectrum so obtained does not resemble the observed spectrum. The dashed lines in Figure VI-2d are curves along which $\psi(r,T)$ is constant.

We find, roughly, that κ must be small enough such that $\psi \gtrsim 15$ for the CAD approximation to apply. Using the nominal interstellar spectrum discussed in Section VI.E.1, we shall find that solutions at 1 AU consistent with the observations are obtained with $\psi \lesssim 6$. In order for the CAD approximation to be valid near 1 AU the absolute interstellar electron intensity would be required to be a factor of $\frac{e^{-6}}{e^{-15}} \approx 8000$ (see equation VI-5c) larger than our calculated intensity. We therefore conclude that the interpretation of a possible $j = AT^2$ segment in the 1969-1971 electron spectra is almost certainly not the manifestation of the validity of the CAD approximation.

In the above analysis we have assumed that the F = constant region in Figure VI-2d is a result of the validity of the CAD approximation (for $\psi \gtrsim 15$). We might ask the question: Is the F = constant region necessarily due to the dominance of adiabatic deceleration over diffusion? To clarify this question we show in Figure VI-2e the phase-space density contours for the diffusion-convection solution, i.e. the solution ignoring adiabatic deceleration, for the identical parameters as in Figure VI-2d. Here we find no large F = constant region, which indicates that, indeed, adiabatic deceleration is responsible for the large blank area in Figure VI-2d. Note, however, the region of spreading in the DC phase-space density contours (Figure VI-2e), which is a result of the fact that $j = AT^2$ segments over a limited energy range can also be produced by approximations which ignore adiabatic deceleration.

b. The FF and DC Approximations

Meyer et al. (1971) and Schmidt (1972) have related modulated

spectra observed near Earth to the interstellar spectrum by using the force-field approximation. Some of the subtleties of this approximation have been pointed out by Garrard (1973). For example, the FF solution ignores adiabatic deceleration, although it does include the Compton-Getting effect. Furthermore, the conditions which produce zero streaming, required by the approximation, are not clear.

In order to determine the region of applicability of the FF and the DC approximations, we show in Figure VI-3a a comparison of these solutions with the numerical solution (FN) of the full transport equation. For all three models we use the same diffusion coefficient, assumed independent of radius with a boundary at 3 AU and with the rigidity dependence (cm^2/sec):

$$\kappa(R) = \begin{cases} 7.15 \times 10^{17}\ \beta R & R > R_c = 300\ MV \\ 7.15 \times 10^{17}\ \beta R_c & R \leq R_c \end{cases}$$

This diffusion coefficient and the interstellar spectrum shown in the figure were used by Meyer et al. in interpreting their 1968 data using the force-field approximation. Below ~100 MeV the FF result diverges significantly (factor of ~10 too small) from the full numerical solution. Schmidt has fit the same data (shown in Figure VI-1a) using the FF approximation with a steeper interstellar spectrum and a somewhat different diffusion coefficient. Since the force-field approximation is inconsistent with the full numerical solution at low energies, the parameters used in deriving these approximate solutions are necessarily inconsistent with ones we derive from fits to the data based on the numerical solution. Note that the DC solution is a better

approximation (within a factor of ~2) of the numerical solution over the whole energy range depicted than is the FF solution.

It is difficult to predict under what circumstances the force-field solution is a reasonable approximation. We find that the numerical and force-field solutions are more consistent if the interstellar electron spectrum is flatter than $T^{-2.5}$ at low energies, (below a few hundred MeV). To illustrate this improvement we show in Figure VI-3b a similar comparison of solutions as in Figure VI-3a except that we have used the interstellar positron spectrum calculated by Ramaty and Lingenfelter (1968). This galactic spectrum flattens out gradually below ~1 GeV and eventually turns over below ~50 MeV. Both the DC and the FF solutions are within a factor of ~2 of the full numerical solution over most of the energy range from 10 MeV to 10 GeV. The region of validity of the FF solution probably also depends on the rigidity dependence of the diffusion coefficient (Urch and Gleeson, 1972).

We find that the DC solution is a fairly good approximation for a wide range of interstellar spectra and diffusion coefficients. Thus, if κ is assumed to be a separable function of r and T, then, for a given interstellar spectrum and the spectra observed near 1 AU, the energy dependence of the appropriate diffusion coefficient can be estimated reasonably accurately by computing $\psi(1,T)$ from equation VI-7. The effect of adiabatic deceleration is to shift the solution in energy. For example, compare in Figure VI-3a the peak position in the numerical solution near 500 MeV with the peak in the DC solution. The observed shift indicates that for the assumed parameters the fractional energy

loss near 500 MeV is roughly 0.25. A more detailed discussion of the energy loss of the galactic electrons which penetrate to 1 AU is given in the next section. These energy losses mean that small adjustments in the diffusion coefficient estimated on the basis of the DC approximation are necessary in order to yield a good fit to the data using the numerical solution of the full transport equation.

2. General Remarks Concerning the Solution of the Transport Equation

In this section we present some general results from a study of both the numerical and analytic solutions of the transport equation (VI-2). In what follows the diffusion coefficient is assumed to be a separable function of radius and rigidity, $\kappa(r,R)=\beta\kappa_1(r)\kappa_2(R)$. Several authors have argued on the basis of their modulation studies that κ must be a non-separable function of radius and rigidity. (Burger and Tanaka, 1970; Burger, 1971; Burger and Swanenburg, 1971; L'Heureux et al., 1972). However, Gleeson and Urch (1972) have pointed out that these arguments are based on the assumption that the rigidity dependence of an assumed separable diffusion coefficient does not change form from year to year. No necessity for such a restriction has been suggested. We shall find that adequate fits to the observed cosmic-ray data can be made using separable diffusion coefficients with different rigidity dependences for different years. In this regard, we note that recent hysteresis studies of neutron monitor data have shown that the rigidity dependence of the modulation parameter changed abruptly several times during the last solar cycle. (Carmichael and Stoker, 1970; Carmichael and Katzman, 1971; Stoker and Carmichael, 1971; Kane, 1972). Thus we feel that there is, as yet, no compelling

observational evidence for either separability or non-separability. The assumption of separability provides us with a convenient framework in which to study the radial and rigidity dependences of the diffusion coefficient.

a. Effects of the Radial Dependence of the Diffusion Coefficient

There are few observational data on the radial dependence of κ. Jokipii and Coleman (1968), from analysis of the interplanetary magnetic field data of Mariner IV, find no drastic changes in the parallel diffusion coefficient, $\kappa_{\parallel}$, between 1 and 1.5 AU. The solar-flare studies of Lupton (1972) imply that a diffusion coefficient independent of radius, r, inside 1 AU is more consistent with the data than one which varies linearly with r. Sari (1972a), using power spectra from Pioneer 6 magnetic-field data, finds $\kappa_{\parallel}$ (50 MeV) varies approximately as $r^{-2.7}$ between 0.82 and 1 AU. Observational data on the radial dependence of $\kappa_{\perp}$ are non-existent. We recall that κ depends on both $\kappa_{\parallel}$ and $\kappa_{\perp}$, whose radial dependences are uncertain, and on θ (see equation VI-3), which is given by

$$\theta(r) = \tan^{-1}\left(\frac{\Omega r}{V}\right) \qquad \text{(VI-14)}$$

where Ω is the angular velocity of the Sun. Thus the radial dependence of κ is highly uncertain.

We do not expect large variations in the calculated electron spectra if we change the radial dependence of κ, since the DC solution, which depends only on the integrated effect of κ from the Earth to the boundary, is a reasonable approximation to the transport equation. However, it is useful to investigate just how much variation we do obtain

by varying the radial dependence of κ, in order to see how well the parameter ψ determines the solution. For this purpose we use an illustrative set of radial functions shown in Figure VI-4a. In addition to the e^{r-1} and r^{o} dependences used by many authors, we include a $2 + r^{3}$ dependence modeled after the diffusion coefficient suggested by Ng and Gleeson (1971) to explain solar-flare observations, a $[(r-3/2)^{4} + 1/4]$ function constructed by Garrard (1973) as an analytic representation of a possible scatter-free region near the Sun, a r^{-1} function suggested recently by Jokipii (1972) as a possible radial dependence beyond 1 AU, and a simple r^{1} dependence. For convenience the diffusion coefficient is assumed to be infinite beyond 3 AU. For the cases illustrated we use the single rigidity dependence of κ shown in Figure VI-4b.

In Figure VI-5a we show the numerical solutions of the transport equation using an interstellar spectrum derived from the non-thermal-radio data (see Section VI.E.1) and each of the 6 radial dependences of κ shown in Figure VI-4a. Also shown are the Caltech and Chicago data (Schmidt, 1972) for 1968. The absolute magnitudes of the diffusion coefficients are normalized such that

$$\eta = \int_{1}^{D} \frac{V dr}{\kappa_1(r)} \qquad \text{(VI-15)}$$

$$= 1950 \text{ MV (appropriate for 1968)}$$

Since

$$\psi(1,R) = \frac{\eta}{\beta \kappa_2(R)}$$

and $\beta\kappa_2(R)$ is the same for each solution, we are assuming that each solution has the same ψ-value at 1 AU. As we see from the figure, all 6 curves are nearly identical, indicating that the solution for electrons is essentially independent of the radial dependence of κ.

We have also investigated the effect of varying the boundary distance D while maintaining $\psi(1,T)$ constant (by adjusting the magnitude of κ). In Figure VI-5b we show the solution for $\kappa_1(r)$ = constant for boundary distances of 3, 5, 10, 15 and 30 AU. The slight increase in energy loss with boundary distance is evident from the small shift of the curves; however, the differences are small compared to the experimental uncertainties in the data.

We conclude from these studies that ψ is indeed the determining parameter in the study of the modulation of electrons.

b. Effects of Adiabatic Deceleration

In Section VI.D.1 we demonstrated that the approximation ignoring energy loss allows a reasonable first estimate of the diffusion coefficient. In order to make refinements to κ we need to include the effect of adiabatic deceleration.

The rate of energy loss through adiabatic decleration is given by

$$\frac{dT}{dt} = -\frac{1}{3}\alpha(T)\ T\ (\vec{\nabla}\cdot\vec{V})$$

(Parker, 1965b). In the case of relativistic electrons ($\alpha = 1$) and a constant radial solar-wind velocity, $\vec{V}$, this equation reduces to

$$\frac{1}{T}\frac{dT}{dt} = -\frac{2V}{3r} \qquad \text{(VI-16)}$$

Thus the particles lose more energy near the Sun than near the boundary. In addition, if the diffusion coefficient is large, particles diffuse in from the boundary very quickly and thus lose less energy than they would if the diffusion coefficient were small. Thus we expect the energy loss to depend on both the magnitude of the diffusion coefficient and the boundary distance, D.

In Figure VI-6 we illustrate an energy-loss calculation. The unmodulated spectra, shown by solid lines, are of the form

$$U(D,T) = A \exp \left[-50 \ (\ell n \ T/T_0)^2 \right]$$

where T_0 takes on the values in MeV of 25, 50, 100, 200, 400, 800, 1600 and 3200. We use the diffusion coefficient of equation VI-13 which is assumed independent of radius within a boundary distance of 3 AU. The envelope formed by the peaks of the unmodulated spectra corresponds to the galactic secondary positron spectrum calculated by Ramaty and Lingenfelter (1968). The corresponding spectra at 1 AU, representing numerical solutions of the transport equation, are shown as dotted lines in the figure. As a consequence of adiabatic deceleration, the peaks in the spectra at 1 AU are shifted in energy from the corresponding peaks in the unmodulated spectra. (Note that the shape of the near-Earth spectrum, as indicated by an envelope of the peaks of the dotted curves, is determined by the particular choice of the rigidity dependence of the diffusion coefficient.)

For κ independent of radius and energy ($\leq$440 MeV in this example) the fractional energy loss is independent of energy (see equation VI-16). As we mentioned before, however, the fractional loss

does depend on the magnitude of κ and the boundary distance D. Since the electron spectra calculated from the transport equation depend primarily on the modulation parameter ψ, we show in Table VI-1 the values of the fractional energy loss (for T_0 = 50 MeV) for several representative combinations of $\psi(1,T_0)$ and D, assuming the functional dependence of the diffusion coefficient given by equation VI-13. The increase in the fractional energy loss with increasing ψ for a given value of D is due to the inverse relationship between ψ and κ, i.e. $\psi = \frac{V(D-1)}{\kappa}$. (Larger ψ implies smaller κ implies larger energy loss.) For a given ψ, D is approximately proportional to κ and the effect of a larger boundary (larger energy loss) is roughly offset by the effect of the correspondingly larger κ (smaller energy loss). From the table the fractional energy losses for electrons are less than roughly 0.5 for typical values of ψ and D. Above 440 MeV, where the diffusion coefficient is proportional to rigidity (in this example), we found that the fractional energy loss (for a given ψ and D) is smaller than that shown in the table.

c. Discussion of the "Flat" Portion of Electron Spectra and Rough Estimates of the Modulation (ψ)

We now discuss the characteristic "flat" region from approximately 100 MeV to 1 GeV of the observed electron spectra shown in Figure VI-1. We have shown that the simple diffusion-convection solution is a reasonable first approximation to the numerical solution of the full transport equation (VI-2) over the energy range 10 MeV - 10 GeV. The force-field solution is a somewhat better approximation above a few hundred MeV but breaks down rather badly in some cases below

TABLE VI-1

Fractional Energy Loss[+] for Representative Values of the Modulation Parameter, $\psi(1,T)$, and the Boundary Distance, D.

D (AU)	$\psi^*(1,T)$ → 1.25	2.5	5.0
3	.19	.27	.35
7	.25	.35	.47
10	.25	.36	.50
15	.25	.39	.52

[+] The values apply to the energy range ($\lesssim$440 MeV in this example) where the diffusion coefficient is independent of energy.

[*] For κ = constant, $\psi = \frac{V(D-1)}{\kappa}$.

~100 MeV. We shall use both approximations in the discussion. The main points of this discussion are:

1) to show that the energy dependence of the observed spectrum is consistent with our understanding of
   a) the interstellar spectrum
   b) the diffusion coefficient and
   c) the DC and FF approximations above ~100 MeV and
2) to demonstrate that an estimate of the absolute modulation can be made from a knowledge of only the energy dependences (and not the absolute magnitudes) of the diffusion coefficient and the interstellar spectrum, together with an observation of a relative peak in the observed spectrum near Earth.

The latter point is interesting because the energy dependence of the interstellar electron spectrum, for example, can be deduced more accurately from the non-thermal-radio-background data than the absolute interstellar electron intensity. (See Section VI.E.1.)

We first examine the simple diffusion-convection solution given by equation VI-5c. Since the differential intensity is given by $j = \frac{\beta c U}{4\pi}$, we can rewrite equation VI-5c (for r = 1 AU) as:

$$j(1,T) = j(D,T)\ e^{-\psi(1,T)} \qquad \text{(VI-17)}$$

where ψ is related to the diffusion coefficient κ through equation VI-6. Measurements of the power spectrum of the interplanetary magnetic field are consistent with $\kappa \propto \beta R^b$ where R is the particle rigidity, βc the particle velocity ($\beta = 1$ for relativistic electrons), and b is rigidity dependent ranging from ~0.5 at low rigidities ($\lesssim$1 GV) to ~1.5 at high

rigidities ($\gtrsim$10 GV). (See Section VI.E.4.) Using this form for the diffusion coefficient, equation VI-17 reads

$$j(1,T) = j(D,T) \exp\left[-\eta/(f(b)T^{b})\right]$$

where η is defined by equation VI-15 and we have replaced R by T which is valid in energy units for relativistic electrons*. (F(b) is chosen to make the energy dependence of κ continuous and is normalized such that f(1)=1. For example, if κ is represented by two joined power-law segments such that for $T \leq T_c$, $b = \frac{1}{2}$, and for $T > T_c$, $b = 1$, then $f(\frac{1}{2}) = \sqrt{T_c}$.) If we assume the interstellar spectrum $j(D,T) \propto T^{-\gamma}$ and if we approximate $\kappa \propto R^{b}$, we find a relative maximum in the near-Earth spectrum at energy T_m given by:

$$T_m = \left(\frac{b\eta}{f(b)\gamma}\right)^{1/b} \qquad \text{(VI-18)}$$

In terms of ψ this condition reduces to

$$\psi(1,T_m) = \frac{\gamma}{b} \qquad \text{(VI-19)}$$

Thus an estimate of the absolute modulation at the observed peak energy T_m is given simply by the ratio of the spectral index of the interstellar spectrum to the exponent of the rigidity dependence of the diffusion coefficient. From the radio data (Section IV.E.1) we find that $\gamma \approx 1.8$ below ~2 GeV; hence, we have $\psi(1,T_m) \approx 1.8$ and 3.6 for values of b of 1 and 1/2, respectively. These values of ψ correspond to

*$R = \frac{pc}{ze}$, where p is the electron momentum. For relativistic electrons ($v \approx c$, $z = 1$), $pc \approx T(\text{MeV}) \approx R(\text{MV})$.

absolute modulation factors, e^{ψ}, of approximately 6 and 36, respectively. From the observed spectra (Figure VI-1) we note that these values apply to an energy near 1 GeV.

We can also apply this procedure to the positron spectra since, again, the energy dependence of the calculated interstellar positron spectrum is known more accurately than its absolute intensity. Near 1 GeV the interstellar spectra presented in Section VI.E.2 (Figure VI-11) have a spectral index of ~2.4. Thus, we have $\psi\ (1,T_m) \sim 2.4$ and 4.8 for b = 1 and 1/2, respectively.

It is interesting to note that the peak in the positron spectrum at 1 AU is expected to occur at a lower energy than the peak in the electron spectrum. From equation VI-18 we have

$$\frac{T_m(e^+)}{T_m(e)} = \left[\frac{\gamma(e)}{\gamma(e^+)}\right]^{1/b}$$
$$= 0.75 \qquad b = 1 \qquad \text{(VI-20)}$$
$$= 0.56 \qquad b = 1/2$$

where we have assumed $\gamma(e) = 1.8$ and $\gamma(e^+) = 2.4$. Unfortunately, positron data of sufficient accuracy to observe this difference do not presently exist. Hopefully, future observations will confirm the prediction. Along these same lines, we note that if the energy dependence of the diffusion coefficient does not change significantly from year to year, the peak energy should move to higher energies with increasing modulation as is observed. (See Figure VI-1.) Larger modulation implies larger ψ implies larger η implies larger T_m.)

These estimates of the modulation parameters and peak-energy

locations are based on the DC approximation. Figure VI-3 indicates that for the choice of parameters considered the peak-energy locations are nearly the same for the FF and FN (full numerical) solutions and that both occur at a somewhat lower energy than that of the DC solution. Thus we might expect an improvement in the estimates of T_m and $\psi(1,T_m)$ by examining the FF approximation.

The FF solution is given by equation VI-9. If we assume $b = 1$ (i.e. $\kappa \propto R^1$), the parameter Φ in equation VI-9 has the simple value:

$$\Phi = \frac{1}{3}\eta \qquad \text{(VI-21)}$$

(Gleeson and Axford, 1968)

Equation VI-9 may be maximized to yield the peak energy T_m:

$$T_m = \frac{2}{3}\frac{\eta}{\gamma} \qquad [\text{FF, } b = 1] \qquad \text{(VI-22)}$$

Note that this value of T_m is just 2/3 of the DC estimate (equation VI-18). The corresponding ψ value is given by:

$$\psi(1,T_m) = \frac{3}{2}\gamma \qquad [\text{FF, } b = 1] \qquad \text{(VI-23)}$$

Equations VI-22 and VI-23 represent our best estimates of T_m and $\psi(1,T_m)$ for the case $\kappa \propto R^{b=1}$. The parameter Φ in equation VI-9 has a complicated energy dependence for other rigidity dependences of κ. Hence, it is difficult to evaluate T_m and $\psi(1,T_m)$ in the FF approximation for $b \neq 1$. However, we mention that a comparison of the numerical and DC solutions of the transport equation (described below and shown in Figure VI-7) indicates that $T_m = 2/3$ of the DC estimate (equation VI-18) is also appropriate for $\kappa \propto R^{b = 1/2}$.

In the electron spectra shown in Figure VI-1 we find the best-resolved peak occurs in the observed 1970 spectrum. The spectrum begins to deviate from a power-law below ~4 GeV and a relative peak is observed in the region near 1 GeV. If we assume the rigidity dependence of κ, we can determine the interstellar electron intensity at ~1 GeV as a function of its spectral index, i.e. of its energy dependence. From the non-thermal-radio-background data we estimate that γ is approximately in the range 1.7 to 1.9 at energies below ~2 GeV (see Section VI.E.1). Assuming $\kappa \propto R^1$ we find from equation VI-23 ψ(1 GeV) $\approx$ 2.55 - 2.85. Since j_{1970} (~1 GeV) $\approx$ .006 electrons/(m^2 sec sr MeV), we estimate from equation VI-17, j_∞(~1 GeV) $\approx$ .077 - .104 electrons/(m^2 sec sr MeV). These values are consistent with our calculation of the galactic electron spectrum from the radio data (see Figure VI-9). We note that with an accurate determination of the rigidity dependence of κ, e.g. from the power-spectra data, we could place more stringent limits on the interstellar electron intensity near 1 GeV than those shown in the figure. (The limits indicated in Figure VI-9 result from uncertainties in the galactic parameters and do not reflect the analysis discussed here.) This particular refinement in the analysis will not be pursued in this thesis.

We are now in a position to interpret the flat portion of the observed electron spectra at Earth during the years 1965-1971. From the power-spectra data (see Figure VI-19) we can infer roughly the rigidity dependence of the diffusion coefficient above a few hundred MV. As an illustration, we idealize $\kappa(R)$ such that below a break-point rigidity R_c, $\kappa \propto R^{1/2}$, and above R_c, $\kappa \propto R^1$. If the values of

η and R_c are such that T_m (equation VI-18) is greater than R_c, we expect a peak in the near-Earth spectrum at $T_m = \frac{2}{3}\frac{\eta}{\gamma}$ ($\approx$ 1 GeV in 1970). If R_c is too small, the diffusion coefficient becomes small enough that the modulation is very large. In this case a well-defined peak is obtained in the numerical solution, which in general is not observed in the data. For larger R_c the diffusion coefficient is larger at low energies and the well-defined peak becomes a broad flat region as is observed. In this example a second "peak", corresponding to the b = 1/2 segment of the diffusion coefficient, would be obtained in the near-Earth solution of the transport equation. In terms of R_c this peak, $T_{1/2}$, can be calculated from equation VI-22 and VI-18 (multiplying by the factor 2/3 on the right-hand side of equation VI-18):

$$T_{1/2} = \frac{3T_1^2}{8R_c} \qquad \text{(VI-24)}$$

where T_1 is the b = 1 peak given approximately by equation VI-22. For $R_c \approx T_1 \approx 1$ GeV, we have $T_{1/2} \approx 3/8\ T_1 \approx 375$ MeV.

In Figure VI-7 we demonstrate the general features described in the example above. The unmodulated spectrum is derived from the non-thermal-radio-background data (Section VI.E.1). Both the full numerical solution and the DC approximate solution are shown for the case where R_c = 750 MV and η = 1950 MV. From equation VI-22 we compute $T_1^{FF} \approx 722$ MeV and from equation VI-24 we obtain $T_{1/2}$ = 261 MeV. These values, which agree with the position of the two "peaks" in the FN solution, are shown in the figure. Note that these values are about 2/3 of the DC peak energies, which are also indicated in the figure. The excellent agree-

ment of the solution with the 1968 data indicates that the particular choice of parameters used in the calculation is reasonable.

We feel that the above interpretation of the flat portion of the spectra forms a good, self-consistent picture with our present knowledge of the rigidity dependence of the diffusion coefficient and of the energy dependence of the interstellar electron spectrum. We also note that by knowing the energy dependences of both the diffusion coefficient and the interstellar electron spectrum and by observing a relative maximum in the near-Earth spectrum, we could, with the analysis presented here, determine the absolute interstellar electron intensity.

E. Quantitative Study of Solar Modulation

In the previous section we have qualitatively discussed the parameters of solar modulation theory. In this section we present a quantitative study of these parameters using:

1) the expected range of the interstellar electron spectrum,
2) the calculated interstellar positron spectrum,
3) a derivation of the modulation parameters and, hence, the diffusion coefficients, using the interstellar spectra of 1) and 2), numerical solutions of the transport equation, and the spectra measured near Earth,
4) a comparison of these diffusion coefficients with those derived from the available power-spectra data, and
5) numerical solutions of the transport equation for cosmic-ray protons and He nuclei using assumed interstellar spectra and the diffusion coefficients derived from the electron modulation study.

1. Determination of the Interstellar Electron Spectrum from the Galactic Non-Thermal-Radio-Background Emission

The galactic non-thermal-radio-background data are generally ascribed to synchrotron emission from relativistic electrons spiraling in the galactic magnetic field. Several authors have examined the radio data and, under certain assumptions on the galactic parameters, have calculated the corresponding galactic electron spectrum (Anand et al., 1968a,b; Verma, 1968; Webber, 1968, Goldstein, Ramaty and Fisk, 1970, Burger, 1971). However, knowledge of the galactic parameters is incomplete and previous studies have not attempted to indicate the possible range of interstellar intensities which are consistent with the acceptable range of the parameters. We shall assume that cosmic-ray electrons are distributed uniformly in the galaxy and estimate a

reasonable range of interstellar electron spectra consistent with the non-thermal-radio-background data and consistent with our knowledge of the galactic parameters. With this range of spectra we shall estimate the expected limits on the cosmic-ray modulation parameter.

In Figure VI-8 we show the non-thermal-radio data in the galactic anticenter direction*. The data above ~5 MHz are from the compilation by Webber (1968). Above ~40 MHz the data are primarily from high resolution surveys (~1° aperture) in which the galactic disk is well resolved. From ~ 5-40 MHz Webber has adjusted the available low (~30°) and medium (~10°) resolution data. He has used the high-resolution measurements of Blythe (1957) at 38 MHz to normalize the emissivities found in the lower-resolution studies to the standard anticenter direction. These adjustments amount to increasing the observed low-resolution intensities by ~10-30%. Below 5 MHz we have plotted the recent data of Alexander et al. (1970) from their instrument on board the RAE-1 satellite. The data from this low-resolution instrument are representative of emission and absorption from a broad region on the order of ~100 degrees in angular extent. Since the disk of the galaxy is only ~0.5 kpc thick (compared to a radius of ~15 kpc) it may be inappropriate to regard these data as representative of emission and absorption in the disk of the galaxy. However, these authors find the intensity below ~ 5 MHz to be nearly isotropic. This finding may indicate that due to interstellar absorption the radio emission at these

*The radio data in the anticenter direction are used in this analysis because they are somewhat easier to interpret than the data available in other directions (e.g. towards the galactic center or the direction of minimum brightness).

frequencies is coming from a local region. Our assumed range of galactic parameters includes values for which the absorption arises within both local ($\lesssim$100 pc) and extensive (~4 kpc) regions. However, even in the latter case the size of the region depends on the assumed galactic structure, such as the distance to absorbing cold clouds, etc. We shall interpret the low-frequency radio data as corresponding to emission and absorption in the disk of the galaxy. (Stephens (1971) has made an alternative interpretation in which emission from a spherical galactic halo is assumed to account for most of the low-frequency emission observed in the halo directions. Below ~200 MeV the interstellar electron intensity he assumes is slightly lower than that derived in this analysis.)

The general features of the radio spectrum in Figure VI-8 are:

1) a segment from ~10 to ~150 MHz which is proportional to $\nu^{-.4}$ with evidence for a steepening to $\nu^{-.7}$ or $-.8$ above ~150 MHz and
2) a segment from 0.4 to 1 MHz which is approximately proportional to $\nu^{1.6}$.

There is a smooth connection between these power-law segments in the intermediate frequency range of 1 to 10 MHz. Above about 10 MHz interstellar absorption becomes negligible (see Appendix B). If we assume the interstellar electron spectrum to be a power law in energy with spectral index γ, the intensity of synchrotron radiation is:

$$I(\nu, B_\perp, L) \propto C\, L\, B_\perp^{\frac{1+\gamma}{2}}\, \nu^{-\alpha} \qquad \nu \gtrsim 10 \text{ MHz} \qquad \text{(VI-25)}$$

(Ginzburg and Syrovatskii, 1964), where

ν is the frequency

$\alpha = \frac{\gamma-1}{2}$ is the resulting power-law index of the radio emission,

L is the line-of-sight emission length,

$B_\perp$ is the perpendicular component of the magnetic field,

C is the constant used in defining the spectrum of cosmic-ray electrons, i.e.,

$$N(W) = CW^{-\gamma}$$

where W is the total energy and N(W) represents the number of electrons per cm^3 per unit energy. Thus the power-law segment of the radio data above 10 MHz proportional to $\nu^{-.4}$ implies that $\gamma \approx 1.8$. We estimate, by constructing straight-line segments through the data points of Figure VI-8, that a range of slopes from -0.35 to -0.45 is consistent with the data. Hence, γ is roughly in the range 1.7 to 1.9.

At low frequencies free-free absorption by interstellar electrons and the Razin suppression of emission (Razin, 1960) must be considered. The Razin effect is due to the ambient electron density which causes the index of refraction to be greater than 1. We include both the Razin effect and free-free absorption in our calculations. We find, as did Ramaty (1971), that the Razin suppression represents in general a much smaller effect than free-free absorption. In Appendix B we show that in the case of large optical depth, and if we ignore the Razin effect,

$$I(\nu,B,L) \propto C\, B_\perp^{\frac{1+\gamma}{2}}\, \nu^{2-\alpha} \qquad \nu \ll 10 \text{ MHz} \qquad \text{(VI-26)}$$

Thus, at low frequencies the intensity is independent of the total line-of-sight emission distance, L. To match the observed $\nu^{1.6}$ dependence in the low-frequency range we again have $\alpha = 0.4$ or $\gamma \approx 1.8$, consistent with the result from the high-frequency data. If we use the 15% error

bars of the data of Alexander et al., as they suggest for the relative error between points, the range of observed slopes below 1 MHz is roughly 1.3 - 1.65, which implies a range of 1.7 to 2.4 for the spectral index of electrons, γ. The addition of Razin absorption will alter this picture slightly; however, this effect can be roughly compensated for by raising the interstellar temperature (see Appendix B).

At higher frequencies ($\gtrsim$ 150 MHz) the radio spectrum appears to be steepening to $\nu^{-(.7 \text{ or } .8)}$ which implies a cosmic-ray electron spectral index $\gamma \approx 2.4$ to 2.6. Most of the emission at 150 MHz comes from a region of the electron spectrum near 2 GeV (Appendix B). Thus we see that an interstellar electron spectrum consistent with the non-thermal-radio-background has a power-law index of ~1.8 below ~2 GeV which steepens to ~2.5 at higher energies. We have chosen a set of reasonable galactic parameters (see Table B-1), assumed a simple galactic model, and calculated the resulting electron spectrum necessary to fit the radio data, assuming the power-law indices of 1.8 and 2.5 mentioned above. In Figure VI-9 we display this nominal spectrum (which is essentially identical to one derived by Goldstein, Ramaty and Fisk, 1970) along with two spectra which result from a study of the reasonable range of galactic parameters*. This calculation is described in detail in Appendix B. We note that at high energies there is roughly a factor of 4 between the bracketing lower and upper spectra.

---

*The electron spectra are plotted between 70 MeV and 5 GeV. This energy range has been chosen so that there is less than 25% contribution to the radio emission at the minimum and maximum frequencies, 0.4 and 600 MHz, from electrons outside this energy range. This definition is consistent with the absolute accuracy of the low-frequency radio data ($\pm$25%).

(For convenience, the electron spectra are shown as connected power-law segments. The coefficients and spectral indices for each segment are given in Table B-2.)

In Figure VI-10 we show the calculated radio background which results from each of these electron spectra. All three curves are consistent with the radio data. In each calculation the different galactic parameters shown in Table B-3 were used.

The galactic electron spectra shown in Figure VI-9 will be used in Section VI.E.3 to derive the cosmic-ray modulation parameter from ~100 MeV to ~5 GeV.

2. Interstellar Positron Spectra from Galactic Nuclear Collisions

Due to the limiting lower frequency of the radio data, the interstellar electron spectra derived in Section VI.E.1 are restricted to energies above ~ 100 MeV. In order to complement the electron modulation studies at lower energies, we use the near-Earth Caltech positron data and the calculated interstellar positron spectrum.

Since there is no evidence to indicate the existence of anti-matter stars or galaxies, it is commonly assumed that there are no sources of primary, directly accelerated positrons. Above ~10 MeV nuclear interactions in the interstellar medium are believed to be the only source of cosmic-ray positrons. (Radioactive decays may contribute at lower energies.) Based on this collison-source mechanism, several authors have attempted to calculate the local interstellar positron spectrum. It is usually assumed that particles propagate by diffusing through the turbulent galactic magnetic field and that a steady-state exists between particle production and loss.

This process is described by:

$$Q(\vec{r},W) = \frac{\partial}{\partial W}\left(\frac{dW}{dt}\,U\right) - \vec{\nabla}\cdot(\kappa\vec{\nabla}U) \qquad \text{(VI-27)}$$

(Jokipii and Meyer, 1968)

where $Q(\vec{r},W)$ is the rate of positron production as a function of position, $\vec{r}$, and total energy, W, $U(\vec{r},W)$ is the positron density, and $\kappa(\vec{r},W)$ is the galactic cosmic-ray diffusion coefficient. The rate of energy loss, $\frac{dW}{dt}$, is determined by losses from ionization, bremmstrahlung, synchrotron radiation, and Compton collisions with starlight and the universal blackbody radiation. A reasonable approximation for the energy dependence of $\frac{dW}{dt}$ is

$$-\frac{dW}{dt} = a + bW + dW^2 \qquad \text{(VI-28)}$$

(Beedle, 1970)

where a is constant (ionization loss), b is constant (bW = bremmstrahlung loss) and $d \propto \frac{B^2}{8\pi} + w_{ph}$, where $\frac{B^2}{8\pi}$ and w_{ph} are the energy densities of the magnetic field and the photons, respectively.

There have been two basic approaches to solving equation VI-27. We briefly discuss each of these.

1) Leakage-lifetime approximation

In this method the diffusion terms and boundary conditions are replaced by a leakage-loss term $U/_{\tau}$, where τ is the "lifetime" of a particle before it escapes from the confinement volume. The production spectrum, magnetic field, hydrogen density, and photon density are considered independent of galactic position within the confinement region (disk or disk + halo). In the energy region most affected by

solar modulation ($\lesssim$1 GeV) the spectra calculated under these assumptions are essentially only dependent on the source function and $\bar{x} = \rho c \tau$, the amount of material traversed by the particles during the time τ. Among the recent calculations based on this method are those of Perola et al. (1968), Ramaty and Lingenfelter ("R&L") (1968), and Arai (1971). The spectra of R&L for $\bar{x} = 4$ g/cm^2 and Arai for $\bar{x} = 3$ and 5 g/cm^2 are shown in Figure VI-11. These authors have used different positron production spectra which accounts for their different calculated intensities. For comparison we also show in Figure VI-11 the measured spectra for 1965-66 and 1968.

2) Diffusion model

Several authors have pointed out that the leakage-lifetime approximation may not be physically justified for electrons. (Shen, 1967; Jokipii and Meyer, 1968; Beedle, 1970.) For example, the term U/τ implies that all particles are assumed to have a constant probability of escape. However, in reaching the boundary an electron may lose much of its energy (particularly high-energy electrons since their loss rate is αW^2). Hence, setting the loss rate to $U(W)/\tau$ where W is the particle's <u>initial</u> energy is not correct. In addition, the assumption of a production spectrum independent of galactic position may not be reasonable and several investigators have assumed different distribution functions for the matter density in the galaxy in making their calculations (Ginzburg and Syrovatskii, 1964; Shen, 1967; Beedle, 1970).

Beedle has solved equation VI-27 using an ellipsoid of revolution for the distribution of matter in the galaxy. He also

assumed the energy-loss rate (equation VI-28) to be independent of position. In Figure VI-11 we show his calculation of the local interstellar positron spectrum using the parameters $\rho = 1$ atom/cm^3, $\frac{B^2}{8\pi} + w_{ph} = 1$ ev/cm^3 and $\kappa = 10^{29}$ cm^2/sec. Of these parameters the calculated spectrum below ~1 GeV is most sensitive to the diffusion coefficient, κ, being ~50% lower at 10 MeV for $\kappa = 10^{30}$ cm^2/sec.

The positron intensity calculated by Beedle is roughly a factor of 10 larger than that derived by Ramaty and Lingenfelter. Below ~1 GeV the difference is primarily due to the different models used in the calculations. As noted by Beedle, his spectrum with $\kappa = 10^{29}$ cm^2/sec is almost identical to the $\bar{x} = \infty$ (i.e. $\tau = \infty$) disk-model spectrum of Perola et al. (1968). (He used their positron production spectrum.) Thus, in his model the particles we observe locally are not being lost through boundary escape. It is also interesting to note that all the calculated spectra of Figure VI-11 have roughly the same energy dependence.

We shall not attempt to choose between the various calculated spectra of Figure VI-11 on the basis of the validity of the models, the production spectra, etc. used in the calculations. Rather, we shall determine positron modulation parameters using both the bracketing high and low spectra of Figure VI-11. By requiring these results to be consistent with those of the electron modulation study, we shall approximately determine the galactic positron intensity.

3. Derivation of Modulation Parameters and Implications for the Low-Energy Interstellar Electron Spectrum

We have presented in Sections VI.E.1 and VI.E.2 our calculation of the expected range of interstellar electron spectra and the inter-

stellar positron spectra calculated by several authors. In addition, we have shown the data from the Caltech magnet spectrometer and from other experimenters covering the period 1965-71 (see Chapter V and Figures VI-1 and 11). We now derive the modulation parameter at Earth,

$$\psi(1,T) = \int_1^D \frac{V dr}{\kappa(r,T)}$$

for each of the years for which we have presented data. The discussion divides itself conveniently into two sections: a) the electron interstellar spectra and near-Earth data are used to derive the modulation parameters and diffusion coefficients above ~100 MeV and b) the positron interstellar spectra and near-Earth data are used primarily for the discussion of the modulation below 100 MeV.

a. Comparisons of Measured and Calculated Electron Spectra

Following the discussion in Section VI.D, we assume the diffusion-convection model is a reasonable first approximation to the transport equation and calculate $\psi(1,T) = \ell n \left[\frac{j(D,T)}{j(1,T)}\right]$ using the near-Earth spectra and the range of galactic spectra of Figure VI-9. In Figure VI-12 a-e we show ψ as a function of energy for the periods 1965-66, 1968, 1969, 1970, and 1971. The points are derived from the data of Figure VI-1 and are shown by circles which are filled for the high and low galactic spectra (connected by dashed lines) and open for the nominal spectrum. (Note that in Figure VI-12e (1971) some of the points are upper limits and hence the errors in the data points extend considerably beyond the dashed lines.)

Since the high and low interstellar spectra differ by roughly a factor of 4 above a few hundred MeV, the resulting uncertainty in ψ, $\Delta\psi$, is

$$\Delta\psi \approx \frac{\ell n\ 4}{2} \approx .7$$

At lower energies ($\lesssim$300 MeV), where the galactic electron spectrum is more uncertain, this error increases.

These ψ-values are derived from the DC approximation. To refine these values we adopt the following procedure: we first determine the rigidity dependence of the diffusion coefficient by drawing power-law segments through the "nominal" ψ-points of Figure VI-12 (open circles). If we assume a constant radial dependence for κ out to a boundary distance D, we have from equation VI-6

$$\kappa(r,R) = \frac{(D-1)V}{\psi(1,R)} \qquad \text{(VI-29)}$$

(We arbitrarily choose D = 10 AU in what follows; note from Figure VI-4b that the calculated spectra are practically independent of D.) Using this diffusion coefficient and the nominal interstellar electron spectrum, we determine the numerical solution of the transport equation. Since the DC approximate solution, upon which the diffusion coefficient is based, differs slightly from the numerical solution, the spectrum generated in this way does not represent the best fit to the data. Better agreement is achieved by adjusting slightly (in the manner described below) the rigidity dependence of the diffusion coefficient. To facilitate computation we use the following model for the diffusion coefficient (consistent with the power-spectra data - see Section VI.E.4):

$$\kappa(r,R) = \begin{cases} \beta\, \kappa_1(r)\, \kappa_2(R) & \\ C\,\beta R & R \geq R_2 \\ C\beta\sqrt{RR_2} & R_1 < R < R_2 \\ C\beta\sqrt{R_1R_2} & R \leq R_1 \end{cases} \qquad \text{(VI-30)}$$

where C is a constant. By adjusting the values of C, R_1, and R_2, we have calculated the electron spectra for the periods 1965-66, 1968, 1969, 1970, and 1971. These spectra are shown in Figure VI-13. The values of C, R_1, R_2, and η (defined by equation VI-15) for each epoch are given in Table VI-2 and the corresponding modulation parameters are shown as solid lines in Figure VI-12. For the present, below ~100 MeV, we have used an extrapolation of the nominal interstellar electron spectrum and a diffusion coefficient which is arbitrarily defined to be independent of energy. Therefore, we do not discuss quantitatively the electron modulation below ~100 MeV. In the next section we shall use the positron spectra in a discussion of the modulation at low energies.

Because of statistical errors of the data, the modulation parameters used in deriving numerical solutions in agreement with the data (solid lines in Figure VI-12) are not the only ones possible. As examples, in each of Figures VI-12a, b, and c we show limiting modulation parameter curves (dotted lines) from which acceptable fits to the data were derived using the same nominal interstellar electron spectrum. We note that these ψ's we have used in achieving consistency with the data differ only slightly from the ones calculated from the

TABLE VI-2

Diffusion Coefficient Parameters -- Electron Modulation Study

	Epoch	η (MV)	R_1 (MV)	R_2 (MV)	$C^*(\times 10^{18})$ (cm^2 sec/MV)
June-July	1965-66 (averaged)	1350	64	900	4.006
June-October	1968	1950	160	750	2.773
June-July	1969	2400	182	1000	2.253
June-July	1970	3300	312	1100	1.639
July	1971	2700	480	480	2.003

* These values are based on a solar wind velocity V = 400 km/sec and on a diffusion coefficient assumed independent of radius with a boundary D = 10 AU.

simple diffusion-convection approximation (open circles in Figure VI-12), confirming the discussion in Section VI.D.1.b.

The dotted modulation parameter curves of Figures VI-12a, b, and c represent an uncertainty in ψ due to the uncertainty of the measured spectra. In discussions of the absolute magnitude of κ we will need to consider the larger limits on ψ (dashed lines in Figure VI-12) which result from the uncertainty in our knowledge of the interstellar electron spectrum.

We have thus determined the rigidity (energy) dependence of the modulation parameter for electrons above ~100 MeV for each of the periods 1965-66, 1968, 1969, 1970, and 1971. Under the assumption κ separable in radius and rigidity, the rigidity dependence of ψ determines that of the diffusion coefficient. We now use the positron data to discuss the modulation parameters and diffusion coefficients at lower energies.

b. Comparisons of Measured and Calculated Positron Spectra

In Chapter V and Figure VI-11 we have shown the positron data for the same years used in the electron study as well as the calculated interstellar positron spectra. As we pointed out in Section VI.E.2 the various calculated interstellar positron intensities differ by a factor of ~10. We now demonstrate that the calculated spectrum of Ramaty and Lingenfelter (lower curve in Figure VI-11) yields modulation parameters consistent with the electron results while the spectrum of Beedle (upper curve) does not.

For the period 1965-66 we used the electron data of Fanselow et al. (1969) to derive the modulation parameters in the preceding section. Their instrument also yielded the only available positron fluxes

above a few hundred MeV in the 1965-66 time period. We have chosen to use only the data of Fanselow et al. in that time period in order to eliminate possible intercalibration problems between various instruments and thus preserve, as much as possible, consistency between positron and electron data. In Figure VI-14a we show a plot of the DC modulation parameter ψ based on the positron data and the calculated galactic positron spectra of both Beedle (circles) and R&L (squares). We have also plotted by lines the ψ from the electron study (Figure VI-12a) appropriate for the period 1965-66 when the positron data were taken. The dashed lines correspond to the estimated limits on ψ derived from the uncertainty in our knowledge of the interstellar electron spectrum. This band is consistent with the ψ-"data points" of R&L; on the other hand, the points of Beedle are in considerable disagreement. In Figures VI-14b, c, d, and e we show similar plots covering the years 1968-1971. In the cases where the modulation parameters from the electron and the positron studies overlap, e.g. 1970 and 1971, the ψ-points of R&L agree better with the electron values than do those of Beedle. Thus we believe that the interstellar positron intensity is roughly that calculated by Ramaty and Lingenfelter. However, we do not imply that the leakage-lifetime model on which his calculation is based is necessarily correct. Since all the calculated positron spectra have roughly the same energy dependence, we only infer from the modulation studies the approximate magnitude of the interstellar intensity. In the galactic nuclear collisions calculation, this magnitude depends on the assumed positron production spectrum as well as on details of the specific model.

There is other evidence that the positron intensity derived by

Beedle is not valid. For example, the intensity of electrons he calculates from galactic nuclear collisions is so high that it passes through the high-energy electron data observed near Earth. Thus, no "primary" source of negatrons is needed if we assume his calculation is correct. However, several authors have concluded from observed positron fractions that there exists a dominant primary source of cosmic-ray negatrons (Beuermann et al., 1969; Fanselow et al., 1969).

It has been suggested, however, that these observed positron fractions may not be representative of the <u>interstellar</u> positron fractions since electrons and positrons may be modulated differently, e.g. because the energy-loss effect depends on spectral shape (Beedle, 1970). To investigate this possibility, we used the numerical solution of the transport equation to calculate the positron fraction at the boundary and at 1 AU for two different cases. In both cases we used the galactic positron spectrum of R&L and, above 100 MeV, the nominal galactic electron spectrum (Figure VI-9). In model 1 we extrapolated the nominal galactic electron spectrum to low energies and used a diffusion coefficient appropriate for 1968 (see eq. VI-30 and Table VI-2). The resulting positron fractions (labeled MODEL 1) are shown in Figure VI-15. We have included the Chicago (1965-66) and Caltech (1969) observations for comparison. At low energies these measured points fall above the calculated curves. We can achieve better agreement by using an interstellar electron spectrum which turns over below 100 MeV (solid line in Figure VI-16b) and by modifying the diffusion coefficient such that below 60 MV, $\kappa \propto 1/R$. (We shall discuss this behavior at low energies shortly.) The resulting positron fractions are labeled MODEL-2 in

Figure VI-15. In general, the net effect is a shift of the 1 AU curve to lower energy with respect to the boundary curve. The shape of the positron-fraction curve is roughly preserved, however. The shifts are not large and the differences are smaller than the statistical errors of the data. Thus, we conclude that the positron fractions measured near Earth are also indicative of conditions in interstellar space and hence that a primary negatron source is required. Hence, we believe that the galactic secondary electron and positron intensities derived by Beedle are too large.

The low-energy values of the positron modulation parameters shown in Figures VI-14b, c, d and e indicate that the modulation is decreasing at low energies. This decrease is most evident in the plots for 1968 and 1969 (Figures VI-14b and c). For example, the solid line in Figure VI-14b represents a modulation parameter consistent with both the electron and positron studies. The segment below 60 MeV is proportional to 1/T (or, equivalently, 1/R). In Figure VI-16a we show the numerical solution of the transport equation at 1 AU using the diffusion coefficient derived from this modulation parameter and the interstellar positron spectrum of Ramaty and Lingenfelter (1968), together with the measured spectrum. The calculated spectrum is in excellent agreement with the low-energy data. In Figure VI-16b we show the numerical solution for the electron flux using the same diffusion coefficient. In order to achieve agreement with the data, the interstellar electron spectrum was turned over below 100 MeV as shown by the upper solid line in the figure.

The indicated energy dependence of the interstellar electron

spectrum in Figure VI-16b is not the only one possible. The dotted lines in Figure VI-14b show the possible range of the positron modulation parameter at low energies in 1968. This range was determined by considering both the uncertainty in the observed 1968 positron spectrum (Caltech) and the uncertainty in the magnitude of the interstellar positron intensity. The latter uncertainty was derived by assuming that the range of the modulation parameter derived from the electron intensity in 1965-66 (dashed lines in Figures VI-12a and VI-14a) also applied to the positron intensity in the region of overlap measured during the same period. (Fanselow et al., 1969). We have used the dotted modulation parameter curves of Figure VI-14b to "demodulate" the 1968 low-energy electron data of L'Heureux et al. (1972) (see Figure VI-1), assuming the diffusion-convection approximation, i.e. $j(D,T) = j(1,T)e^{\psi(1,T)}$. In Figure VI-17 we indicate the resulting range of interstellar electron spectra below ~50 MeV as a shaded region bounded by dotted lines. Above ~70 MeV we show as a shaded band the range of spectra consistent with the analysis of the non-thermal-radio-background data (Section VI.E.1 and Appendix B). For comparison we also show (solid line) the galactic electron spectrum of Figure VI-16b. We conclude from Figure VI-17 that the electron spectrum must flatten below ~100 MeV if the positron and electron modulation studies are to be consistent.

These general features, i.e. the turn-over in the galactic electron spectrum and $\kappa\alpha\frac{1}{R}$, which are based on the 1968 positron modulation study, are also supported by the 1969 results. In fact, the lowest-energy positron data point at ~14 MeV is almost the same in 1968 and

1969, implying that nearly equal modulation was observed during the two years at low energies. The higher-energy positron data for 1969 are statistically not as accurate as the 1968 data and therefore a detailed analysis is not warranted.

It is interesting to note that the solar-flare proton studies of Lupton (1972) are consistent with a 1/R dependence of $\kappa_2(R)$ at low rigidities. In the 1-10 MeV (43-137 MV) region he finds κ is roughly independent of kinetic energy. Since $\kappa \propto \beta \kappa_2(R)$, κ = constant implies $\kappa_2(R) \propto \frac{1}{\beta}$. For non-relativistic protons this is equivalent to $\kappa_2(R) \propto \frac{1}{R}$.

We note that Lupton's solar-flare studies determine the magnitude of κ between the Sun and the Earth, whereas the modulation studies yield information on the diffusion coefficient beyond 1 AU. For the June 7, 1969 event Lupton (1972) derives a radial diffusion coefficient of ~1 - 3.5 x 10^{20} cm^2/sec for the 1-10 MeV protons. If we assume κ independent of radius with a boundary at 12 AU (see next section) and use the positron modulation parameter from Figure VI-14b (solid line), we derive $\kappa \approx 7.5 \times 10^{19}$ cm^2/sec for the low-energy protons. Thus the solar-flare result is a factor of ~3 larger than this estimate from the positron modulation study. This disagreement may imply that a) the boundary is at a larger distance than 12 AU or b) κ is larger inside 1 AU than beyond. For example, if we assume $\kappa \propto \frac{1}{r}$ outside 1 AU, then a boundary distance of ~9 AU yields a modulation-derived κ consistent with the solar-flare result.

We note that solar-flare studies have generally used boundary distances of ~3 - 6 AU in order to fit the observed exponential

decay. However, recent evidence (Marshall and Stone, 1972) indicates that during the time interval of the flare observations an equilibrium condition may not be reached and a larger boundary is also consistent with the data.

In summary, the important conclusions from the positron modulation studies are a) the interstellar positron spectrum of R&L provides consistency between electron and positron modulation studies above ~100 MeV and b) below ~100 MeV the diffusion coefficient must increase and the interstellar electron system must flatten considerably to maintain consistency between positron and electron modulation.

4. Relation of Cosmic-Ray Diffusion Coefficient to Power Spectra of the Interplanetary Magnetic Field and Implications for the Radial Dependence of the Diffusion Coefficient

The diffusion coefficient derived from the electron and positron modulation studies is an "average" κ for the entire modulation region, i.e. the modulation parameter essentially determines $\int_1^D \frac{dr}{\kappa(r,T)}$.

On the other hand, measurements of the power spectrum of the interplanetary magnetic field, made near 1 AU, determine the local diffusion coefficient. Therefore, a quantitative comparison of these diffusion coefficients can provide information on the radial dependence of κ, including estimates of the size of the modulation region.

The basic theory relating the cosmic-ray diffusion coefficient to the magnetic-field power spectrum is described in the review paper of Jokipii (1971). Two methods of calculating the parallel diffusion coefficient are given, which yield the same result only if $P_\perp \alpha \nu^{-1}$, where $P_\perp$ is the spectral density of the perpendicular fluctuations and

ν is the frequency. The different methods result from the use of different approximations to the basic Fokker-Planck equation describing the evolution of the particle distribution function. Recently, Earl (1972b) has developed an improved approach based on eigenfunctions of the operator which describes pitch-angle scattering. The evaluation of the lowest-order eigenfunction leads to a precise expression for the parallel diffusion coefficient. This method is easily applied when the power spectrum can be represented by a power law in frequency with one index. For typical values of the index (-.5 to - 2) Earl finds that the second method discussed by Jokipii, the perturbation method (1971; see also: Jokipii, 1966; Hasselmann and Wibberentz, 1968), yields results within 10% of his calculation. The other method (Jokipii, 1968) gives results that differ considerably from those of Earl. In this discussion we use the perturbation method of Jokipii rather than Earl's method for two reasons: 1) the calculation is in terms of an integral of the power spectrum over frequency and hence it is more easily applied to various functional forms of $P_{\perp}(\nu)$ and 2) Jokipii's method allows a determination of the appropriate rigidity range of the diffusion coefficient corresponding to the frequency range of the observed power spectrum.

If the magnetic-field fluctuations are approximated as one-dimensional waves propagating along the field direction, we can represent Jokipii's integral equation for the parallel diffusion coefficient as:

$$\kappa_{\parallel}(R) = \frac{\beta c R^2}{V} \int_0^1 \mu' \left[\int_0^{\mu'} \frac{\mu d\mu}{P_{\perp}\left(\nu = \frac{VB}{2\pi\mu R}\right)} \right] d\mu' \qquad \text{(VI-31)}$$

where R is particle rigidity, V is the solar-wind velocity, B is the magnetic field strength, and $\mu=\beta_{\parallel}/\beta=\cos\varphi$ where $\beta_{\parallel} c$ is the component of the particle velocity, βc, along the direction of the field and φ is the pitch angle. Note that $P_{\perp}(\nu)$ refers to a frequency spectrum defined for negative as well as positive frequencies. The published power spectra are defined for positive frequencies only and hence must be multiplied by a factor of 1/2 before insertion in equation VI-31.

Power spectra during the relevant time period have been published by Jokipii and Coleman (1968), Sari and Ness (1969), Bercovitch (1971), and Quenby and Sear (1971). In Figure VI-18 we show the data from these authors in the range 10^{-6} - 10^{-2} Hz for the indicated time periods.

Sari (1972b) has noted that, in evaluating $\kappa_{\parallel}$, the power spectrum observed by the spacecraft must be converted to the power spectrum "observed" by a particle spiraling along the average magnetic field line. The power spectra of Figure VI-18 represent power at wavelengths which are frozen into the field and convected past the spacecraft in the radial direction. Particles, however, are scattered by the power at wavelengths along the field direction. It can be shown that if $P_{\perp} \propto \nu^{-q}$ then the corrected power spectrum is:

$$P_{\perp}^{\text{corrected}} = (\cos\theta)^{q-1} P_{\perp}^{\text{observed}}$$

where θ is the angle between the average field direction and the Earth-Sun line ($\sim 48^{\circ}$ at 1 AU). For q = 1.5, typical at high frequencies, the correction at 1 AU is about 16%. (Note that the above correction differs by a factor of cos θ from that derived by Sari (1972b).)

We approximate the observed power spectra by power-law segments, apply the correction mentioned above, and use equation VI-31 to compute $\kappa_{\parallel}$ for each of the power spectra (except the high-frequency data of Sari and Ness in which q = 2 where equation VI-31 breaks down). In each case we have assumed V = 400 km/sec and B = 5γ (1γ = 10^{-5} gauss). The results are displayed in Figure VI-19.

We note that for a given rigidity, R, contributions to $\kappa_{\parallel}(R)$ in equation VI-31 come from the power spectrum at all frequencies <u>greater</u> than $\nu_{min} = \frac{VB}{2\pi R}$. For B = 5$\gamma$ and V = 400 km/sec the numerical relation between ν_{min} in Hz and particle rigidity in GV is

$$\nu_{min} = \frac{0.955 \times 10^{-4}}{R} \qquad \text{(VI-32)}$$

Since a given power spectrum only extends up to some maximum frequency, ν_{max} ($\approx 10^{-4}$ - 10^{-2} Hz), it follows from equation VI-32 that for $R \leq R_{min} = \frac{0.955 \times 10^{-4}}{\nu_{max}}$ <u>none</u> of the contribution to $\kappa_{\parallel}$ is derived from the measured power density of the field fluctuations. In calculating $\kappa_{\parallel}$ from equation VI-31 it is necessary to extrapolate the measured power spectra of Figure VI-18 to higher frequencies. The diffusion coefficients shown in Figure VI-19 are plotted to a lower-limit rigidity, R_{low} such that <u>less</u> than <u>50%</u> of the contribution to $\kappa_{\parallel}$ is from the <u>extrapolated</u> portion of the power spectrum.

These diffusion coefficients can be characterized by a parameter b where

$$\kappa_{\parallel} \propto R^{b}$$

In general, we find that b ≈ 1.5 - 2 near 100 GV and is slowly decreasing to perhaps .5 in the region near 1 GV.

We now compare these diffusion coefficients with those derived from the electron modulation study. In that study we used the radial diffusion coefficient, κ_{rr}, which depends on both $\kappa_{\parallel}$ and $\kappa_{\perp}$ and is given in terms of these quantities by equation VI-3. By substituting $\theta = 48^{\circ}$ (i.e. the 1-AU value) in the equation we have

$$\kappa_{rr} = 0.45\kappa_{\parallel} + 0.55\kappa_{\perp} \qquad \text{(VI-33}$$

At present there is no consensus on the value of $\kappa_{\perp}$. It has been suggested that perpendicular diffusion is dominated by the random walk of the field lines (Jokipii, 1966; Jokipii and Parker, 1969), as measured by the power at zero frequency:

$$\kappa_{\perp}(R) \approx \begin{cases} \frac{1}{4}\frac{\beta cV}{B^2} P_{\perp}(\nu = 0) & R \leq 1 \text{ GV} \qquad \text{(VI-34a)} \\ \frac{1}{2}\frac{\beta cV}{B^2} P_{\perp}(\nu = 0) & R \gg 1 \text{ GV} \qquad \text{(VI-34b)} \end{cases}$$

Jokipii and Parker (1969) have noted that $P_{\perp}(\nu)$ must have zero slope at low frequencies and have estimated $\kappa_{\perp}$ by making a low-frequency extrapolation of the observed power spectrum of Jokipii and Coleman (1968). However, the power at zero frequency is difficult to measure and such extrapolations represent only estimates of the perpendicular diffusion coefficient. Furthermore, these extrapolations may represent a large overestimate of $\kappa_{\perp}$ for the following reason. A large part of the observed power at low frequencies may be due to tangential discontinuities being swept past the spacecraft. Such discontinuities may be visualized

as representing an interplanetary medium composed of many relatively disordered flux tubes of plasma. Within a given flux tube the field has roughly the same average direction. It is not clear whether the contribution to the magnetic-field power spectrum from such discontinuities should be removed before extrapolating to zero frequency in estimating $\kappa_\perp$.

Because of the systematic nature of the uncertainty of $\kappa_\perp$ we shall consider two limiting estimates: 1) we shall extrapolate the power spectra to zero frequency and use equation VI-34 to estimate $\kappa_\perp$, and 2) we shall also consider the case $\kappa_\perp \approx 0$ (i.e. $\kappa_\perp \ll \kappa_\parallel$).

As an example, we compare the radial diffusion coefficient from the 1968 modulation study with that derived from the power spectrum of Quenby and Sear (1971). In Figure VI-20 we show the κ_{rr} derived from the power-spectra data for the period 12/68-3/69 using equation VI-33. Curves 1 and 2 correspond to the results for $\kappa_\perp = 0$ and $\kappa_\perp = 4 \times 10^{21}$ cm^2/sec, respectively. The latter estimate is the zero-frequency extrapolation result using equation VI-34a. (The high-rigidity result for $\kappa_\perp$ given by equation VI-34b is only a factor of 2 larger than the low-rigidity value. Since $\kappa_\perp \ll \kappa_\parallel$ at high rigidities, the use of equation VI-34a for the entire rigidity range is reasonable.) The error bars on the two curves indicate the 2σ uncertainty in the observed power spectrum assigned by Quenby and Sear. Since the quantity determined from the cosmic-ray modulation is an integral, $\psi(r, R) = \int_r^D \frac{V dr'}{\kappa(r', R)}$, the actual magnitude of the modulation-derived κ at 1 AU depends on its assumed radial dependence

including the boundary distance, D. Assuming a constant radial dependence with a boundary at 12 AU we obtain from the 1968 modulation study the diffusion coefficient shown as the solid line in Figure VI-20. The 3 representative error bars indicate the approximate uncertainty derived from the limiting modulation parameter curves of Figure VI-12b. Although there is only a limited region of overlap, the rigidity dependences of the diffusion coefficients derived from the power-spectra method and from the modulation study are consistent.

We can place limits on the possible value of the boundary distance, D, by requiring that the magnitude of the modulation-derived κ agree with that from the power spectra study. As an illustration, we show in Figure VI-21 a comparison at 1 GV of these diffusion coefficients as a function of boundary distance assuming κ <u>independent</u> of radius. The two power-spectra estimates of κ are shown as horizontal bands, corresponding to the 2σ uncertainty of the data. The boundary dependence of the modulation-derived κ is:

$$\kappa(D,\ 1\ GV) = \frac{V \cdot (D-1)}{\psi(1\ AU,\ 1\ GV)}$$

and the band in this case results from the uncertainty in our knowledge of the interstellar electron spectrum. The crosshatched areas represent the intersections of the bands. We find that if $\kappa_\perp$ is negligible, boundary distances of 6-15 AU are required for consistency between the two diffusion coefficients, under the assumption κ independent of radius. If $\kappa_\perp$ is 4×10^{21} cm^2/sec (the value inferred from the zero-frequency extrapolation of the Quenby and Sear power spectrum), we obtain the boundary range 11-25 AU.

If we assume a different radial dependence for κ, the integral definition of the modulation parameter (equation VI-6) still determines the magnitude of the diffusion coefficient at 1 AU as a function of boundary distance. By requiring this magnitude to be consistent with that derived from the power spectrum we can calculate the limits on D for any specified radial dependence of κ. As a simple example, we consider the case $\kappa_\perp \ll \kappa_\parallel$ and assume κ is a separable function of radius and rigidity with the radial dependence $\kappa_1(r) \alpha r^n$. We calculate the minimum and maximum D for different values of the index n. At the comparison rigidity of 1 GV in 1968 it can be shown from the definition of ψ (equation VI-6) that the functional forms of D_{min} and D_{max} in AU for the case considered are given by:

$$D_{min}^{1-n} = 1 + 5.0\ (1-n) \qquad \text{(VI-35a)}$$

$$D_{max}^{1-n} = 1 + 14.2\ (1-n) \qquad \text{(VI-35b)}$$

In Figure VI-22 we show plots of these limiting boundary distances as a function of the index n. The horizontal bar at n = 0 indicates the 6-15 AU range we obtain for κ independent of r. If the index n has a value n_c such that $D_{min}^{1-n_c} \leq 0$, we cannot obtain consistency between the diffusion coefficients derived from the magnetic-field power spectrum and from the electron modulation study for any value of D. From equation VI-35a we obtain

$$n_c \geq 1.2$$

for the case $\kappa_\perp \ll \kappa_\parallel$. For $\kappa_\perp = 4 \times 10^{21}$ cm^2/sec the condition is $n_c \geq 1.1$. Thus, if κ is assumed to increase with r faster than $\sim r^{1.1}$, there is not enough calculated modulation of electrons beyond 1 AU to agree with the observed modulation.

Recently, Jokipii (1972) has calculated the radial dependence of κ for two types of fluctuations: 1) Alfvén waves and 2) frozen-in irregularities. Beyond about 1 AU he finds for Alfvén waves, $\kappa_{rr} \propto r^0$, and for frozen-in fluctuations, $\kappa_{rr} \propto 1/r$. From equation VI-35 (or Figure VI-22) we find that a 1/r dependence would imply a boundary range of ~3.3 - 5.5 AU (4.6 - 7.0 AU for $\kappa_\perp = 4 \times 10^{21}$ cm^2/sec). The r^0 behavior gives the 6-15 AU range we derived above.

5. Comparisons of Measured and Calculated Spectra of Cosmic-Ray Protons and He Nuclei

In Section VI.E.3 we discussed the numerical solutions of the transport equation for electrons and positrons for the periods June-July 1965-66 (averaged), June-October 1968, June-July 1969, June-July 1970, and July 1971. Electron spectra consistent with the data were calculated using the nominal interstellar electron spectrum (Section VI.E.1) and the diffusion coefficients described by equation VI-30 using the values of the parameters listed in Table VI-2.

The transport equation for cosmic-ray nuclei is the same as that for electrons (equation VI-1). It follows that we should be able to use the electron-derived diffusion coefficients in deriving numerical solutions appropriate for the nuclei. In this section we present such solutions under the following restrictions and assumptions:

1) rigidity dependences of the diffusion coefficient derived from the electron modulation parameters based on the nominal

interstellar electron spectrum

2) diffusion coefficient independent of radius with boundary at 12 AU. (Calculated spectra for boundaries in the range 6-25 AU, derived in Section VI.E.4, are identical above a few hundred MeV/nucleon and differ by less than 20% above ~40 MeV/nucleon.)

3) constant solar-wind velocity of 400 km/sec

4) interstellar spectra of nuclei given by

$$j = A(W - m/4)^{-2.65} \quad p/(m^2 \text{ sec sr MeV/nucleon})$$

where W is the total energy per nucleon, m is the nucleon rest energy and A is 1.07×10^9 and 7.67×10^7 for protons and He nuclei, respectively. (See Garrard (1973) for discussion of this particular form of the interstellar spectra.)

Cosmic-ray proton and He-nuclei data similar to those compiled by Garrard (1973) for the periods 1965-1970 are shown in Figure VI-23 a-d and Figure VI-24 a-d, respectively. In each figure we show one or two calculated spectra using diffusion coefficients described by equation VI-30 with the parameters listed in Table VI-3. Each calculated spectrum is marked with a number corresponding to an entry in the table. (Garrard used parameters similar to those shown in Table VI-3. His calculated spectra are slightly steeper at low energies, however, since he used boundary distances of 2.7 and 6.1 AU.) A complete discussion of the relation between the calculated and observed spectra is given by Garrard (1973). We include a short description for each of the epochs listed in Table VI-3.

TABLE VI-3

Diffusion Coefficient Parameters - Nuclei Modulation Study

Entry Number	η (MV)	R_1 (MV)	R_2 (MV)	C^* ($\times 10^{18}$) (cm^2 sec/MV)	Data Epoch and Figure Reference
1	1350	62	800	4.905	1965-66 VI-23a and VI-24a
2	1950	160	750	3.389	1968p VI-23b; 1967-68α VI-24b
3	2860	172	1500	2.311	1969 VI-23c and VI-24c
4	3070	229	1300	2.153	
5	3300	286	1200	2.003	1970 VI-23d and VI-24d

* These values are based on a diffusion coefficient assumed independent of radius with a boundary at 12 AU.

1965-66 (Figures VI-23a and VI-24a):

The calculated curve is based on the same parameters as used in the 1965-66 electron study. The curve is slightly above the low-energy proton measurements and slightly below the corresponding He-nuclei data points. We regard the fits as adequate for this "two-year" epoch.

1968 p and 1967-68α (Figures VI-21b and VI-24b):

The same parameters are used as in the 1968 electron study. The fit is good for both the proton and He-nuclei spectra.

1969 (Figures VI-23c and VI-24c):

We include two curves. Curve 3 is derived using parameters consistent with the electron study. Both the proton and He-nuclei measurements fall below the curve. A better fit is obtained by increasing ψ by ~7% (curve 4). This change is justified since the 1969 nuclei data were taken in August-September whereas the electron data were collected in June-July. Since ψ may have changed by as much as 40% from summer 1969 to summer 1970 (see Table VI-2), a 7% change over a two-month period is reasonable. (The turn-up in the observed proton spectrum below ~40 MeV, which is not reproduced in the calculated spectra, may be due to solar emission (Garrard, 1973).)

1970 (Figures VI-23d and VI-24d)

The calculated He-nuclei curve is slightly below the data points but the curve does fall within the error bars. The observed proton spectrum is much flatter than the calculated curve. Since this period is near solar maximum, the flattening may result from a combination of depressed galactic fluxes and possibly enhanced solar emission.

In general we regard the fits for the nuclei spectra for 1965-

1970 as adequate. We note that we have achieved reasonably good agreement despite the many restrictions imposed, i.e. the use of the ψ's derived from the electron data using only the nominal interstellar electron spectrum, the particular interstellar spectra of nuclei assumed, and the restriction κ independent of r. We have not, however, ruled out the possibility of different interstellar nuclei spectra or more complicated radial dependences of κ. On the other hand it is not necessary to invoke them. In addition, the argument (e.g. Burger and Swanenburg, 1971) that a diffusion coefficient which is non-separable in its rigidity and radial dependences is necessary to fit the electron and nuclei data is not seen to be true. However, we cannot rule out a non-separable diffusion coefficient.

In summary, we find that the good agreement between the calculated and measured nuclei spectra indicate that

a) the interstellar proton and He-nuclei spectra used are reasonable (although it must be remembered that at low energies ($<$ few hundred MeV) the near-Earth spectra are relatively insensitive to the interstellar spectra) and

b) the diffusion coefficients derived from the electron modulation studies are appropriate for the nuclei as well.

Thus the nuclei form the final element in our consistent picture of the solar modulation of cosmic rays.

VII. SUMMARY

In this thesis we have derived the expected range of the interstellar spectra of positrons and electrons ($e^+ + e^-$) and have discussed the mechanism of solar modulation of cosmic rays.

We have based our studies on cosmic-ray positron and electron spectra, measured by us and by other investigators. The observations covered an energy range of ~10 MeV to ~10 GeV and the time period 1965-1971. The studies presented here have led to the following conclusions:

1) Analytic Approximations to the Cosmic-Ray Transport Equation

We have used numerical solutions of the full transport equation describing cosmic-ray propagation in the interplanetary medium to discuss the validity of several analytic approximations to the equation. We have found that:

a) In order for the convection-adiabatic deceleration approximation to be valid the interstellar intensity of electrons is required to be a factor of ~8000 greater than that inferred from the analysis of the galactic non-thermal-radio-background data.

b) The force-field approximation is inadequate at low energies. The diffusion coefficients and interstellar spectra derived by Meyer et al. (1971) and Schmidt (1972) using this approximation are inconsistent with our conclusions for energies

below ~100-200 MeV.

c) The diffusion-convection approximation yields a reasonable first-order solution of the transport equation for both electrons and positrons. Energy loss by adiabatic deceleration ($\lesssim 50\%$) leads to a shift in energy of the numerical solution at 1 AU from the DC approximate solution, but, on the whole, the spectral shape is preserved. In the DC approximation the logarithm of the ratio of the interstellar cosmic-ray intensity to the near-Earth intensity is the modulation parameter $\psi(1,R) = \int_1^D \frac{V dr}{K(r,R)}$. Thus, if the diffusion coefficient, K, is assumed to be a separable function of radius, r, and rigidity, R, the DC approximation may be used to estimate the rigidity dependence of K from a knowledge of the near-Earth and interstellar electron (or positron) spectra.

In addition, we have used the diffusion-convection and force-field approximations, together with numerical solutions of the full transport equation, to discuss the expected behavior of the electron spectrum at 1 AU at energies above ~100 MeV. Assuming a nominal galactic electron spectrum, we found that the flat portion of the near-Earth electron spectrum from ~100 MeV to 1 GeV can be attributed to a change in the rigidity dependence of the diffusion coefficient near 1 GV. We have also shown that a knowledge of only the energy

dependences of the interstellar spectrum and the interplanetary cosmic-ray diffusion coefficient is sufficient to estimate the absolute solar modulation of electrons (or positrons) at the energy of a relative maximum in the near-Earth spectrum. Further analysis may lead to improved estimates of the absolute interstellar positron and electron intensities.

2) Interstellar Electron and Positron Spectra

We have made a new derivation of the approximate range of the interstellar electron spectrum at energies between ~100 MeV and ~5 GeV from the non-thermal-radio-background data. Uncertainties in our knowledge of the galactic parameters used in the analysis lead to an uncertainty of about a factor of 4 in the electron intensity above ~300 MeV and to larger uncertainities at lower energies.

We have discussed several interstellar positron spectra calculated by other investigators for the energy range 10 MeV - 10 GeV. Since the calculated absolute intensities differ considerably, we determined the appropriate spectrum by requiring consistency between the electron and positron modulation studies at energies above ~100 MeV. We have used the most consistent interstellar positron spectrum (i.e. that proposed by Ramaty and Lingenfelter (1968)) and the Caltech positron data to study the modulation of both positrons and electrons at low energies. From this study we concluded that the interstellar cosmic-ray electron spectrum must flatten considerably below ~100 MeV. Our solar modulation studies indicate that the ratio of positrons to electrons in interstellar space is nearly the same as that at 1 AU. We thus conclude that the low values of the positron fraction measured near 1 AU imply that cosmic-ray electrons with energies above ~10 MeV have a predominantly primary origin.

3) Diffusion Coefficient and Size of the Modulation Region

From a comparison of the interstellar and near-Earth electron (and positron) spectra we calculated the modulation parameters for the periods 1965-66, 1968, 1969, 1970, and 1971. These parameters were used to derive the approximate rigidity dependences of the diffusion coefficients for these periods. These rigidity dependences were compared with those calculated from measurements of the power spectrum of the interplanetary magnetic field. In the limited rigidity range where the comparison is possible, these rigidity dependences were consistent. For rigidities below ~60 MV we derived diffusion coefficients which increased with decreasing rigidity. This increase at low rigidities is consistent with the rigidity dependence inferred from the solar-flare proton studies of Lupton (1972). A comparison of the magnitudes of the diffusion coefficients derived from the solar-flare and the modulation studies indicates that at low energies K may be larger inside 1 AU than beyond or that the distance to the boundary of the modulation region may be relatively large (~30 AU).

We have also derived limits on the possible radial dependence of K by requiring that the magnitude of the modulation-derived diffusion coefficient be consistent with that derived from the power-spectra study. Assuming $K(r) \propto r^n$, we found that $n \lesssim 1.1$. For K independent of radius, consistency between the magnitudes of the diffusion coefficients requires the boundary of the solar modulation region to be in the range 6-25 AU.

We have also applied the diffusion coefficients derived from these electron modulation studies to the cosmic-ray nuclei.

Assuming a particular form for the interstellar spectra of protons and the nuclei, we have calculated spectra of these particles at 1 AU which are consistent with the observations. Since our complete analysis was done assuming a diffusion coefficient which is a separable function of radius and rigidity, and consistency with the measured spectra was achieved, we found (as have Gleeson and Urch (1972)) no necessity to invoke the non-separable diffusion coefficients proposed by some authors.

APPENDIX A

Details of Data Analysis

1. Selection Criteria for Data Analysis

The selection criteria for "acceptable events" are essentially the same for both detector configurations MOD-1 and MOD-2. The criteria have been explained in detail by Rice (1970). A brief review of the procedure will be given as well as a description of the differences between MOD-1 and MOD-2 selection criteria.

a. Spark Chamber Performance

Initially, the trajectory of a particle in each spark chamber is determined by making a least-squares fit of the measured spark locations to a straight line. In some events either no spark or a spurious spark is registered in one or more modules within a spark chamber. In these cases the module is ignored in the least-squares fit. If more than one plane in a chamber malfunctions, the event is categorized as a "multi-error" event and rejected from analysis. "Perfect" events are those in which all 8 planes determine the trajectory in the two chambers, and "one-error" events are those in which an error is detected in one plane in either or both of the chambers.

The trajectories of the "perfect" and "one-error" events are subjected to further tests to determine their acceptability. The average deviation of the measured spark locations must be within 1.25 mm of the best-fit straight line or the event is rejected. In addition, the extrapolated trajectories in each chamber must fall within

the acceptance cone of the detector.

In connection with the above criteria, multiple-particle events can be recognized by the multiple-spark-indicator (MSI) bit (see Chapter II). In analyzing the 1968 data it was necessary to ignore this bit because some of the modules developed persistent spurious sparks at the edge away from the pick-up coil. As explained by Rice, this condition did not significantly affect the data. The frequency of occurrence of these spurious edge sparks was subsequently reduced and in later years it was necessary to ignore the MSI bit in no more than one module per flight. The MSI feature is somewhat more important in the analysis of MOD-2 data since the 2 g/cm^2 of material above the upper spark chamber (gas Čerenkov counter) is a possible source of contaminating particles. The contamination due to this effect is discussed in Appendix A.4.c.

b. Trajectory-Consistency Check

This simple test, which utilizes the symmetry of the detector and the magnetic field, determines whether the calculated trajectories in the two spark chambers are consistent with the bending expected in the field for the computed deflection angle. In Figure A-1 we show a projected particle trajectory assuming no scattering and an idealized, uniform magnetic field that is completely confined to the gap. Outside the gap the trajectories are straight line segments whereas inside the field region of the magnet the path is an arc of a circle. From simple geometry it can be shown that for the idealized path shown

$$\Delta = \lambda_1 - \lambda_2 = 0 \quad . \tag{A-1}$$

This equation (which is also valid for a field with symmetrical fringing above and below the magnet gap) is a necessary and sufficient condition for $\overset{\frown}{cd}$ to be joined smoothly to the straight-line segments $\overline{ca}$ and $\overline{db}$ (see Figure A-1 for definition of symbols). The angles λ_1 and λ_2 are calculated from the trajectories in the spark chambers. However, the idealized values of λ_1 and λ_2 are not determined because of multiple scattering and the intrinsic angular resolution of the detector (see Appendix A.2). The expected angular distribution for Δ due to these effects has been calculated (Rice, 1970), and the result for the standard deviation of Δ is

$$\sigma_\Delta = \sqrt{\sigma_\theta^2 + 4\sigma_\omega^2} \qquad \text{(A-2)}$$

where ω and θ (the deflection angle) are defined in Figure A-1. The uncertainty in θ, σ_θ, depends on the angular resolution of the detector and is derived in Appendix A.2 (equation A-11). The uncertainty in ω, σ_ω, results from the uncertainty in the spark locations of the modules defining the line segment $\overline{ab}$. Rice (1970) derived $\sigma_\omega \approx .0014$ radians. Using this value for σ_ω and equation A-11, equation A-2 reads:

$$\sigma_\Delta \approx \begin{cases} \sqrt{(.17\theta)^2 + (.004)^2} & \text{MOD-1} \qquad \text{(A-3a)} \\ \sqrt{(.068\theta)^2 + (.004)^2} & \text{MOD-2} \qquad \text{(A-3b)} \end{cases}$$

A possible further contribution to σ_Δ due to non-uniformities in the magnetic field was found to be negligible.

In the case of MOD-2 observations we adopt a selection criterion such that events with a Δ more than approximately 2σ away

from zero are rejected. Using a Gaussian approximation for the Δ-distribution with the σ_Δ of equation A-3b, we would obtain for the selection criterion:

$$\Delta \leq \Delta_c$$

$$\Delta_c^2 = (.136\theta)^2 + (.008)^2$$

However, at low energies (large θ) where multiple scattering is important the Gaussian approximation is not very accurate. For example, Figure A-3b shows the probability for electrons to scatter through angle greater than φ versus momentum x φ. (This distribution function is calculated in Appendix A.2). At the "2σ" level (ordinate = 0.025) there is considerable disagreement in the actual computed distribution (curve 1) and the Gaussian approximation (curve 2) used in deriving σ_θ in equation A-2. Based on these considerations we adopt as a criterion on Δ for acceptance of an event

$$\Delta \leq \Delta_c$$

$$\Delta_c^2 = (.155\theta)^2 + (.008)^2 \qquad \text{MOD-2} \qquad \text{(A-4a)}$$

Thus at high energies ($\theta \approx 0$), $\Delta_c \approx .008 \approx 2\sigma_\Delta$ and we reject ~5% of valid MOD-2 events. At low energies (large θ), $\Delta_c \approx .155\theta$. From Figure A-3b at $p\Delta_c = .155p\theta = 1.37$ (equation II-2b implies $p\theta = 8.85$) we find that we are rejecting about 7% of the valid events.

The selection criterion for MOD-1 events is based on similar considerations (Rice, 1970):

$$\Delta \leq \Delta_c$$

$$\Delta_c^2 = (.32\theta)^2 + (.008)^2 \qquad \text{MOD-1} \qquad \text{(A-4b)}$$

However, the scattering angle distributions shown in Figures A-3a and b are slightly different from the distributions calculated by Rice. At low energies $p\Delta_c \approx .32p\theta \approx 1.15$ (equation II-2b implies $p\theta = 3.55$). Thus we are rejecting about 11% of the valid MOD-1 events at low energies. The high-energy rejection is ~5%. These limits and standard deviations apply equally well to the cosmic-ray nuclei since the scattering term is negligible for these events. Thus, the criteria introduce essentially no bias according to particle species or rigidity. On the other hand, the criteria are such that there is very little probability that an event will be accepted which includes spurious sparks in the trajectory determination.

In Figure A-2 we show the Δ distributions for the analyzable (perfect + one-error) events as measured at the Caltech Synchrotron for positrons of 85 and 790 MeV energy using the MOD-1 detector. The smooth curves represent the calculated Gaussian distributions based on the standard deviation given by equation A-3a. The shaded areas show the events which are rejected because of the Δ-criterion (equation A-4b).

2. Rigidity Resolution

The resolution of the MOD-1 detector system has been described in detail (Rice, 1970). Much of that discussion is relevant to the present description. However, some refinements in the calculations have been made and therefore a general discussion will be presented.

The ability of the detector to measure the rigidity of a particle is principally affected by 1) multiple scattering within the chambers or magnet gap and 2) the intrinsic angular resolution. Multiple scattering of the electrons adds a random angular deviation to the true deflection angle. Most of the scattering occurs at the wire planes and aluminized mylar covers adjacent to the magnet gap. A rough calculation of this effect was made previously by Rice. We have made a more refined calculation which uses a better approximation to the true mass distribution of the wires and which also includes scattering in the gas of the chambers and magnet gap. In Figures A-3a and b we show (curve 1) the distribution of projected scattering angle φ in the y-z plane (see Figure A-1 for definition of this plane) calculated for electrons of momentum p according to the theory of Moliere (Galbraith and Williams, 1964). Both the differential distribution $\frac{dN}{d\varphi}$, which is normalized by dividing by the momentum p, and the integral angular distribution $N(>\varphi)$ are shown plotted vs. $p\varphi$. As plotted, curve 1 can be used for all electron momenta above a few MeV/c. We also show in Figure A-3a and b (curve 2) a Gaussian distribution with $\sigma_{p\varphi} = .60$ MeV/c radians. This distribution will be used to approximate the true scattering-angle distribution. In particular, note that the integral

distributions for curves 1 and 2 are equal at $p\varphi = \sigma_{p\varphi} = .60$ MeV/c radians (Figure A-3b). The long large-angle scattering tail, which is not well reproduced in the Gaussian approximation, is accounted for in the trajectory-consistency checking (see Appendix A.1.b).

If $\sigma_{p\varphi}$ is the standard deviation of the distribution as plotted, then

$$\sigma_{\varphi} = \frac{\sigma_{p\varphi}}{p} \tag{A-5}$$

We thus have:

$$\sigma_{\varphi} = \frac{.60}{p} \text{ radians} \tag{A-6}$$

By substituting for p the values from equation II-2 we obtain

$$\sigma_{\varphi} = \begin{cases} .17\theta & \text{MOD-1} \quad \text{(A-7a)} \\ .068\theta & \text{MOD-2} \quad \text{(A-7b)} \end{cases}$$

where θ is the deflection angle of the particle.

The intrinsic angular resolution derives from the approximately Gaussian distribution of the measured spark locations about the true trajectory position in each module. If we let σ_A represent the standard deviation of the deflection angle due to the intrinsic angular resolution, then the standard deviation of the measured angle is given by

$$\sigma_{\theta} = \sqrt{\sigma_{\varphi}^2 + \sigma_A^2} \tag{A-8}$$

In Figure A-4 we show the angular distribution obtained for 790 MeV positrons (nominal $\theta = .0045$ radians) at the Caltech Synchrotron using the detector configuration MOD-1. The smooth curve is a least-

squares fit of the data to a Gaussian distribution; the best-fit standard deviation is σ_θ = .0023 radians, which implies σ_A = .0021 radians from equations A-7a and A-8. However, the calibration runs were made with the beam aligned with the detector system, whereas during a flight particles have incident angles of as much as 30^o. The distribution of the measured spark locations about the true trajectory position is expected to be broader at larger incident angles since the ion pairs are distributed over a large transverse distance. This argument is substantiated by the fact that the average of the mean deviations of the measured spark locations about the least-squares fit trajectories is approximately 60% larger for flight data and ground-based muon runs than for the calibration runs. Therefore, we expect that σ_A appropriate for flight data might be slightly larger than that deduced from the calibrations.

It is possible to determine σ_A directly from the flight data. More than 90% of the particles which trigger the detector system during a flight are nuclei with energy greater than 400 MeV/nucleon, the threshold of the lucite Čerenkov counter. Of these particles approximately 90% are protons and 10% He nuclei. For these particles the effect of scattering is small and, hence, their distribution reflects the intrinsic angular resolution described by σ_A.

The expected rate of protons (p/m^2 sec sr) in the deflection interval $\theta_i - \theta_{i+1}$ is

$$N_i = \int_{\theta_i}^{\theta_{i+1}} d\theta' \int_{1000}^{\infty} dR\ j(R)\ P(\theta,\theta') \qquad \text{(A-9)}$$

where

$j(R)$ = differential rigidity spectrum of protons (p/m^2 sec sr MV)

and $P(\theta,\theta')$ is the Gaussian probability distribution function defined by equation IV-1. In Figure A-5 we show the angular distribution of particles observed during the local nighttime interval of flight 71C2 with deflection angles in the range -.008 to +.015 radians. The smooth solid curve is the predicted angular distribution of cosmic-ray protons calculated from equations A-9 and IV-1 using a proton spectrum appropriate for solar maximum and σ_A = .0025 radians. The dashed curve represents a similar calculation except that the proton spectrum appropriate for solar minimum is used. It is seen that the variation in the proton spectrum over the solar cycle shifts the peak of the distribution but does not significantly alter the width. Thus the standard deviation, σ_A, which we derive in this manner does not strongly depend on the assumed proton spectrum. Curves were calculated with the solar maximum proton spectrum for several different values of σ_A. In each case the location of the peak of the calculated distribution was shifted to match the peak location of the observed data. For each distribution we then calculated chi-squared, χ^2, defined by

$$\chi^2 = \sum_i [(y_i - n_i)/\sqrt{n_i}]^2 \qquad \text{(A-10)}$$

where

n_i = observed number of particles in i^{th} channel. (Each channel is .001 radians wide.)

y_i = calculated number of protons in the i^{th} channel.

A plot of χ^2 versus σ_A is shown in Figure A-6. The minimum occurs for $\sigma_A \approx .0025$ radians which is the value we adopt for the analysis of flight data. Using equations A-7a, A-76, and A-8 we have

$$\sigma_\theta = \begin{cases} \sqrt{(.17\theta)^2 + (.0025)^2} & \text{MOD-1} \quad \text{(A-11a)} \\ \sqrt{(.068\theta)^2 + (.0025)^2} & \text{MOD-2} \quad \text{(A-11b)} \end{cases}$$

Using these equations, we calculate the deflection resolution P, FWHM, as

$$P = \frac{2.36\sigma_\theta}{\theta} = \begin{cases} \sqrt{(.40)^2 + \left(\frac{.0059}{\theta}\right)^2} & \text{MOD-1} \quad \text{(A-12a)} \\ \sqrt{(.16)^2 + \left(\frac{.0059}{\theta}\right)^2} & \text{MOD-2} \quad \text{(A-12b)} \end{cases}$$

A plot of the resolution versus rigidity is shown in Figure A-7. The filled circles represent resolution measurements made with positrons at the Caltech Synchrotron in configuration MOD-1.

3. Raw Flux Parameters

a. Live Time (t_L)

The detector is insensitive for a fraction of the time interval over which the data are summed in the raw flux computation. For example, the phase-B one-minute rate counting period occurs every 16 minutes. In addition, the total live time, t_L, during the 15 minute phase-A period is given by:

$$t_L = (900 - n_e t_e)\ (1 - n_a t_a) \text{ seconds} \qquad \text{(A-13)}$$

where

n_e = number of events recorded

t_e = time required to write a word (.35 sec)

n_a = total guard counter rate (cts/sec)

t_a = dead time following anti-coincidence (2 μsec)

provided

$$n_a t_a \ll 1$$

which applied throughout all flights. The fractional dead time during a typical phase-A period at float altitude ranged from .14 in 1969 to .22 in 1971.

b. Spark Chamber Efficiency (D_{GC})

Since every triple coincidence, $T1 \wedge T2 \wedge \overline{LC}$, is a potentially valid event, the spark chamber detection efficiency is:

$$D = \frac{n}{N} \qquad \text{(A-14)}$$

where

n is the number of analyzable events

N is the total number of triple coincidences

In the case of MOD-2 data, the detection efficiency can be defined in terms of gas Čerenkov events, i.e. $T1 \wedge T2 \wedge L\check{C} \wedge G\check{C}$,

$$D_{G\check{C}} = \frac{n_{G\check{C}}}{N_{G\check{C}}} \tag{A-15}$$

where

$n_{G\check{C}}$ is the number of analyzable $G\check{C}$ events

$N_{G\check{C}}$ is the total number of $G\check{C}$-event coincidences

Typically, D was .7 - .8 for a flight and $D_{G\check{C}}$ was approximately given by

$$D_{G\check{C}} \approx D + .05 \tag{A-16}$$

This small difference is probably due to the different species of particles which make up the $G\check{C}$ and NON-$G\check{C}$ events. (Less than 10% of the events are $G\check{C}$ events; roughly 3/4 of these are electrons above 15 MeV and the remaining 1/4 are nuclei above ~22 GeV/nucleon. The bulk of events triggering the detector are of the NON-$G\check{C}$ type and consist mostly of protons above ~400 MeV.) Further analysis is in progress to determine the exact cause of the difference between D and $D_{G\check{C}}$. However, since the difference is small compared to the statistical accuracy of the data and since D can be obtained over short time intervals with much greater statistical accuracy than $D_{G\check{C}}$, we adopt the following method for estimating the spark chamber detection efficiency: we first determine D for the ascent and float intervals and then apply a correction factor

based on the difference of D and $D_{GC\check{C}}$ over the total float period (where better statistics prevail).

c. Gas Čerenkov Efficiency Factor ($\check{C}_{eff}$)

The gas Čerenkov counter was fabricated in January, 1970. Shortly afterward, it was calibrated at the Caltech Synchrotron as described in Section II.B. The efficiency was determined to be approximately 98%. However, oxidation of the mirror surfaces that reflect the light inside the counter can degrade the efficiency. Although ground-based muon runs provide a check of the Čerenkov counter operation, changes in the efficiency of less than 10% are masked by the statistical accuracy of the data. A comparison of ground-based muon runs in 1970 and 1971 show no significant differences; however, in order to correct for possible smaller changes in the gas Čerenkov counter efficiency we use the flight data to directly calculate the efficiency factor. As an example, we show in Figure A-8 the hourly count rate of both gas-Čerenkov and non-gas-Čerenkov events in the lowest three energy ranges for flight 71C2. We make the following interpretation of the particles making up the two classes of events

1) The GČ events in the energy ranges considered consist of electrons only.
2) The NON-GČ events consist of misfit nuclei, background produced by nuclei, and also the electrons which did not trigger the GČ counter because its efficiency is less than 100%.

Under the above interpretation, a night-day difference in the NON-GČ count rate is due to its electron component. All other NON-GČ events,

which always have rigidities above cutoff, should retain a constant count rate from night to day. The electron counting rate increases by a factor of 3 or 4 from night to day due to the large flux of re-entrant albedo electrons present at these low energies during the day-time interval. In the following we use the two-component model for the NON-GČ events and compare the night-day ratios of both classes of events. From these ratios we shall determine the fraction of electrons in the NON-GČ data. Thus, both the count rate of GČ electrons and NON-GČ electrons can be determined and, hence, the gas Čerenkov counter efficiency can be computed.

We define the following symbols:

e_n = nighttime GČ rate (electrons)

e_d = daytime GČ rate (electrons)

$\bar{e}_n$ = nighttime NON-GČ rate of electrons

$\bar{e}_d$ = daytime NON-GČ rate of electrons

p = time-independent rate of all other NON-GČ events

$y = \dfrac{\bar{e}_d + p}{\bar{e}_n + p}$ = ratio of day to night NON-GČ rates

$x = \dfrac{e_d}{e_n} = \dfrac{\bar{e}_d}{\bar{e}_n}$ = ratio of day to night electron rates

Both quantities x and y are determined from the data. It follows that the ratio of the two components of the NON-GČ class of events is given by:

$$\frac{p}{\bar{e}_n} = \frac{x - y}{y - 1}$$

Since we measure the counting rate at night for NON-GČ events, $p + \bar{e}_n$,

we derive the counting rate of the electron component of the NON-GC events at night:

$$\bar{e}_n = \frac{p + \bar{e}_n}{\frac{p}{\bar{e}_n} + 1}$$

The nighttime GC rate, e_n, is measured and thus the gas-Cerenkov efficiency at all energies above GC threshold is:

$$C_{eff} = \frac{e_n}{e_n + \bar{e}_n}$$

Table A-1 shows the result of this calculation for the flights of 1970 and 1971. The error bars result from the statistical errors in the average day and night counting rates. The night-day transitions are most distinct in flights 70C2 and 71C2, and hence, we take as Cerenkov efficiency factors, C_{eff}, the values .93 and .84 for 1970 and 1971, respectively.

TABLE A-1

Gas Čerenkov Efficiency Factors ($\check{C}_{eff}$)

Energy Interval (MeV) \ Flight Number	70C1	70C2	71C1	71C2
14.3 - 29.0	.92 ± .12	.93 ± .12	.72 ± .09	.83 ± .11
29.0 - 58.5	.91 ± .06	.93 ± .03	.81 ± .05	.84 ± .05
58.5 - 122	undetermined	.99 ± .04	.96 ± .08	.84 ± .06

4. Background Corrections

a. Upward-Moving Particles

With the detector in the MOD-1 configuration, a fraction of the upward-moving particles (splash albedo and those due to γ-ray interactions in the lucite Čerenkov counter) contribute a small contamination to the low-energy data (due to the ~4% backward detection efficiency in LČ). These corrections have been described in connection with the 1968 data (Rice, 1969, 1970).

As a result of further calibrations at the Caltech Synchrotron we have made improved estimates of the γ-ray contamination. The new corrections are given in Tables V-1 and V-2 (Chapter V). The magnitudes of these corrections are not significantly different from those used by Rice (1970); however, the estimated errors have been reduced because of the more extensive machine calibrations.

These calibrations also showed that the ~4% of backward-moving electrons which trigger the detector are rejected from analysis about twice as often as forward-moving electrons. Therefore, we have correspondingly adjusted the earlier splash-albedo corrections of Rice (1970). If we assume the typical detection efficiency of 0.75 for forward-moving particles (see Appendix A.3.b), it can be shown that the earlier corrections of Rice should be multiplied by the factor 2/3. The new splash-albedo corrections are listed in Tables V-1a and b and V-2a and b.

No corrections for upward-moving particles were necessary for the MOD-2 configuration (1970 and 1971) since the gas Čerenkov counter completely discriminates against these particles.

b. Atmospheric Muons and Pions

The contamination of the MOD-1 data due to atmospheric muons and pions was shown to be negligible by Rice (1970). In the case of MOD-2 data, the muons and pions must have energy greater than about 2.5 GeV and 3.4 GeV, respectively, to be above the effective threshold of the gas Čerenkov counter. At 2.4 g/cm^2 altitude pions of energy 3.4 Gev decay within about 0.06 g/cm^2 of their point of production. Therefore, the flux of pions compared to that of muons may be ignored.

From the pion production spectrum of Perola and Scarsi (1966) and the formulas of Verma (1967), we have calculated the muon spectrum at 2.4 g/cm^2 (see Rice (1970) for details of the method). Above 2.5 GeV this spectrum is approximately:

$$j_\mu(T) = .853\ T^{-2.94}\ \mu^{\pm}/m^2\ \text{sec sr GeV} \qquad \text{(A-17)}$$

where T is muon kinetic energy in GeV. Most of these high-energy particles have smaller bending angles than the .006 radians threshold value used in the data analysis. Folding the spectrum given by equation A-17 with the resolution function (equation IV-1) we find only 2% of these particles fall within the deflection interval $.006 \leq |\theta| \leq .009$. The percentage contribution to any of the other intervals is much smaller. We derive a count rate in the .006 - .009 radians interval of 5.7×10^{-7} $\mu^{\pm}$/sec which is less than 0.2% of the measured count rate of positrons or negatrons in this interval and therefore negligible.

c. Secondaries Produced in the Gas Čerenkov Counter

The 2 g/cm^2 of material above the upper spark chamber is

potentially a source of contamination arising from interactions by cosmic-ray nuclei and γ-rays. We treat first the problem of nuclear interactions.

We consider two possible ways in which products of nuclear interactions in the GČ counter could simulate electron events ($T1 \wedge T2 \wedge \check{LC} \wedge \check{GC}$):

1) Two or more particles (pions or protons) above LČ threshold could be produced with one traveling through the detector system triggering LČ, while another passes through one of the 1/2-inch quartz windows (which protect the GČ phototubes) triggering the GČ counter.
2) A high-energy particle above GČ threshold could be produced in the material above the flat mirrors of the GČ counter and travel through the detector system triggering both Čerenkov counters (LČ and GČ).

The first possibility requires that one of the particles be emitted at a relatively large angle (order of 90^{o}). Using information in the tables of Bertini (1967) on the angular and energy distribution of secondary protons and pions from interaction $p+O^{16}$ (fluorine and sulfur tables were not available), we estimate that the upper limit on the rate of such events is $\sim 5 \times 10^{-6}$ particles/sec in any one energy range. This rate is less than 1% of the measured count rate and therefore negligible. In the second case we are only concerned with particles above the effective gas Čerenkov threshold (Section II.B). We illustrate

the magnitude of the correction by considering the production of pions. The mean lifetime of 3.4 GeV charged pions is 6.1×10^{-7} seconds. Thus a pion of this energy will travel roughly 180 meters before decaying. Since the entire spectrometer is just over a meter long, we ignore pion decay in the calculation. In order to trigger the gas Čerenkov counter, the particle must be produced in the 1 g/cm^2 of material above the mirrors. Considering the rather complex geometry of the detector, we shall calculate an upper limit to the contamination. We first replace the GČ counter by a 1 g/cm^2 slab of air. Then we use the pion production spectrum of Perola and Scarsi (1966) to calculate the flux of pions that emerge from the bottom of such a layer which is exposed to the cosmic-ray nuclei flux. Above 3.4 GeV, the differential flux of pions at 1 g/cm^2 can be represented by the power law:

$$j_\pi(T) = 16.5T^{-2.35} \quad \pi^\pm/m^2 \text{sec sr GeV} \qquad \text{(A-18)}$$

When we fold this spectrum with the resolution of the detector we derive a count rate of 1.85×10^{-5} $\pi^\pm$/sec in the highest energy interval. Considering both charge signs, this represents only 2% of the measured count rate for positrons in this energy interval in 1971 and less than .5% of the negatrons. In addition, the high-energy nuclear interactions which produce the pions have a high multiplicity and even the very small contamination derived above is drastically reduced because of the anti-coincidence counters and the multiple-spark-indicator feature. Therefore we consider the contamination from nuclear interactions negligible.

Cosmic-ray nuclei also produce knock-on electrons as they pass

through the gas Čerenkov counter. When expressed in terms of g/cm^2 the probability functions describing knock-on production are proportional to Z/A where Z and A are the charge and mass numbers of the material traversed. Thus the production spectrum of knock-ons will be essentially material-independent. We use the production spectrum derived by Beuermann (1971) for air appropriate to the cosmic-ray nuclei flux level of 1968. Since knock-on electrons of 15 MeV are produced by protons with energy greater than ~3 GeV, where solar modulation effects are not large, the use of the 1968 proton spectrum for the period 1968-1971 introduces negligible error. Beuermann's production rate for the interval $10 \leq T \leq 100$ MeV is given approximately by:

$$Q(T) = .035\ T^{-2.7}\ e^-/g\ sec\ sr\ MeV \qquad (A\text{-}19)$$

This rate corresponds to a flux of $\sim.10\ e^-/m^2$ sec sr MeV in the lowest energy interval (14.3 - 29 MeV). This flux represents some 25% of the measured flux in this energy interval at 2.4 g/cm^2 in 1971. However, using the formulas of Rossi (1952), we calculate that a 15 MeV knock-on electron emerges at no more than $3\ 1/2^o$ from the forward direction. Hence, we would expect a very large fraction of these events (proton + knock-on electron) to be multiple-particle events which are rejected from analysis. In addition, the 1 g/cm^2 of material is an upper limit since particles produced near the mirrors will not have sufficient pathlength to trigger the gas Čerenkov counter. Taking these effects into account, we consider the contamination due to knock-on electrons to be negligible.

A possible source of contamination could arise in the high-

energy intervals if a proton above lucite Čerenkov counter threshold produces a T1∧T2∧LČ coincidence and also produces a knock-on electron, which triggers GČ but which fails to be registered in the spark chambers. This could happen, for example, if the electron experienced a large single scattering or if the multiple-spark-detection efficiency were less than 100%. We estimate from the knock-on production spectrum that less than 0.1% of the nuclei above the lucite Čerenkov counter threshold will produce a knock-on electron of sufficient energy to trigger the gas Čerenkov counter. However, approximately 4% of the cosmic-ray protons above the LČ threshold are also above the GČ threshold. Thus the above contamination is only ~1/40 of that due directly to the high-energy nuclei (see Appendix A.4.d) and therefore negligible.

Electrons can also be produced in the gas Čerenkov counter by Compton scattering and pair-production from γ-rays. In order to calculate the fluxes of positrons and negatrons resulting from these effects we assume the following:

1) The 1 g/cm^2 of material above the mirrors has an average charge number, Z, of 10 and an average mass number, A, of 20.
2) The probability functions of Rossi (1952) are used. In the case of pair production we use the complete-screening approximation which gives a larger flux of electrons for our conditions than does the no-screening approximation.
3) We use the atmospheric γ-ray spectrum at 2.4 g/cm^2 residual atmosphere from the calculations of Beuermann (1971) with the electron and cosmic-ray nuclei spectra

appropriate for 1971.

In Figures A-9 and A-10 we show the assumed γ-ray spectrum and the resultant positron and negatron spectra, respectively. For negatrons the sum of the Compton scattering and pair-production processes is shown. In the 14.3 - 29 MeV interval we derive positron and negatron fluxes of .010 p/m^2 sec sr MeV and .012 p/m^2 sec sr MeV, respectively. These values represent only ~4% of the measured fluxes at float altitude in 1971 and therefore represent a negligible contribution.

d. High-Energy Cosmic-Ray Nuclei

Cosmic-ray nuclei above approximately 22 GeV/nucleon also trigger the gas Čerenkov counter. Most of these particles are confined to bending angles smaller than those used in the calculation of electron fluxes (i.e. $\lesssim$ .006 radians). Because of the resolution of the detector, however, a small fraction of these particles are observed with larger bending angles. As an example, we show in Figure A-11 the angular distribution of GČ events for the total float period for 1971. The dotted curve represents the calculated distribution of the sum of primary and secondary electrons. The remaining events are high-energy nuclei. The smooth curve is a Gaussian distribution with σ = .0025 radians and this curve was used to calculate the contamination in the highest energy interval. The results for 1970 and 1971 are given in Tables V-3b, V-4b, V-5b, and V-6b. The proton contamination in the 983 - 1475 MeV interval is ~25% for positrons and ~6% for negatrons. The contribution is negligible at lower energies. The error in the values is estimated at ~50% on the basis of uncertainties in the

instrument resolution and spark chamber alignment.

e. Accidental Gas Čerenkov Coincidences

About 90% of the particles which trigger the detector are cosmic-ray protons above ~1000 MV, the threshold of the lucite Čerenkov counter. Accidental GČ coincidences tag some of these particles as electrons. Since 1000 MV corresponds to a nominal $\theta \approx .009$ radians, these events primarily contaminate the high-energy positron data. We have used the measured rate of cosmic-ray nuclei, the accidental GČ-coincidence rate (Section II.b), and the resolution of the detector to calculate the expected rate of these events in the highest energy intervals. The results are given in Tables V-3b and V-5b. The maximum contribution to the data is 16% in the 983 - 1475 MeV positron interval in 1971. The 50% estimated error is based on uncertainties in detector resolution and spark-chamber alignment.

f. Spark Chamber Alignment

Because the fiducial wires cannot be precisely lined up for all 8 planes it is possible to have a built-in offset in the deflection angle. An initial alignment is made by using the deflection-angle distribution of the cosmic-ray nuclei above lucite Čerenkov counter threshold. This procedure is similar to the one described in Appendix A.2 in determining the instrument resolution. However, in the resolution calculation we were interested in determining the <u>width</u> of the deflection-angle distribution of the nuclei. In the alignment procedure we are interested in comparing the locations of the <u>peaks</u> of the measured and calculated deflection-angle distributions. These

distributions are shown in Figure A-5 for flight 71C2. Alignment factors have already been introduced in the data in computing the observed histogram. The two curves were calculated using solar minimum and solar maximum proton spectra, respectively. Since the peak in these curves differ by only .0015 radians over a solar cycle, we feel that our deflection zero is accurate to approximately .0005 radians.

In the case of MOD-2 high-energy data the alignment was refined by using the $G\bar{C}$ proton distribution (see Figure A-11). The average bending angle of these particles ($T \geq 22$ GeV/nucleon) is calculated to be ~0.00018 radians. It was necessary to adjust the data by about .0005 radians in 1970 and 1971.

In Table A-2 we summarize the corrections to the data discussed in this section (A.4). Only the last two entries (high-energy protons and accidental $G\bar{C}$ coincidences) are considered non-negligible. These two corrections and those due to atmospheric secondaries are included in the data tables of Chapter V.

TABLE A-2

Summary of Corrections Discussed in Section A.4*

Description of Correction (MOD-2)	Section Discussed	Energy Intervals Affected	Probable Contribution (%)
Upward-moving particles	A.4.a	low energies	0
Atmospheric muons and pions	A.4.b	983-1475 MeV	0.2
Products of nuclear interactions in $\bar{GC}$	A.4.c	medium and high energies	<2
Knock-ons in $\bar{GC}$	A.4.c	low-energy e^-	~ 0
Knock-ons in $\bar{GC}$ scattered out of acceptance cone	A.4.c	high energies	0
Compton-scattered electrons and pair-produced electrons in $\bar{GC}$	A.4.c	14.3-29 MeV	<4
Cosmic-ray protons above $\bar{GC}$ threshold	A.4.d	983-1475 MeV	25 e^+ 6 e^-
Accidental $\bar{GC}$ coincidences	A.4.e	983-1475 MeV	16 (e^+-1971)

*Unless otherwise noted a correction applies to both charge signs. The correction for spark chamber alignment was made before computing the raw fluxes (Chapter V) and hence no correction for this effect is listed.

5. Correction of Fluxes to The Top of The Atmosphere

In the final stage of data analysis we correct the locally observed fluxes to their values at the top of the atmosphere. This correction is complicated by the energy loss (bremmstrahlung and ionization) experienced by the particles in the material above the spectrometer and by the decreasing resolution of the detector at high energies (or, equivalently, small bending angles). In computing the "raw" fluxes at float altitude (data tables of Chapter V), we have not taken into account the resolution, i.e. we have assumed that the resolution is perfect and have calculated the flux by dividing the measured rate in a given energy interval by the width of that interval (and by the geometrical factor). However, in the highest two energy intervals of the MOD-2 observations the ratio $\frac{\sigma_\theta}{\Delta\theta_i}$ is relatively large (σ_θ is the standard deviation of the deflection-angle distribution given by equation A-11b and $\Delta\theta_i$ is the width of the i^{th} deflection-angle bin given in Table IV-1), and there is considerable probability, particularly above 1 GeV, that a particle is assigned to the wrong energy interval. Thus, at high energies, dividing by the numerical width of the energy interval is not necessarily a correct way of relating the observed rate to the true particle flux. We describe a procedure which accounts for the effect of resolution as well as energy loss in correcting the measured fluxes to the top of the atmosphere. The method is based on a similar calculation by Fanselow (1968).

We begin with a trial primary electron spectrum incident at the top of the atmosphere. (Such a spectrum is also used in the

secondary subtraction procedure described in Chapter IV.) We then write in matrix form the equation relating the expected rates at float depth to the assumed incident spectrum. We invert the resulting matrix and thus derive the spectrum at the top of the atmosphere from the observed rates at float altitude. Our procedure also allows us to calculate the uncertainty in the fluxes at the top of the atmosphere. Because of the effect of resolution, these uncertainties in the data of the two highest energy intervals are larger than those of the raw fluxes at float altitude.

The assumed incident primary spectrum $j_I(T)$ is modified by energy-loss effects as the particles pass through the atmosphere and the ~ 2 g/cm^2 of material between the top of the gas Čerenkov counter and the upper spark chamber. We denote the residual primary spectrum at the top of the upper spark chamber by $j_S(T)$. We calculate $j_S(T)$ from $j_I(T)$ by folding in the bremmstrahlung energy-loss probability distribution and by including the average ionization energy loss.

We first calculate the effect of bremmstrahlung energy loss. The probability $P(T,T')dT'$ that a particle with kinetic energy T will have energy between T' and T' + dT' after passing through x radiation lengths of material is given by Rossi (1952):

$$P(T,T')\ dT' = dT'\ \frac{\left[\ell n\ (T/T')\right]^{\gamma-1}}{T\ \Gamma(\gamma)} \qquad \text{(A-20)}$$

where $\gamma = x/\ell n\ 2$ and $\Gamma(\gamma)$ is the gamma function (Abramowitz and Stegun, 1964). The spectrum after correcting for bremmstrahlung loss is

$$j(T') = \int_{T'}^{\infty} j_I(T)\ P(T,T')\ dT \qquad \text{(A-21)}$$

We then obtain $j_S(T)$, the residual spectrum at the top of the upper spark chamber, from $j(T')$ by correcting for ionization loss using the tables of Berger and Seltzer (1964).

The expected rates at float altitude are obtained through the response of the magnet spectrometer to $j_S(T)$. We have

$$M_i = \int_0^\infty R_i(T)\, G(T)\, j_S(T)\, dT$$
$$\approx \sum_{j=1}^{\ell} \int_{T_j^S}^{T_{j+1}^S} R_i(T)\, G(T)\, j_S(T)\, dT \qquad \text{(A-22)}$$

where

M_i = expected rate in the i^{th} energy interval (p/sec)

$R_i(T)dT$ = probability that particle with kinetic energy T will be observed in the i^{th} energy interval

$G(T)$ = geometrical factor as a function of T

T_j^S, T_{j+1}^S = lower- and upper-limit energies defining the j^{th} energy interval.

ℓ = number of energy intervals. (Electrons with energy greater than the largest measured interval are placed in a bin from 1.475 - 40 GeV.)

The superscript S on T_j^S and T_{j+1}^S denotes the fact that the quantities are measured at the upper spark chamber.

The response function $R_i(T)$ in equation A-22 is related to the resolution function described earlier in Appendix A.2. $P(\theta,\theta')d\theta'$, the probability that a particle with rigidity corresponding to a bending

angle θ will be observed with bending angle between θ' and $\theta' + d\theta'$, is given by

$$P(\theta,\theta')d\theta' = \frac{d\theta'}{\sigma_\theta \sqrt{2\pi}} \exp\left[\frac{-(\theta-\theta')^2}{2\sigma_\theta^2}\right] \qquad \text{(A-23)}$$

where θ and σ_θ are given by equations II-2 and A-11, respectively. Then the response function is

$$R_i(T) = \int_{\theta_i}^{\theta_{i+1}} P(\theta,\theta')d\theta' \qquad \text{(A-24)}$$

(Note θ is a function of T by equation II-2)

In Figure A-12 we show plots of R_i versus T for each energy interval for the MOD-2 configuration. A curve corresponding to perfect resolution would be a rectangular box with amplitude 1 and with vertical sides at the two energies corresponding to the energy-interval end points, which are indicated by dotted vertical lines in the figure. For low energies the resolution is good while for the highest energy interval used in the analysis the relatively large ratio of $\sigma_\theta/\Delta\theta_7$ causes $R_7(T)$ to significantly overlap the adjacent energy intervals.

The M_i of equation A-22 represent the expected rates at <u>float altitude</u> for the assumed incident primary spectrum, taking into account the energy loss of the electrons and the resolution of the detector. It proves useful to write an equation for the corresponding rates at the <u>top of the atmosphere</u>, N_i, assuming that the detector has <u>perfect</u> resolution and that <u>no</u> energy losses occur in the GC counter:

$$N_i = \int_{T_i^I}^{T_{i+1}^I} G(T)\, j_I(T)\, dT \qquad \text{(A-25)}$$

The superscript I denotes the fact that the quantities are measured at the top of the atmosphere. It is usual in the literature to shift the energy intervals by the ionization energy loss which occurs for each particle. The bremmstrahlung loss distribution is such that most particles lose very little energy and hence an average shift for this effect is not applied. Thus, the energy at the top of the atmosphere, T_i^I, is related to the energy at the upper spark chamber, T_i^S, by

$$T_i^I = T_i^S + \delta T_i \tag{A-26}$$

where δT_i is the ionization energy lost by an electron with energy T_i in passing through the material between the top of the atmosphere and the upper spark chamber.

We can write a relation between the N_i (which we are seeking) and the M_i in the following way:

$$M_i = \sum_{j=1}^{\ell} \left[\int_{T_j^S}^{T_{j+1}^S} R_i(T)\, G(T)\, j_S(T) \Big/ \int_{T_j^I}^{T_{j+1}^I} G(T)\, j_I(T)dT \right] N_j \tag{A-27}$$

Note that we have simply multiplied and divided each term of equation A-22 by the rate at the top of the atmosphere, N_j. Equation A-27 can be expressed as a matrix equation:

$$M_i = \sum_{j=1}^{\ell} F_{ij}\, N_j \tag{A-28}$$

where

$$F_{ij} = \int_{T_j^S}^{T_{j+1}^S} R_i(T)\, G(T)\, j_S(T)dT \Big/ \int_{T_j^I}^{T_{j+1}^I} G(T)\, j_I(T)dT \tag{A-29}$$

If H_{ij} is an element of the inverse of the F matrix, the rates at the top of the atmosphere are given by:

$$N_i = \sum_{j=1}^{\ell} H_{ij} M_j \qquad \text{(A-30)}$$

Furthermore:

$$\sigma_{N_i}^2 = \sum_{j=1}^{\ell} \left[\frac{\partial N_i}{\partial M_j}\right]^2 \sigma_{M_j}^2 = \sum_{j=1}^{\ell} H_{ij}^2 \sigma_{M_j}^2 \qquad \text{(A-31)}$$

where σ_{M_j} is the standard deviation for the observations and σ_{N_i} is the resulting standard deviation for the N_i.

Equations A-30 and A-31 represent the desired results. Equation A-30 gives the corrected rates (N_i) at the top of the atmosphere in terms of the rates at the detector at float altitude (M_i). If we replace the M_j in equation A-30 by the actual measured rates, $\mathfrak{M}_j$, then we derive a set of N_i from which a better approximation for the trial input spectrum can be made. From this new trial spectrum the F_{ij} and H_{ij} are recalculated and a new set of N_i derived. The process can be repeated until the N_i converge. (Note that since the rates, N_i, correspond to a detector with perfect resolution, it is appropriate to divide by the width of the energy interval in converting the rates to differential fluxes.) However, in some cases the measured rates are only upper limits and in these cases the matrix-inversion procedure for determining the corrected rates cannot be applied. Therefore, we modify the procedure for determining the corrected fluxes in the following way. For a given trial input spectrum we determine the ratios

$\frac{N_i}{M_i}$, where N_i and M_i are the calculated rates in the i^{th} energy interval at the top of the atmosphere and at float altitude, respectively. If $\mathcal{M}_i$ are the measured rates at float altitude, then we determine the $\mathcal{N}_i$, the estimated corrected rates at the top of the atmosphere, by $\mathcal{N}_i = \frac{N_i}{M_i} \times \mathcal{M}_i$. These $\mathcal{N}_i$ are used to define a new trial input spectrum and the procedure is repeated until the $\mathcal{N}_i$ are consistent with the input spectrum.

We do not modify the procedure (equation A-31) for calculating the expected uncertainties in the fluxes at the top of the atmosphere. This procedure takes full advantage of the matrix-inversion technique and yields larger errors in the corrected high-energy data than those listed for the raw fluxes (data tables of Chapter V), which are based on statistical errors only. In deriving the errors we need a knowledge of the error in the data for each of the energy intervals, including the 1.475 - 40 GeV interval. The number of electrons in this interval is not measured directly since a significant fraction of the gas Čerenkov events with $|\theta| \leq .006$ radians are high-energy protons ($\geq$22 GeV). It is possible to roughly deduce the number from the observed deflection-angle distribution of these events and from a knowledge of the resolution of the detector (see Figure A-11). We estimate the error in the data from this interval to be $\leq$25%. In making the corrections we have assumed a 25% error in this interval ($\geq$1.475 GeV) which increases the relative error in the highest measured energy interval (0.983-1.475 GeV) by ~25% over the result obtained if zero error is assumed for the integral flux above 1.475 GeV. The error in the data at lower energies

is not affected by the estimate.

We found that the above matrix-inversion procedure was not necessary for the MOD-1 observations, which extend to only 200 MeV, i.e. the matrix was essentially diagonal because of the excellent resolution at low energies. The fluxes corrected to the top of the atmosphere for both MOD-1 (1968, 1969) and MOD-2 (1970, 1971) observations are given in the tables and figures of Chapter V.

APPENDIX B

Interstellar Electron Spectrum from Non-Thermal-Radio-Background Data

The synchrotron emission (ergs/sec·cm^3·sr·Hz) by electrons spiraling in a uniform magnetic field is given by Ginzburg and Syrovatskii (1964) as:

$$\epsilon(\nu) = \frac{\sqrt{3}}{4\pi}\frac{e^3 B_\perp}{mc^2}\int_{mc^2}^{\infty}\left[1 + (1-\tilde{\eta}^2)\cdot\left(\frac{W}{mc^2}\right)^2\right]^{-1/2} \left\{\frac{\nu}{\nu_c'}\int_{\nu/\nu_c'}^{\infty} K_{5/3}(\eta)\, d\eta\right\} N(W)dW \qquad \text{(B-1)}$$

where ν is the frequency of emission

e is the charge of the electron

$B_\perp$ is the mean value of the magnetic field perpendicular to the line of sight

m is the mass of the electron

c is the speed of light

W is the total energy of the electron

N(W) is the number density of relativistic electrons

$K_{5/3}(\eta)$ is a modified Bessel function of the second kind

$\tilde{\eta} = \sqrt{1 - \frac{ne^2}{\pi m \nu^2}}$ is the refractive index of an ionized gas with n electrons per cm^3 and

$$\nu_c' = \nu_c\left[1 + (1-\tilde{\eta}^2)\left(\frac{W}{mc^2}\right)^2\right]^{-3/2} \qquad \text{(B-2)}$$

where ν_c is the critical frequency given by

$$\nu_c = \frac{3eB_\perp}{4\pi mc}\left(\frac{W}{mc^2}\right)^2 \qquad \text{(B-3)}$$

The terms involving $1-\tilde{\eta}$ in equations B-2 and B-3, which result from the ambient electron density in the interstellar medium, cause a suppression of the emission at low frequencies (Razin, 1960; Lerche, 1971).

For the case of a vacuum ($\tilde{\eta} = 1$) equation B-1 has been solved exactly for an electron spectrum which is a power law in energy over a sufficiently large range (Ginzburg and Syrovatskii, 1964). The result is

$$\epsilon(\nu) = \frac{\sqrt{3}}{1+\gamma}\,\Gamma\left(\frac{3\gamma-1}{12}\right)\Gamma\left(\frac{3\gamma+19}{12}\right)\frac{e^3}{4\pi mc^2}\left(\frac{3e}{2\pi m^3c^5}\right)^{\frac{\gamma-1}{2}} C\, B_\perp^{\frac{1+\gamma}{2}}\, \nu^{\frac{1-\gamma}{2}} \qquad \text{(B-4)}$$

where C and γ are parameters defining the electron spectrum:

$$N(W) = C\, W^{-\gamma}$$

and $\Gamma(x)$ is the gamma function (Abramowitz and Stegun, 1964).

To obtain the total intensity of radiation over a given line-of-sight distance we must include the free-free absorption by the medium. The absorption coefficient for the radio frequencies of interest to us is given by:

$$k(\nu) = 10^{-2}\,\frac{n^2}{T^{3/2}\,\nu^2}\left[17.7 + \ell n\,\frac{T^{3/2}}{\nu}\right] \qquad \text{(B-5)}$$

(Ginzburg, 1964) where T is the electron temperature. The total intensity is then given by solving the differential equation:

$$\frac{dI}{ds} = \epsilon(\nu) - k(\nu)I \qquad \text{(B-6)}$$

where ds is an element of length along the line of sight. The solution of equation B-6 depends on the structure of the interstellar medium.

Several recent reviews have dealt with the physical properties of the interstellar medium (Field, 1970, 1971; Heiles, 1971; Dalgarno and McCray, 1972; Wentzel, 1972). The observations indicate a medium composed of dense, cold clouds with diameters of a few parsecs separated by a hot, rarefied intercloud region with a scale of hundreds of parsecs. This structure has also been predicted by theoretical studies (Field et al., 1969; Hjellming et al., 1969; Shu et al., 1972). We shall take as a model of the interstellar medium a uniform distribution of cold clouds with diameter ℓ_c and separation distance ℓ_i. (This model with ℓ_c = 1 pc and ℓ_i = 1 kpc is identical to that used by Goldstein, Ramaty and Fisk (1970)). The subscript convention is "c" for "cold" clouds and "i" for "intercloud". The first cold cloud is assumed to lie at a distance ℓ_i. In Figure B-1 we show a schematic diagram of the assumed galactic structure. Our position in the galaxy is labeled s. We assume there are m clouds (and thus m intercloud separations).

In the hot intercloud region we have both emission and absorption. If there were only one such intercloud region, the solution to equation B-6 would be

$$I_s = \frac{\epsilon}{k_i} (1 - e^{-\tau_i})$$

where the optical depth τ_i is defined by

$$\tau_i = \int_0^{\ell_i} k_i \, ds \qquad \text{(B-7)}$$

(The optical depth of a cold cloud is similarly defined by changing the

subscripts to c.)

Since, typically, $\ell_c \ll \ell_i$ we may assume the emission in cold clouds is negligible. Solving equation B-6 for $\epsilon = 0$ implies that the radiation penetrating through a cold cloud is partially absorbed with an absorption factor $e^{-\tau_c}$. Thus the solution of equation B-6 for the assumed galactic structure (see Figure B-1) can be written as the following series of equations

GALACTIC POSITION	INTENSITY
s	$I_s = \frac{\epsilon}{k_i}(1-e^{-\tau_i}) + I_1 e^{-\tau_i}$
1	$I_1 = I_2 e^{-\tau_c}$
2	$I_2 = \frac{\epsilon}{k_i}(1 - e^{-\tau_i}) + I_3 e^{-\tau_c}$
3	$I_3 = I_4 e^{-\tau_c}$
4	$I_4 = \frac{\epsilon}{k_i}(1 - e^{-\tau_i}) + I_5 e^{-\tau_c}$
	$\vdots$
2n-1	$I_{2n-1} = I_{2n} e^{-\tau_c}$
2n	$I_{2n} = \frac{\epsilon}{k_i}(1 - e^{-\tau_i}) + I_{2n+1} e^{-\tau_c}$
	$\vdots$
2m-1	$I_{2m-1} = 0$
2m	$I_{2m} = 0$

(B-8)

where we have assumed that there are an integral number of intercloud separations with $\frac{L}{\ell_i} = m$ = integer where L is the total emission distance.

By substitution we obtain:

$$I_s = \frac{\varepsilon}{k_i}(1-e^{-\tau_i}) + e^{-\tau_i}e^{-\tau_c}\left[\frac{\varepsilon}{k_i}(1-e^{-\tau_i}) + e^{-\tau_i}e^{-\tau_c}\left[\frac{\varepsilon}{k_i}(1-e^{-\tau_i})\right.\right.$$
$$\left.\left. + e^{-\tau_i}e^{-\tau_c}\left[\frac{\varepsilon}{k_i}(1-e^{-\tau_i}) + e^{-\tau_i}e^{-\tau_c}\ [\ \ldots\ ]\right.\right.\right.$$

The factor $\frac{\varepsilon}{k_i}(1-e^{-\tau_i})$ is common to all terms. We thus have

$$I_s = \frac{\varepsilon}{k_i}(1-e^{-\tau_i})\left\{1+e^{-(\tau_i+\tau_c)}+e^{-2(\tau_i+\tau_c)}+\ldots+e^{-(m-1)(\tau_i+\tau_c)}\right\}$$

The term in braces is just $\frac{1-e^{-m(\tau_i+\tau_c)}}{1-e^{-(\tau_i+\tau_c)}}$.

Hence, the solution to equation B-6 for our model is:

$$I(\nu) = \frac{\varepsilon}{k_i}\,\frac{(1-e^{-\tau_i})\left[1-e^{-\frac{L}{\ell_i}(\tau_i+\tau_c)}\right]}{\left[1-e^{-(\tau_i+\tau_c)}\right]} \qquad \text{(B-9)}$$

At high frequencies k becomes small (equation B-5) and thus τ is small (equation B-7). Equation B-9 becomes

$$I(\nu) \approx \frac{\varepsilon}{k_i}\,\tau_i\,\frac{L}{\ell_i} = \varepsilon L \qquad \text{(B-10)}$$

Using equation B-4 for $\varepsilon(\nu)$ we obtain

$$I(\nu) \propto C\ L\ B_{\perp}^{\frac{1+\gamma}{2}}\ \nu^{-\alpha} \qquad \text{(high frequencies)}$$

where we define $\alpha = \frac{\gamma-1}{2}$ as the power-law index of the radio emission spectrum.

At low frequencies, τ is large and equation B-9 becomes

$$I(\nu) \approx \frac{\varepsilon}{k_i}$$

and using equations B-4 and B-5 we have

$$I(\nu) \propto C\, B_{\perp}^{\frac{1+\gamma}{2}}\, \nu^{2-\alpha}\, T_i^{3/2}\, n_i^{-2}\, \frac{1}{\left[17.7+\ell n \frac{T_i}{\nu}\right]^{3/2}} \quad \text{(low frequencies)} \qquad \text{(B-11)}$$

Thus at low frequencies interstellar absorption changes the spectral shape to roughly $\nu^{2-\alpha}$. (Note that the logarithmic term varies quite slowly with energy). We note that the intensity at low frequencies is independent of the total line-of-sight distance, L.

At intermediate frequencies and for the general case including the Razin effect and an arbitrary electron spectrum, we must solve equations B-1, B-5, and B-9 numerically. (The term in braces $\{\ \}$ in equation B-1 is available in tabular form (Ginzburg and Syrovatskii, 1964)). If one knew the value of all the parameters involved in the equations - principally $B_{\perp}$, L, ℓ_i, ℓ_c, T_i, T_c, n_i, and n_c - one could vary the energy dependence and magnitude of the electron spectrum until the computed radiation intensity matched the observations (Figure VI-8). However, there is considerable uncertainty in some of the parameters - particularly the intercloud ambient electron temperature T_i - and this uncertainty should be reflected in an uncertainty in the interstellar cosmic-ray electron spectrum. To illustrate the approximate range of interstellar electron spectra possible we:

1) choose a nominal set of galactic parameters and calculate the galactic electron spectrum necessary to account for the radio emission in the galactic anticenter direction,
2) vary each parameter through its range and for each variation calculate, using the nominal electron spectrum, the resulting radio-emission spectrum, and

3) compare these spectra with the observed radio-background emission. Since the emitted power is directly proportional to the number of electrons, we can derive a multiplicative factor versus frequency that can be applied to the electron spectrum once the conversion factor between electron energy and emission frequency is established. Using these multiplicative factors we can estimate the electron spectrum that is required to produce a radio-emission spectrum in agreement with the observations for a given set of parameters.

We now discuss the possible range of the parameters involved in the calculation.

1) $B_{\perp}$ - Theoretical arguments concerning the dynamics of the galaxy place the average magnetic field between 3 and 5 μ-gauss. (Parker, 1969b). Recent studies of dispersion and rotation measures observed for 18 pulsars indicate an average interstellar field of ~3.5 μ-gauss with an estimated error of .5 μ-gauss. (Manchester, 1972). The value of 3.5 μ-gauss corresponds to the largest fields found and it is thought that the lines of sight to the two pulsars involved lie along the direction of the magnetic field. Moffet (1971) from a survey of the polarization properties of pulsars also derives magnetic fields of a few microgauss. In this study we use a nominal value of 5 μ-gauss and illustrate the variation in the calculated radio spectra for the range 3-5 μ-gauss.

2) L - The emission length for a uniform galaxy would just be the distance to the edge of the galaxy. The size and structure of the galaxy and our location in it have been deduced from optical and

radio astronomy observations (Blaauw and Schmidt, 1965; Allen, 1963). The solar system is approximately 8-10 kpc from the galactic center and the diameter of the galaxy is ~25-30 kpc. The distance to the edge of the galaxy in the anticenter direction is estimated to be ~4-5 kpc. However, the galaxy is quite inhomogenous, being composed of spiral arms. Thus the use of an average emission length of 4 or 5 kpc might be misleading. We have chosen to use 4 kpc as our nominal value but include the range L = 2-6 kpc in our calculations.

3) ℓ_i and ℓ_c - The average fraction of the line of sight intercepted by cold clouds depends on the viewing direction. A model of the interstellar medium which uses the data (dispersion measures and 21-cm absorption) from two pulsars, NP 0532 and CP 0328, which lie roughly in the anticenter direction, yield a range of ℓ_c/ℓ_i (the "filling factor") of 0.006-0.081 (Hjellming et al., 1969). Other models yield similar results - for example, Field et al. (1969) obtain a range 0.02-0.04 and Dalgarno and McCray (1972) in their recent review paper use values of 0.007-0.041 for the filling factor. We shall take the larger range 0.006-0.08 in the calculations with a nominal value of 0.02. The recent observations of 21-cm hydrogen absorption by Greisen (1973) indicate that clouds having dimensions of $\ell_c \approx 1$ pc are common. In our model we shall consider variations in ℓ_c of from 1-10 pc. The possible values of ℓ_i we shall use are 13-1670 pc corresponding to the assumed filling factor range of 0.006-0.08.

4) T_i and T_c - The observations of 21-cm absorption yield an estimate of the spin temperature* of neutral hydrogen. The high resolution studies of Hughes et al. (1971) and Radhakrishnan et al. (1972) indicate that the spin temperatures in clouds range from ~15° - 250°K. This range is somewhat larger than those considered in the theoretical models. We shall take T_c = 250°K as the nominal value and consider the effect of varying T_c through this total range. There is little accurate observational evidence for the spin temperature of the intercloud medium but the lower limit is roughly 500°K (from observations of emission features in which no detectable absorption is observed - Hughes et al., 1971; Radhakrishnan et al., 1972). However, the spin temperature may be much lower than the gas kinetic temperature in the low density intercloud region (Dalgarno and McCray, 1972). Upper limits to the kinetic temperature may be estimated from velocity dispersion measurements. Heiles (1967) has found an emission feature with a velocity dispersion corresponding to $T_i < 4000°K$, although Field (1971) finds none with upper limits less than 8000°K. Mention should be made of the theoretical models of the two-component system which generally fix the temperature with a rather high value. For example, Habing and Goldsmith (1971) use $T_i \approx 5000\text{-}8000°K$ and Shu et al. (1972) obtain $T_i \approx 7500°K$. The theoretical models, however, are not, as yet,

*The spin temperature relates the number of hydrogen atoms in each of the two hyperfine ground state levels. In dense clouds, where collisional excitation is important, the spin and kinetic temperatures are expected to be equal. (Field, 1958)

experimentally well verified (Greisen, 1973). We shall take the range $T_i \approx 500\text{-}10000^{\circ}K$ and use the upper limit for our nominal value.

5) n_c and n_i - The frequency dispersion of pulse arrival time from pulsars provides a measure of the density of free electrons along the line of sight. For example, for the Crab Nebula pulsar NP 0532 $\int n_e \, d\ell = 57 \text{ cm}^{-3}\text{pc}$ (listed by Maran, 1969). The distance to the pulsar is 2020 pc (Trimble, 1968) and hence we derive $n_e \approx 0.03 \text{ cm}^{-3}$. Most theoretical models predict little contrast in the cloud and intercloud electron densities. Field et al. (1969) use $n_i = 0.02$ in their model and Hjellming et al. (1969) use $n_i \approx 0.03$ and $n_c \approx 0.04\text{-}0.05$. Bridle and Venugopal (1969) find that $n_i = 0.02$ is consistent with a variety of data. Dalgarno and McCray (1972) in their review use values of $n_i \approx 0.03\text{-}0.05$ and $n_c \approx 0.06$ (for cosmic ray heating). We shall use the nominal values $n_i = 0.03$ with a range 0.02-0.05 and $n_c = 0.02$ with a range 0.02-0.06.

In summary, we present in Table B-1 the nominal values of the parameters together with their possible range considered here.

Using the nominal values of the parameters we obtain an interstellar electron spectrum which yields from equation B-1, B-5, and B-9 a radio spectrum in agreement with the observations. This spectrum can be represented in $p/(m^2 \text{ sec sr MeV})$ by

$$j(W) = \begin{cases} 1.34 \times 10^4 \, W^{-1.8} & W < 2000 \text{ MeV} \\ 2.75 \times 10^6 \, W^{-2.5} & W \geqslant 2000 \text{ MeV} \end{cases} \qquad \text{(B-12)}$$

TABLE B-1

Galactic Parameters Used in the Analysis

Parameter (Units)	Nominal	Range
$B_\perp$ (μ-gauss)	5	3-5
L (kpc)	4	2-6
ℓ_i (pc)	50	13-1670*
ℓ_c (pc)	1	1-10
T_i (^oK)	10000	500-10000
T_c (^oK)	250	15-250
n_i (cm^{-3})	.03	.02-.05
n_c (cm^{-3})	.02	.02-.06

*In our model the value of ℓ_i is determined by the assumed range of the filling factor (ff = ℓ_c/ℓ_i), .006 - .08.

where W is the total energy of the electron.

Using this electron spectrum we first calculate numerically a rough correspondence between electron energy and emission frequency. An approximate analytical expression for the frequency of maximum intensity from an electron of energy W is:

$$\nu_m(\text{MHz}) \approx 0.29\nu_c = 4.6B_\perp W^2 \qquad \text{(B-13)}$$

where $B_\perp$ is in μ-gauss and W is in GeV (Ginzburg and Syrovatskii, 1964). However, this correspondence does not take into account the spectrum of electrons, and since there is contribution to a given frequency from a considerable range of electron energies we might expect some deviation from equation B-13 for a steep interstellar spectrum. In Figure B-2 we show a calculation of the relative contribution to the synchrotron emission at ν = 10 MHz from electrons with energies between 100 MeV and 10 GeV using the nominal interstellar electron spectrum given by equation B-12. The peak contribution comes from W ≈ 330 MeV. The arrow at 660 MeV corresponds to the prediction of equation B-13, which is based on a flat electron spectrum. The difference by a factor of 2 in the estimates roughly applies throughout the range of observations, 0.4-600 MHz. We note that 0.4 MHz, which is the lower limit of the radio observations, corresponds to ~60-80 MeV electrons. Thus below this energy the radio data provide little information on the inter-

[illegible] electron spectrum.

In Figure B-3 we show a plot (solid line) of the peak energy versus frequency which we obtained from plots similar to Figure B-2 covering the entire range of radio data for the nominal 5 μ-gauss field.

The dashed line refers to a calculation using $B_{\perp} = 3$ μ-gauss. We shall use Figure B-3 as a guide in estimating the electron energies at which changes in the electron intensity are necessary in order to produce calculations of the synchrotron spectrum in agreement with the observations.

As mentioned earlier, the change of a single parameter in equations B-1, B-5, and B-9 will produce a change in the computed radio spectrum. If at each frequency we compute the ratio of the observed radio spectrum to the computed spectrum, we obtain a set of multiplicative factors F(W) which can be applied, using Figure B-3, to the nominal interstellar spectrum to derive the adjusted galactic electron spectrum necessary to produce the observed synchrotron emission. We show in Figure B-4 the result of such a calculation. The nominal electron spectrum of equation B-12 has been used; each line corresponds to a change of the labeled parameter.

The effects of the interstellar medium at the low frequencies (low energies) are clearly shown. The range of parameters considered implies that below ~300 MeV (corresponding to ~10 MHz) the interstellar electron spectrum becomes increasingly uncertain due to uncertainties in the properties of the medium.

At high energies ($\gtrsim$ 300 MeV) only $B_{\perp}$ and L cause uncertainties in the interstellar electron spectrum. From equation B-10 we have:

$$I(\nu) \propto C\, B_{\perp}^{1.4}\, L$$

where we have set the interstellar electron spectral index $\gamma = 1.8$ ($W < 2000$ MeV) and C determines the magnitude of the electron spectrum. Thus

$$C \propto \frac{1}{B_{\perp}^{1.4} L}$$

We can estimate the error in C from the range of values of $B_{\perp}$ and L. If we assume that these parameters are Gaussian distributed about the mid-points of their ranges with the end-points of the range taken as the 1-σ limits, we derive

$$\frac{\sigma_C^2}{C^2} = (1.4)^2 \frac{\sigma_B^2}{B^2} + \frac{\sigma_L^2}{L^2}$$

$$\approx 0.375$$

or

$$\frac{\sigma_C}{C} = 0.61 \qquad \text{(B-14)}$$

Below ~300 MeV the functional dependence of the calculated radio spectrum on the many interstellar medium parameters cannot be easily determined. At these energies it is not obvious how to perform an appropriate statistical analysis, and, instead, we characterize the variation by an envelope which encloses the maximum variation for a single parameter. The total envelope of variation considered, which at energies above ~300 MeV is determined from equation B-14, is shown as the dashed curve in Figure B-4. Our estimate of a reasonable range of interstellar electron spectra is obtained by multiplying the nominal electron spectrum (equation B-12) by the factors corresponding to this envelope. These high and low spectra are shown in

Figure VI-9*. The explicit energy dependence, represented by power-law segments, is given in Table B-2 for all three spectra. For certain choices of galactic parameters each of the electron spectra can produce a radio spectrum in agreement with the data. The resulting radio spectra for the three electron spectra are shown in Figure VI-10; the particular galactic parameters used in each calculation are given in Table B-3.

It must be remembered that the galactic parameters used are not all independent quantities, e.g. Hjellming et al. (1969) show that if the clouds are in pressure equilibrium then the temperatures, neutral hydrogen densities, and electron densities for both the clouds and intercloud medium are uniquely related. However, not all the theoretical models predict the same values for the galactic parameters. In particular, we note that T_i, the intercloud temperature, is highly uncertain and it accounts for a very large variation of the spectrum at low energies. We feel that our procedure for calculating a reasonable range of the interstellar electron spectrum is the best that presently can be done.

---

*The electron spectra are plotted for energies between 70 MeV and 5 GeV. We have calculated the relative contribution to the synchrotron emission at ν = 0.4 MHz from electrons of different energies. (The relative contribution to the intensity at ν = 10 MHz is shown in Figure B-2.) Electrons with energies below 70 MeV contribute $\lesssim$ 25% of the emission at frequencies above 0.4 MHz. This percentage contribution is the same as the quoted absolute accuracy of the low-frequency radio data (Alexander et al., 1970). Similarly, we have chosen 5 GeV as the upper-limit energy since electrons with higher energy contribute $\lesssim$ 25% to the radio emission at frequencies below 600 MHz, the upper-limit frequency of the observations used in the analysis (Figure VI-8).

TABLE B-2

Power-law Approximations of the Calculated Galactic Electron Spectra: $j = AT^{-\gamma}(m^2 \cdot sec \cdot sr \cdot MeV)^{-1}$

SPECTRUM	ENERGY RANGE (MeV)	A ($\times 10^6$)	γ
LOW	70-2000	.0134	1.80
	2000-5000	2.75	2.50
NOMINAL	70-2000	.0254	1.80
	2000-5000	5.19	2.50
HIGH	70-100	3.45	2.16
	100-150	43.4	2.71
	150-300	1.38×10^5	4.32
	300-500	3.61	2.47
	500-2000	.0559	1.8
	2000-5000	11.42	2.5

TABLE B-3

Galactic Parameters Corresponding to the Galactic Electron Spectra of Figure VI-9

PARAMETER	LOW SPECTRUM MODEL	NOMINAL SPECTRUM MODEL	HIGH SPECTRUM MODEL
$B_{\perp}$ (μ-gauss)	5	5	3
L(pc)	7	4	4
ℓ_i(pc)	833	50	50
ℓ_c(pc)	5	1	1
T_i(^oK)	10000	10000	3000
T_c(^oK)	250	250	70
n_i(cm^{-3})	.03	.03	.03
n_c(cm^{-3})	.02	.02	.02

REFERENCES

Abraham, P. B., K. A. Brunstein and, T. L. Cline, "Production of Low-Energy Cosmic-Ray Electrons", Phys. Rev., 150, 1088, 1966.

Abramowitz, M., and I. A. Stegun, Handbook of Mathematical Functions, p. 253, Dover, New York, 1964.

Alexander, J. K., L. W. Brown, T. A. Clark, and R. G. Stone, "Low Frequency Cosmic Noise Observations of the Constitution of the Local System", Astron. and Astrophys., 6, 476, 1970.

Allen, C. W., Astrophysical Quantities, Athlone Press, London, 1963.

Anand, K. C., R. R. Daniel, and S. A. Stephens, "Radio Emitting Electrons in the Galaxy and the Solar Modulation of Cosmic Rays", Nature, 217, 25, 1968a.

Anand, K. C., R. R. Daniel, and S. A. Stephens, "Electrons Magnetic Fields and Background Radio Emission in the Galaxy", Proc. Ind. Acad. Sci., 67, 267, 1968b.

Arai, K., "On the Galactic Electrons Produced by Cosmic-Rays", Science Reports of the Tohoku University, 54, 1, 1971.

Beedle, R. E., "A Study of the Low Energy Electron Component of the Cosmic Radiation", Ph.D. Thesis, University of New Hampshire, 1970.

Bercovitch, M., "The Heliocentric Radial Density Gradient of Relativistic Cosmic Rays in 1967-68", Proc. 12th Int. Conf. Cosmic Rays, Hobart, 2, 579, 1971.

Berger, M. J., and S. M. Seltzer, "Tables of Energy Losses and Ranges of Electrons and Positrons (NASA SP-3012)", NASA, 1964.

Bertini, H. W., "Preliminary Data from Intranuclear-Cascade Calculations of 0.75-, 1-, and 2-GeV Protrons on Oxygen, Aluminum and Lead, and 1-GeV Neutrons on the Same Elements", Oak Ridge National Laboratory - TM - 1996, 1967.

Beuermann, K. P., "Secondary Electrons and Photons in the Upper Atmosphere", J. Geophys. Res., 76, 4291, 1971.

Beuermann, K. P., C. J. Rice, E. C. Stone, and R. E. Vogt, "Cosmic-Ray Negatron and Positron Spectra Between 12 and 220 MeV", Phys. Rev. Letters., 22, 412, 1969.

Beuermann, K. P., C. J. Rice, E. C. Stone, and R. E. Vogt, "Cosmic-Ray Negatron and Positron Spectra Observed Near Fort Churchill in 1968", Acta Physica Academiae Scientiarum Hungaricae, 29, Suppl. 1, 173, 1970.

Blaauw, A., and S. Schmidt, ed., Galactic Structure, p. 167-202, University of Chicago Press, 1965.

Blythe, J. H., "Results of a Survey of Galactic Radiation at 38 Mc/s", Mon. Not. R. Astr. Soc., 117, 652, 1957.

Bridle, A. H., and V. R. Venugopal, "Distribution and Temperature of Interstellar Electron Gas", Nature, 224, 545, 1969.

Burger, J. J., "A Phenomenological Approach to the Modulation of Cosmic Rays", Astrophys. J., 166, 651, 1971.

Burger, J. J., and B. N. Swanenburg, "Long-Term Solar Modulation of Cosmic-Ray Electrons With Energies Above 0.5 GeV", 12th Int. Conf. on Cosmic Rays, Hobart, 2, 554, 1971.

Burger, J. J., and Y. Tanaka, "Implications of the Observed Solar Modulation of Cosmic-Ray Electrons", Astrophys. J., 162, 305, 1970.

Cain, J. C., S. J. Hendricks, R. A. Langel, and W. V. Hudson, "A Proposed Model for the International Geomagnetic Reference Field - 1965", J. Geomag. and Geoelectricity, 19, 335, 1967.

Carmichael, H., and J. Katzman, "Steplike Nature of the 11 Year Modulation in Solar Cycle 19", Proc. 12th Int. Conf. Cosmic Rays, Hobart, 2, 744, 1971.

Carmichael, H., and P. H. Stoker, "Five Sudden Alterations of the Rigidity Dependence of the 11-year Modulation Since February 1965", (abstract), EOS, Trans. Am. Geophys. Union, 51, 802, 1970.

Cline, T. L., and G. Porreca, "Cosmic-Ray Electrons and Positrons of Energies of 2 to 9.5 MeV Observed in Interplanetary Space", Acta Physica Academiae Scientiarum Hungaricae, 29, Suppl. 1, 145, 1970.

Dalgarno, A., and R. A. McCray, "Heating and Ionization of HI Regions", Annual Review of Astronomy and Astrophysics, 10, 375, 1972.

Dessler, A. J., "Solar Wind and Interplanetary Magnetic Field", Rev. Geophys., 5, 1, 1967.

Earl, J. A., "Cloud-Chamber Observations of Primary Cosmic-Ray Electrons", Phys. Rev. Letters., 6, 125, 1961.

Earl, J. A., "Modulation of Cosmic-Ray Electrons", University of Maryland Technical Report 72-080, July, 1972a.

Earl, J. A., "Diffusion of Charged Particles in a Random Magnetic Field", University of Maryland Technical Report No. 73-032, September, 1972b.

ESSA Solar Geophysical Data, Nos. 287-325, World Data Center A, Boulder, Colorado, 1968-1971.

Fan, C. Y., G. Gloeckler, B. McKibben, K. R. Pyle, and J. A. Simpson, "Differential Energy Spectra and Intensity Variation of 1-20 MeV/Nucleon Protons and Helium Nuclei in Interplanetary Space", Can. J. Phys., 46, 5498, 1968.

Fan, C. Y., G. Gloeckler, and J. A. Simpson, "Galactic Deuterium and Its Energy Spectrum Above 20 MeV Per Nucleon", Phys. Rev. Letters, 17, 329, 1966.

Fanselow, J. L., "The Primary Cosmic-Ray Electron Spectrum Between 0.09 and 8.4 BeV in 1965", Astrophys. J., 152, 783, 1968.

Fanselow, J. L., R. C. Hartman, R. H. Hildebrand, and P. Meyer, "Charge Composition and Energy Spectrum of Primary Cosmic-Ray Electrons", Astrophys. J., 158, 771, 1969.

Field, G. B., "Excitation of the Hydrogen 21-Cm Line", Proc. Inst. Radio Engr., 46, 240, 1958.

Field, G. B., Interstellar Gas Dynamics, ed. H. J. Habing, Springer-Verlag, 1970.

Field, G. B., Proc. NRAO Conf. on Interstellar Molecules, Greenbank, 1971.

Field, G. B., D. W. Goldsmith, and H. J. Habing, "Cosmic-Ray Heating of the Interstellar Gas", Astrophys. J., 155, L149, 1969.

Fisk, L. A., "Solar Modulation of Galactic Cosmic Rays, 2", J. Geophys. Res., 76, 221, 1971.

Galbraith, W., and W. S. E. Williams, ed., High Energy and Nuclear Physics Data Handbook, p. VII-1, Rutherford Lab., Chilton, England, 1964.

Garrard, T. L., "A Quantitative Investigation of the Solar Modulation of Cosmic-Ray Protons and Helium Nuclei", Ph.D. Thesis, California Institute of Technology, 1973.

Ginzburg, V. L., Propagation of Electromagnetic Waves in a Plasma, Pergamon Press, Oxford, 1964.

Ginzburg, V. L., and S. I. Syrovatskii, The Origin of Cosmic Rays, Pergamon Press, New York, 1964.

Gleeson, L. J., and W. I. Axford, "Cosmic Rays in the Interplanetary Medium", Astrophys. J., 149, L115, 1967.

Gleeson, L. J., and W. I. Axford, "Solar Modulation of Galactic Cosmic Rays", Astrophys. J., 154, 1011, 1968.

Gleeson, L. J., and I. H. Urch, "Energy Losses and Modulation of Galactic Cosmic Rays", Astrophysics and Space Science, 11, 228, 1971.

Gleeson, L. J., and I. H. Urch, "Cosmic-Ray Diffusion Coefficient in Interplanetary Space", J. Geophys. Res., 77, 4259, 1972.

Goldstein, M. L., L. A. Fisk, and R. Ramaty, "Energy Loss of Cosmic Rays in the Interplanetary Medium", Phys. Rev. Letters, 25, 832, 1970.

Goldstein, M. L., R. Ramaty, and L. A. Fisk, "Interstellar Cosmic Ray Spectra from the Nonthermal Radio Background From 0.4 to 400 MHz.", Phys. Rev. Letters, 24, 1193, 1970.

Gosling, J. T., R. T. Hansen, and S. J. Bame, "Solar Wind Speed Distribution: 1962-1970", J. Geophys. Res., 76, 1181, 1971.

Greisen, E., "Aperture Synthesis of Interstellar Neutral Hydrogen in Absorption", Ph.D. Thesis, California Institute of Technology, 1973.

Habing, H. J., and D. W. Goldsmith, "Heating of the Interstellar Medium by X-Rays and by Cosmic Rays", Astrophys. J., 166, 525, 1971.

Hasselmann, K., and G. Wibberentz, "Scattering of Charged Particles by Random Electromagnetic Field", Zeitschrift für Geophysik, 34, 353, 1968.

Hayakawa, S., H. Okuda, Y. Tanaka, and Y. Yamamoto, "Cosmic Electrons and Gamma-Rays", Suppl. Progr. Theor. Phys., 30, 153, 1964.

Heiles, C., "Physical Conditions and Chemical Constitution of Dark Clouds", Annual Reviews of Astronomy and Astrophysics, 9, 293, 1971.

Hjellming, R. M., C. P. Gordon, and K. J. Gordon, "Properties of Interstellar Clouds and the Inter-Cloud Medium", Astron. and Astrophys., 2, 202, 1969.

Hovestadt, D., and P. Meyer, "The Geomagnetic Cut-Off at Ft. Churchill and the Primary Cosmic Ray Electron Spectrum from 10 MeV to 12 GeV in 1968", Acta Physica Academiae Scientiarum Hungariae, 29, Suppl. 2, 525, 1970.

Hsieh, K. C., G. M. Mason, and J. A. Simpson, "Cosmic Ray ^{2}H from Satellite Measurements, 1965-1969", Astrophys. J., 166, 221, 1971.

Hughes, M. P., A. R. Thompson, and R. S. Colvin, "An Absorbtion-Line Study of the Galactic Neutral-Hydrogen at 21 cm", Astrophys. J. Suppl., 23, 323, 1971.

Israel, M. H., and R. E. Vogt, "Characteristics of the Diurnally Varying Electron Flux near the Polar Cap", J. Geophys. Res., 74, 1969.

Jokipii, J. R., "Cosmic Ray Propagation, 1, Charged Particles in a Random Magnetic Field", Astrophys. J., 146, 480, 1966.

Jokipii, J. R., "Cosmic Ray Propagation, 2, Diffusion in the Interplanetary Magnetic Field", Astrophys. J., 149, 504, 1967.

Jokipii, J. R., "Addendum and Erratum to Cosmic-Ray Propagation, 1", Astrophys. J., 152, 671, 1968.

Jokipii, J. R., "Gradient and Curvature Drifts of Energetic Solar Particles in the Solar Wind", Acta Physica Academiae Scientiarum Hungaricae, 29, 379, 1970.

Jokipii, J. R., "Propagation of Cosmic-Rays in the Solar Wind", Reviews of Geophysics and Space Physics, 9, 27, 1971.

Jokipii, J. R., "Radial Variation of Magnetic Fluctuations and the Cosmic-Ray Diffusion Tensor in the Solar Wind", to be published, 1972.

Jokipii, J. R., and P. J. Coleman, Jr., "Cosmic-Ray Diffusion Tensor and Its Variation Observed in Mariner 4", J. Geophys. Res., 73, 5495, 1968.

Jokipii, J. R., J. L'Heureux, and P. Meyer, "Diurnal Intensity Variation of Low-Energy Electrons Observed Near the Polar Cap", J. Geophys. Res., 72, 4375, 1967.

Jokipii, J. R., and P. Meyer, "Storage and Diffusion of Cosmic-Ray Electrons in the Galaxy", Phys. Rev. Letters, 20, 752, 1968.

Jokipii, J. R., and E. N. Parker, "Stochastic Aspects of Magnetic Lines of Force with Application to Cosmic-Ray Propagation", Astrophys. J., 155, 777, 1969.

Kane, R. P., "Nature of the Long-term and Short-term Modulations of Cosmic-Ray Intensity", J. Geophys. Res., 77, 5573, 1972.

Lerche, I., "On the Origin of the Nonthermal Radio Emission at 0.4 to 6.5 MHz", Astrophys. J., 166, 311, 1971.

Lezniak, J. A., and W. R. Webber, "Solar Modulation of Cosmic Ray Protons, Helium Nuclei, and Electrons: A Comparison of Experiments with Theory", J. Geophys. Res., 76, 1605, 1971.

L'Heureux, J., C. Y. Fan and P. Meyer, "The Quiet-Time Spectra of Cosmic-Ray Electrons of Energies Between 10 and 200 MeV Observed on OGO-5", Astrophys. J., 171, 363, 1972.

Luhmann, J. G., "A Study of the Solar Modulation of Low Energy Cosmic-Ray Electrons Between 1965 and 1970", University of Maryland Technical Report 71-127, June, 1971.

Lupton, J. E., "Solar Flare Particle Propagation -- Comparison of a New Analytic Solution with Spacecraft Measurements", Ph.D. Thesis, California Institute of Technology, 1972.

Manchester, R. N., "Pulsar Rotation and Dispersion Measures and the Galactic Magnetic Field", Astrophys. J., 172, 43, 1972.

Maran, S. P., Report on the Fourth Texas Symposium on Relativistic Astrophysics, 1969.

Marshall, F. E., and E. C. Stone, "Propagation of Solar Flare Protons at Early and Late Times", (abstract). EOS, Trans. Amer. Geophys. Union, 53, 1085, 1972.

Mason, G. M., "Interstellar Propagation of Galactic Cosmic-Ray Nuclei $2 \leq Z \leq 8$ in the Energy Range 10-1000 MeV per Nucleon", Astrophys. J., 171, 139, 1972.

McDonald, F. B., "Primary Cosmic-Ray Proton and Alpha Flux Near the Geomagnetic Equator", Phys. Rev., 109, 1367, 1958.

McDonald, F. B., T. L. Cline, and G. M. Simnett, "Multifarious Temporal Variations of Low-Energy Relativistic Cosmic-Ray Electrons", J. Geophys. Res., 77, 2213, 1972.

Meyer, P., P. J. Schmidt, and J. L'Heureux, "Measurements of the Primary Cosmic Ray Electron Spectrum Between 20 MeV and 20 GeV and Its Changes with Time", Proc. 12th Int. Conf. on Cosmic Rays, Hobart, 2, 548, 1971.

Meyer, P., and R. Vogt, "Electrons in the Primary Cosmic Radiation", Phys. Rev. Letters, 6, 193, 1961.

Moffet, A. T., "Polarization of Pulsars", The Crab Nebula, ed. Davies and Smith, 195, 1971.

Ng, C. K., and L. J. Gleeson, "On the Propagation of Solar Cosmic Rays", Proc. 12th Int. Conf. on Cosmic Rays, Hobart, 2, 498, 1971.

Ormes, J. F., and W. R. Webber, "Proton and Helium Nuclei Cosmic Ray Spectra and Modulations between 100 and 2000 MeV/Nucleon", J. Geophys. Res., 73, 4231, 1968.

Parker, E. N., Interplanetary Dynamical Processes, John Wiley and Sons, New York, 1963.

Parker, E. N., "Dynamical Theory of the Solar Wind", Space Science Reviews, 4, 666, 1965a.

Parker, E. N., "The Passage of Energetic Charged Particles through Interplanetary Space", Planetary Space Sci., 13, 9, 1965b.

Parker, E. N., "Theoretical Studies of the Solar Wind Phenomenon", Space Sci. Rev., 9, 325, 1969a.

Parker, E. N., "Galactic Effects of the Cosmic-Ray Gas", Space Sci. Rev., 9, 651, 1969b.

Perola, G. C., and L. Scarsi, "Flux and Energy Spectrum of Secondary Electrons in the Upper Atmosphere", Il Nuovo Cimento, 46, 718 1966.

Perola, G. C., L. Scarsi, and G. Sironi, "Secondary Cosmic-Ray Electrons Produced in Interstellar Medium. II - The Secondary Electron Equilibrium Spectrum in the Galaxy", Il Nuovo Cimento, 53 B, 459, 1968.

Quenby, J. J., and J. F. Sear, "Interplanetary Magnetic Field Fluctuation Measurements and the Long Term Modulation", Proc. 12th Int. Conf. on Cosmic Rays, Hobart, 2, 771, 1971.

Radhakrishnan, V., J. D. Murray, P. Lockhart, and R. P. J. Whittle, "Galactic 21-Centimeter Observations in the Direction of 35 Extragalactic Sources", Astrophys. J. Suppl., 24, 15, 1972.

Ramaty, R., "The Influence of the Ionized Medium on Synchrotron Emission in Interstellar Space", Astrophys. J., 174, 157, 1972.

Ramaty, R., and R. E. Lingenfelter, "Galactic Cosmic-Ray Electrons", J. Geophys. Res., 71, 3687, 1966.

Ramaty, R., and R. E. Lingenfelter, "Solar Modulation and the Galactic Intensity of Cosmic-Ray Positrons and Negatrons", Phys. Rev. Letters, 20, 120, 1968.

Razin, V. A., Izvo Vysshikh Vchebn, Zavedenii Radiofiz., 3, 584, 1960.

Rice, C. J., "Gamma-Ray Produced Background in $e^{\pm}$ Gondola", Space Radiation Laboratory Internal Report No. 14, 1969.

Rice, C. J., "Primary Cosmic-Ray Positrons and Negatrons in 1968 at Energies Between 11 and 204 MeV", Ph.D. Thesis, California Institute of Technology, 1970.

Roelof, E. C., "Transport of Cosmic Rays in the Interplanetary Medium", Canad. J. Phys., 46, 5990, 1968.

Rossi, B., High Energy Physics, Prentice-Hall, New York, 1952.

Rygg, T. A., and J. A. Earl, "Balloon Measurements of Cosmic Ray Protons and Helium over Half a Solar Cycle 1965-1969", J. Geophys. Res., 76, 7445, 1971.

Sari, J. W., "Modulation of Cosmic Rays by Interplanetary Magnetic Field", EOS, Trans. Amer. Geophys. Union, 53, 480, 1972a.

Sari, J. W., "Modulation of Low Energy Cosmic Rays", Ph.D. Thesis, University of Maryland, 1972b.

Sari, J. W., and N. F. Ness, "Power Spectra of the Interplanetary Magnetic Field", Solar Phys., 8, 155, 1969.

Schmidt, P. J., "Cosmic-Ray Electron Spectrum and Its Modulation Near Solar Maximum", J. Geophys. Res., 77, 3295, 1972.

Shen, C. S., "Energy Spectrum and the Origin of Cosmic-Ray Electrons Above 12 BeV", Phys. Rev. Letters, 19, 399, 1967.

Shu, F. H., V. Milione, W. Gebel, C. Yuan, D. W. Goldsmith and W. W. Roberts, "Galactic Shocks in an Interstellar Medium with Two Stable Phases", Astrophys. J., 173, 557, 1972.

Simnett, G. M., and F. B. McDonald, "Observations of Cosmic-Ray Electrons Between 2.7 and 21.5 MeV", Astrophys. J., 157, 1435, 1969.

Smart, D. F., "Calculation of the Daily Variation of Cosmic-Ray Cutoff Rigidities at Fort Churchill, Canada", Proc. 12th Int. Conf. on Cosmic Rays, Hobart, 3, 843, 1971.

Smart, D. F., and M. A. Shea, "Daily Variation of Electron and Proton Geomagnetic Cutoffs Calculated for Fort Churchill, Canada", J. Geophys. Res., 77, 4595, 1972.

Steljes, J. F., "Cosmic Ray NM-64 Neutron Monitor Data-I to XVI", Atomic Energy of Canada Limited, Chalk River, Ontario, 1965-1971.

Stephens, S. A., "An Analysis of the Low Frequency Radio Continuum in the Galaxy", Astron. and Astrophys., 11, 311, 1971.

Stoker, P. H., and H. Carmichael, "Steplike Changes in the Long-Term Modulation of Cosmic Rays", Astrophy. J., 169, 357, 1971.

Trimble, V., "Motions and Structure of the Filamentary Envelope of the Crab Nebula", Astron. J., 73, 535, 1968.

Urch, I. H., and L. J. Gleeson, "Galactic Cosmic Ray Modulation from 1965-1970", preprint submitted to Astrophysics and Space Science, 1972.

Verma, S. D., "A Calculation of the Flux and Energy Spectrum of Secondary Electrons at High Altitudes in the Atmosphere", Proc. Ind. Acad. Sci., 66, 125, 1967.

Verma, S. D., "High Energy Electrons and Emission of the Omnidirectional Synchrotron Radiation in Radio Frequencies and X-Ray Regions", Astrophys. J., 152, 537, 1968.

Webber, W. R., "On the Relationship Between Recent Measurements of Cosmic-Ray Electrons, Non-thermal Radio Emissions from the Galaxy and the Solar Modulation of Cosmic Rays", Aust. J. Phys., 21, 845, 1968.

Wentzel, D. G., "Interstellar Motions: Minuet or Rock?", Publications of the Astronomical Society of the Pacific, 84, 225. 1972.

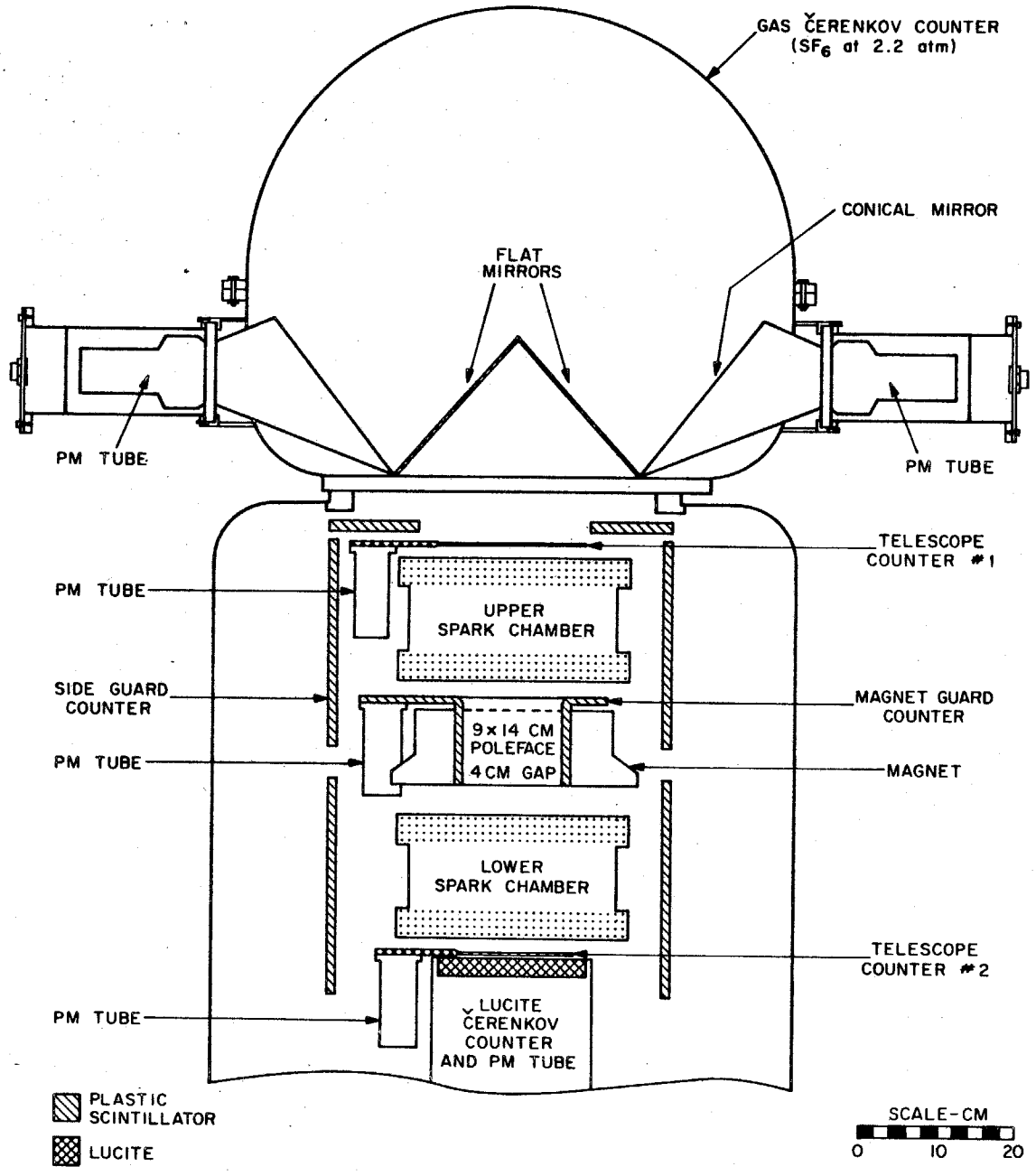

Figure II-1: Cross-section of the $e^{\pm}$ detector system

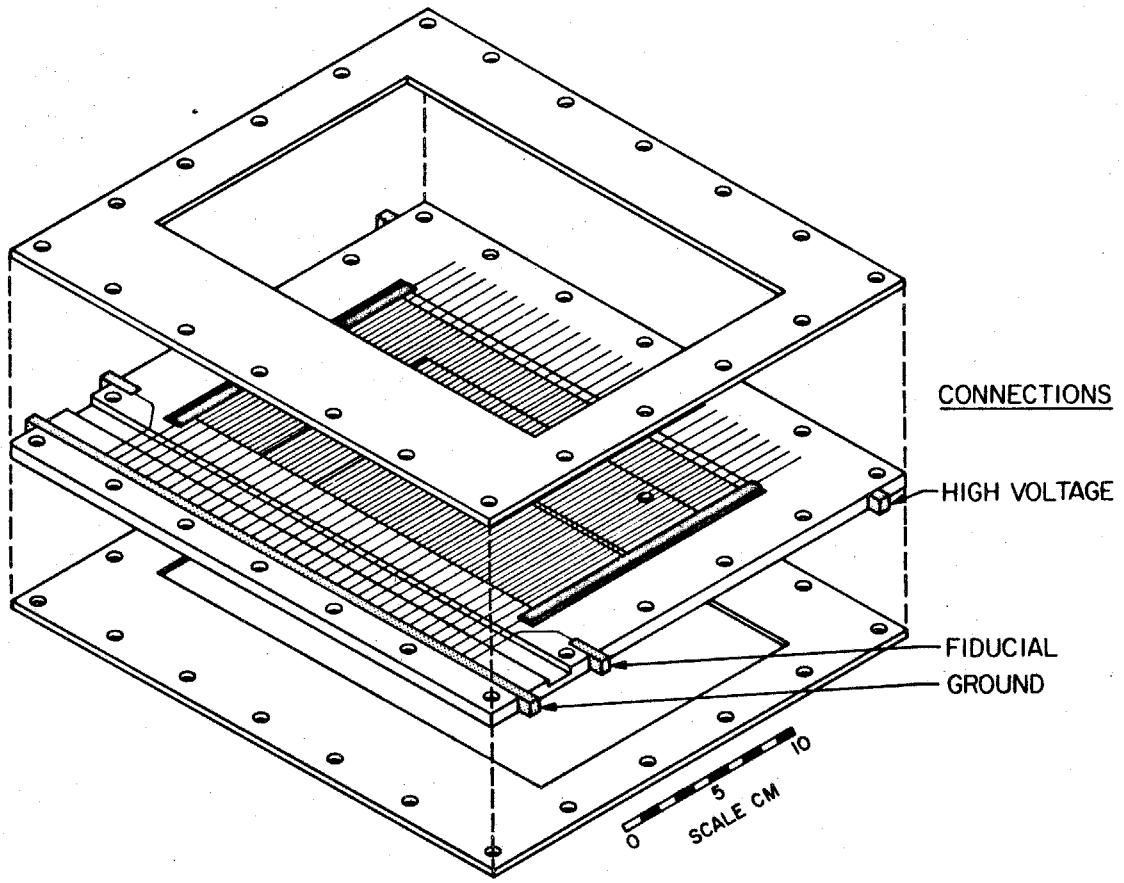

Figure II-2: Exploded view of a spark-chamber module.

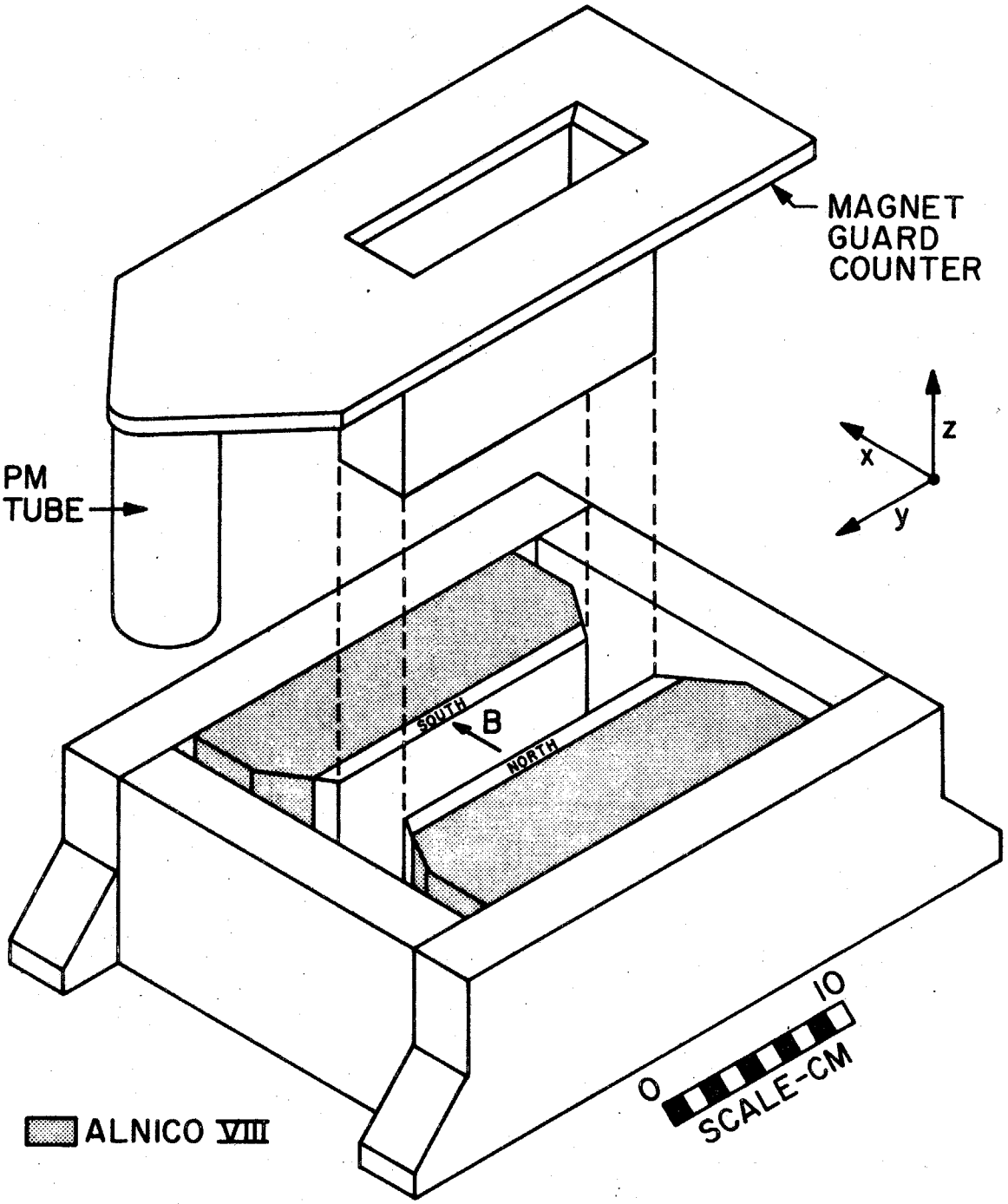

Figure II-3: Exploded view of the MOD-2 magnet and magnet guard counter. For clarity the origin of the coordinate system is shown displaced from its location at the center of the magnet gap.

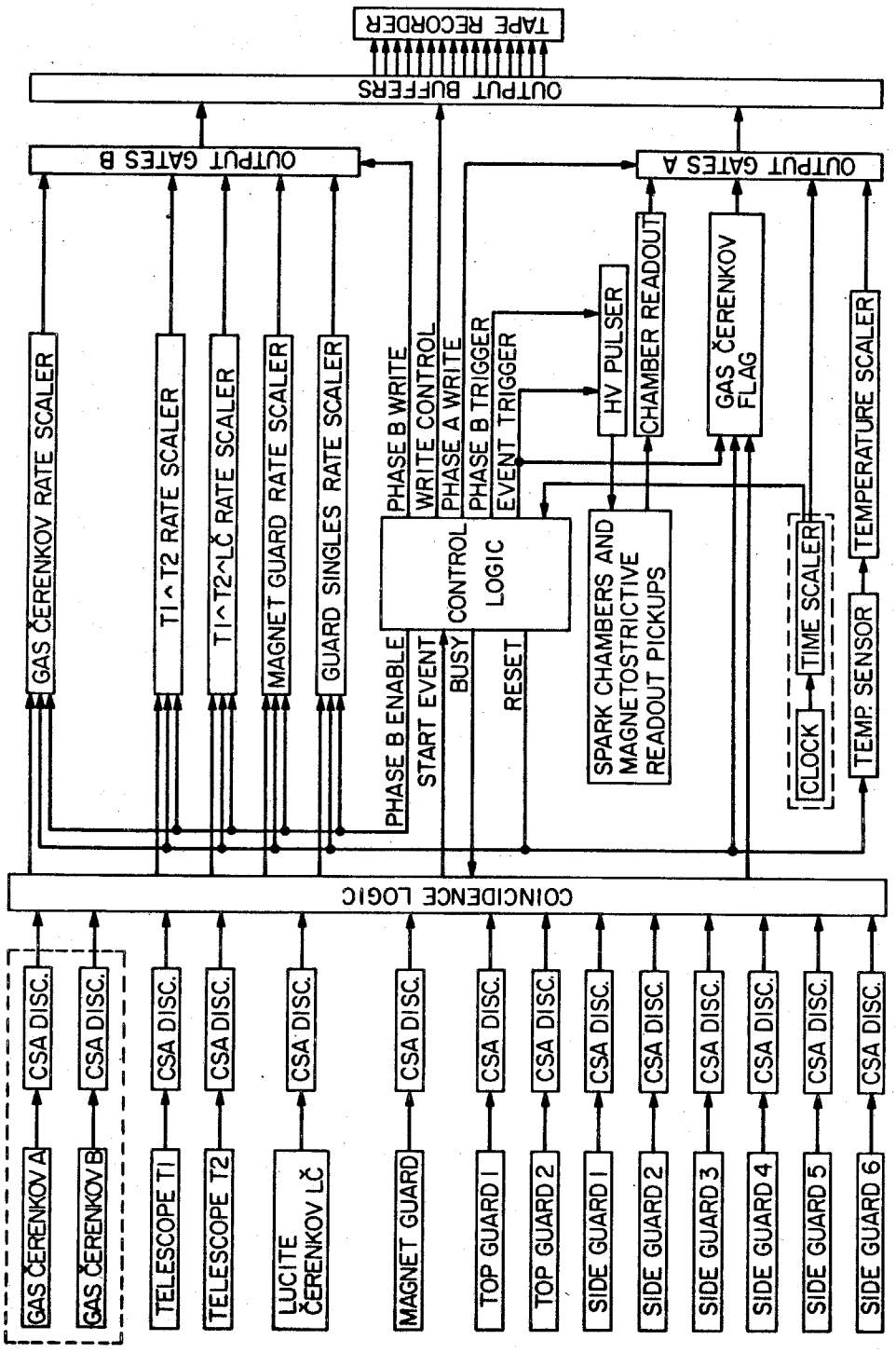

Figure II-4: Electronic block diagram. Dashed lines indicate components enclosed by spark noise shields.

CSA DISC = charge sensitive amplifier and discriminator.

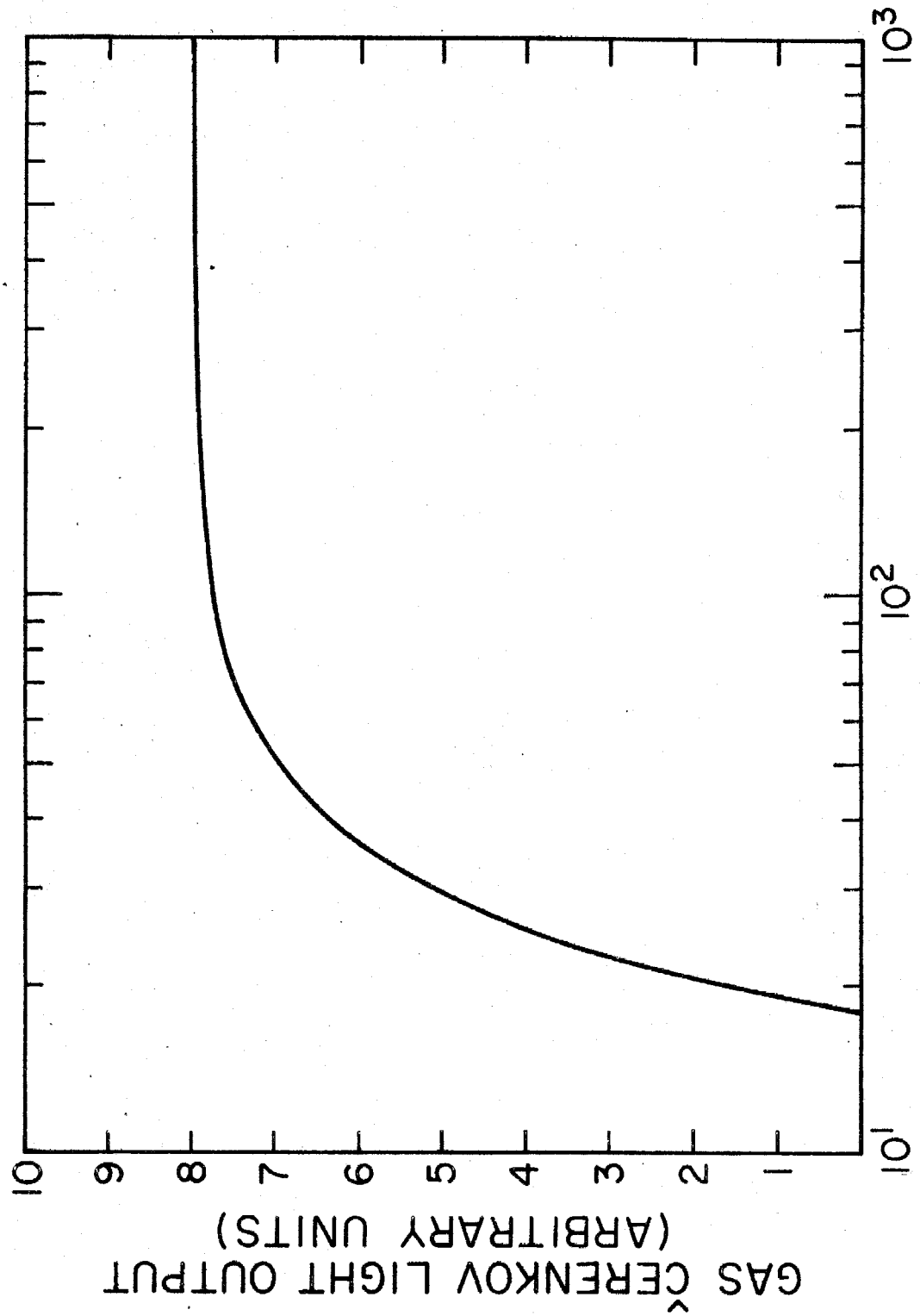

Figure II-5: Gas Čerenkov counter light output as a function of energy for singly-charged particles.

Figure II-6: Magnetic flux density in the gap of the analyzing magnet versus position. The curves represent the field components along three paths parallel to the z axis in the magnet gap. See Figure II-3 for definition of the coordinate system employed.

1. Solid curve: x = 1 y = 6 cm

2. Dashed curve: x = 0 y = 6 cm

3. Dotted curve: x = 0 y = 0 cm

B_z and B_y for paths 2 and 3 are identically zero and are therefore not shown explicitly.

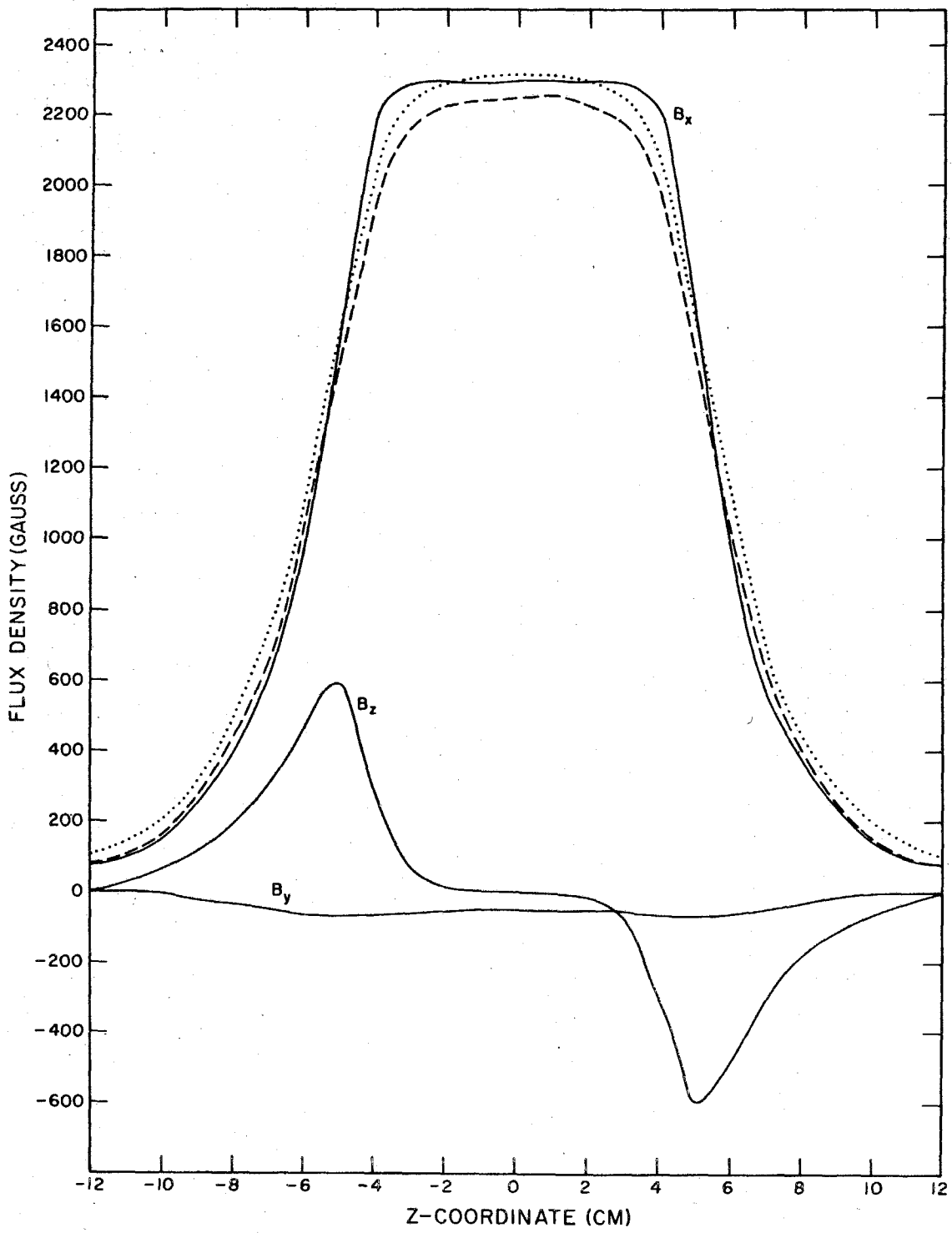
2400
2200
2000
1800
1600
1400
1200
1000
800
600
400
200
0
-200
-400
-600
FLUX DENSITY (GAUSS)
B_x
B_z
B_y
-12
-10
-8
-6
-4
-2
0
2
4
6
8
10
12
Z-COORDINATE (CM)

Figure II-6

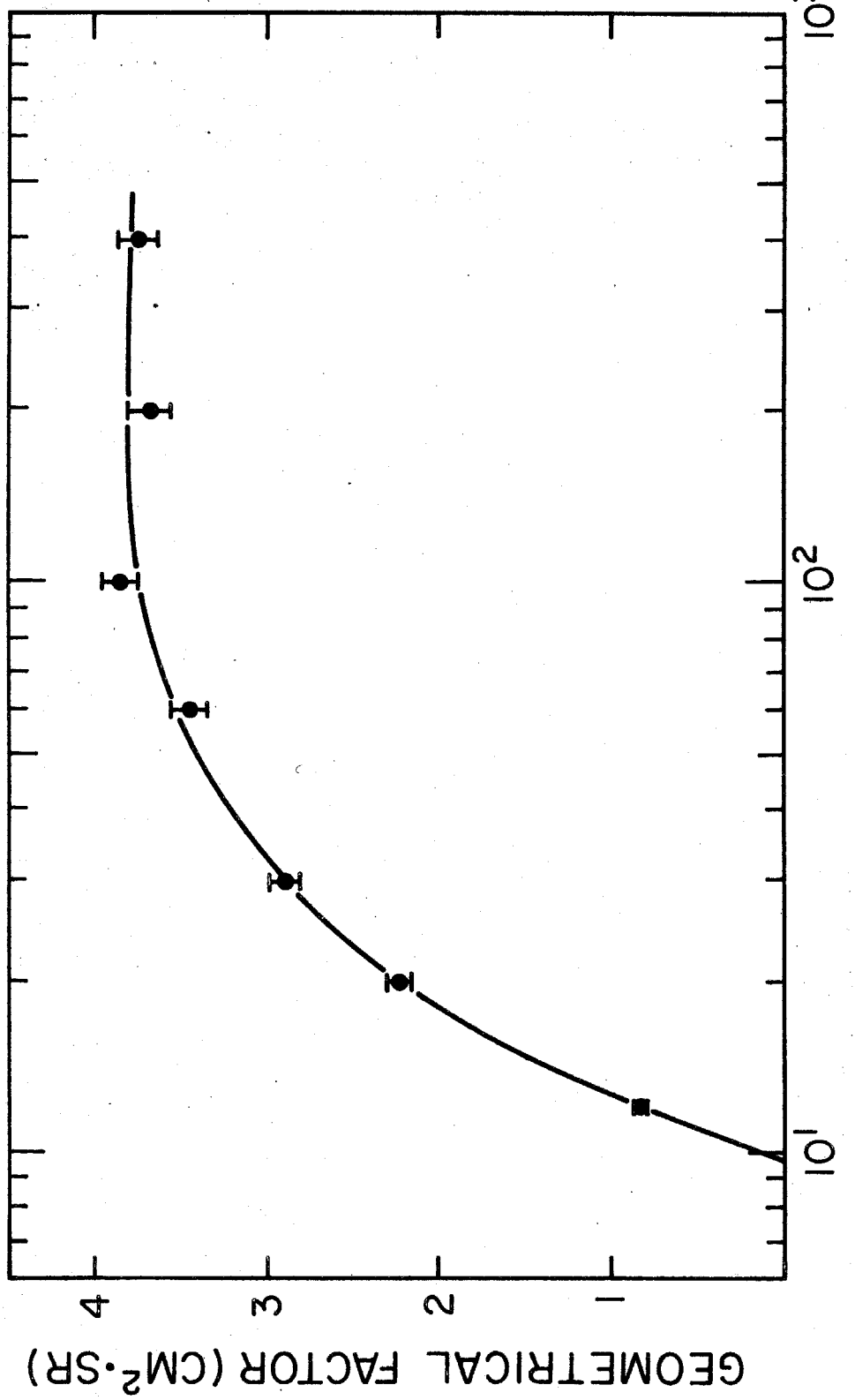

Figure II-7: Geometrical factor of the MOD-2 detector versus particle rigidity.

Figure II-8: Range of trajectory deflection angles in the MOD-2 detector as a function of particle rigidity. The mean value, r.m.s. deviation (solid bar), and extreme values (dashed bar) of rigidity x deflection angle are shown for a random distribution of 1000 incident trajectories at each of 7 rigidities.

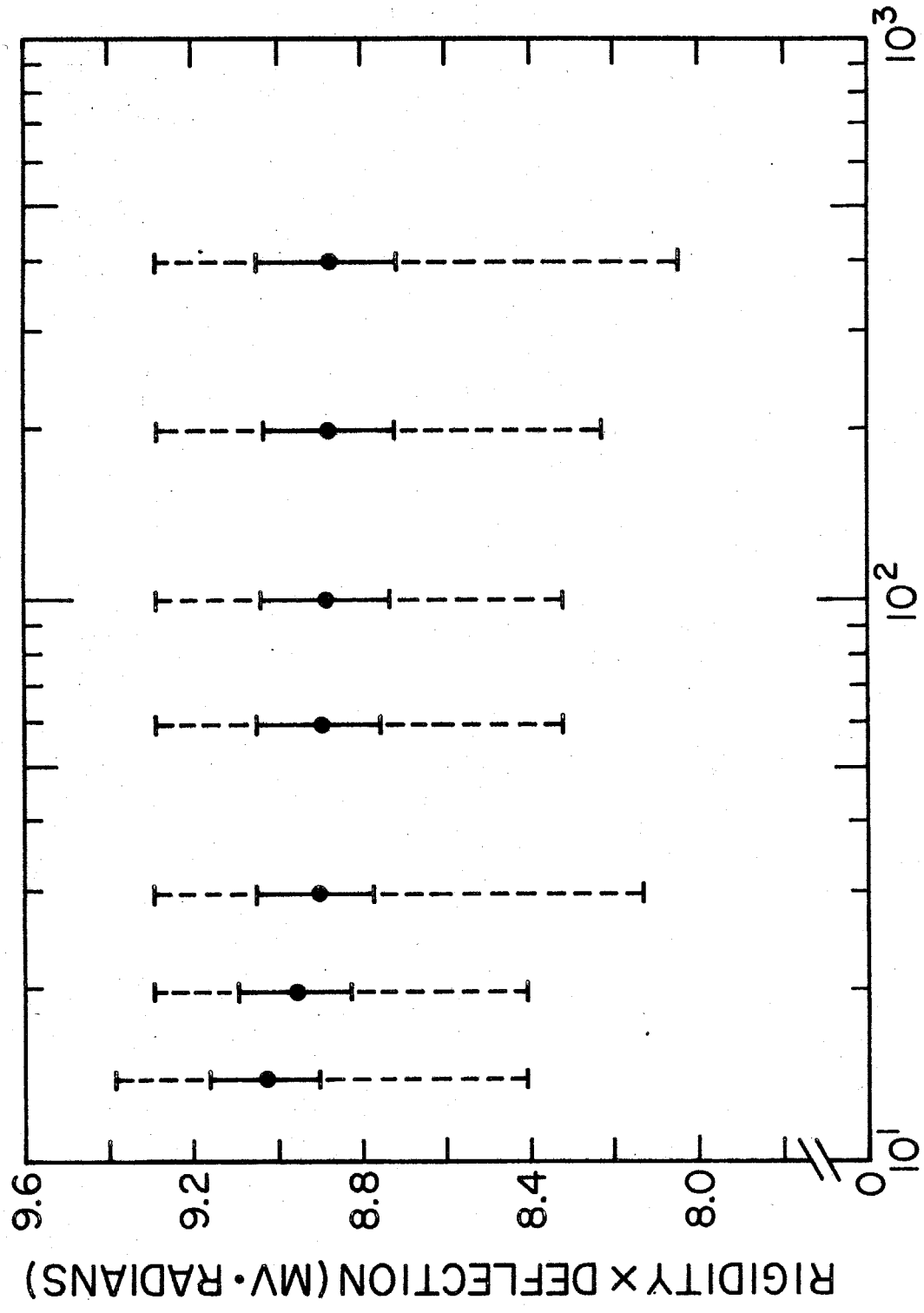
RIGIDITY × DEFLECTION (MV • RADIANS)
9.6
9.2
8.8
8.4
8.0
0
10^1
10^2
10^3
RIGIDITY (MV)

Figure II-8

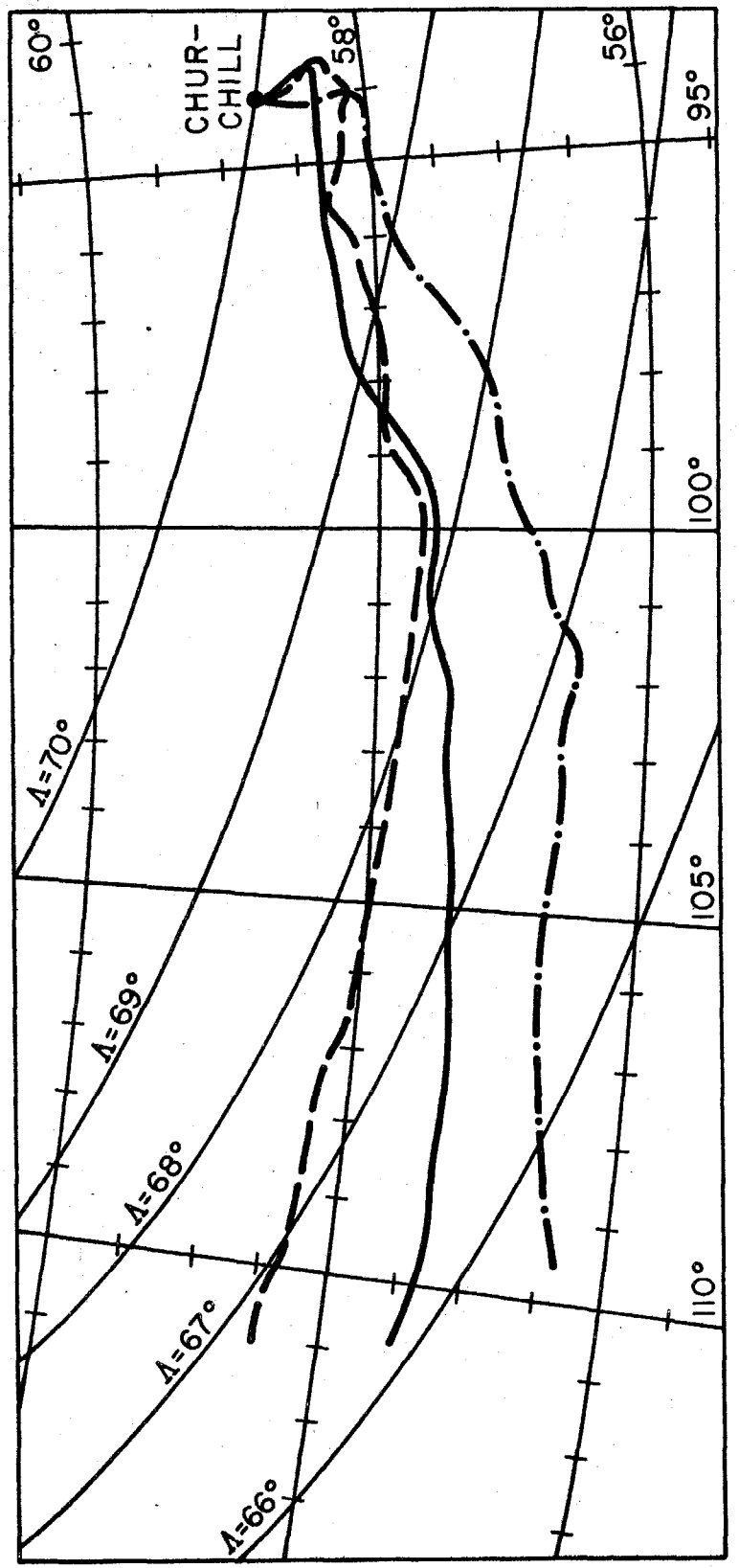

Figure III-1: Trajectories of three typical balloon flights. Invariant geomagnetic latitude contours are derived from the internal geomagnetic field only (Cain et al., 1967).

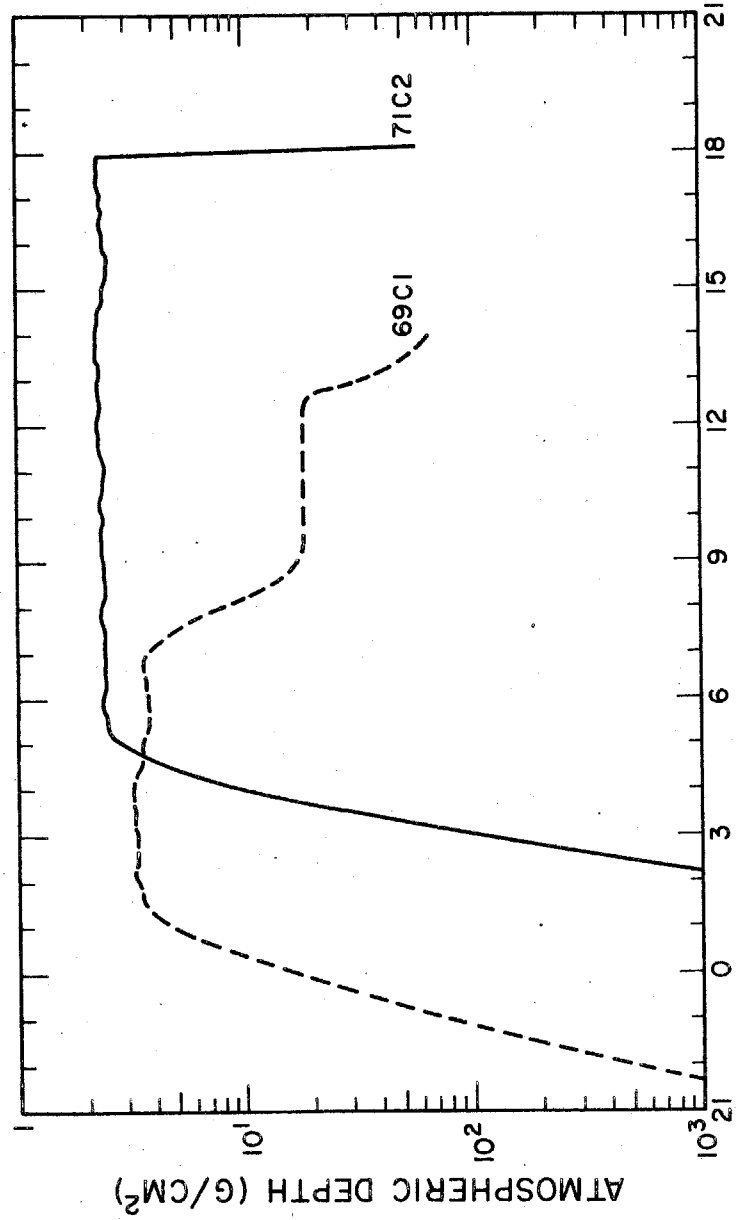

Figure III-2: Two representative time-altitude profiles. The curves are labeled with the flight number.

Figure III-3: Deep River Neutron Monitor counting rate versus time. The vertical bars indicate the times of balloon flights. The approximate periods of solar minimum and solar maximum are indicated by the horizontal bars.

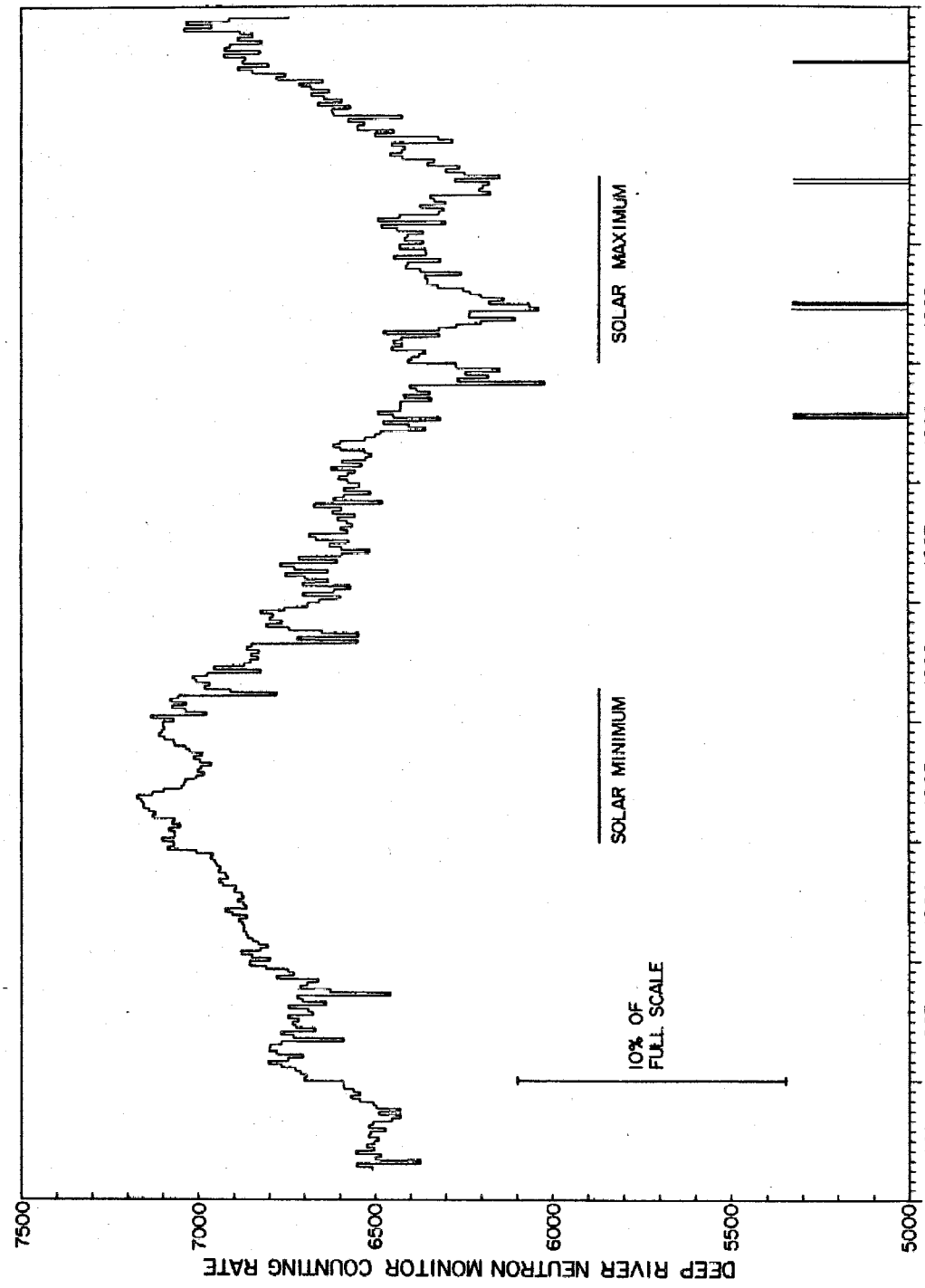
DEEP RIVER NEUTRON MONITOR COUNTING RATE
7500
7000
6500
6000
5500
5000
SOLAR MINIMUM
SOLAR MAXIMUM
10% OF FULL SCALE
1962
1963
1964
1965
1966
1967
1968
1969
1970
1971
DATE

Figure III-3

Figure IV-1: Typical event rate versus local time (Flight 71C2). Negatrons (solid histogram) and positrons (dotted histogram) are shown separately. Typical 1-σ error limits are indicated. The nighttime period used in the analysis is indicated.

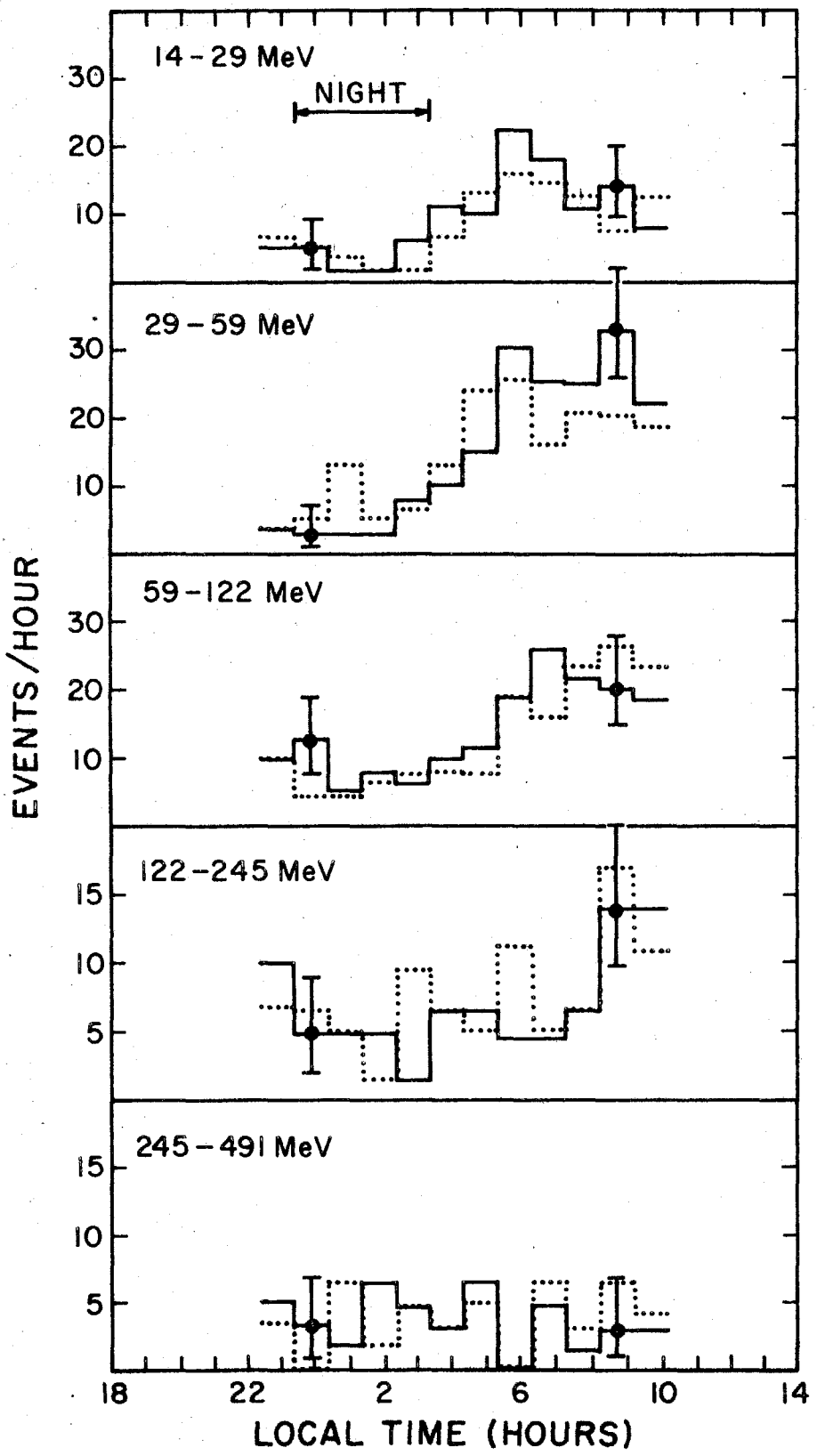
14 - 29 MeV
NIGHT
29 - 59 MeV
59 - 122 MeV
122 - 245 MeV
245 - 491 MeV
EVENTS/HOUR
LOCAL TIME (HOURS)
18
22
2
6
10
14

Figure IV-1

Figure IV-2: Representative examples of the measured event rate versus atmospheric depth. The energy intervals indicated are those measured at the magnet. Also shown is the separation into primary and atmospheric secondary components as determined by the least-squares fitting technique described in the text.

Dashed curve: best-fit primary contribution

Dotted curve: best-fit secondary contribution

Solid-curve: best-fit total positrons or negatrons.

The χ^2 probability, P, is indicated for each fit.

Figure IV-2a: Energy range with a relatively large contribution of residual primaries at float altitude.

Figure IV-2b: Energy range with essentially zero primary flux at float altitude.

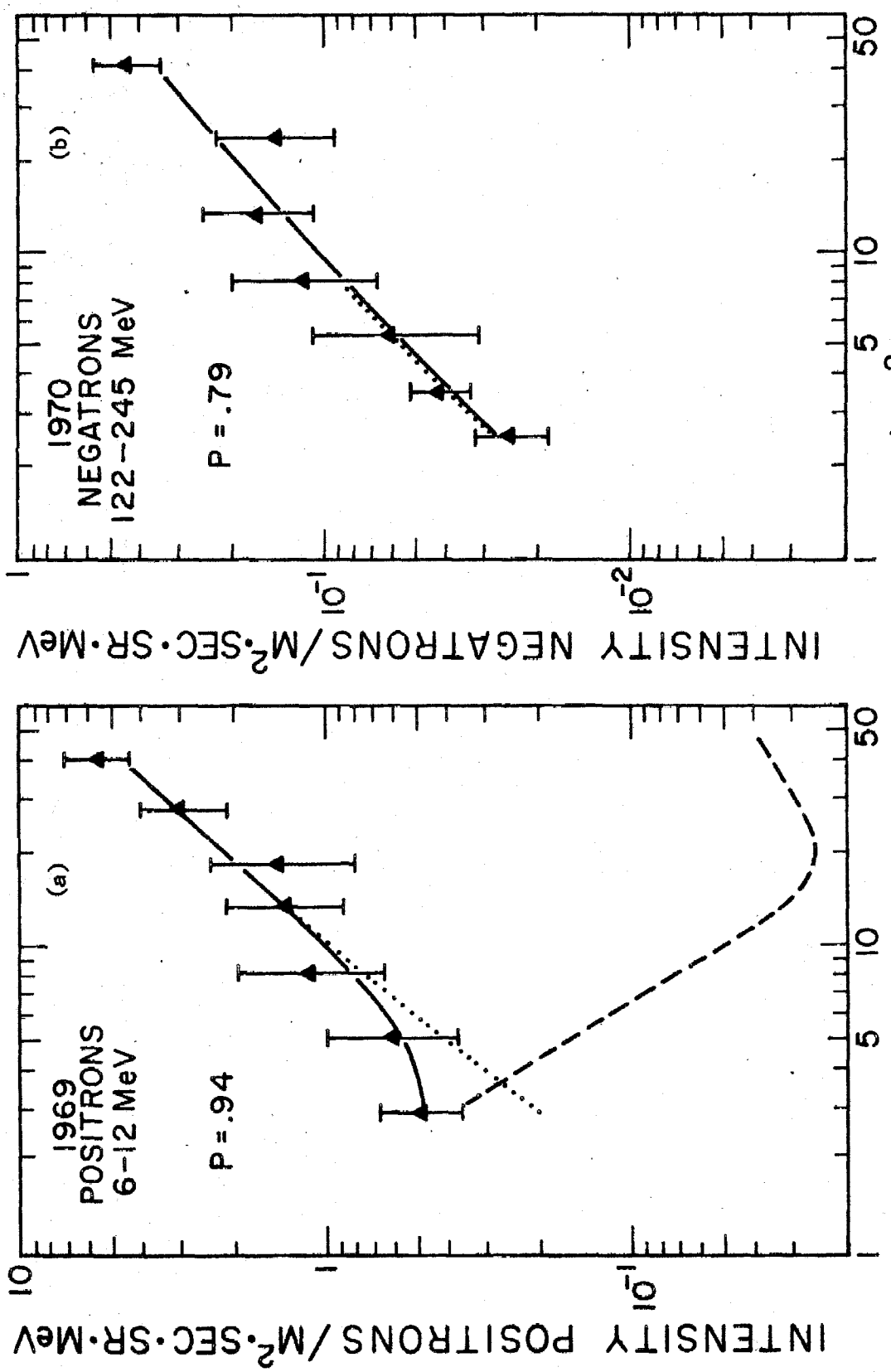

Figure IV-2a and b

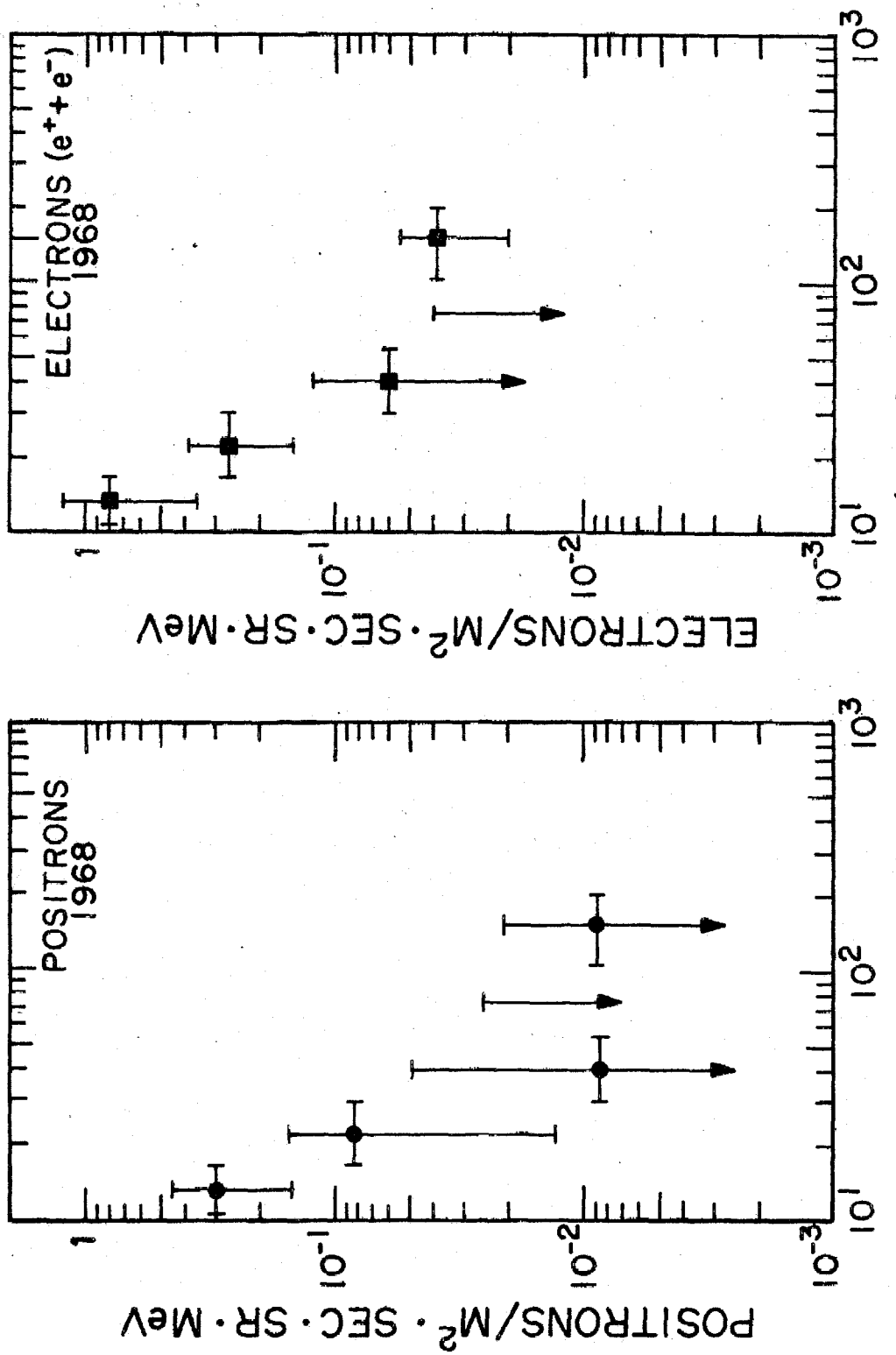

Figure V-1: Primary positron and electron spectra (at 0 g/cm^2) derived from the 1968 observations.

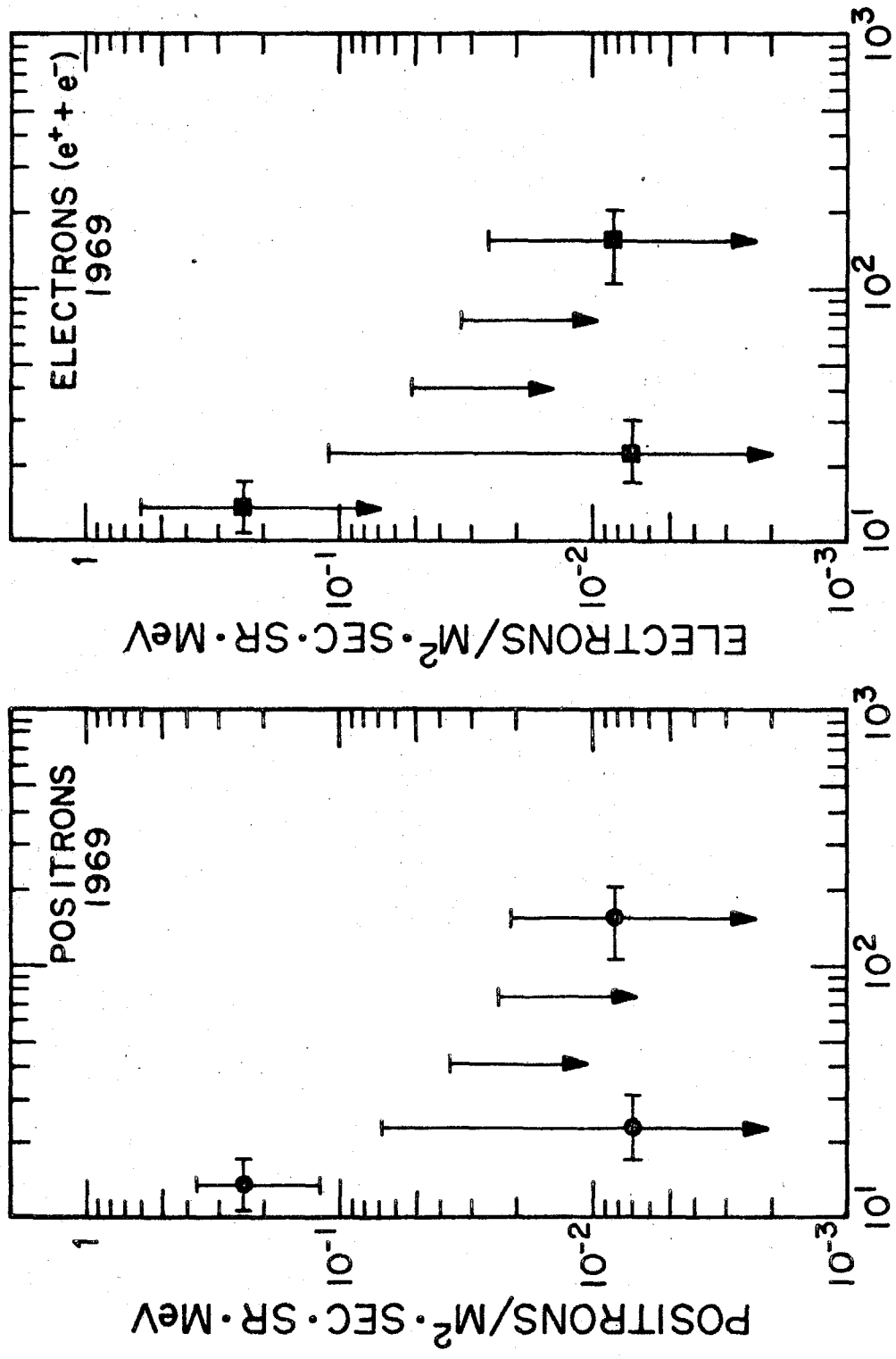

Figure V-2: Primary positron and electron spectra (at 0 g/cm^2) derived from the 1969 observations.

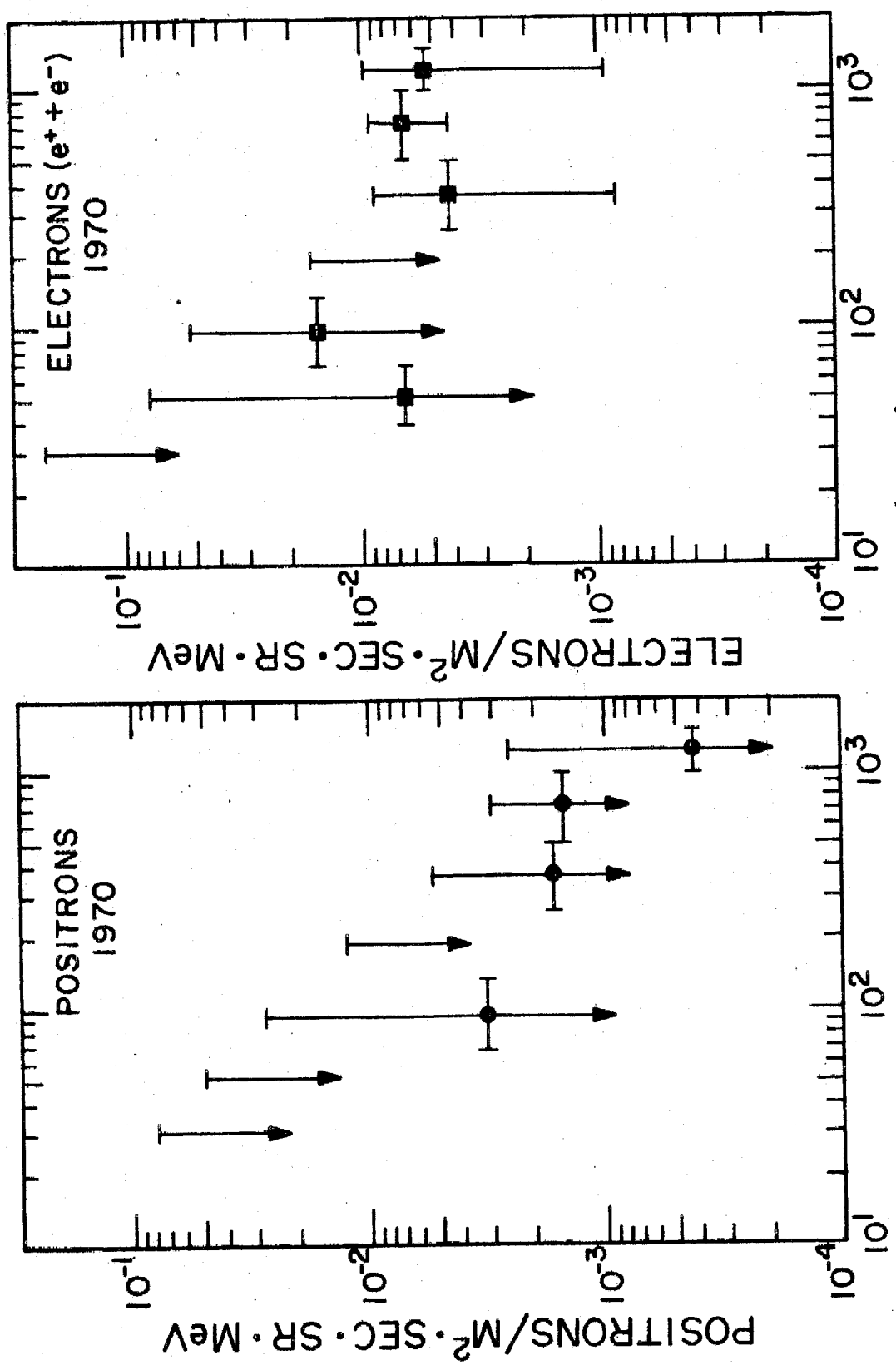

Figure V-3: Primary positron and electron spectra (at 0 g/cm^2) derived from the 1970 observations.

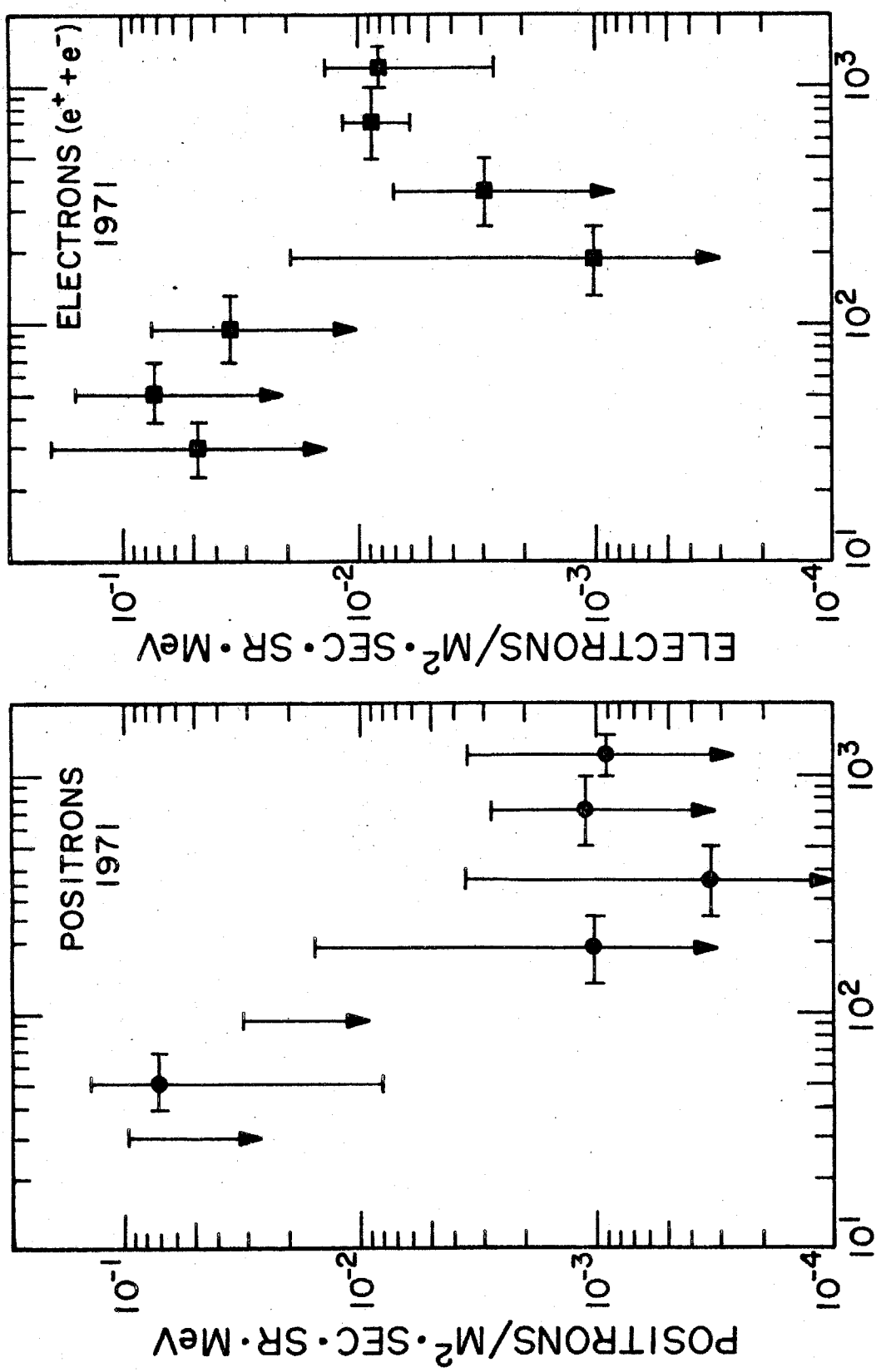

Figure V-4: Primary positron and electron spectra (at 0 g/cm^2) derived from the 1971 observations.

Figure VI-1: Selected near-Earth electron spectra for the period 1965-1971. The Caltech data are shown as filled squares (1968) and filled circles (1971). The Chicago data are represented by open diamonds (Fanselow et al., 1969), open squares (L'Heureux et al., 1972; Schmidt, 1972), and open circles and triangles (Schmidt, 1972). Data from the Goddard Space Flight Center (GSFC) experiment on the IMP-IV satellite are shown as crosses (Simnett and McDonald, 1969).

For clarity the data have been separated into two graphs.

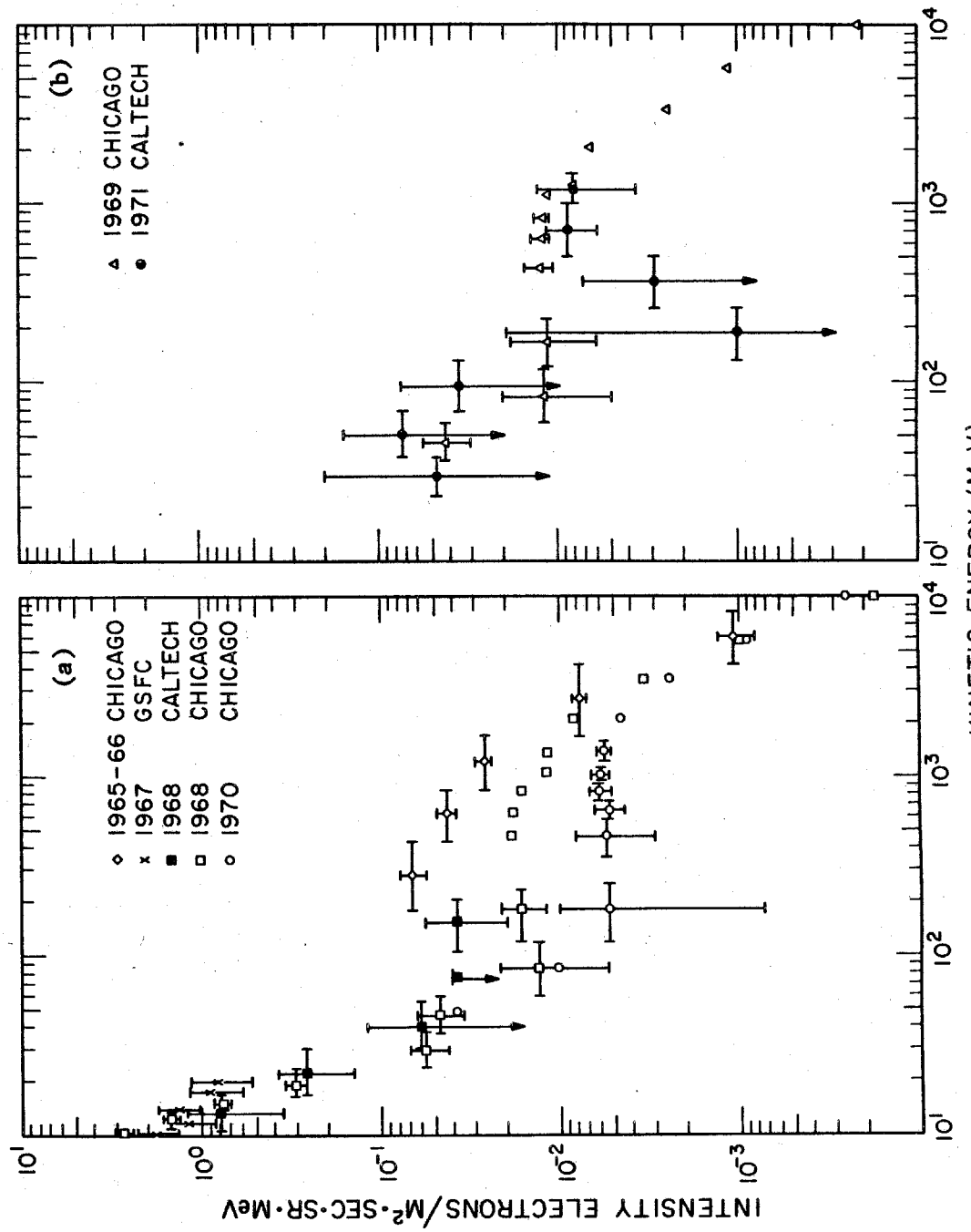

Figure VI-1a and b

Figure VI-2: Illustration of the dependence of the modulated spectrum on the magnitude of the diffusion coefficient. Numerical solutions are calculated using an interstellar electron spectrum of the form

$$j_{\infty}(T) = 2.70 \times 10^{6}\ T^{-2.5}\ \ p/m^{2}\cdot sec\cdot sr\cdot MeV$$

and a diffusion coefficient of the form

$$\kappa(R) \begin{cases} \alpha\ R & R > R_c \\ = \text{constant} & R \leq R_c \end{cases} .$$

Figure VI-2a: Calculated electron intensity at 1 AU versus kinetic energy for R_c = 440 MV.

Figure VI-2b: Contours of constant phase - space density, F, for R_c = 440 MV.

Figure VI-2c: Calculated electron intensity at 1 AU versus kinetic energy for R_c = 100 MV. A $j \propto T^2$ curve (dashed) is shown for comparison.

Figure VI-2d: Contours of constant phase-space density for R_c = 100 MV. Contours of constant ψ (r,T) (defined by equation VI-6) are shown as dashed lines.

Figure VI-2e: Phase-space density contours derived from the <u>diffusion-convection</u> approximation for R_c = 100 MV.

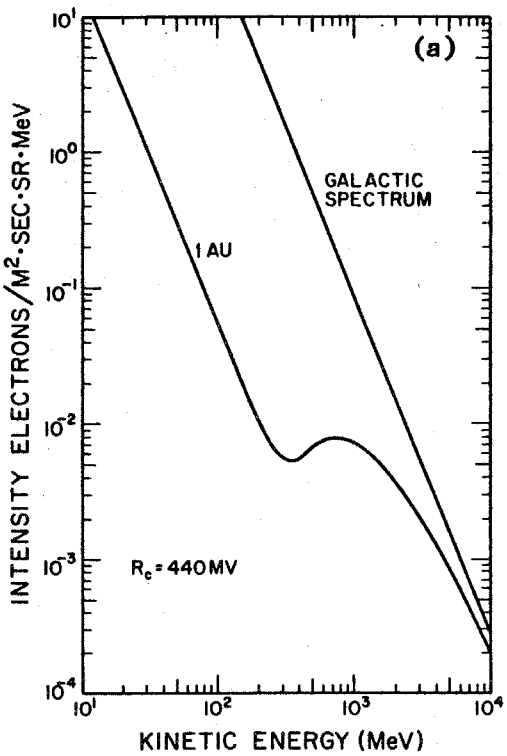

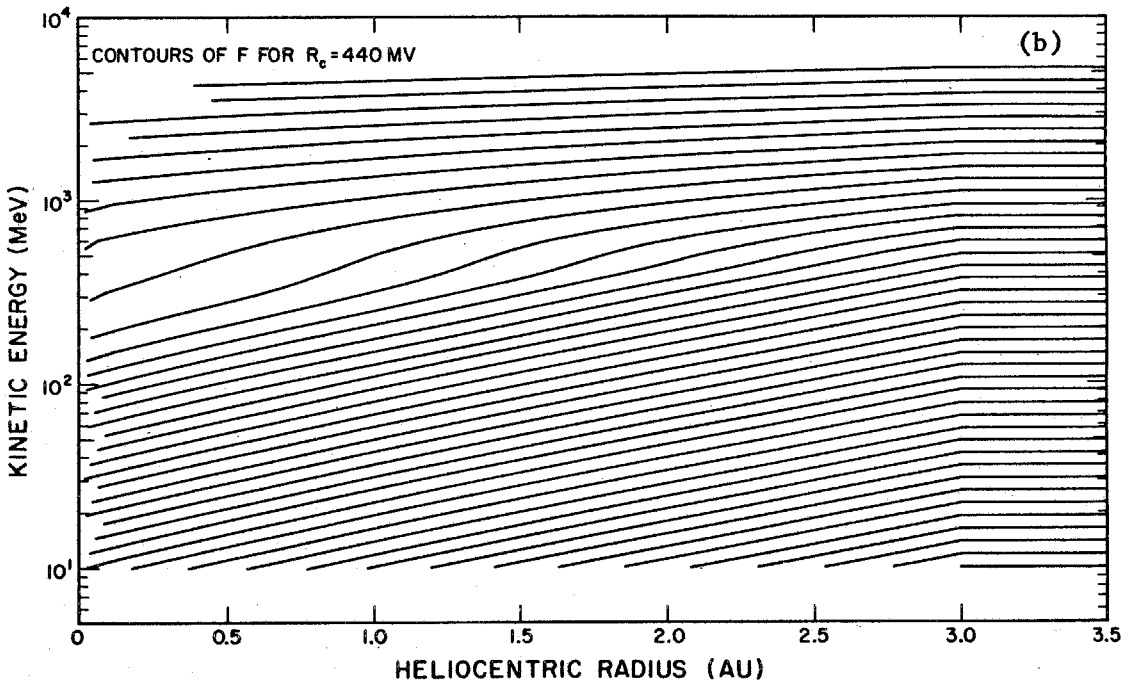

Figure VI-2a and b

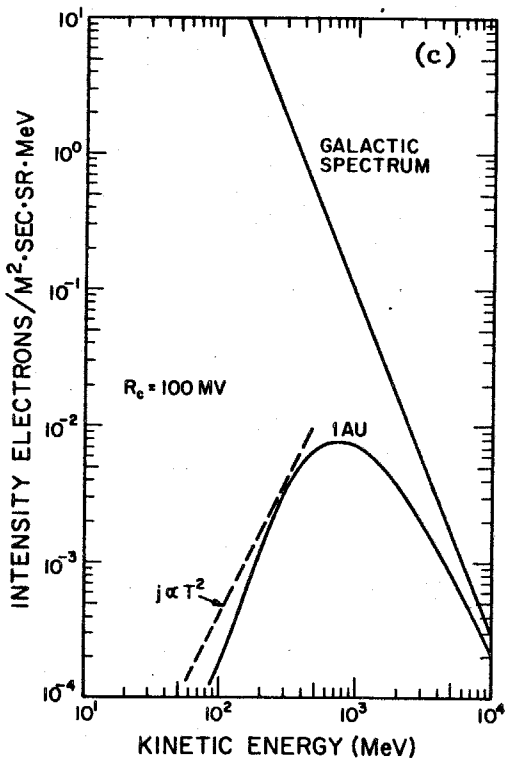

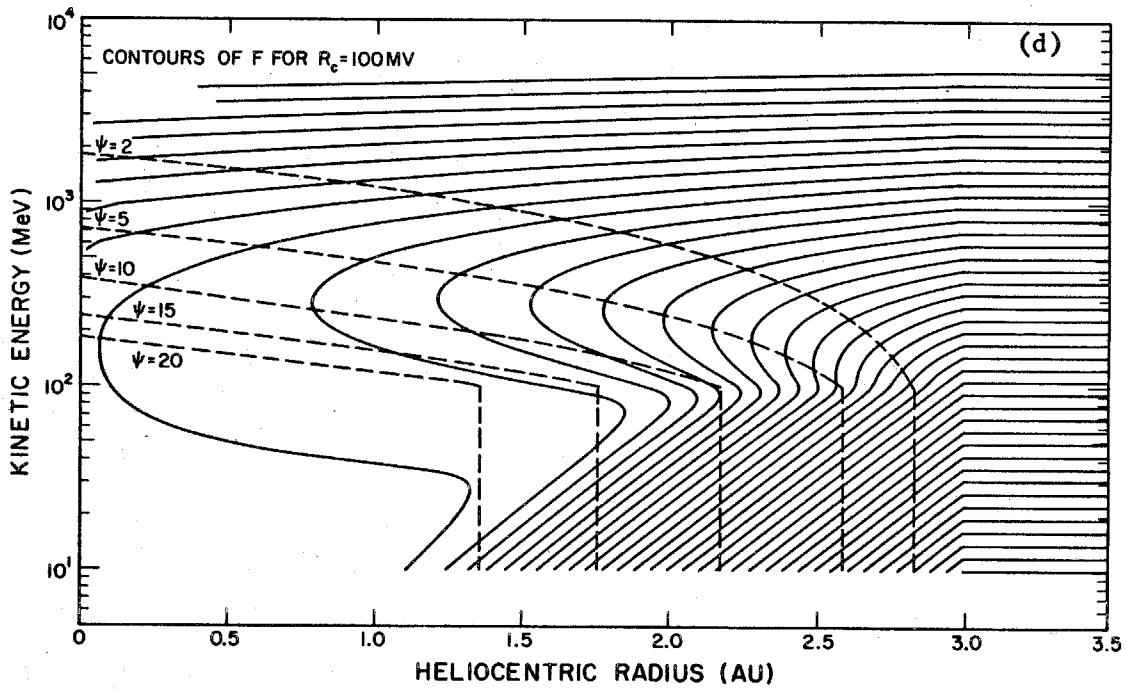

Figure VI-2c and d

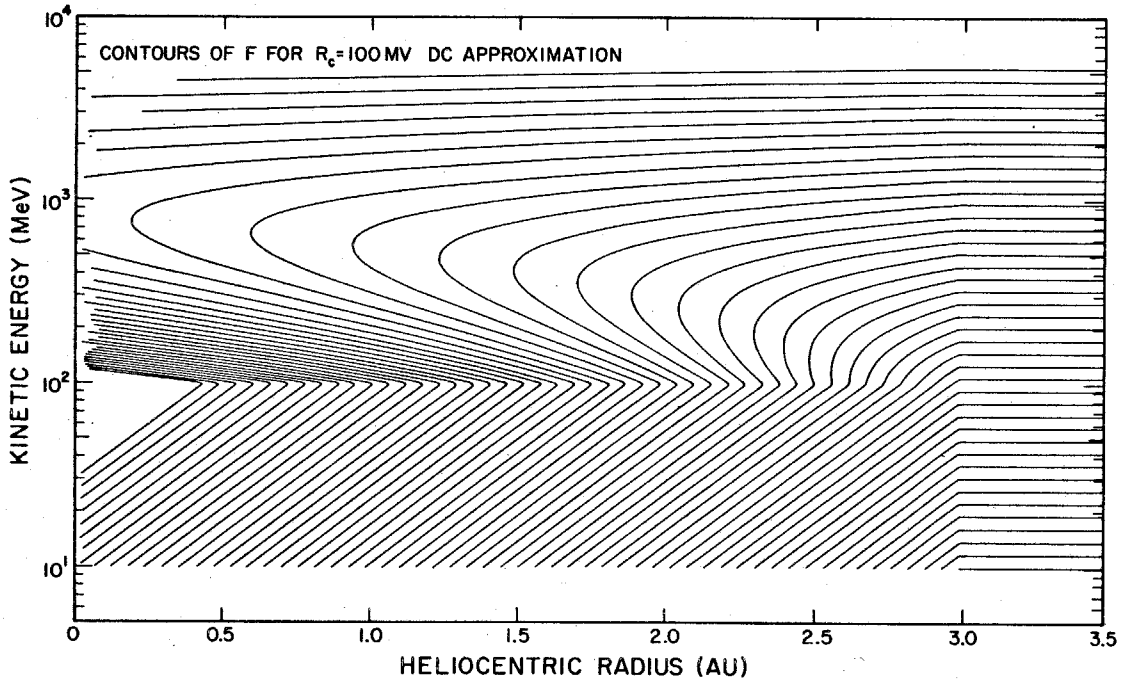
CONTOURS OF F FOR R_c=100 MV DC APPROXIMATION
KINETIC ENERGY (MeV)
10^4
10^3
10^2
10^1
0
0.5
1.0
1.5
2.0
2.5
3.0
3.5
HELIOCENTRIC RADIUS (AU)

Figure VI-2e

Figure VI-3: Comparison of the 1 AU spectra derived from the force-field (FF) approximation, diffusion-convection (DC) approximation, and the numerical (FN) solution of the full transport equation for two different galactic spectra. The diffusion coefficient used in deriving each spectrum is described in the text.

Figure VI-3a: Electron spectra at 1 AU derived from a galactic electron spectrum proposed by Meyer et al. (1971).

Figure VI-3b: Positron spectra at 1 AU derived from a galactic positron spectrum calculated by Ramaty and Lingenfelter (1968).

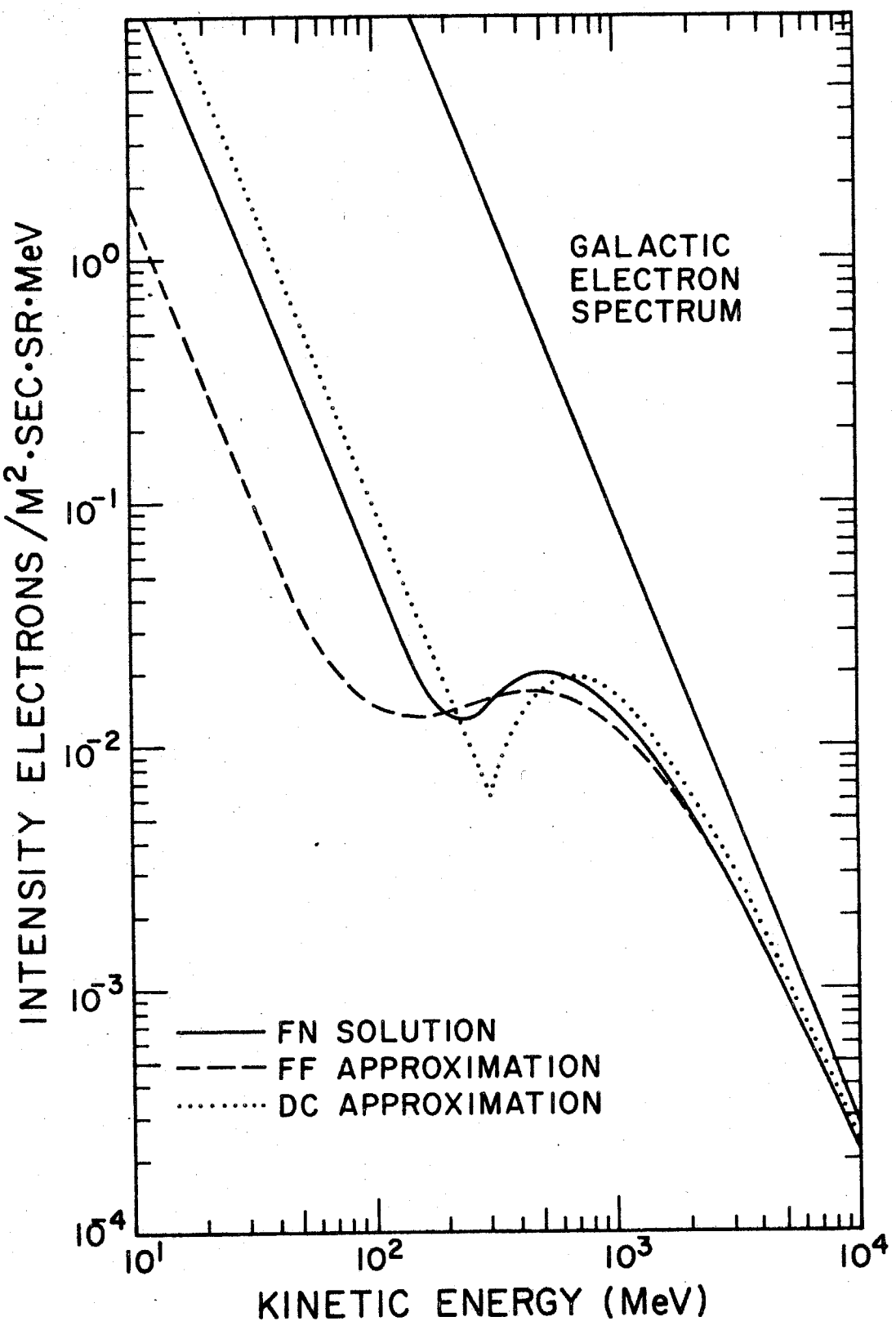
GALACTIC
ELECTRON
SPECTRUM
FN SOLUTION
FF APPROXIMATION
DC APPROXIMATION
INTENSITY ELECTRONS/M².SEC·SR·MeV
KINETIC ENERGY (MeV)
10⁰
10⁻¹
10⁻²
10⁻³
10⁻⁴
10¹
10²
10³
10⁴

Figure VI-3a

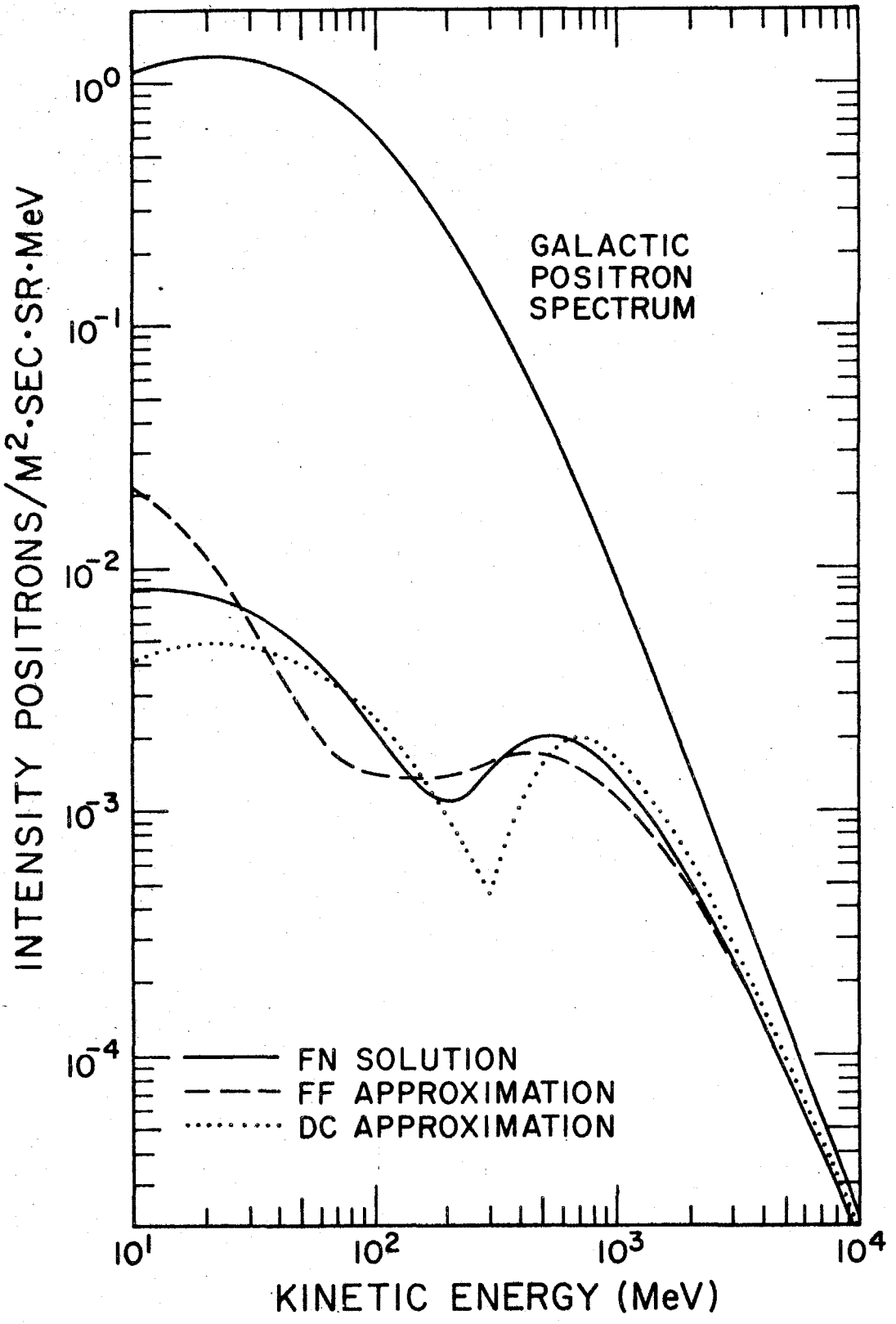
GALACTIC
POSITRON
SPECTRUM
INTENSITY POSITRONS/M²·SEC·SR·MeV
KINETIC ENERGY (MeV)
FN SOLUTION
FF APPROXIMATION
DC APPROXIMATION
10⁰
10⁻¹
10⁻²
10⁻³
10⁻⁴
10¹
10²
10³
10⁴

Figure VI-3b

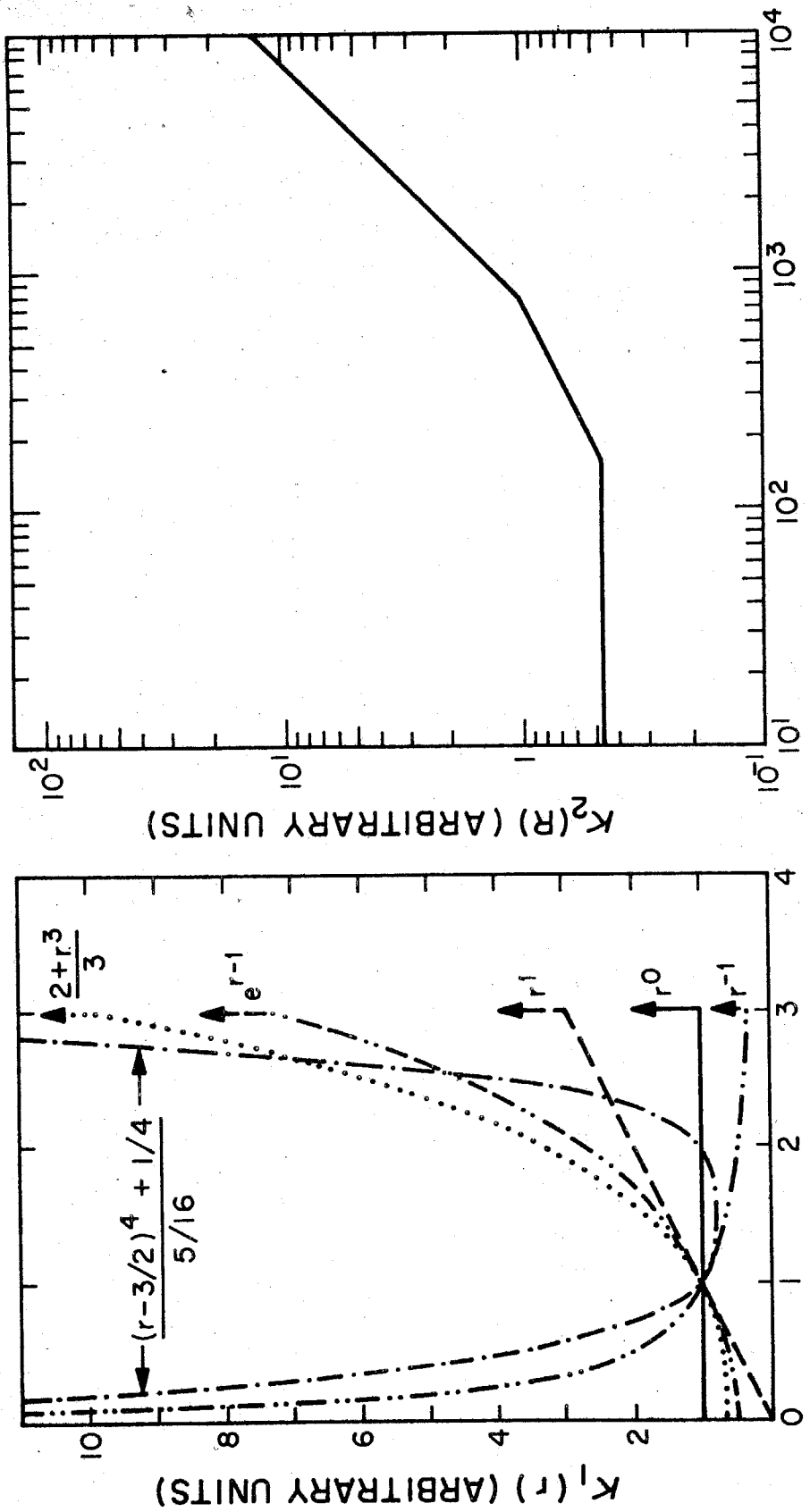

Figure VI-4: Radial and rigidity dependences of the diffusion coefficient used in calculating the numerical solutions of the transport equation shown in Figure VI-5a. A boundary distance of 3 AU has been assumed for convenience.

Figure VI-5: Calculated electron spectra at 1 AU for different forms of $\kappa_1(r)$ and different values of the boundary distance, D. In each calculation the nominal galactic electron spectrum from the analysis of the non-thermal-radio-background data has been used with a power-law extrapolation below ~100 MeV (equation B-12). The rigidity dependence of the diffusion coefficient used is given in Figure VI-4b. The magnitudes of the different radial functions $\kappa_1(r)$ at r = 1 AU have been adjusted so that each calculated spectrum is derived using the same value of

$$\psi(1,R) = \int_1^D \frac{Vdr}{\kappa(r,R)} \quad .$$

The near-Earth electron spectrum observed in 1968 (references in Figure VI-1) is shown for comparison.

Figure VI-5a: The calculated spectra using the 6 different radial dependences of κ shown in Figure VI-4a.

Figure VI-5b: The calculated spectra assuming κ independent of radius with assumed boundary distances of 3, 5, 10, 15, and 30 AU, respectively.

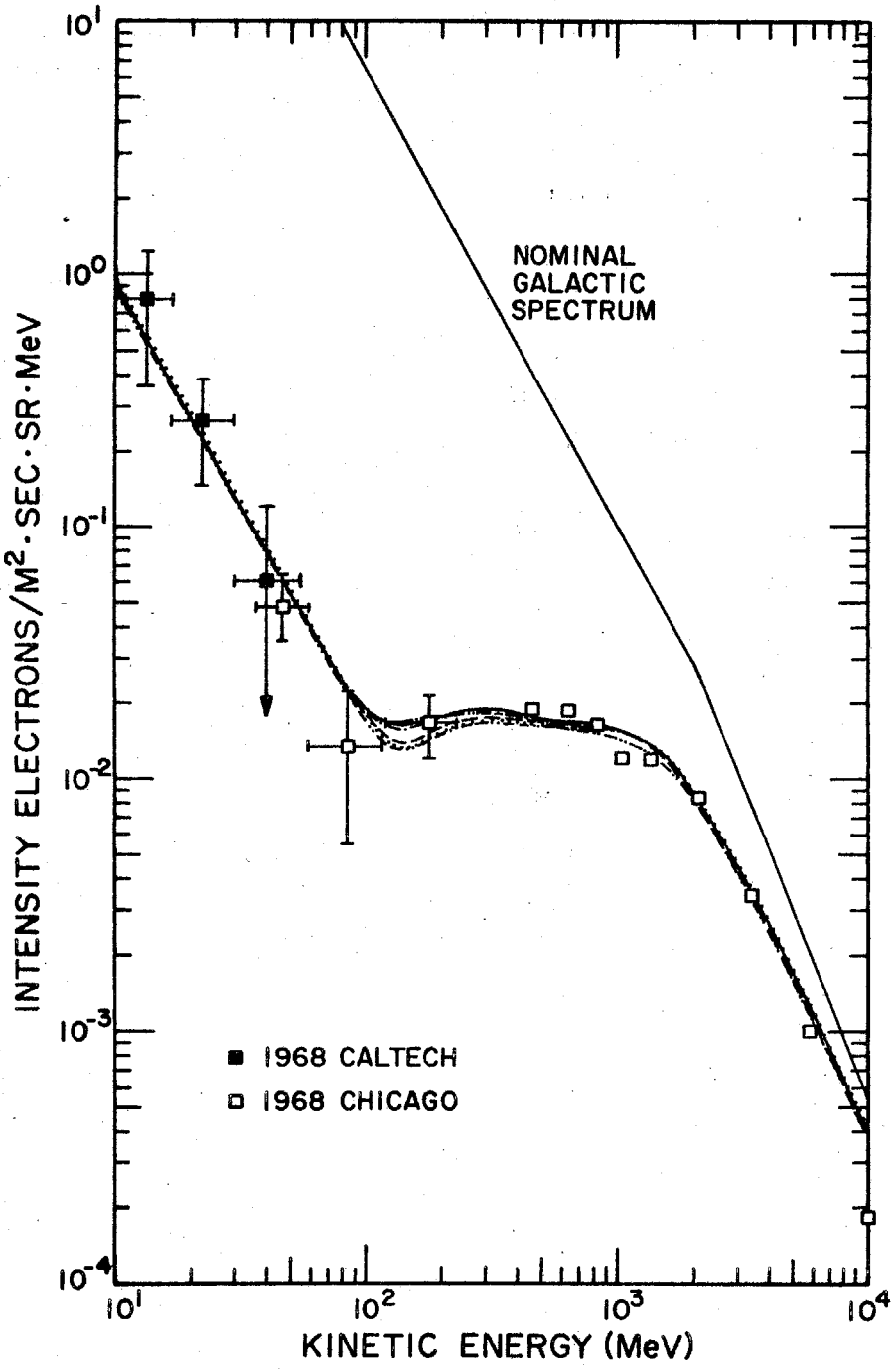
NOMINAL
GALACTIC
SPECTRUM
1968 CALTECH
1968 CHICAGO
INTENSITY ELECTRONS/M^2·SEC·SR·MeV
KINETIC ENERGY (MeV)
10^1
10^0
10^{-1}
10^{-2}
10^{-3}
10^{-4}
10^1
10^2
10^3
10^4

Figure VI-5a

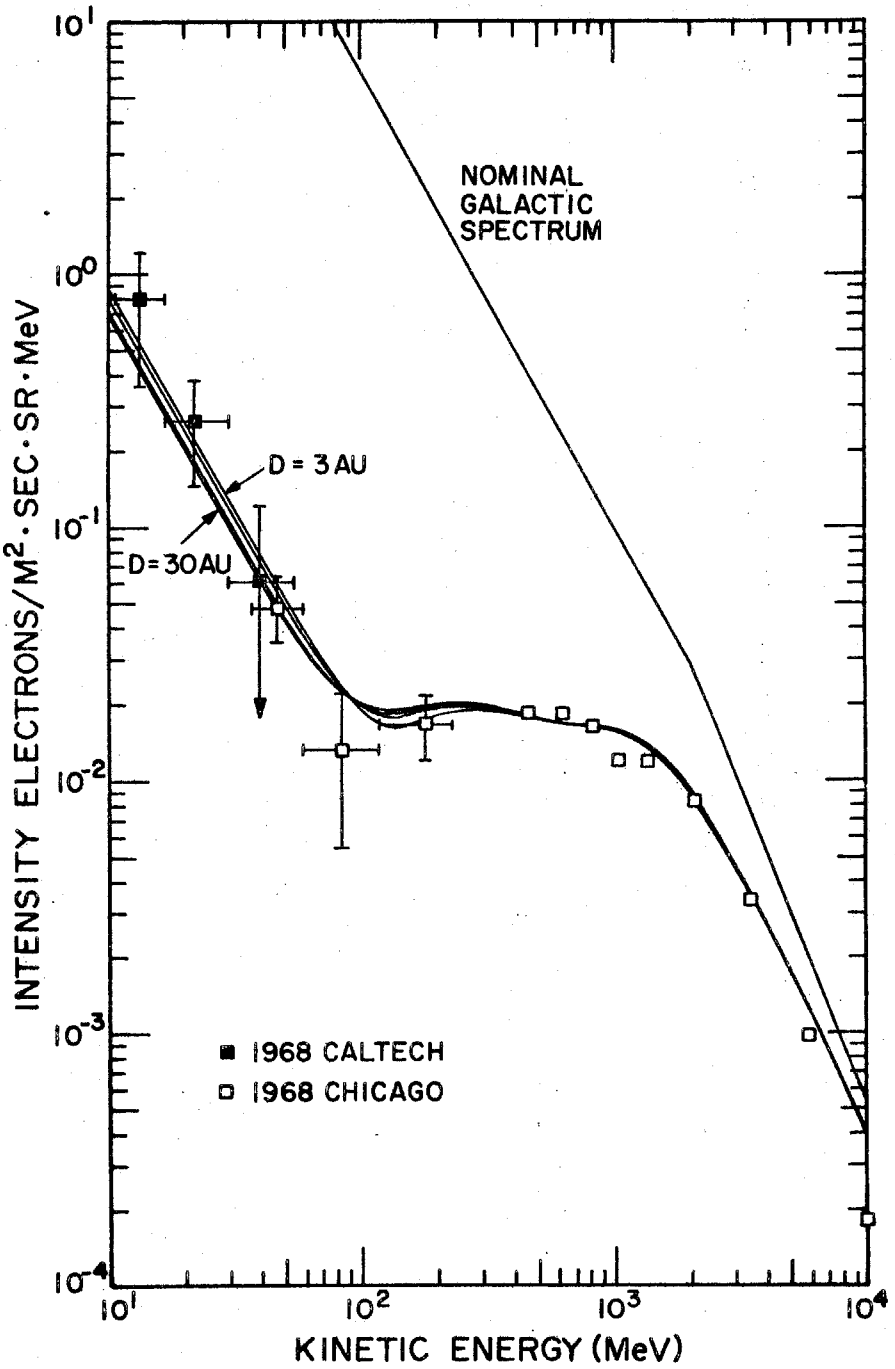
NOMINAL
GALACTIC
SPECTRUM
D = 3 AU
D = 30 AU
1968 CALTECH
1968 CHICAGO
INTENSITY ELECTRONS/M² · SEC · SR · MeV
KINETIC ENERGY (MeV)
10¹
10⁰
10⁻¹
10⁻²
10⁻³
10⁻⁴
10¹
10²
10³
10⁴

Figure VI-5b

Figure VI-6: Illustration of a calculation of the energy loss of positrons in diffusing from the boundary to 1 AU. The assumed unmodulated spectra are shown as solid lines. The corresponding near-Earth spectra, representing numerical solutions of the transport equation, are shown as dotted lines. The dashed curve indicates the galactic positron spectrum derived by Ramaty and Lingenfelter (1968). The diffusion coefficient used is independent of radius within a boundary of 3 AU; the rigidity dependence is given by equation VI-13.

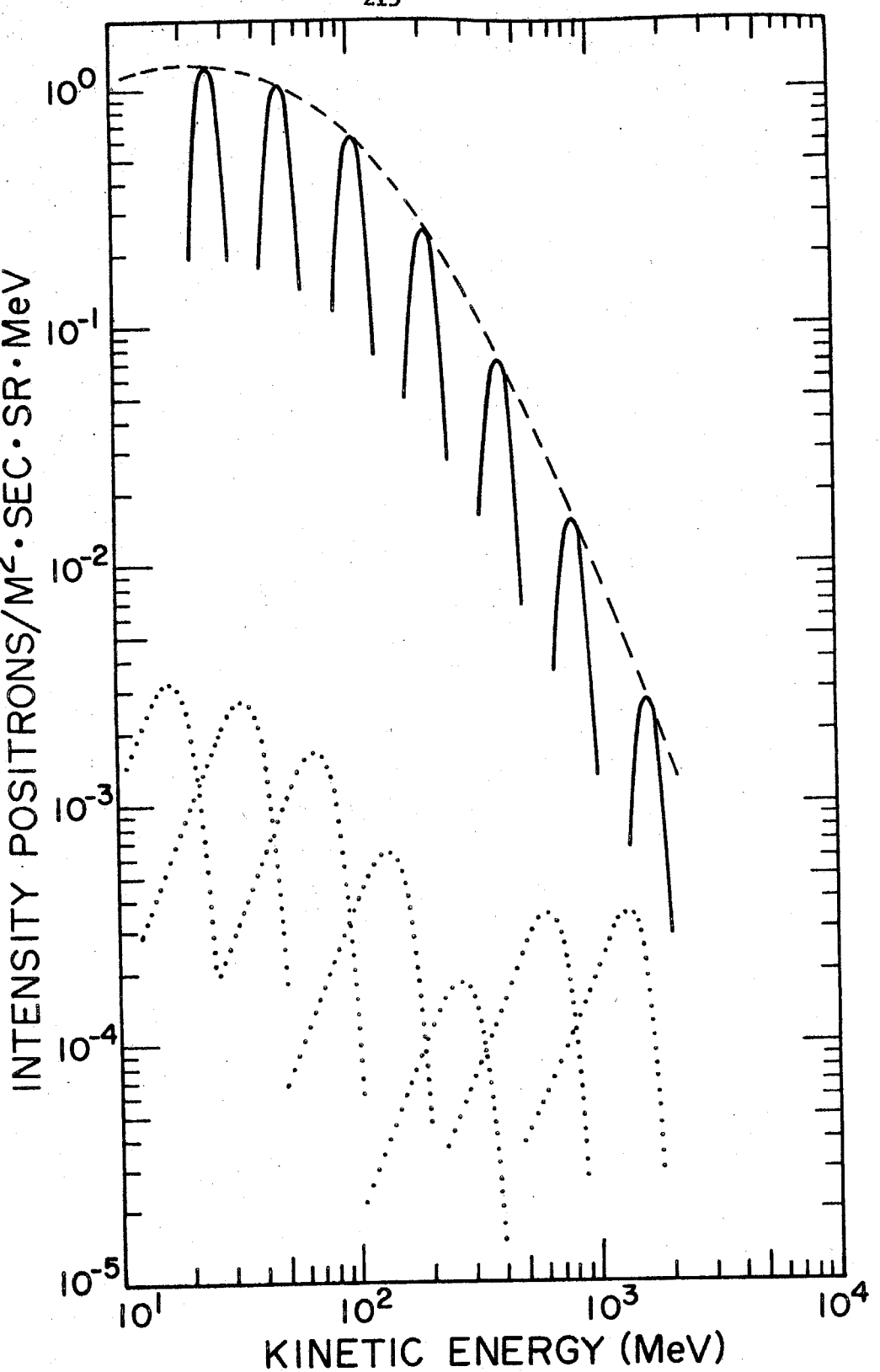
INTENSITY POSITRONS/M^2 • SEC • SR • MeV
10^0
10^{-1}
10^{-2}
10^{-3}
10^{-4}
10^{-5}
10^1
10^2
10^3
10^4
KINETIC ENERGY (MeV)

Figure VI-6

Figure VI-7: Calculated electron spectra at 1 AU for a diffusion coefficient of the form:

$$\kappa(R) \propto \begin{cases} R^{1} & R > R_c = 750 \text{ MV} \\ R^{1/2} & R \leq R_c \end{cases}$$

(The complete description of the diffusion coefficient used is given by equation VI-30 with parameters of Table VI-2 for 1968.) Both the numerical solution (FN) of the full transport equation and the diffusion convection approximate solution (DC) are shown. The positions of the relative "peaks" discussed in the text are shown. The values of these peak locations are:

$T_1^{DC} = 1083$ MeV (Eq. VI-18, b = 1)

$T_{1/2}^{DC} = 391$ MeV (Eq. VI-18, b = 1/2)

$T_1^{FF} = 722$ MeV (Eq. VI-22)

$T_{1/2} = 261$ MeV (Eq. VI-24)

The near-Earth electron spectrum observed in 1968 (references in Figure VI-1) is shown for comparison.

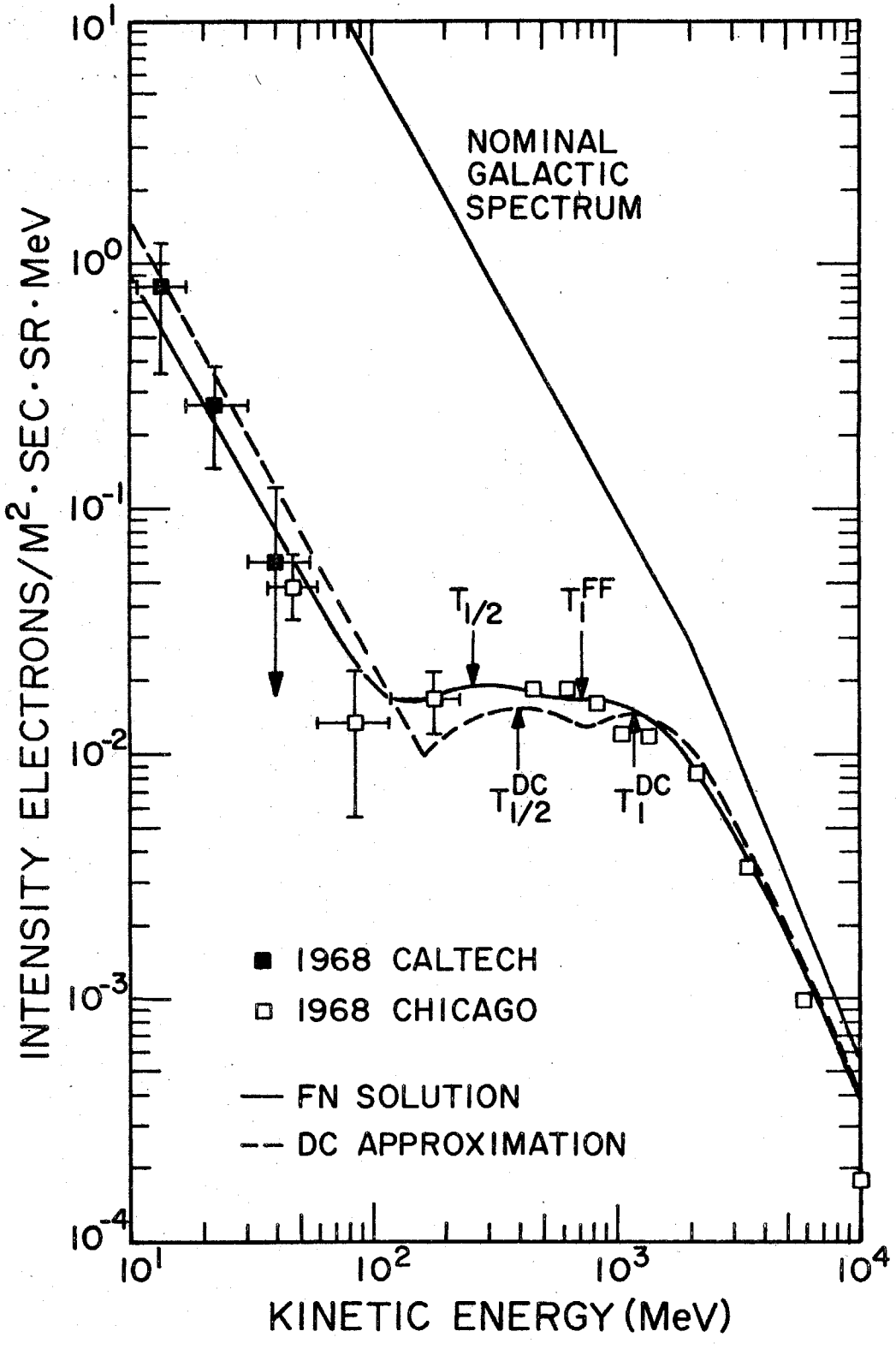
NOMINAL
GALACTIC
SPECTRUM
$T_{1/2}$
T_1^{FF}
$T_{1/2}^{DC}$
T_1^{DC}
1968 CALTECH
1968 CHICAGO
FN SOLUTION
DC APPROXIMATION
INTENSITY ELECTRONS/M^2·SEC·SR·MeV
KINETIC ENERGY (MeV)
10^1
10^0
10^{-1}
10^{-2}
10^{-3}
10^{-4}
10^1
10^2
10^3
10^4

Figure VI-7

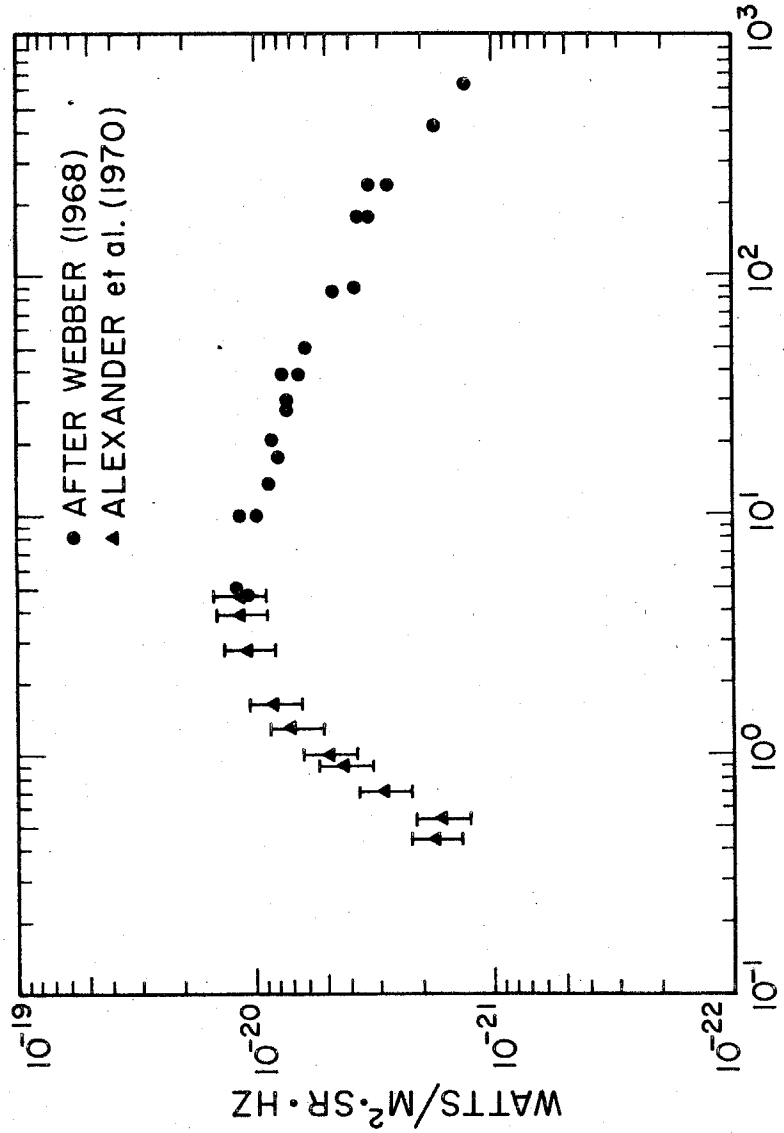

Figure VI-8: The frequency spectrum of the non-thermal-radio background in the galactic anticenter direction.

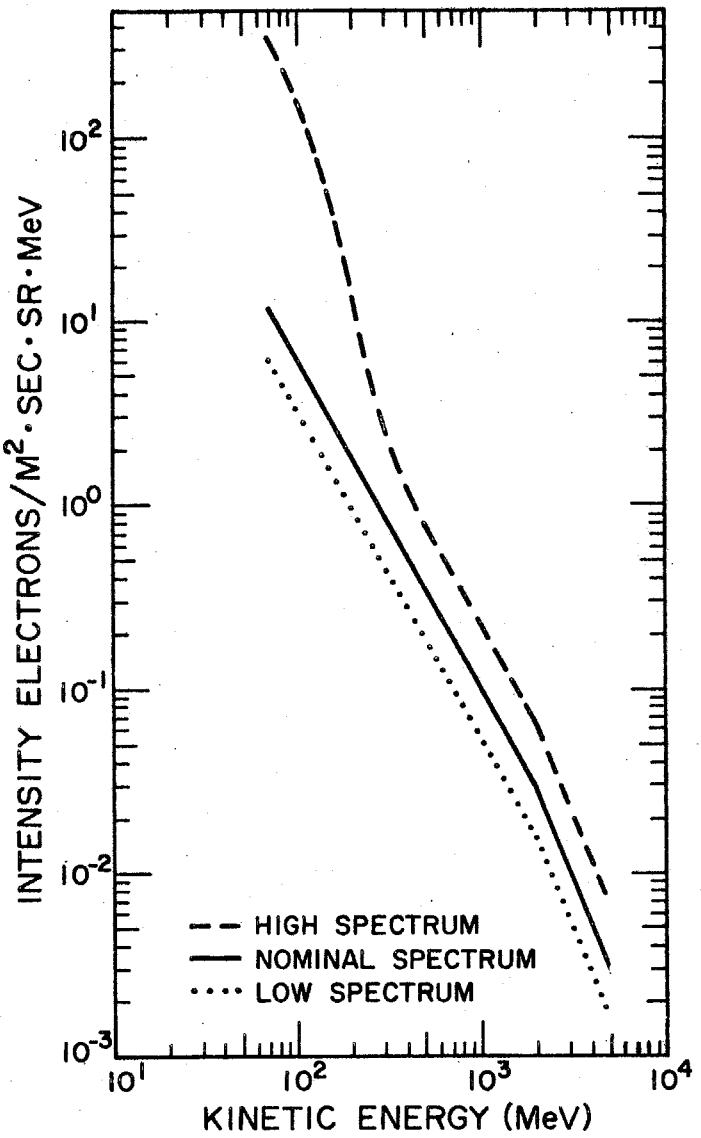

Figure VI-9: Interstellar electron spectra derived from the non-thermal-radio-background data. The high and low spectra reflect the discussed range of galactic parameters. (Appendix B).

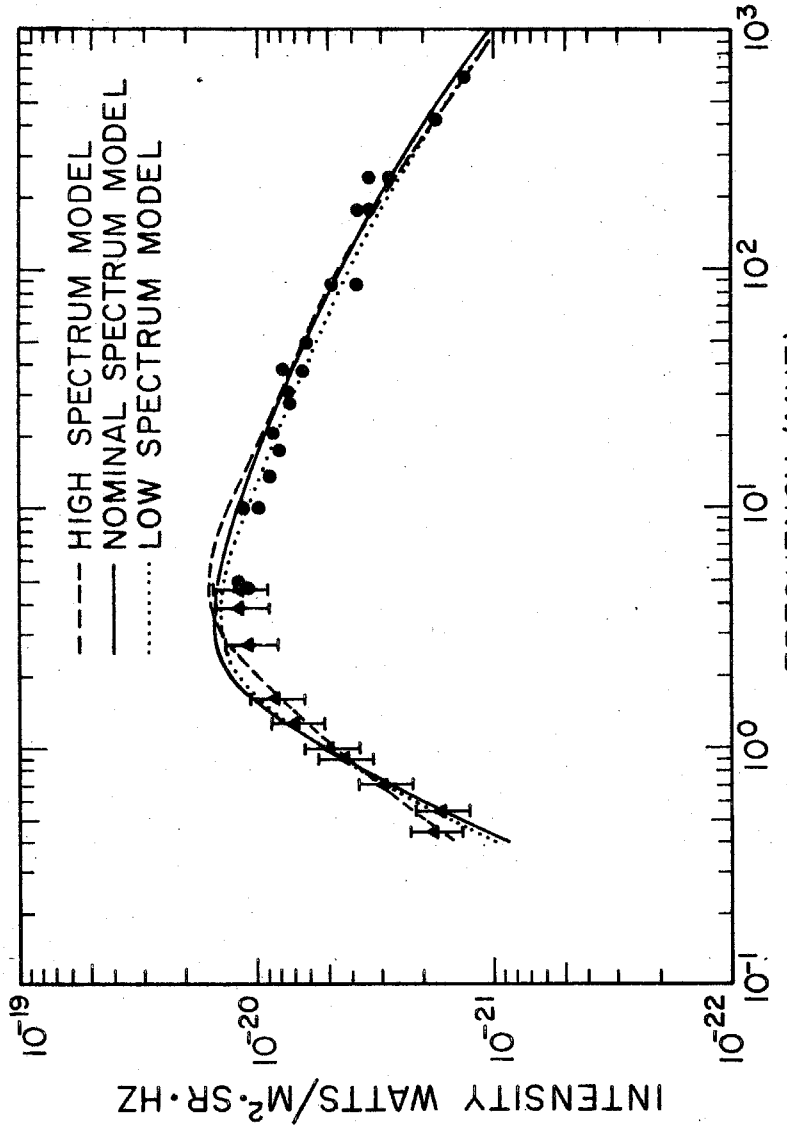

Figure VI-10: Calculated radio spectra corresponding to the three interstellar electron spectra of Figure VI-9. In each calculation the different galactic parameters of Table B-3 were used. References for the observed data (circles and triangles) are given in Figure VI-8.

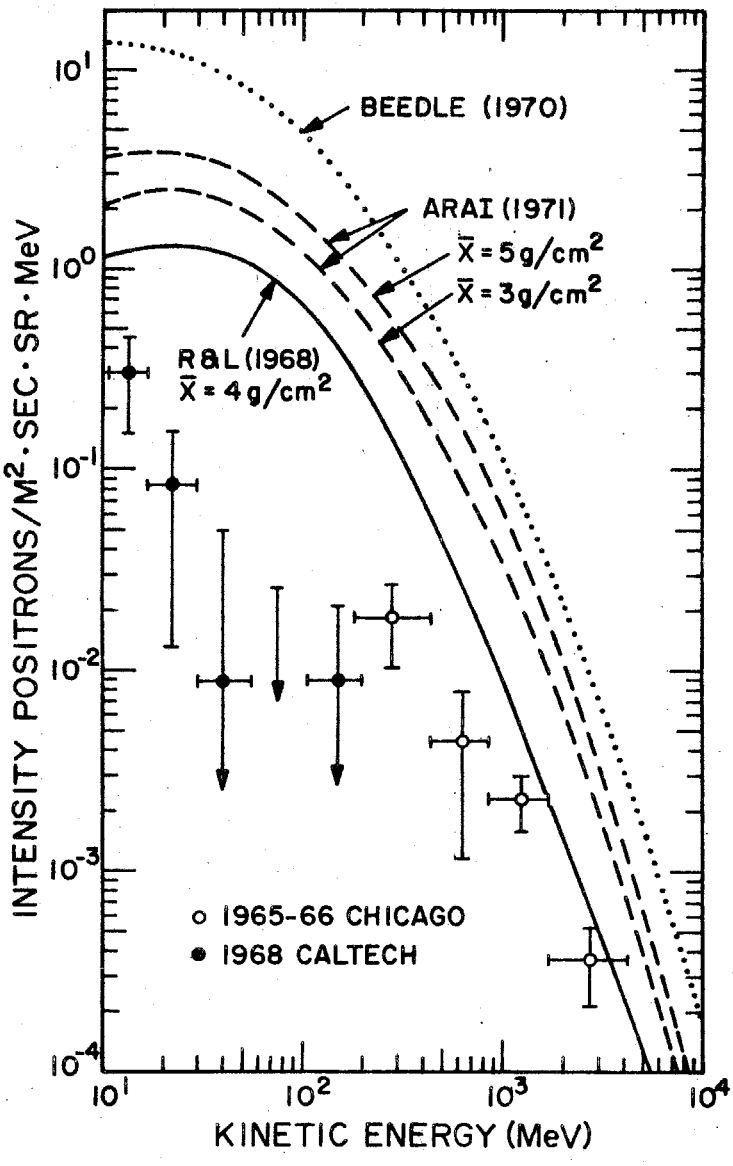

Figure VI-11: Interstellar positron spectra calculated from galactic nuclear collisions by different investigators. The near-Earth spectra measured in 1965-66 (Fanselow et al., 1969) and 1968 (Caltech) are shown for comparison.

Figure VI-12a-e: Electron modulation parameters, $\psi(1,T)$, for the period 1965-1971. The data points are calculated from the DC approximation using the near-Earth electron data shown in Figure VI-1 and the calculated galactic electron spectra of Figure VI-9 (open circles - nominal galactic spectrum; upper filled circles - high spectrum; lower filled circles - low spectrum). The dashed lines indicate the approximate range of ψ from the possible range of galactic spectra. In each figure the solid line represents the modulation parameter used (together with the nominal galactic electron spectrum) in deriving a numerical solution of the transport equation in agreement with the observed near-Earth spectra. The dotted lines in Figures VI-12a,b, and c correspond to limiting modulation parameter curves from which acceptable numerical solutions (using the same nominal galactic electron spectrum) can also be derived.

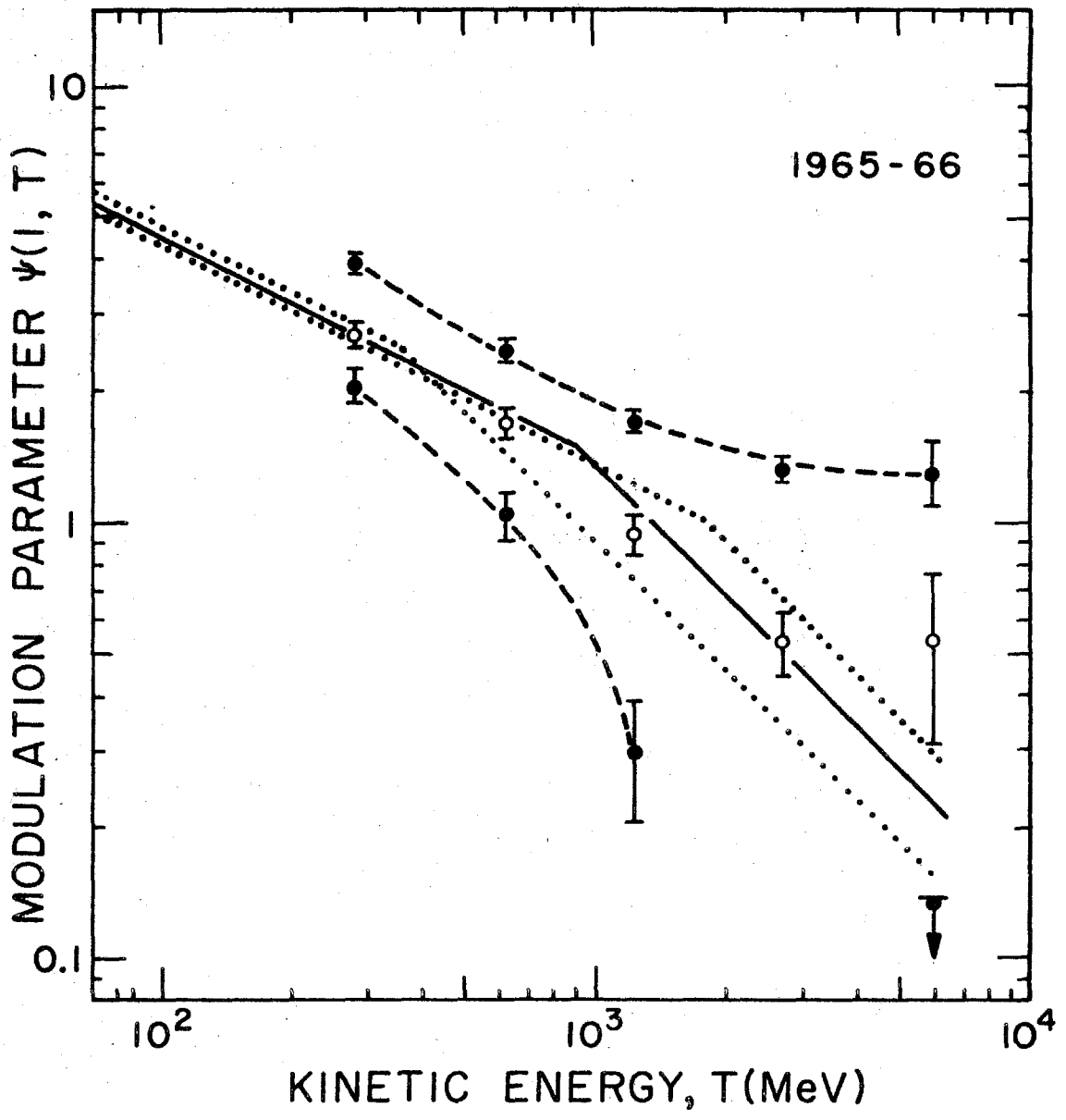

Figure VI-12a

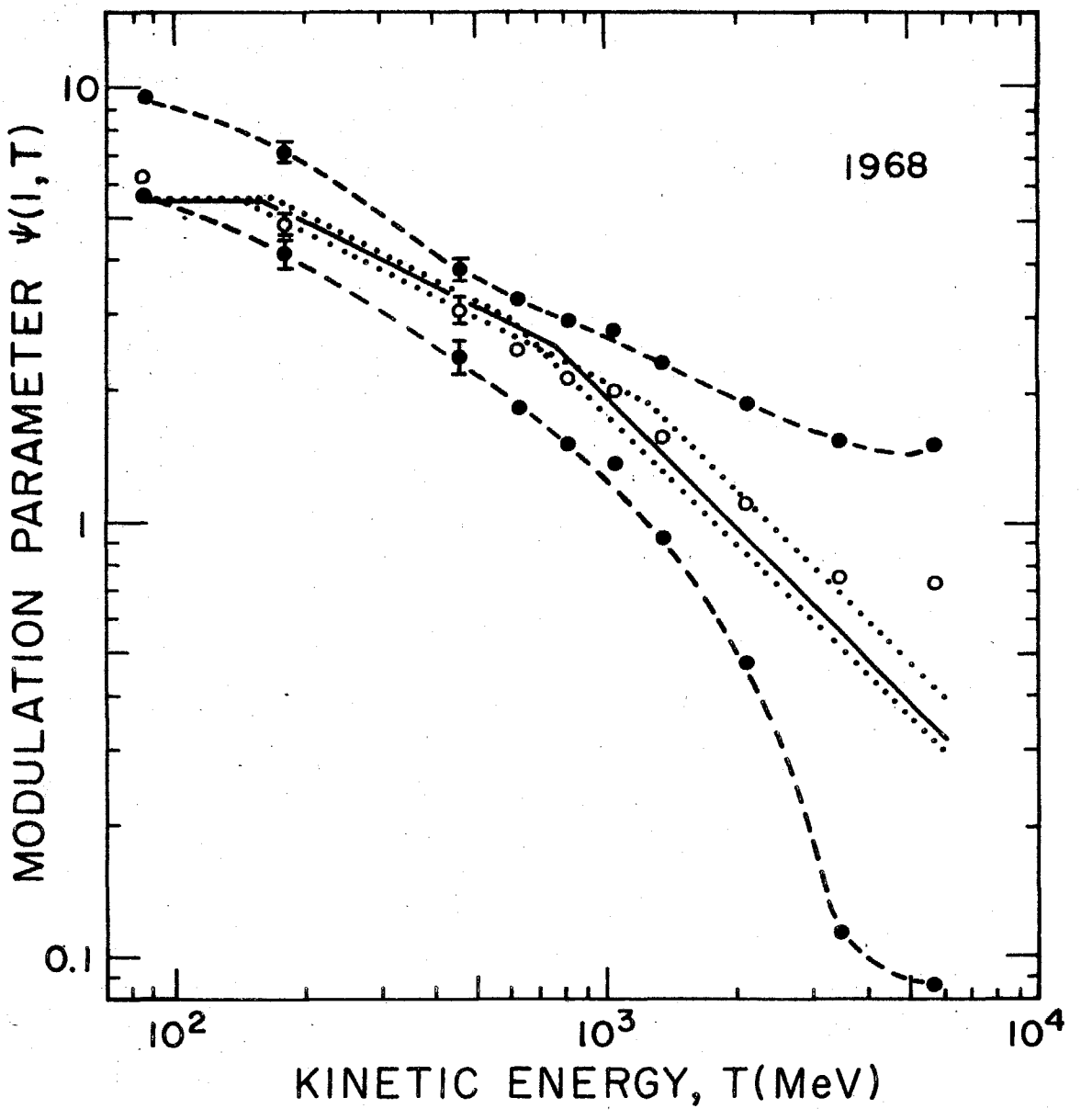

Figure VI-12b

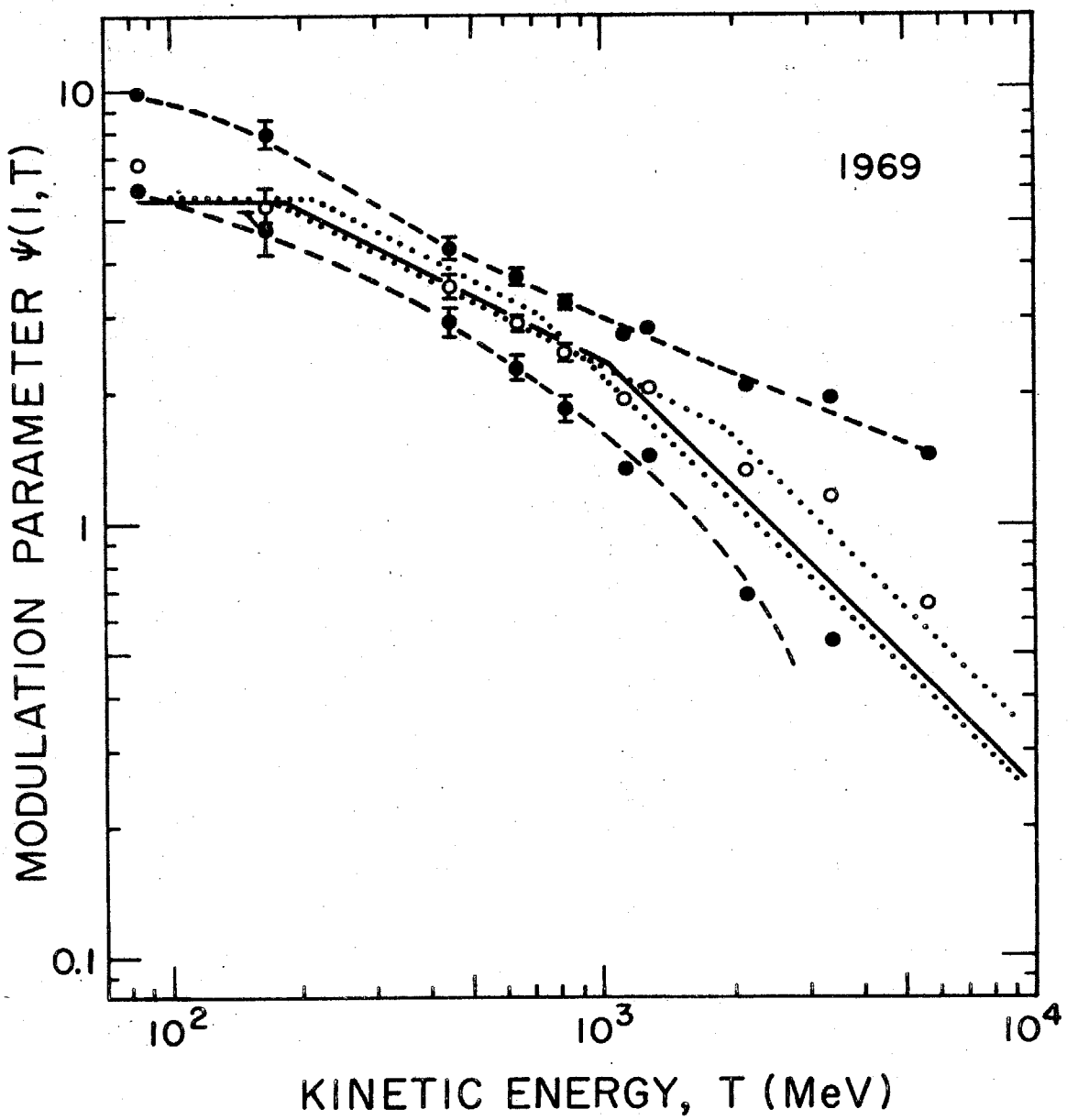

Figure VI-12c

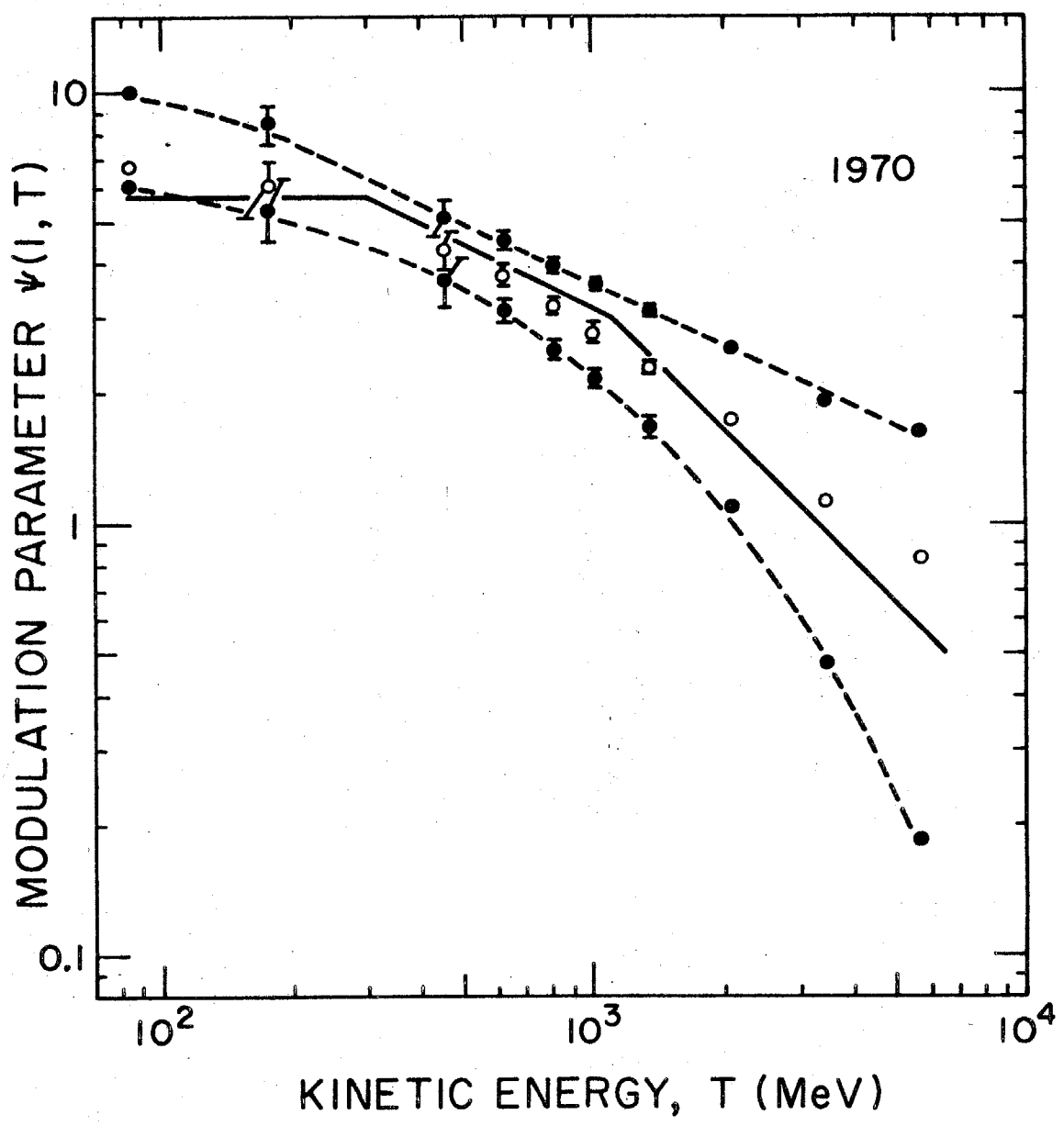

Figure VI-12d

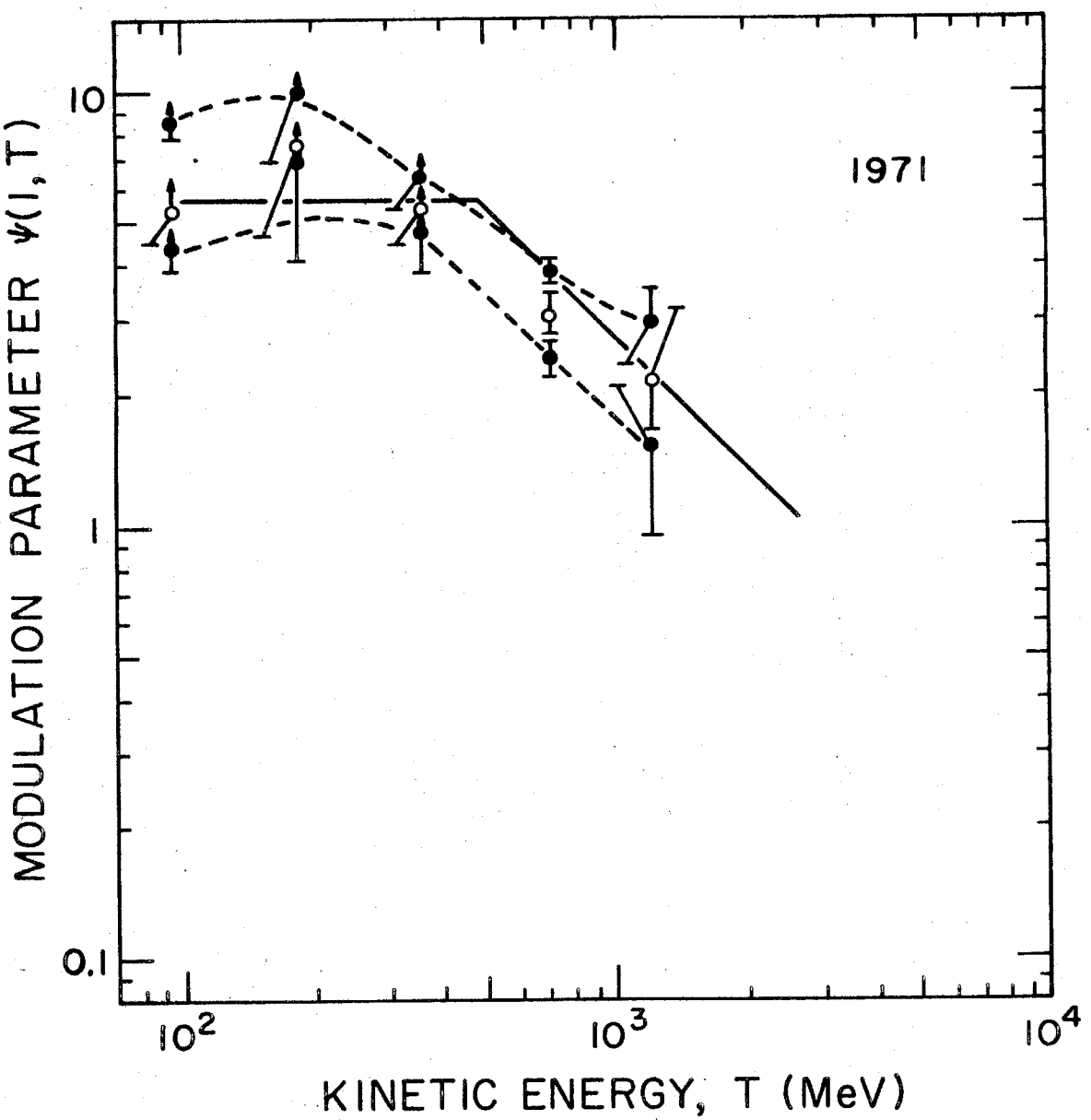

Figure VI-12e

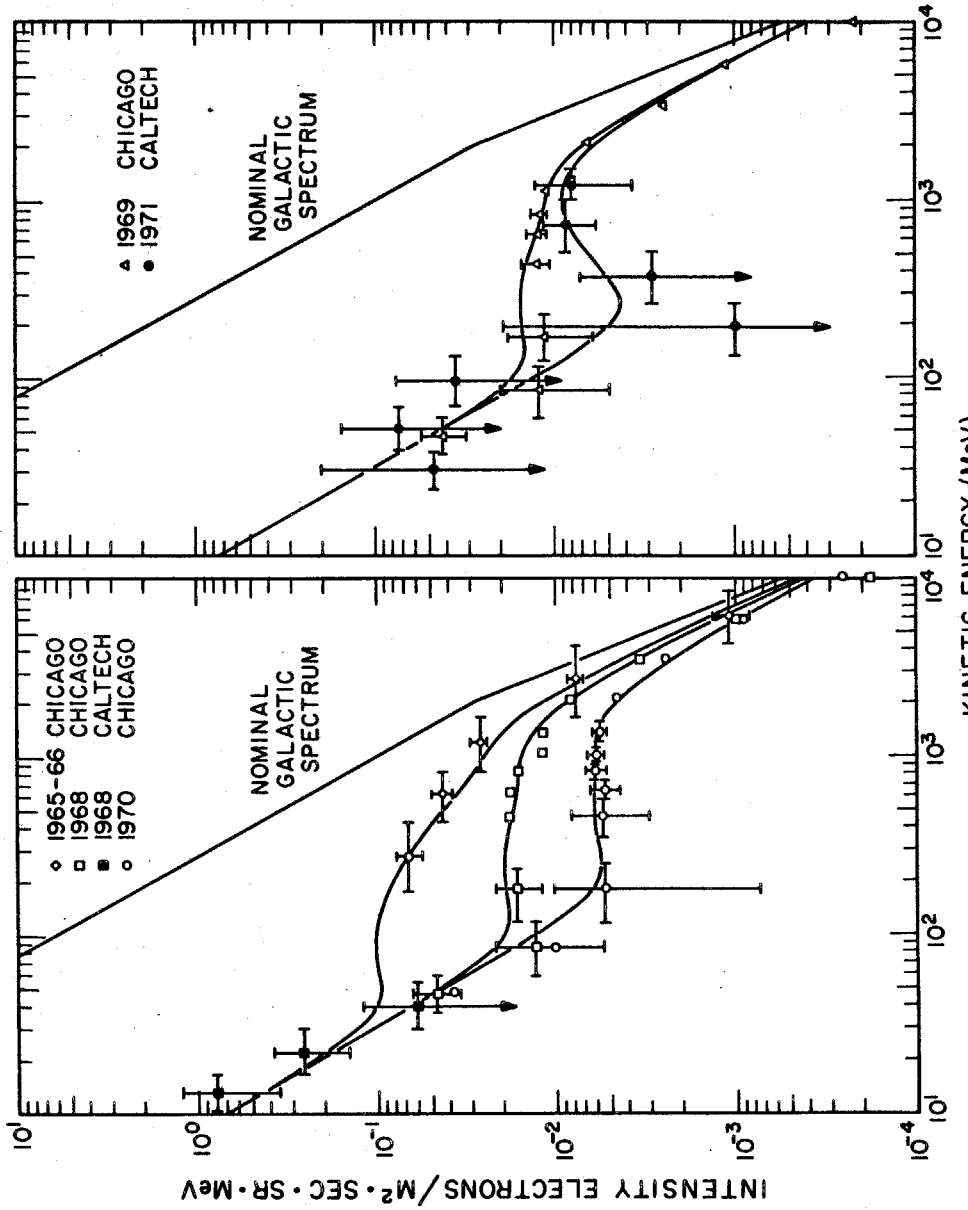

Figure VI-13: Calculated and measured electron spectra at 1 AU for the period 1965-1971. The observed data are from Figure VI-1. The smooth curves represent numerical solutions of the transport equation using the nominal interstellar electron spectrum (Figure VI-9) and the diffusion coefficient defined by equation VI-30 with the parameters listed in Table VI-2.

Figure VI-14: Positron modulation parameters, $\psi(1,T)$, for the period 1965-1971. The data points refer to the $\psi(1,T)$ calculated from the DC approximation using the spectra observed near Earth (1965-66, Fanselow et al., 1969; 1968-1971, Caltech) and the interstellar positron spectra of Ramaty and Lingenfelter (1968) and Beedle (1970). Above ~100 MeV the solid and dashed lines are the electron modulation parameters from Figure VI-12. In Figure VI-14b the modulation parameter represented by the solid line was used to derive the numerical solutions of the transport equation shown in Figure VI-16a and b. The dotted lines in Figure VI-14b correspond to the possible range of positron modulation parameters which was used to derive the range of the interstellar electron spectrum at low energies ($\lesssim$50 MeV) shown in Figure VI-17.

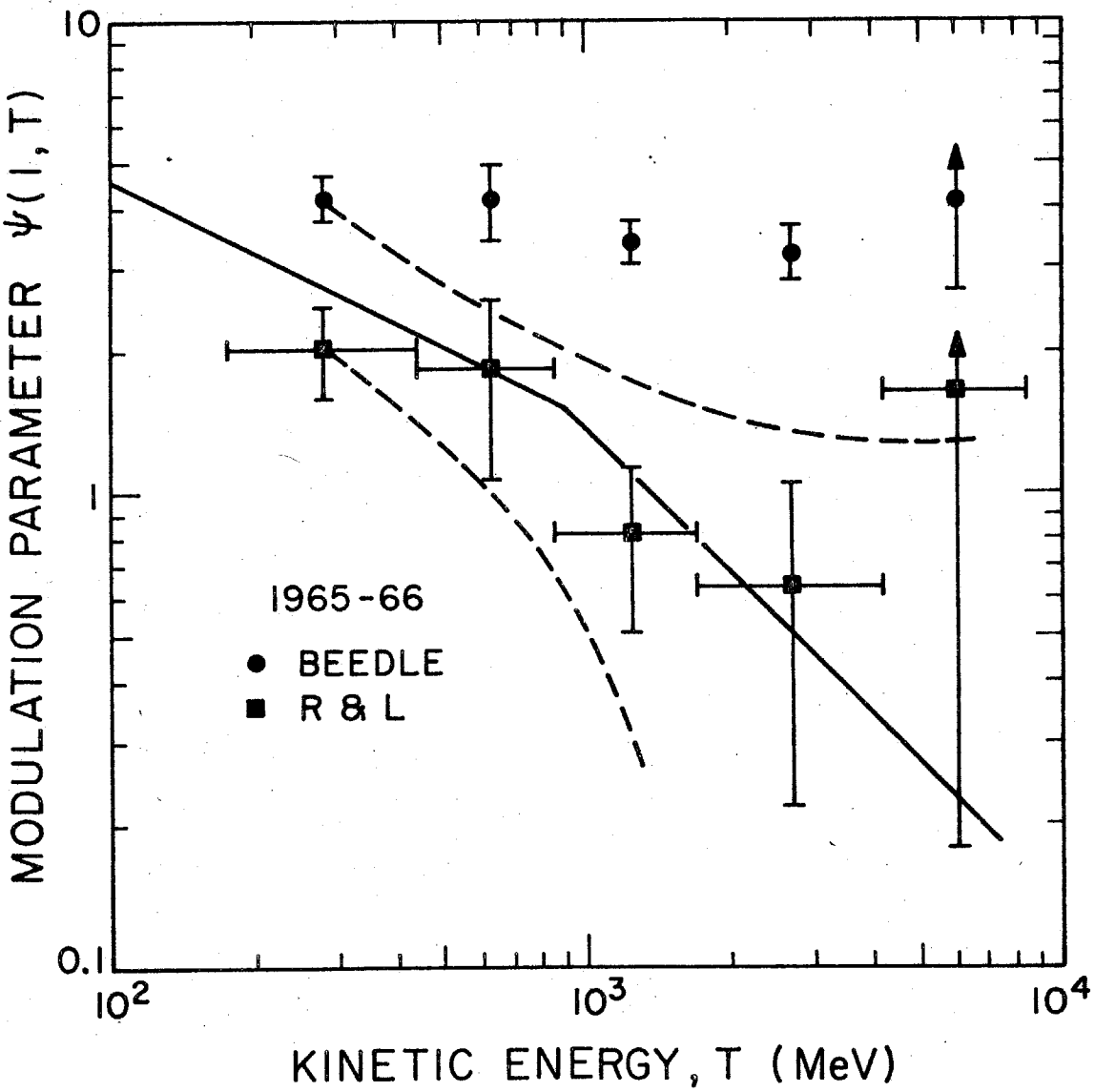

Figure VI-14a

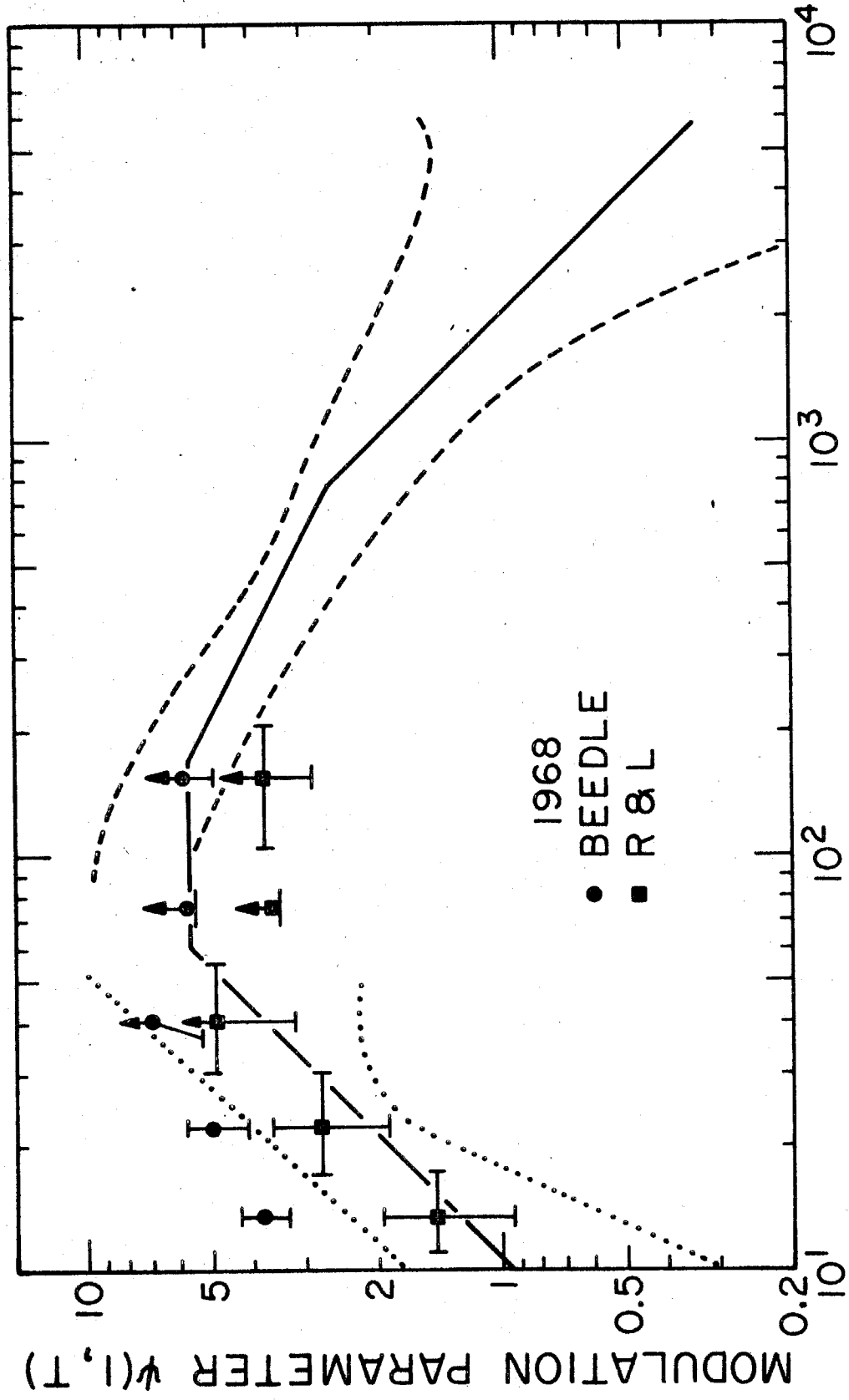

Figure VI-14b

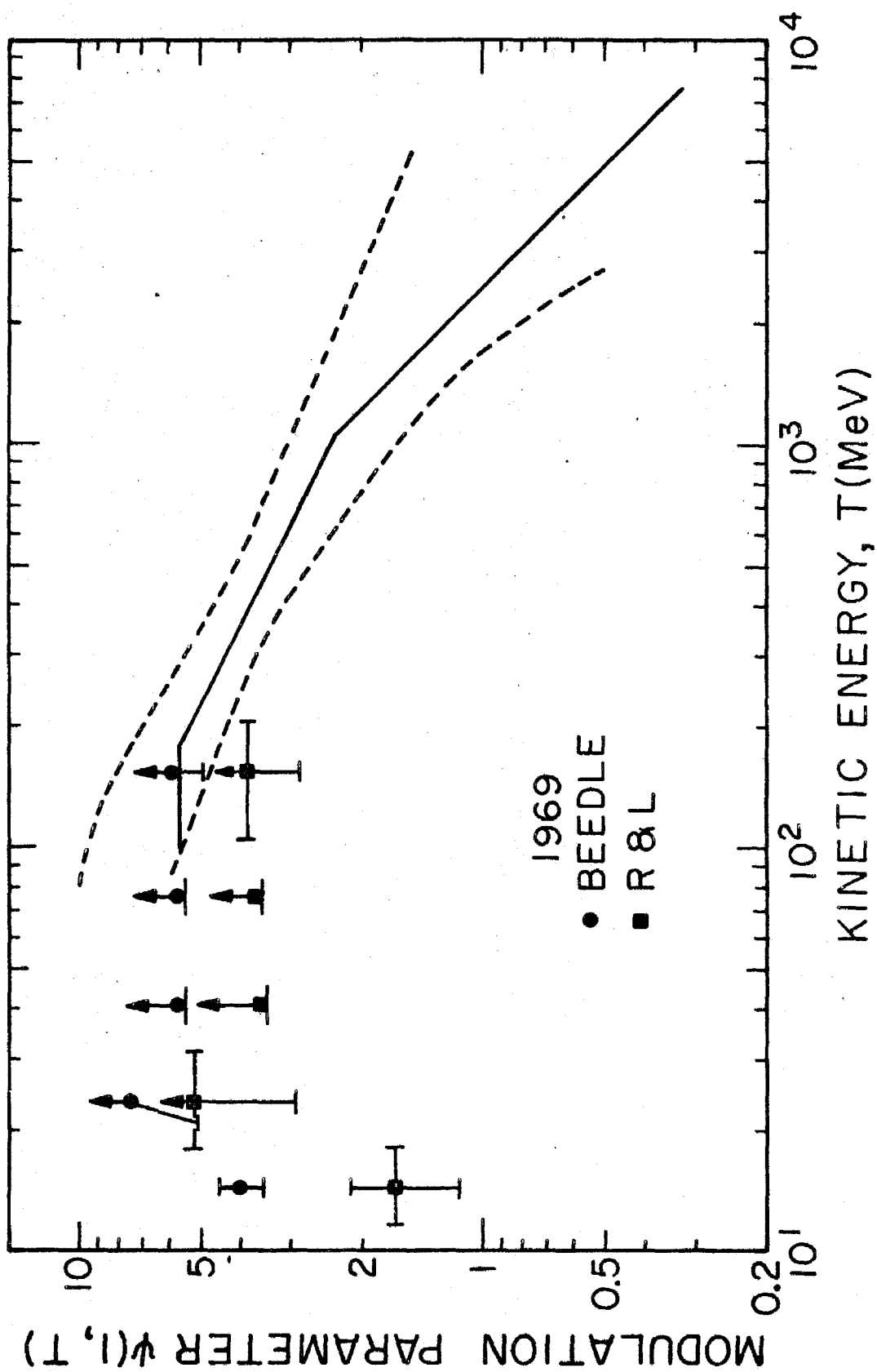

Figure VI-14c

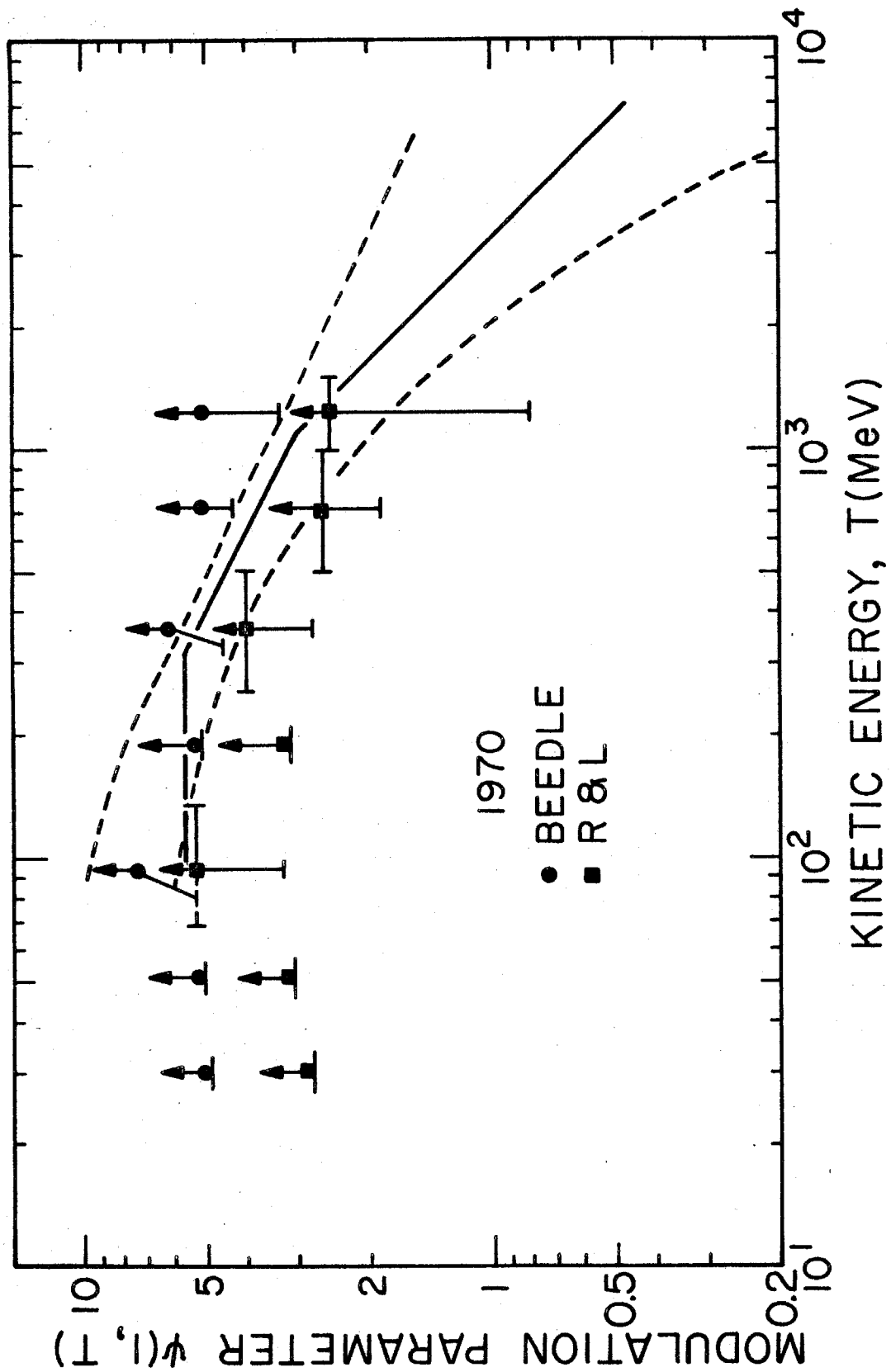

Figure VI-14d

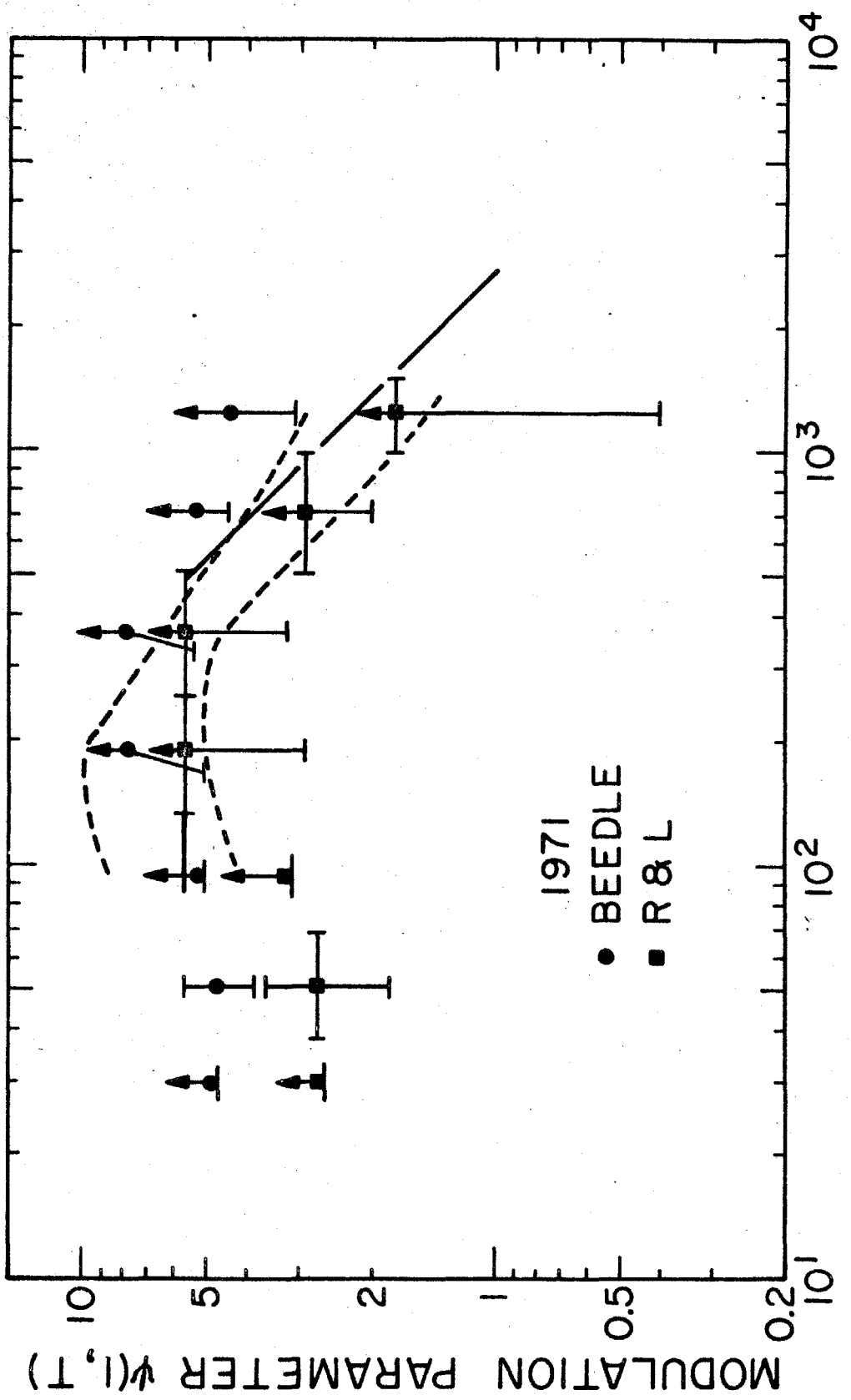

Figure VI-14e

Figure VI-15: Calculated and measured positron fractions as a function of energy for two different models of the galactic electron spectrum and diffusion coefficient. The calculated fractions at the boundary (solid) and at 1 AU (dashed) are shown. Above 100 MeV the diffusion coefficient for both model 1 and model 2 is given by equation VI-30 with the parameters listed in Table VI-2 for 1968. The galactic positron spectrum of Ramaty and Lingenfelter (1968) is assumed in the calculations.

MODEL 1: The nominal galactic electron spectrum from analysis of the non-thermal-radio-background data (Section VI.E.1) is used with a power-law extrapolation below 100 MeV (equation B-12). The diffusion coefficient for all energies is described by equation VI-30.

MODEL 2: The interstellar electron spectrum shown in Figure VI-16b (solid line) is used. The rigidity dependence of the diffusion coefficient is described by equation VI-30 except that below 60 MV $\kappa(R)$ is assumed proportional to 1/R.

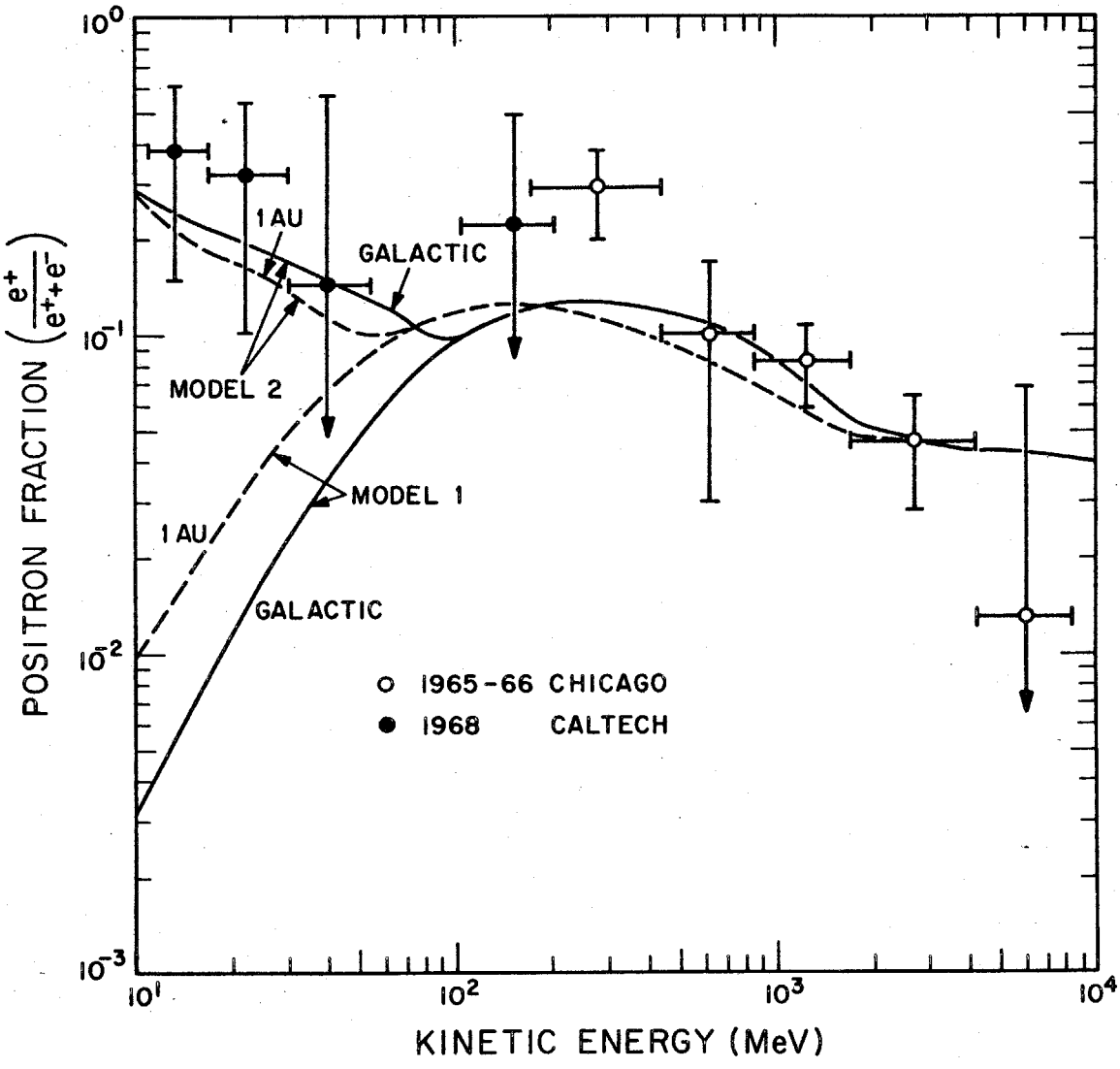
POSITRON FRACTION $\left(\frac{e^+}{e^+ + e^-}\right)$
KINETIC ENERGY (MeV)
1 AU
GALACTIC
MODEL 2
MODEL 1
1 AU
GALACTIC
1965-66 CHICAGO
1968 CALTECH

Figure VI-15

Figure VI-16: Positron and electron spectra derived from the modulation parameter of Figure VI-14b (solid line). Below 60 MV, $\kappa(R) \propto 1/R$. Above 60 MV, $\kappa(R)$ is given by equation VI-30 using the parameters listed in Table VI-2 for 1968.

Figure VI-16a: The calculated positron spectrum at 1 AU derived from a galactic spectrum calculated by Ramaty and Lingenfelter (1968). The near-Earth spectrum observed in 1968 (Caltech) is shown for comparison.

Figure VI-16b: The calculated electron spectrum at 1 AU derived from the indicated galactic electron spectrum. In order that the calculated and observed spectra at 1 AU agree (references for observations in Figure VI-1), the nominal galactic electron spectrum cannot be extrapolated by a power-law below ~100 MeV but must be modified as shown.

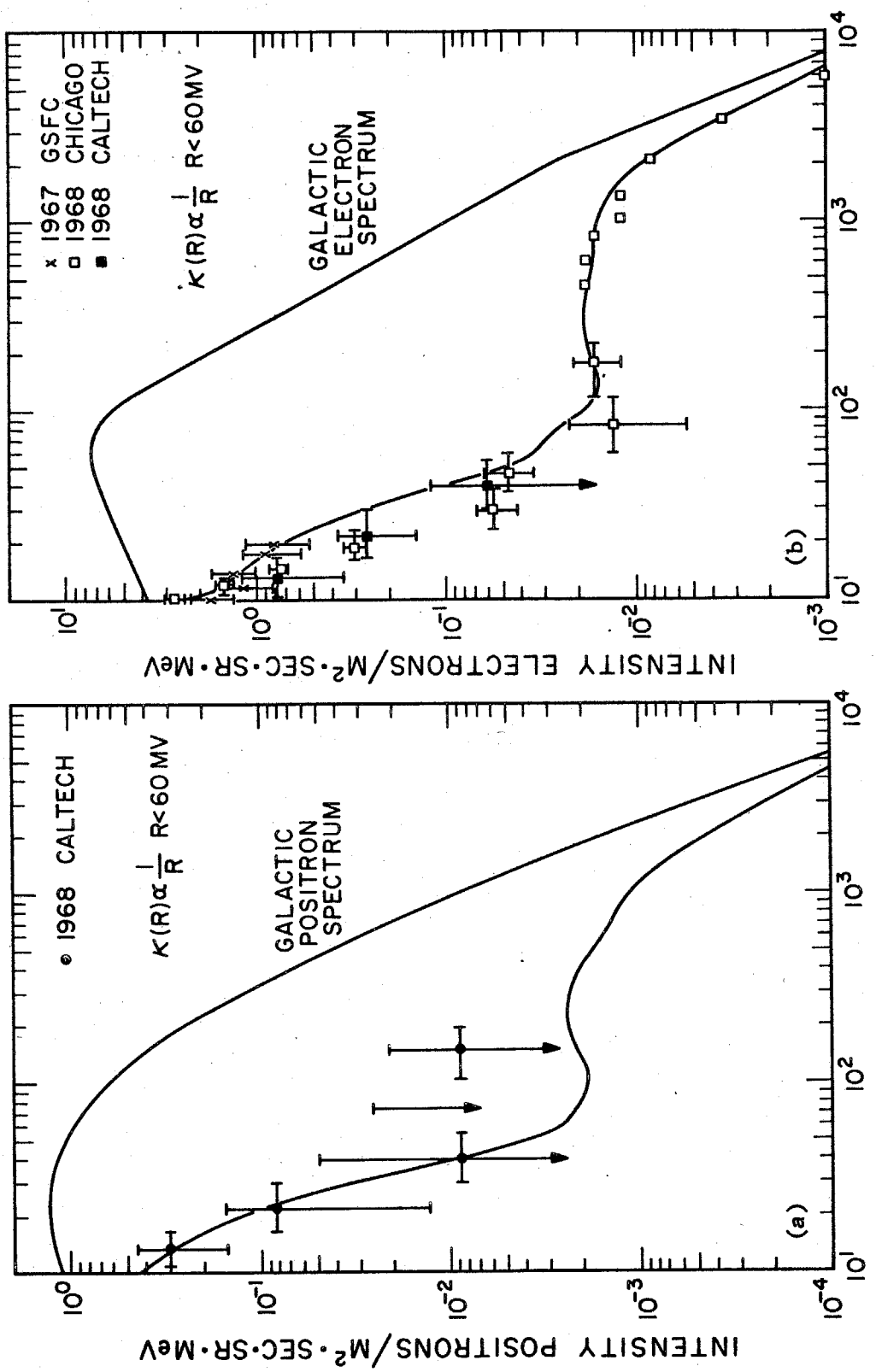
× 1967 GSFC
□ 1968 CHICAGO
■ 1968 CALTECH
$K(R)\alpha\frac{1}{R}$ R<60MV
GALACTIC ELECTRON SPECTRUM
(b)
INTENSITY ELECTRONS/M²·SEC·SR·MeV
● 1968 CALTECH
$K(R)\alpha\frac{1}{R}$ R<60 MV
GALACTIC POSITRON SPECTRUM
(a)
INTENSITY POSITRONS/M²·SEC·SR·MeV
KINETIC ENERGY (MeV)

Figure VI-16

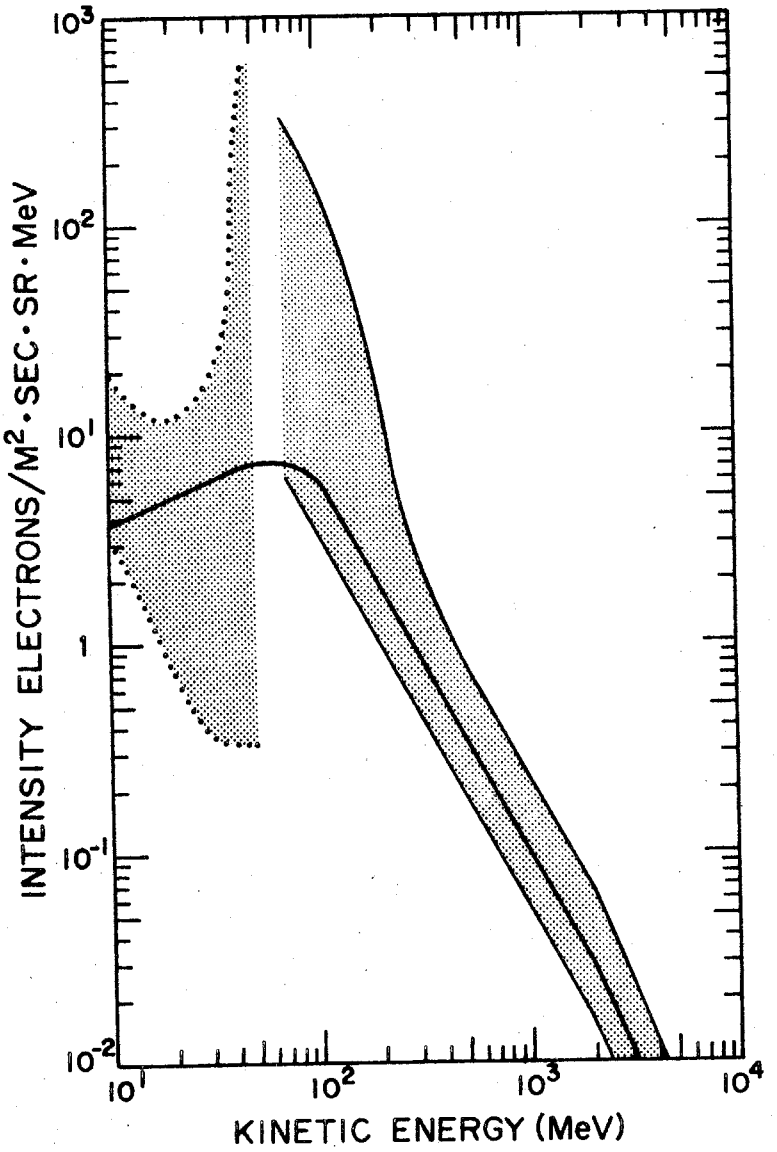

Figure VI-17: Approximate range of the interstellar electron spectrum. The shaded region (bounded by dotted lines) below ~50 MeV indicates the range of demodulated electron data using the limiting positron modulation parameters shown as dotted lines in Figure VI-14b. The shaded region above ~70 MeV is the approximate range from the analysis of the non-thermal-radio-background data (Section VI.E.1). For comparison the assumed galactic electron spectrum of Figure VI-16b is shown as the solid line.

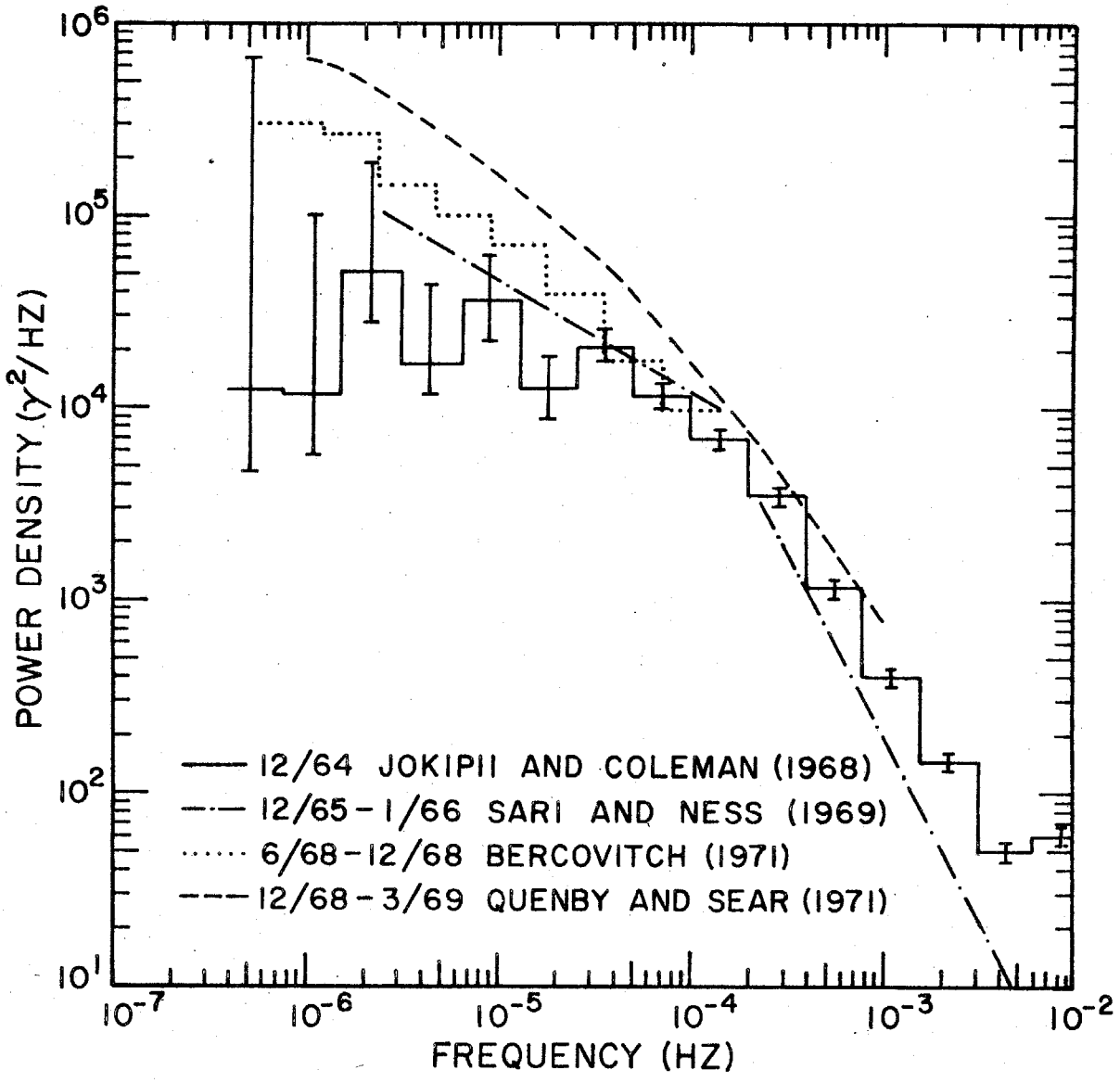

Figure VI-18: Observed power spectra of the interplanetary magnetic field.

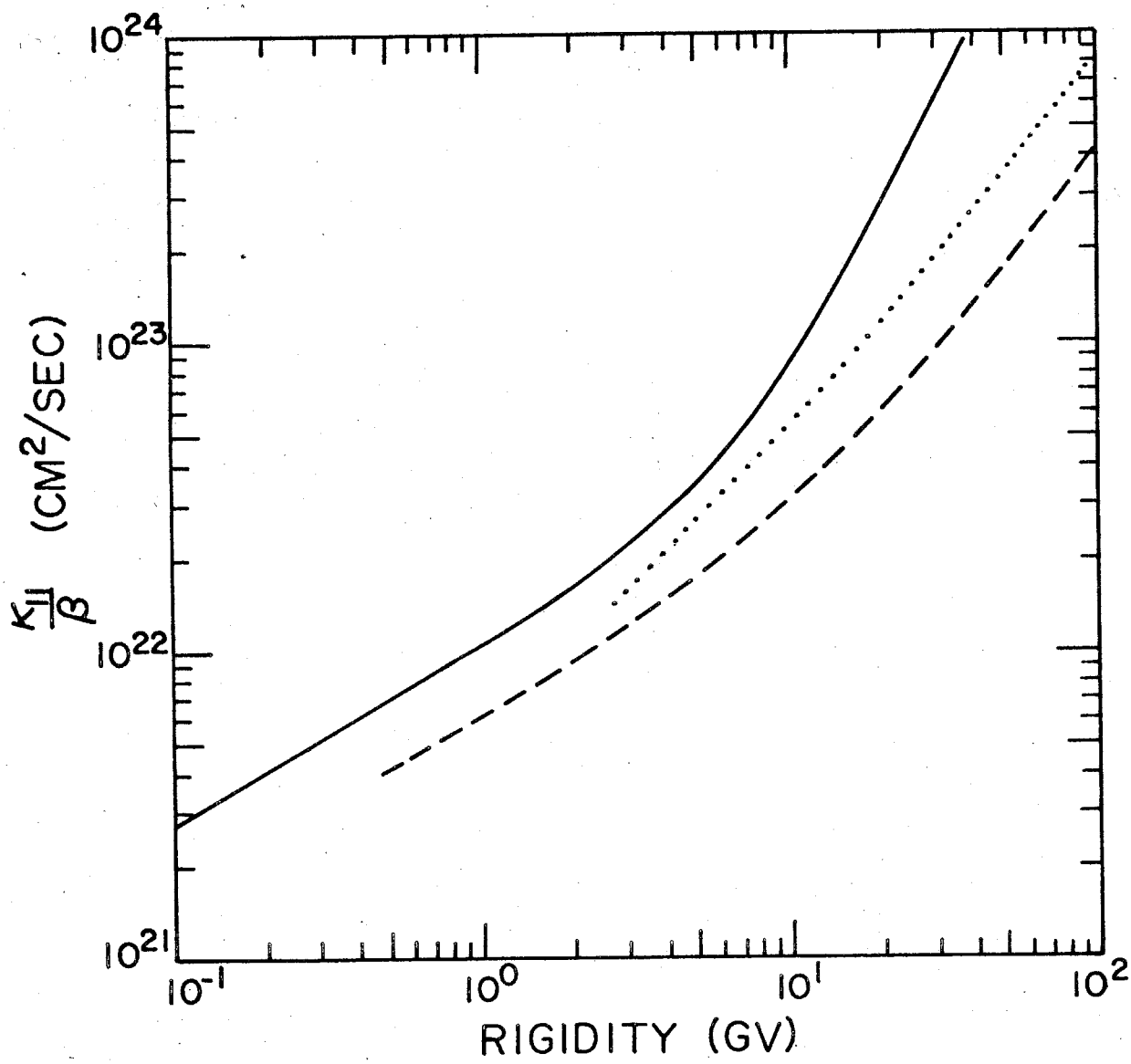

Figure VI-19: Parallel diffusion coefficients calculated from the power-spectra data (Figure VI-18) of Jokipii and Coleman (1968) (solid line), Bercovitch (1971) (dotted line), and Quenby and Sear (1971) (dashed line).

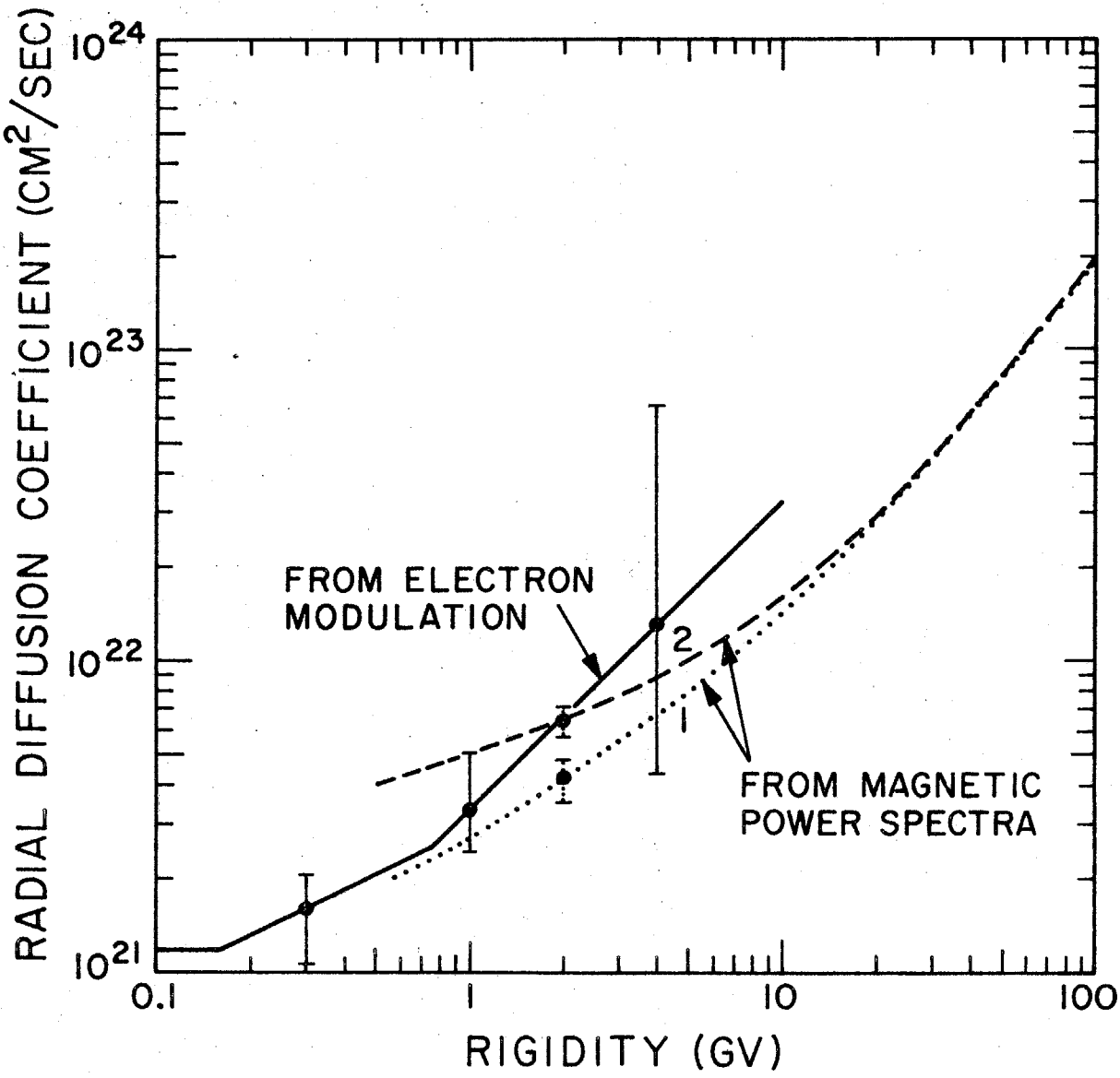

Figure VI-20: Radial diffusion coefficients derived from the 1968 electron modulation study and from the magnetic power spectra of Quenby and Sear (1971) (12/68-3/69). Two power-spectra-derived curves are shown. Curve 1 is derived under the assumption $\kappa_\perp \ll \kappa_\parallel$, and curve 2 corresponds to the case $\kappa_\perp = 4 \times 10^{21}$ cm^2/sec. The error bars on curves 1 and 2 correspond to a 2σ uncertainty in the power-spectra data. The electron modulation result is derived from the modulation parameter of Figure VI-12b (solid line) assuming κ independent of radius with a boundary at 12 AU. The three error bars correspond to the limiting $\psi(1,T)$ (dashed lines in Figure VI-12b) based on the possible range of galactic electron spectra (Figure VI-9).

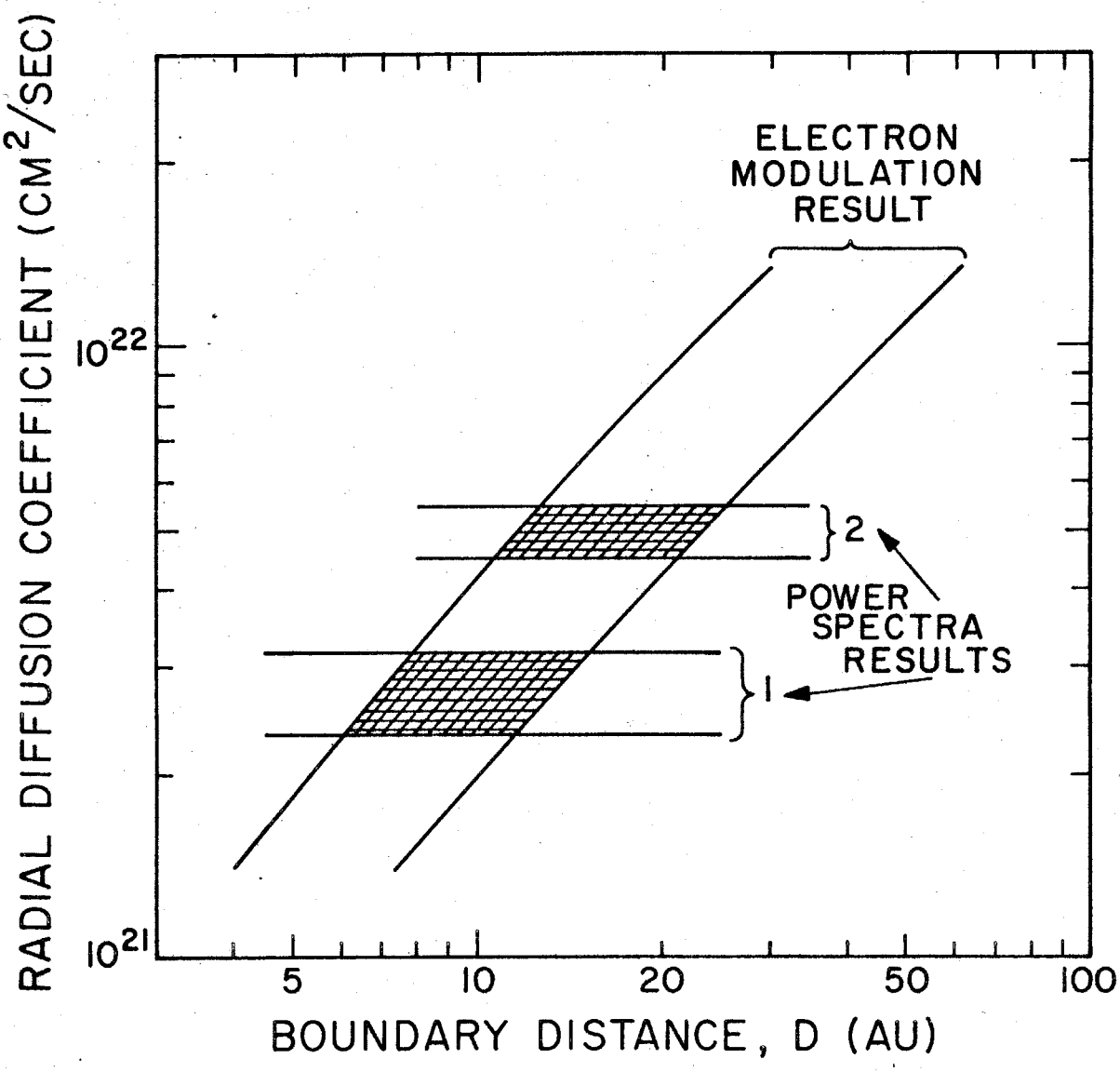

Figure VI-21: Comparison (at 1 GV) of the radial diffusion coefficient from Figure VI-20 as a function of boundary distance, D. The bands reflect the uncertainties indicated in Figure VI-20. The power-spectra results (curve 1 was derived assuming $\kappa_\perp \ll \kappa_\parallel$ and curve 2 corresponds to the case $\kappa_\perp = 4 \times 10^{21}$ cm^2/sec) are independent of the assumed boundary distance. The modulation result is derived assuming κ independent of radius inside D. The crosshatched areas indicate the range of boundary distances required for consistency between the two diffusion coefficients for the case $\kappa_1(r)$ = constant.

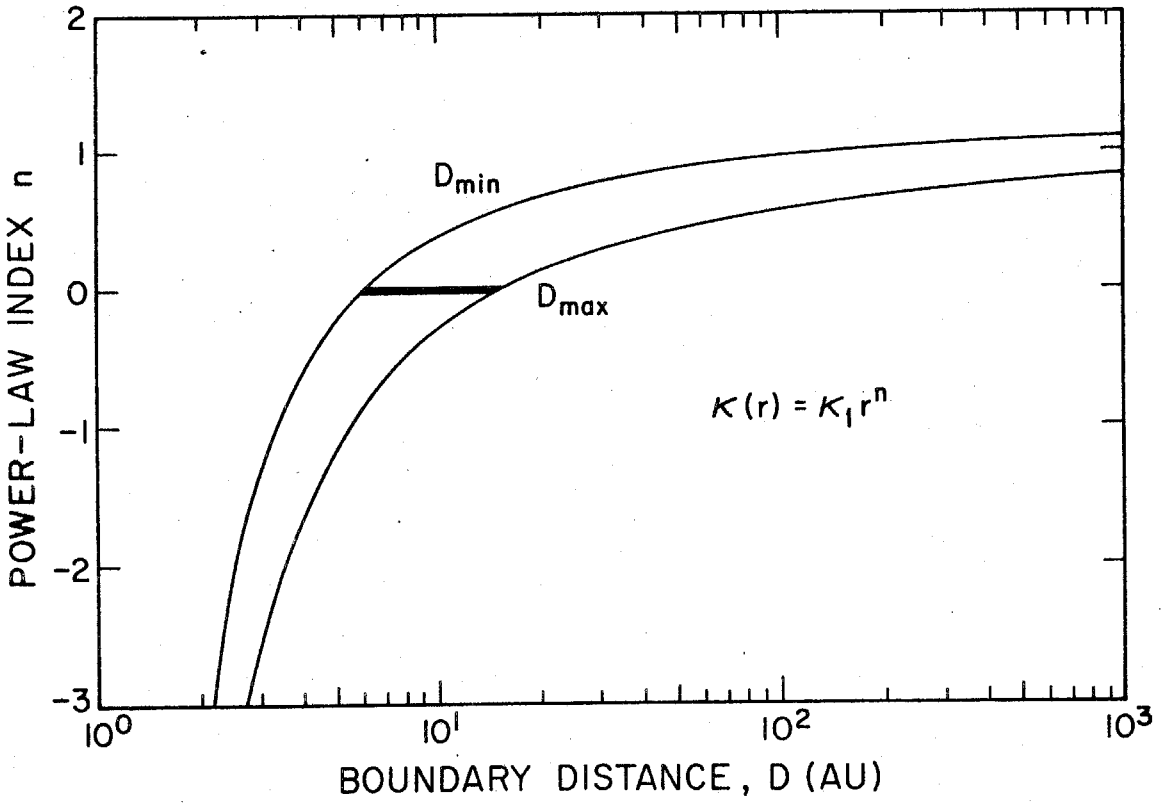

Figure VI-22: Limits on boundary distance, D, for various radial dependences of the radial diffusion coefficient, κ. The minimum and maximum D are plotted for different values of the power-law index n for the case $\kappa_\perp \ll \kappa_\parallel$. The horizontal bar at n = 0 indicates the range 6-15 AU obtained for κ independent of radius (see Figure VI-21).

Figure VI-23: Comparison of the measured and calculated proton spectra at 1 AU for the time periods shown. The same interstellar spectrum has been used in deriving each calculated spectrum. The numbers associated with the calculated curves refer to entry numbers in Table VI-3. The data collected with Caltech instruments are shown as filled circles (Garrard, 1973). Data from other references are

Figure VI-23a: Open circles - Fan et al. (1966)
Crosses - Ormes and Webber (1968)
Triangles - Fan et al. (1968)
Open diamond (for solar minimum in 1954)- McDonald (1958)

Figure VI-23b: Open squares - Lezniak and Webber (1971)

Figure VI-23c: Open squares - Hsieh et al. (1971)

Note that the low-energy portion of the interstellar spectrum is shown as a dashed line. Due to adiabatic deceleration in the interplanetary medium the calculated spectrum at 1 AU is insensitive to the interstellar intensity below ~100 MeV.

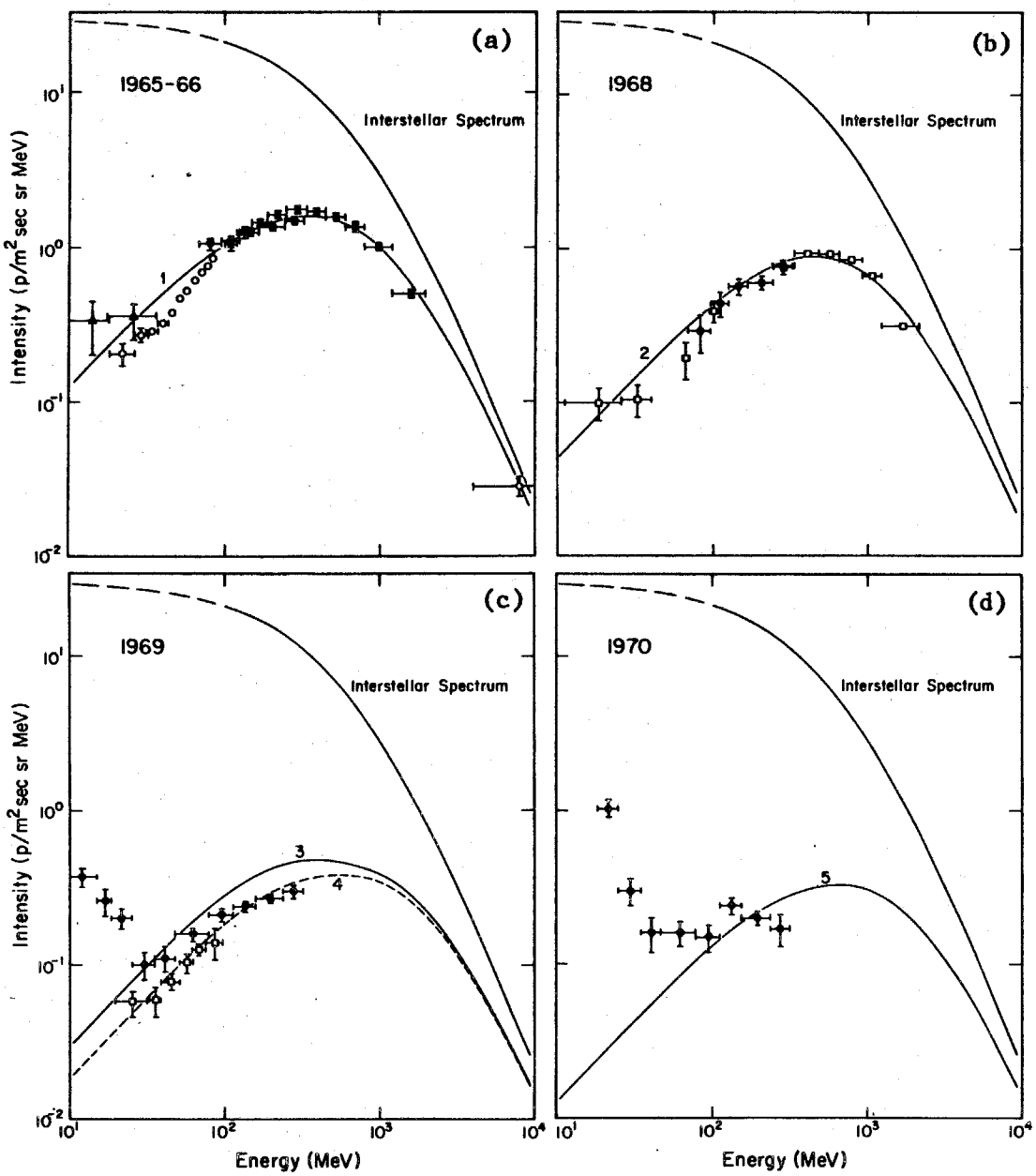
(a)
1965-66
Interstellar Spectrum
1
(b)
1968
Interstellar Spectrum
2
(c)
1969
Interstellar Spectrum
3
4
(d)
1970
Interstellar Spectrum
5
Intensity (p/m²sec sr MeV)
Energy (MeV)

Figure VI-23

Figure VI-24: Comparison of measured and calculated He nuclei spectra at 1 AU for the time periods shown. The same interstellar spectrum has been used in deriving each calculated spectrum. The numbers associated with the calculated curves refer to entry numbers in Table VI-3. The data collected with Caltech instruments are shown as filled circles (Garrard, 1973). Data from other references are:

Figure VI-24a: Open circles - Fan et al. (1966)
Crosses - Ormes and Webber (1968)
Triangles - Fan et al. (1968)

Figure VI-24b: Open squares - Lezniak and Webber (1971)

Figure VI-24c: Triangles - Mason (1972)

Note that the low-energy portion of the interstellar spectrum is shown as a dashed line. Due to adiabatic deceleration in the interplanetary medium the calculated spectrum at 1 AU is insensitive to the interstellar intensity below ~100 MeV/nucleon.

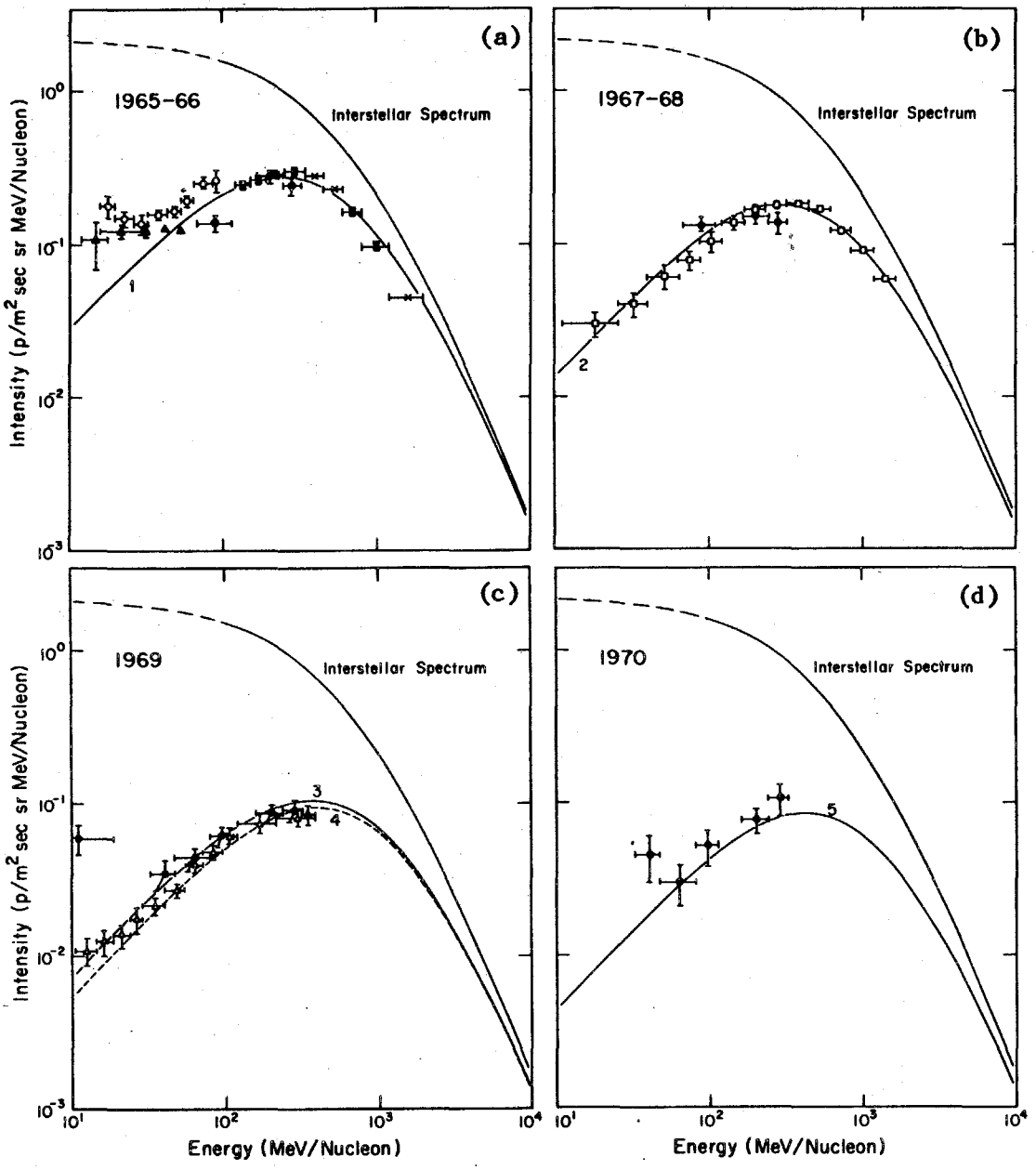
(a)
1965-66
Interstellar Spectrum
1
(b)
1967-68
Interstellar Spectrum
2
(c)
1969
Interstellar Spectrum
3
4
(d)
1970
Interstellar Spectrum
5
Intensity (p/m² sec sr MeV/Nucleon)
Energy (MeV/Nucleon)

Figure VI-24

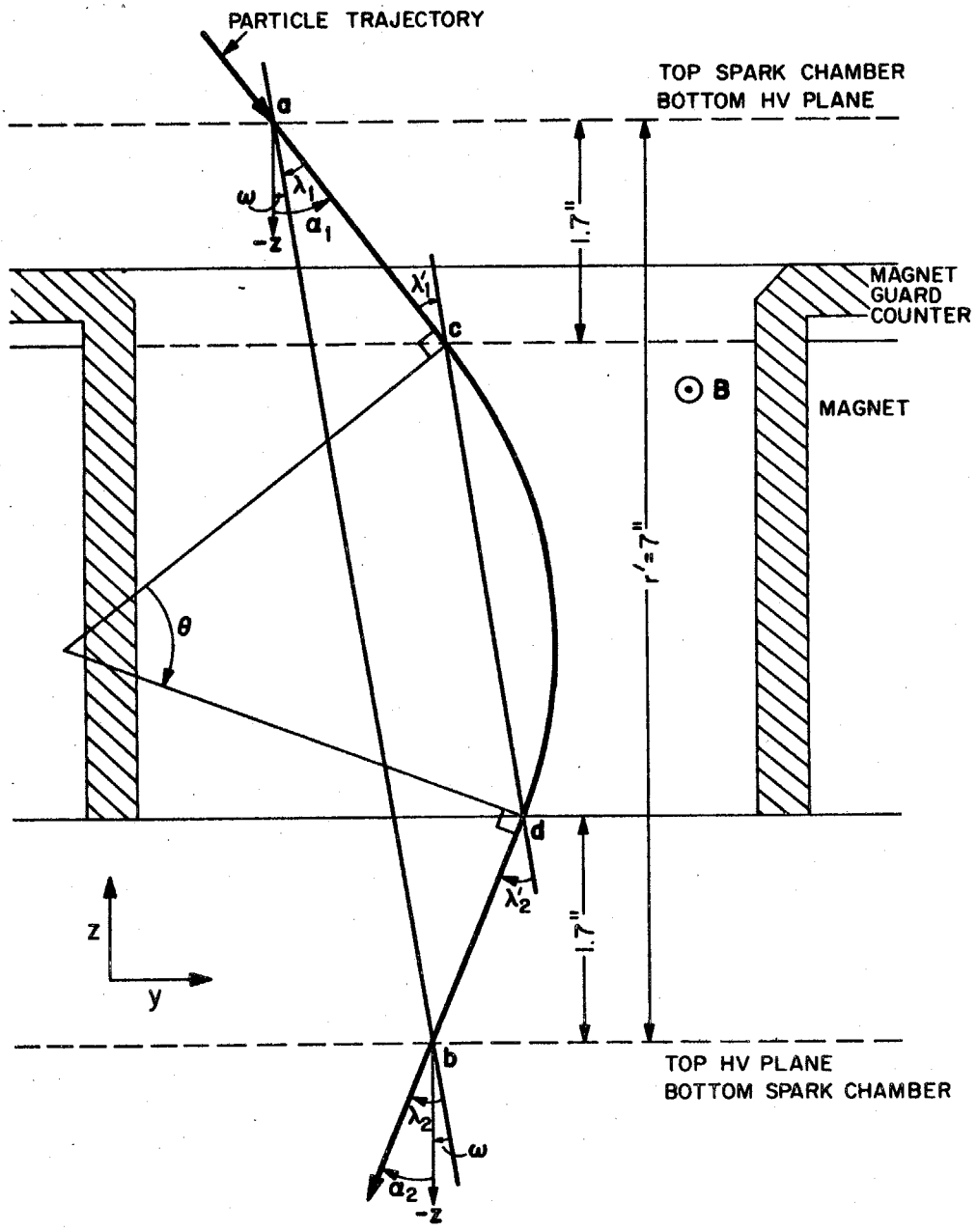

Figure A-1: Schematic view of a particle trajectory seen in projection. Parameters used in trajectory self-consistency checking are shown.

Figure A-2: Measured distributions of the trajectory parameter Λ using the MOD-1 detector. Also shown are the theoretical Gaussian distributions using the standard deviation of equation A-3a. The crosshatched areas are the rejection zones according to equation A-4b.

Figure A-2a: Mono-energetic beam of 790 MeV positrons.

Figure A-2b: Mono-energetic beam of 85 MeV positrons.

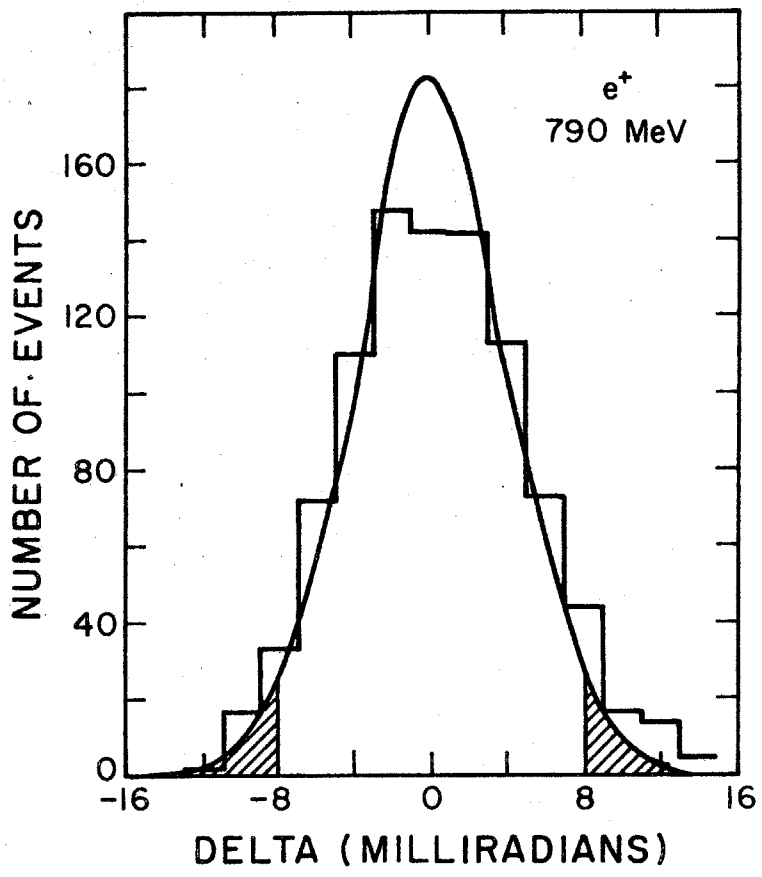

Figure A-2a

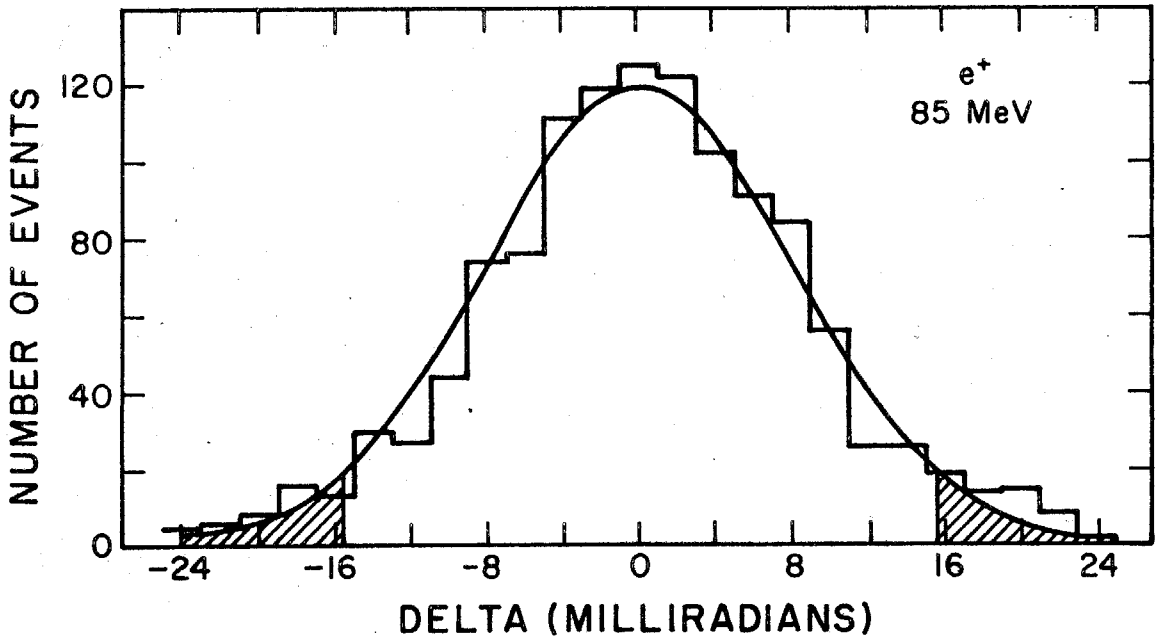

Figure A-2b

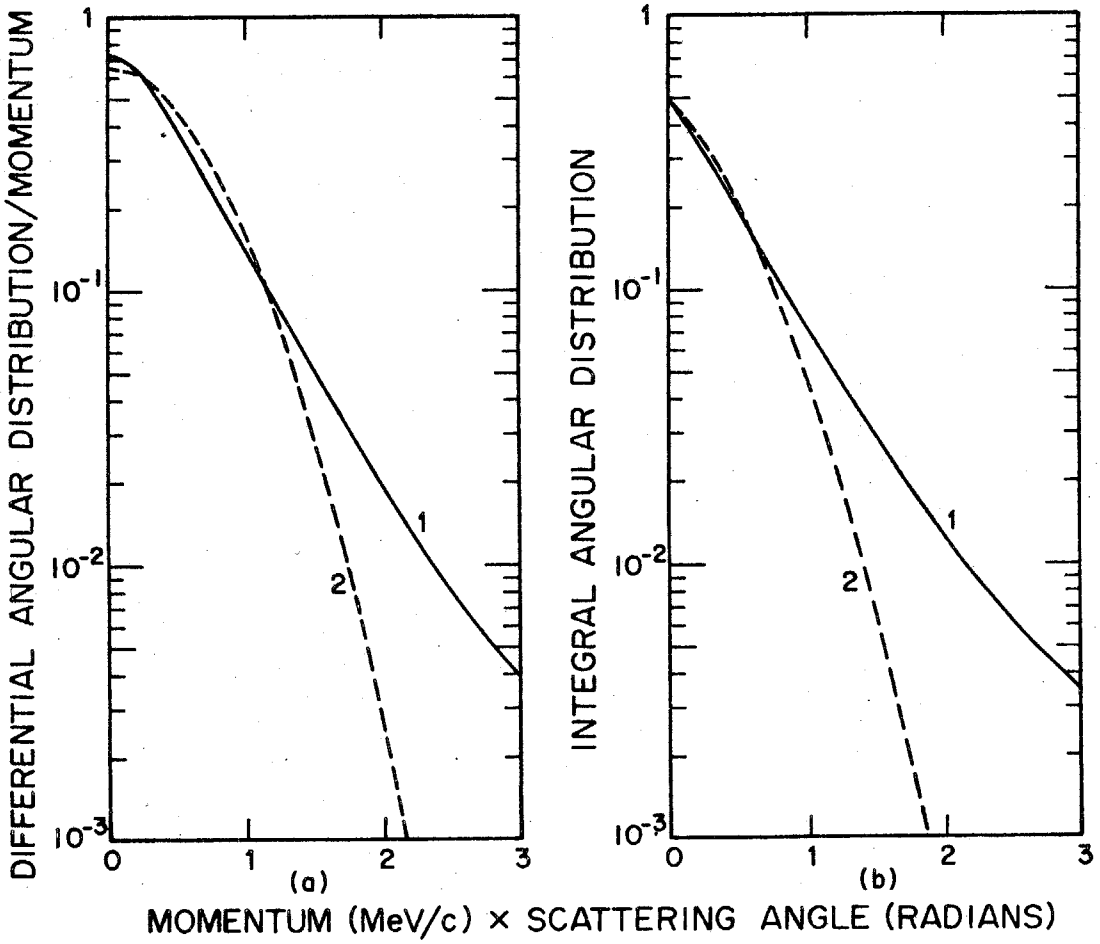

Figure A-3: Calculated electron scattering-angle distribution. Curve 1 is the angular distribution of the projected scattering angle. As plotted, the curve is valid for all electron momenta above a few MeV/c. Curve 2 is a Gaussian distribution with σ = .60 MeV/c radians. Only one sign of the scattering angle is shown since the distribution is symmetric about zero.

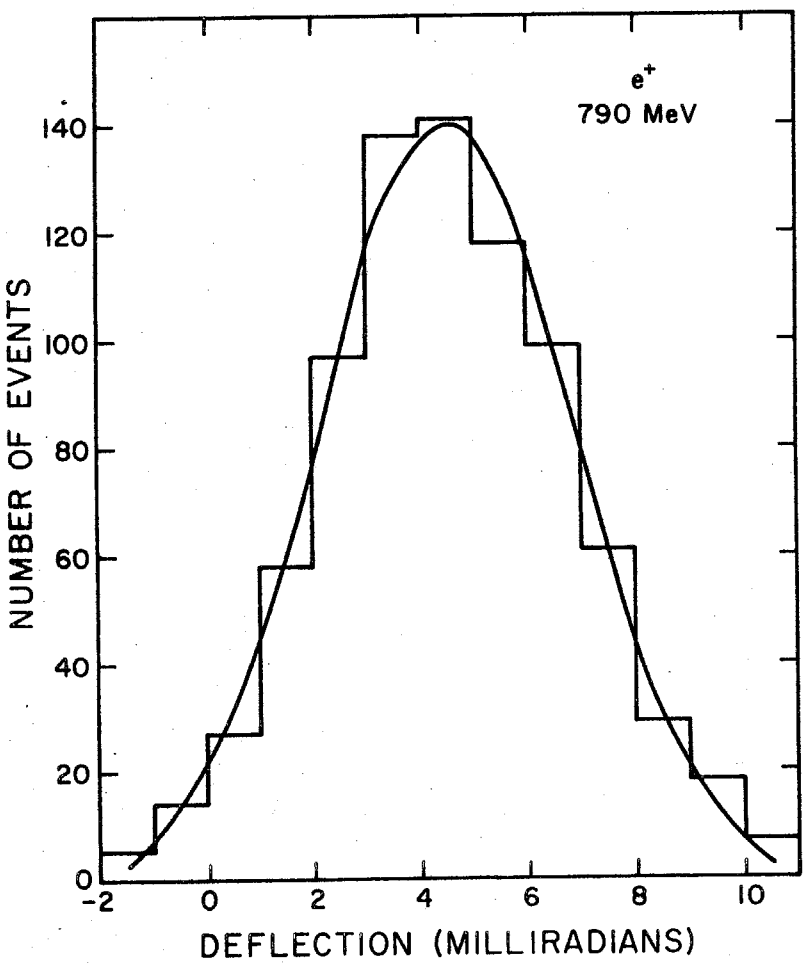

Figure A-4: Distribution of measured deflection angles in a 790 MeV positron beam (nominal θ = .0045 radians). The smooth curve is a least-squares fit of the data to a Gaussian distribution (σ = .0023 radians).

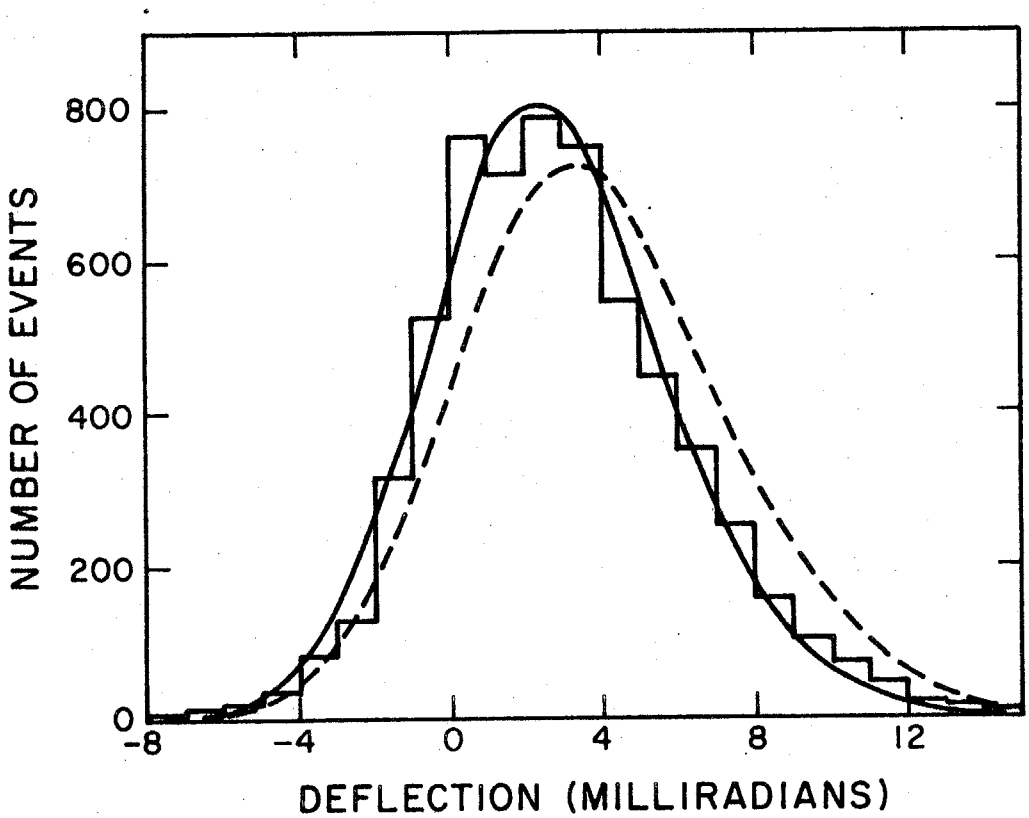

Figure A-5: Distribution of small deflections measured during the nighttime period of flight 71C2. The predicted angular distributions of cosmic-ray protons (solid curve-solar maximum spectrum; dashed curve-solar minimum spectrum) are shown for the instrument angular resolution function with σ_A = .0025 radians.

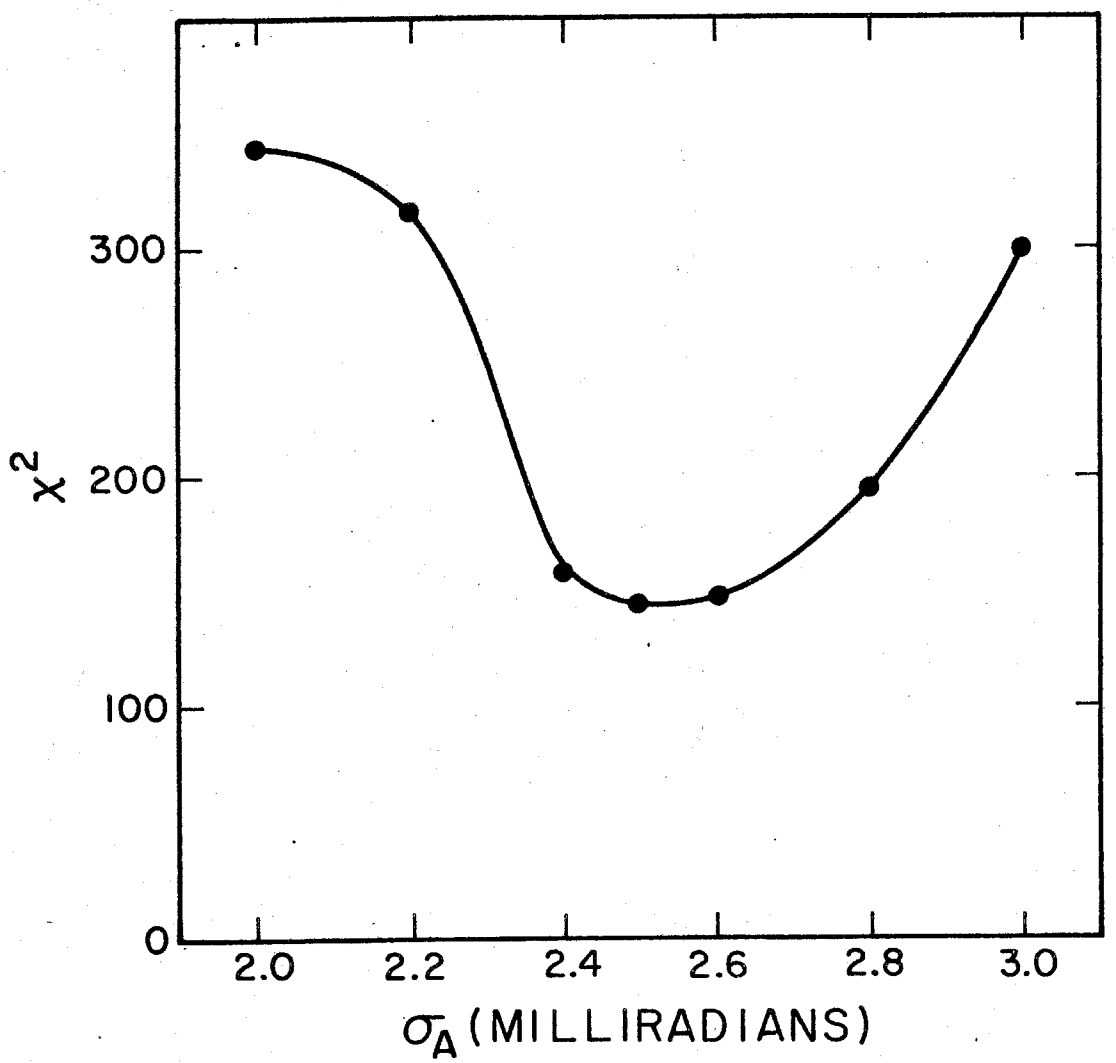

Figure A-6: χ^2 versus σ_A for fitting the calculated angular distribution to the measured distribution of cosmic-ray protons shown in Figure A-5. The proton spectrum appropriate for solar maximum has been assumed.

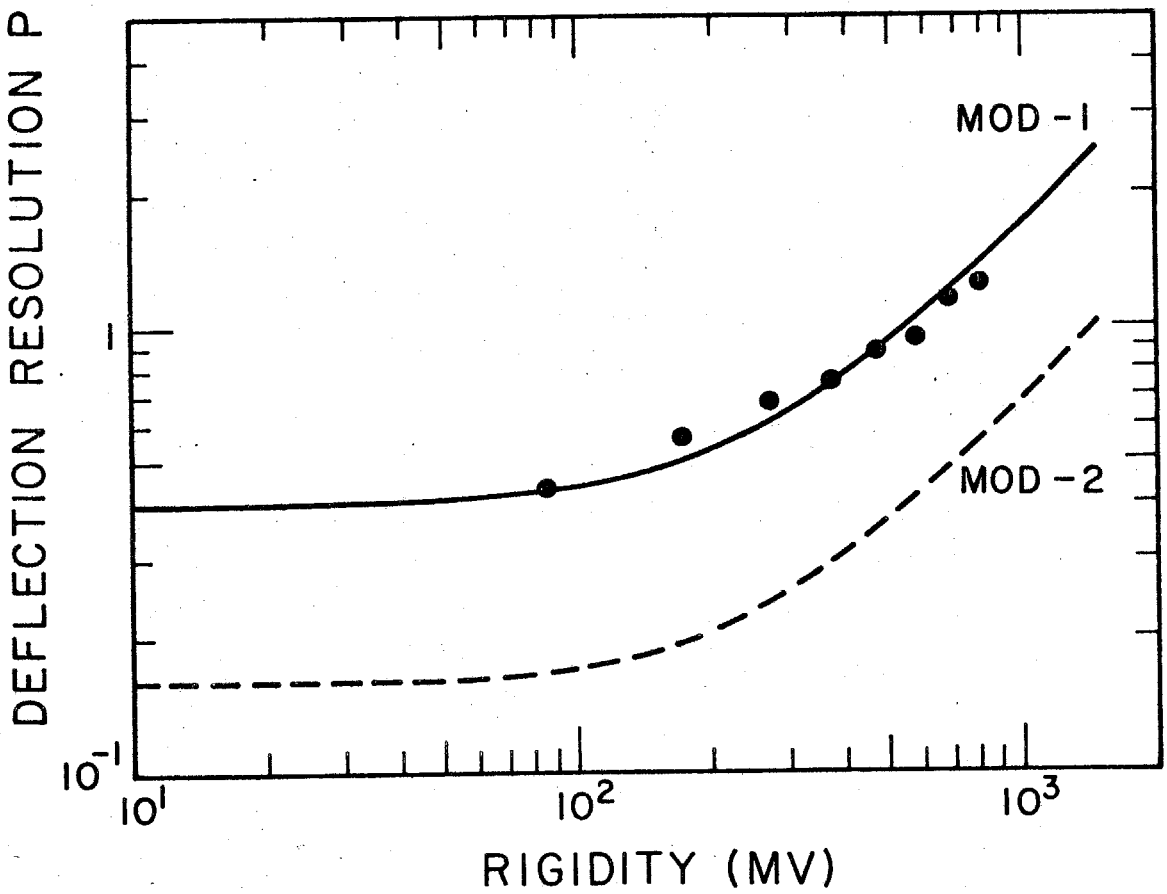

Figure A-7: Deflection resolution P, FWHM, of the detector versus rigidity. The data points represent measurements in a mono-energetic positron beam using the MOD-1 detector. Calculated curves for the detector in both the MOD-1 configuration (solid) and MOD-2 configuration (dashed) are shown.

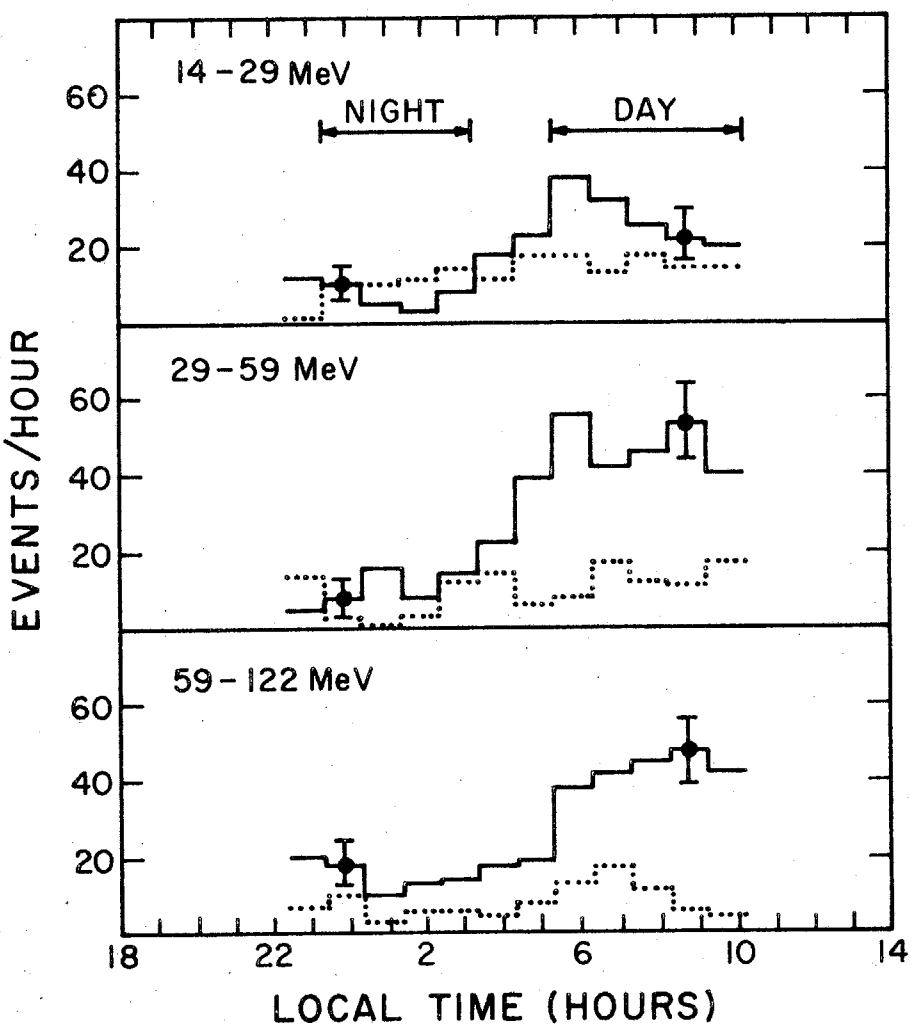

Figure A-8: Measured count rate of $G\check{C}$ (solid) and NON-$G\check{C}$ (dotted) events in the three lowest energy intervals for flight 71C2. The respective night and day analysis intervals are indicated.

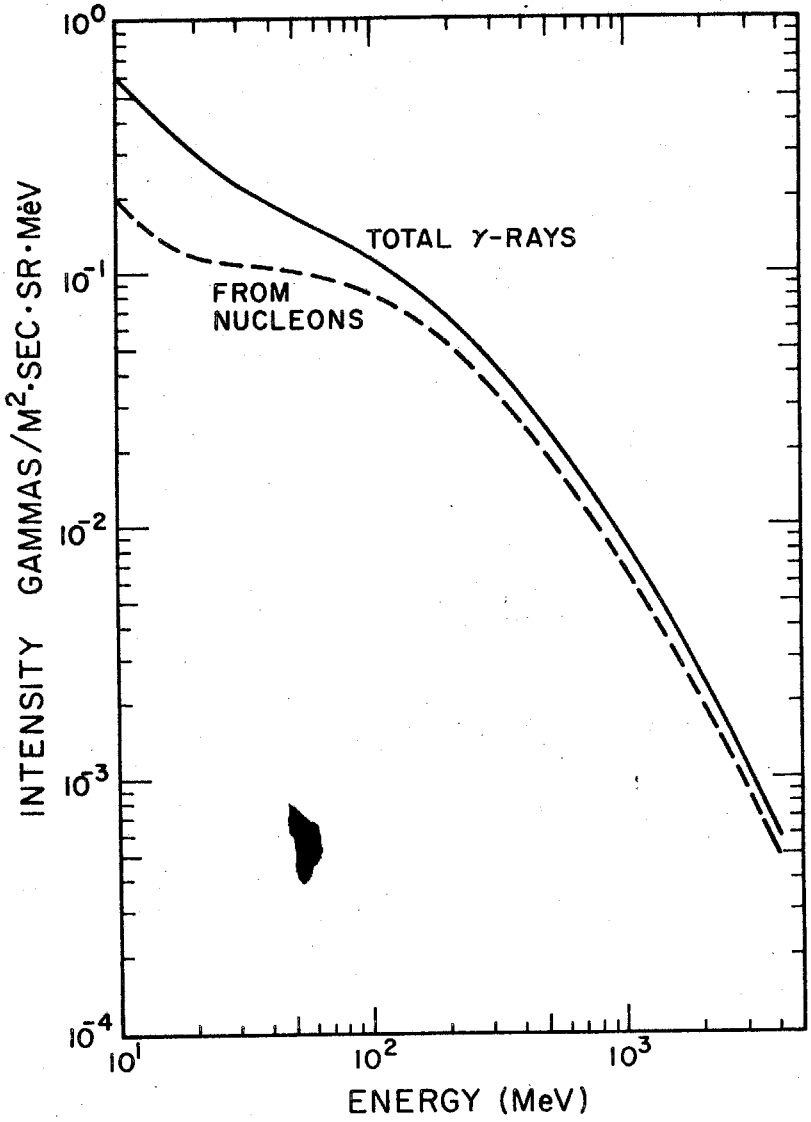

Figure A-9: Gamma-ray spectrum at 2.4 g/cm^2 altitude used in calculating the flux of negatrons and positrons produced in the gas Čerenkov counter. The gamma-ray spectra from the calculations of Beuermann (1971) resulting from cosmic-ray nuclei alone (dashed) and nuclei + electrons (solid) are shown.

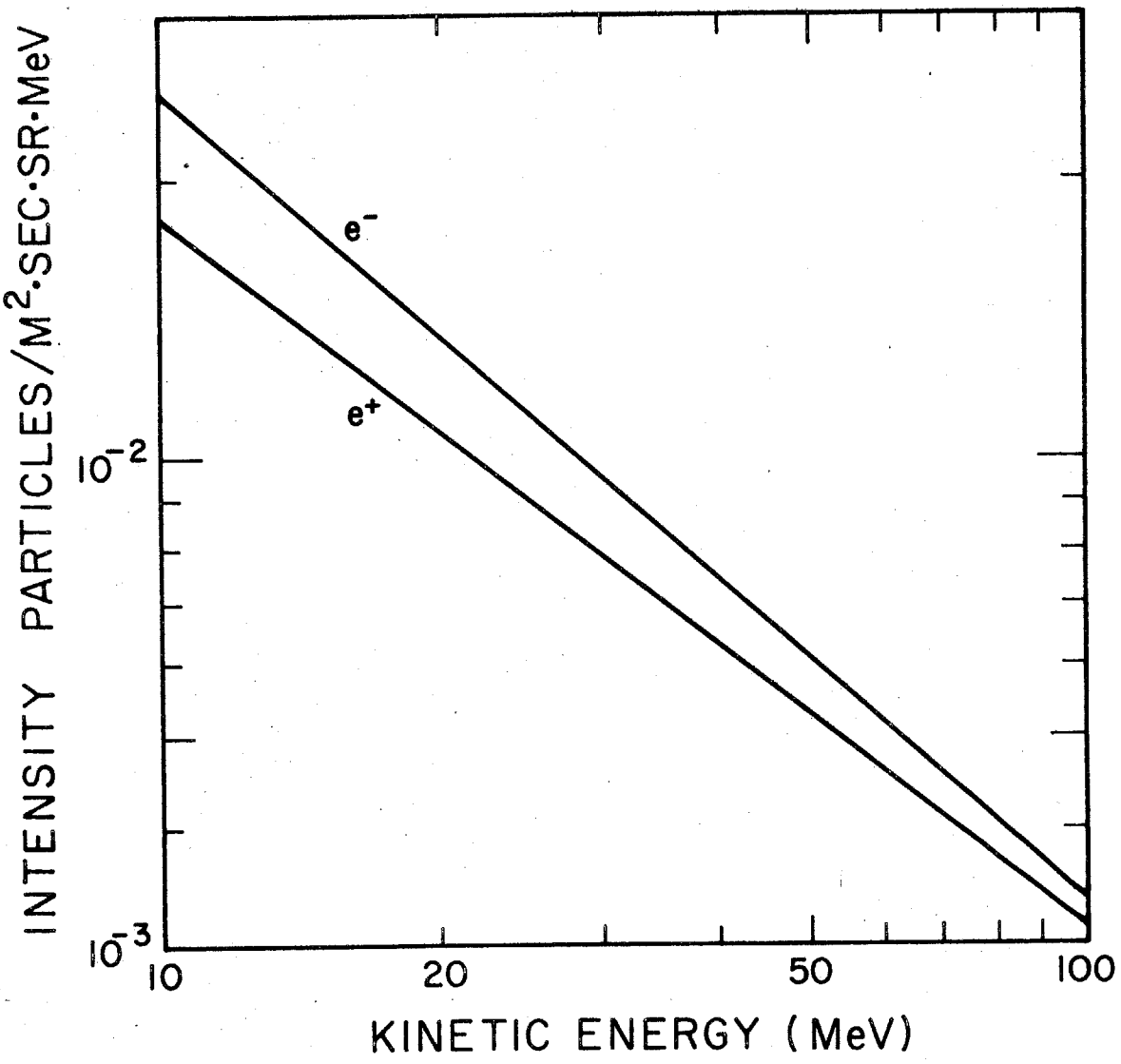

Figure A-10: Positron and negatron spectra from interactions of γ-rays in the gas Čerenkov counter.

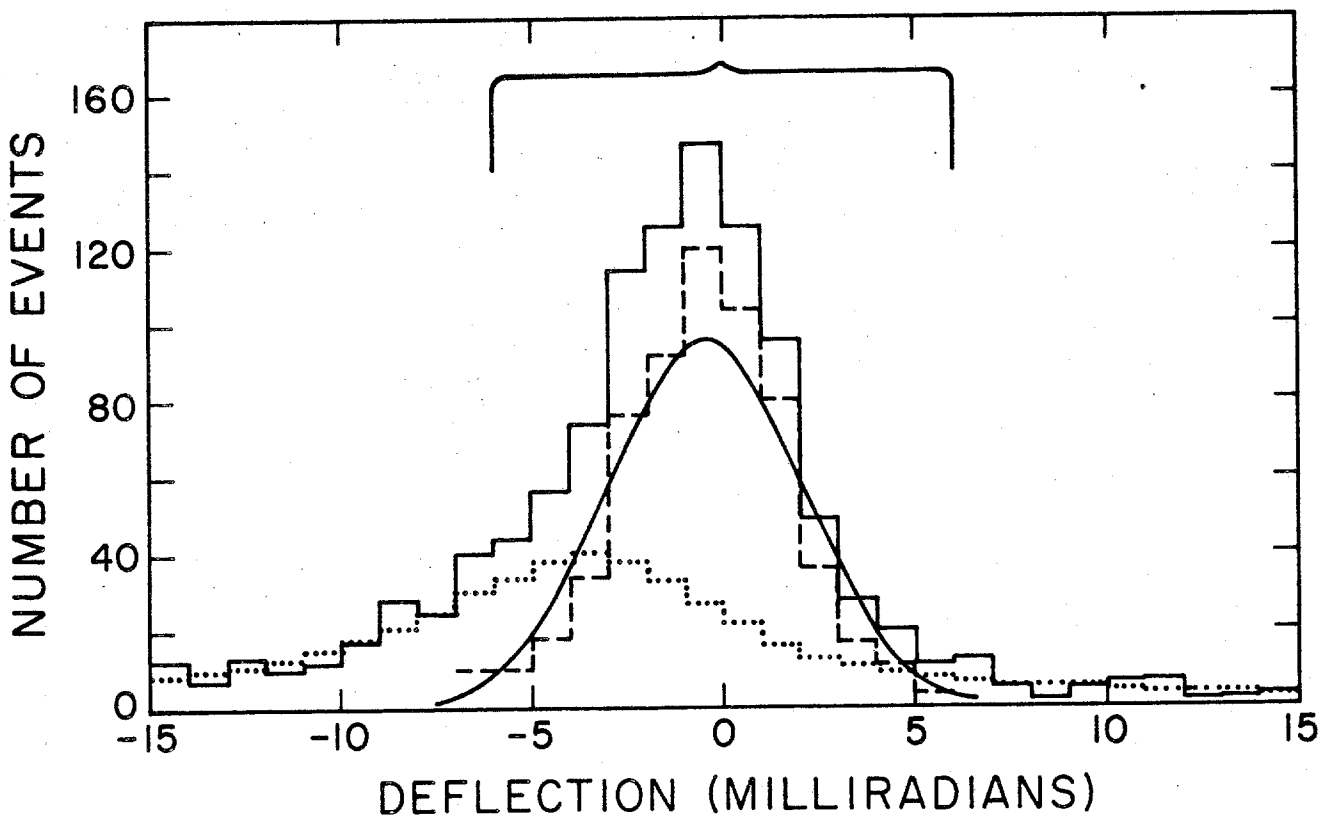

Figure A-11: Deflection-angle distribution of GC events for total observation period of 1971. The measured distribution is shown as a solid histogram. The calculated distribution of the sum of primary and secondary electrons is shown as the dotted histogram. The difference in the solid and dotted histogram is shown as the dashed histogram and represents the distribution of high-energy cosmic-ray nuclei. The solid curve is a Gaussian distribution with σ = .0025 radians. The bracketed region, where electrons cannot be resolved from nuclei, was excluded from analysis.

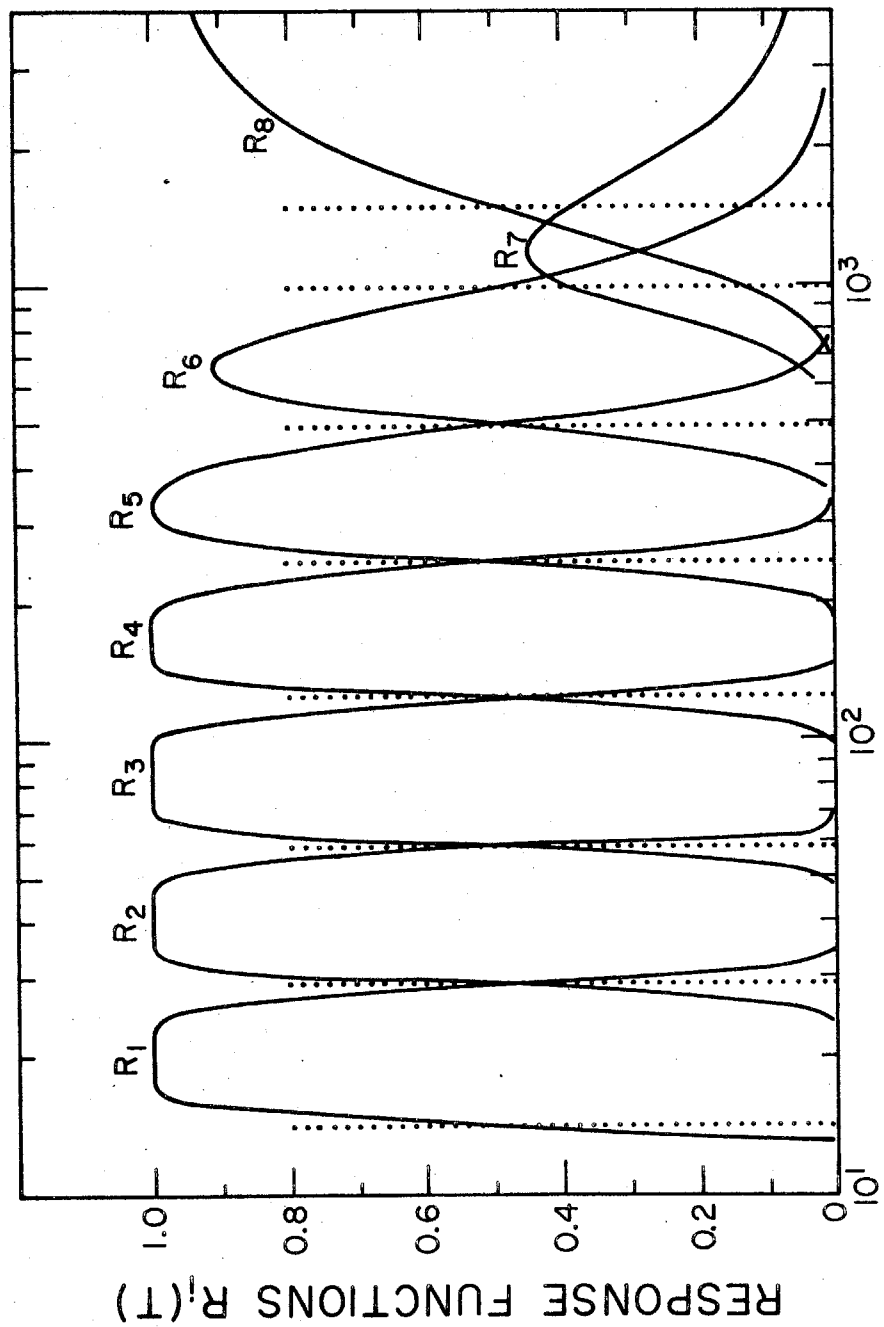

Figure A-12: Response functions, $R_i(T)$, for the MOD-2 detector system. Each curve represents the probability that a particle with kinetic energy T will be observed in the i^{th} energy interval. The dotted vertical lines indicate the end-points of the energy intervals described in Table IV-1.

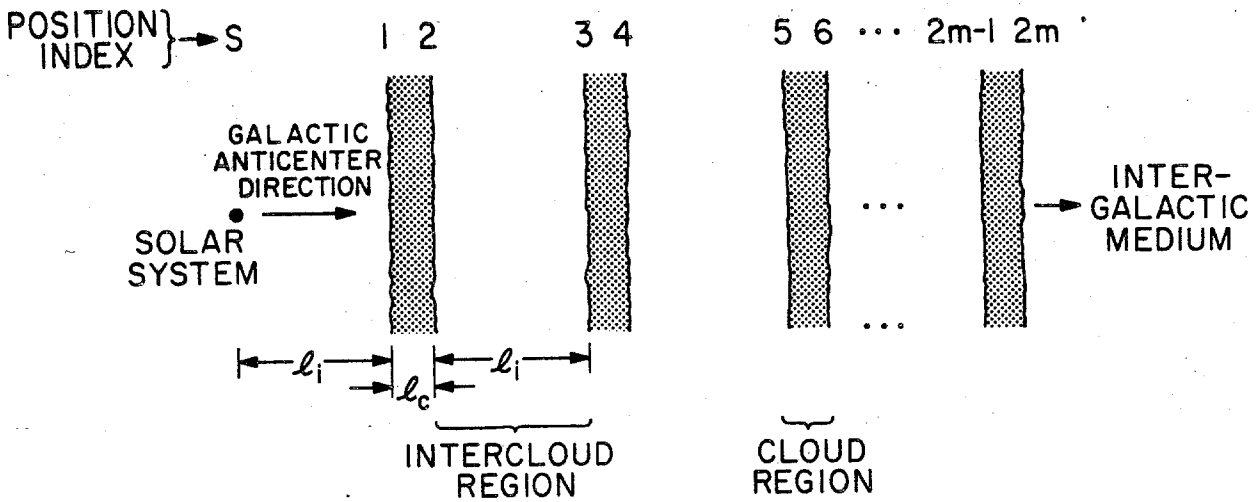

Figure B-1: Model of the galactic structure used in the calculations. The position of the solar system is labeled S. The clouds are all assumed to have width ℓ_c and are assumed to be separated by the distance ℓ_i. Each cloud boundary is labeled by a position index number; the radio intensity at each labeled position is given by equation B-8.

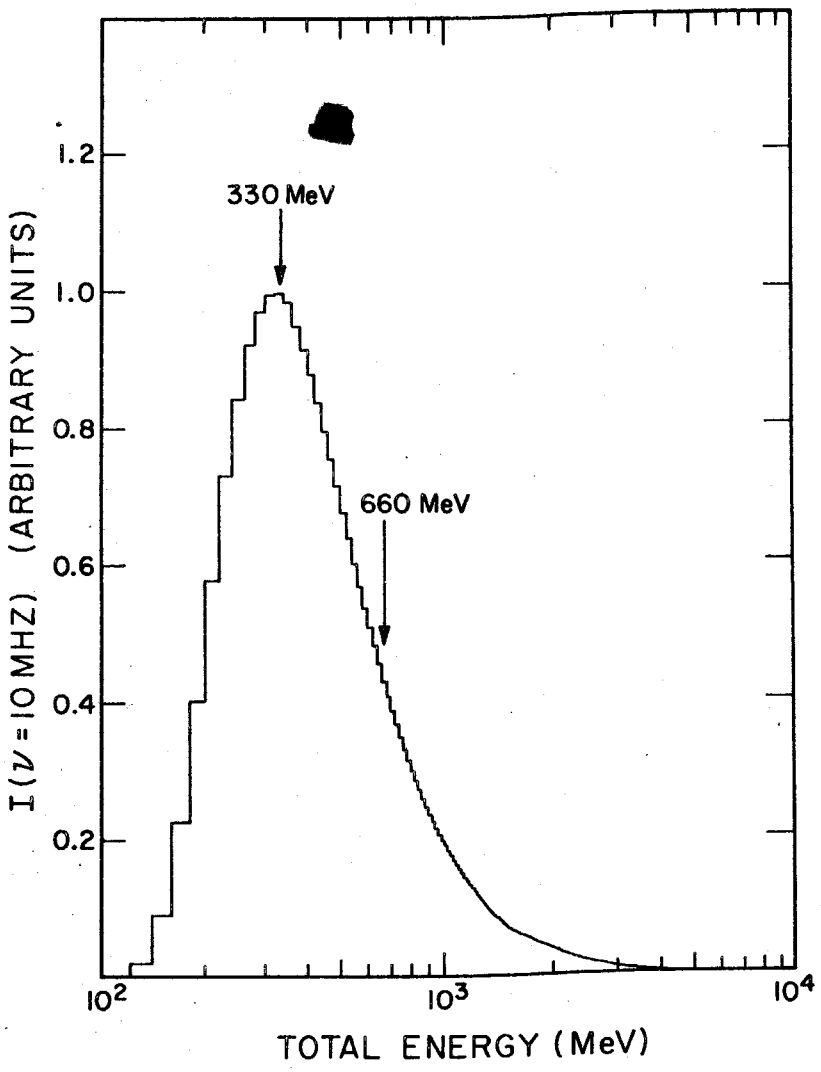

Figure B-2: Relative contribution to synchrotron intensity I at ν = 10 MHz from cosmic-ray electrons of different energies. The nominal galactic electron spectrum (equation B-12) has been used.

Figure B-3: Correspondence between radio frequency and electron energy. The energy at which electrons make the maximum contribution to the synchrotron intensity at the frequency ν is plotted for two different values of the magnetic field strength. In each calculation the nominal galactic electron spectrum (equation B-12) has been assumed.

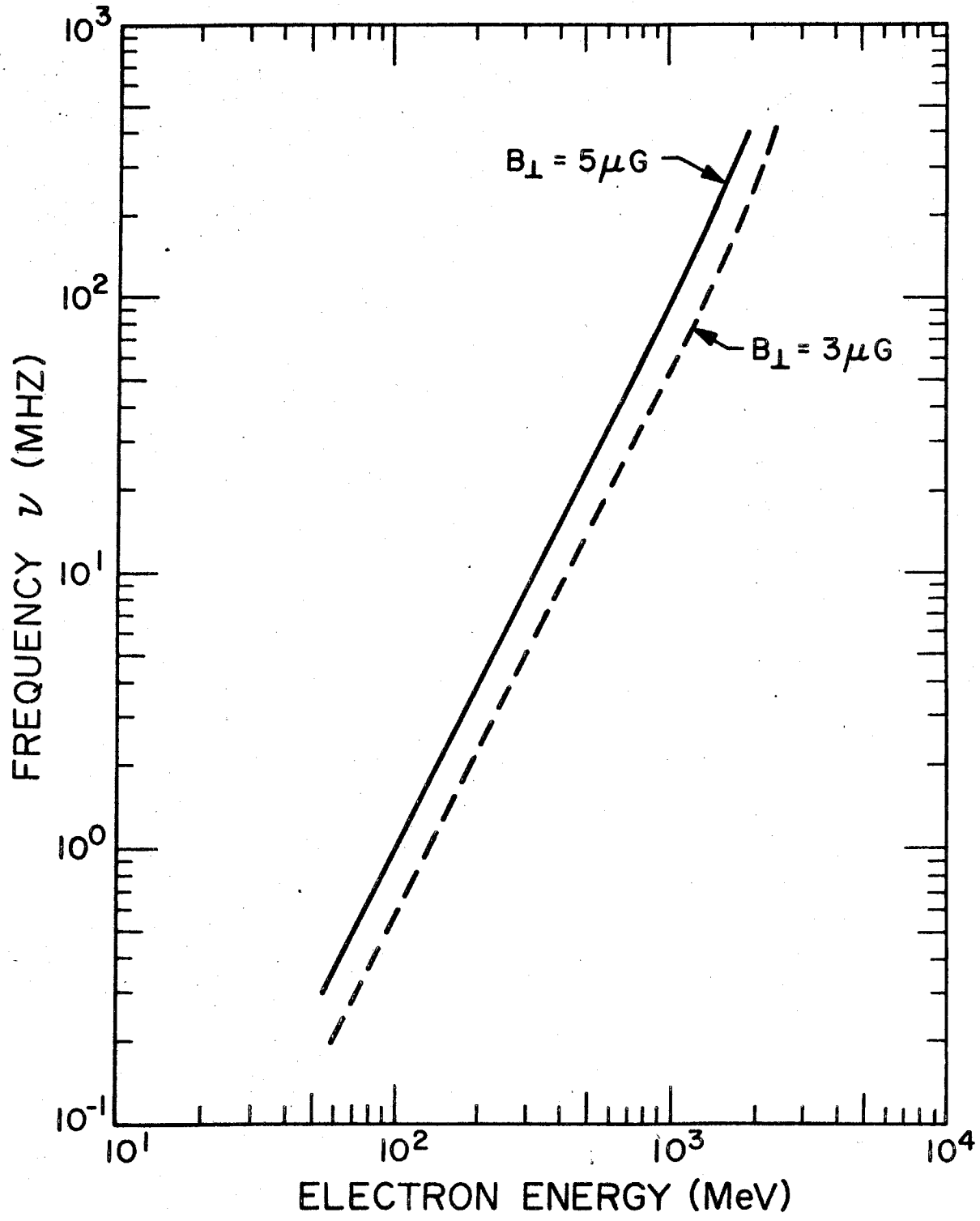
10^3
10^2
10^1
10^0
10^{-1}
FREQUENCY ν (MHZ)
$B_\perp = 5\mu G$
$B_\perp = 3\mu G$
10^1
10^2
10^3
10^4
ELECTRON ENERGY (MeV)

Figure B-3

Figure B-4: Relative variation of interstellar electron spectrum for the range of galactic parameters discussed in the text. F(W) is the ratio of the calculated interstellar electron intensity to the nominal interstellar intensity (equation B-12) at electron energy W. The nominal set of parameters is indicated by the bracket. Each labeled solid curve is calculated by changing the value of only the indicated parameter from the nominal set. The dashed lines correspond to the assumed range of variation used in computing the high and low galactic electron spectra shown in Figure VI-9.

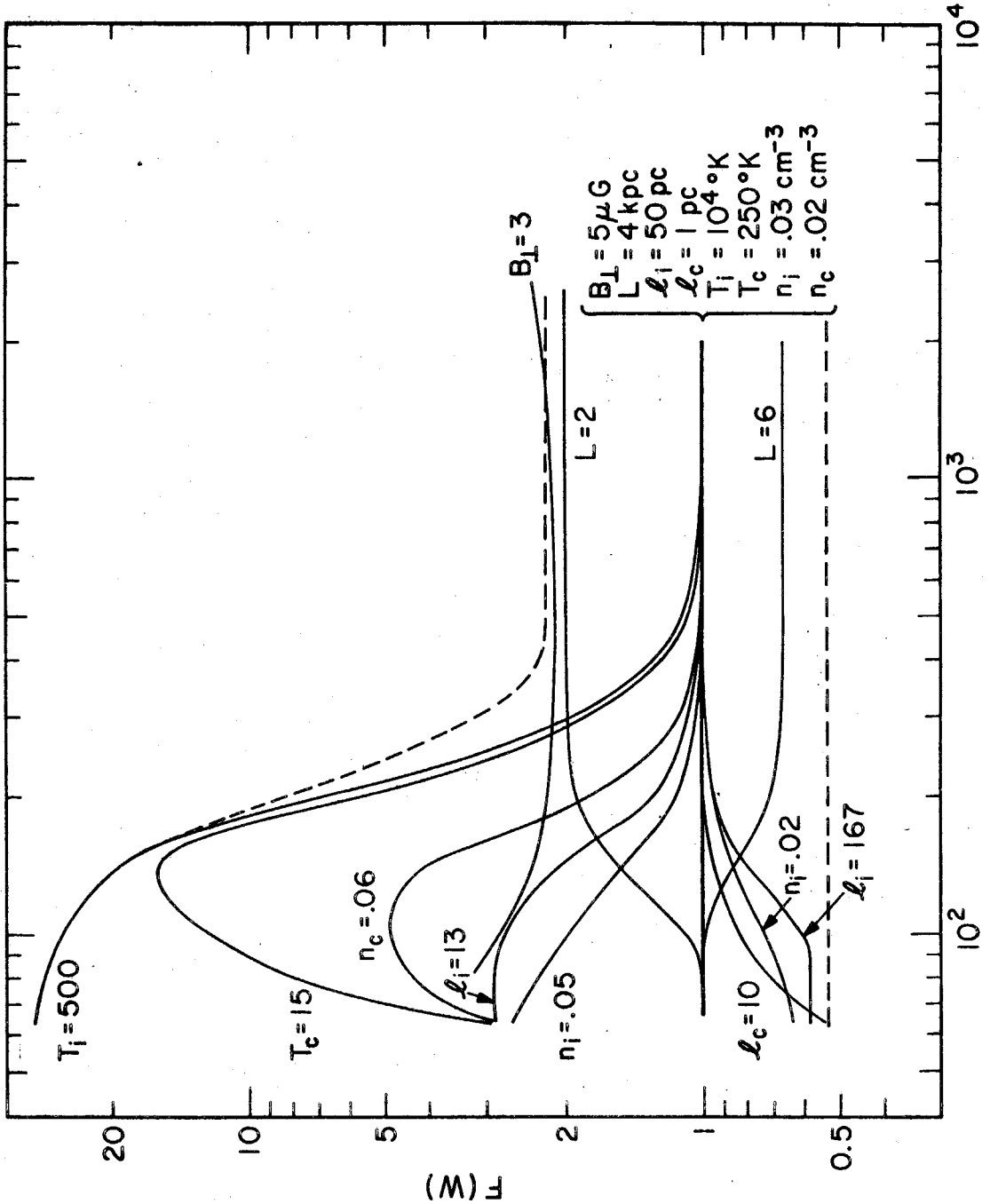
Γ (W)
TOTAL ENERGY, W (MeV)
$B_\perp = 5\mu G$
$L = 4$ kpc
$\ell_i = 50$ pc
$\ell_c = 1$ pc
$T_i = 10^4$ °K
$T_c = 250$ °K
$n_i = .03$ cm^{-3}
$n_c = .02$ cm^{-3}
$B_\perp = 3$
L=2
L=6
$T_i = 500$
$T_c = 15$
$n_c = .06$
$\ell_i = 13$
$n_i = .05$
$\ell_c = 10$
$n_i = .02$
$\ell_i = 167$
20
10
5
2
1
0.5
10^2
10^3
10^4

Figure B-4